Degassing of open-vent low-silica volcanoes

Thesis

Degassing of open-vent low-silica volcanoes

José Luis Palma Lizana

Submitted in accordance with the requirements for the degree of

Doctor of Philosophy

Department of Earth Sciences

Faculty of Sciences

The Open University

March 2009

Abstract

Open-vent activity at volcanoes of low-silica composition, such as Stromboli (Italy), Villarrica (Chile), Mt. Erebus (Antarctica), is characterised by persistent passive gas emission and recurrent mild explosive outgassing. Four styles of bubble bursting activity have been recognised in such volcanoes: seething magma, small short-lived lava fountains, strombolian explosions and gas puffing. At Villarrica, one of the two case study volcanoes, seething magma consists of continual bursts of bubbles up to a few metres in diameter, with varying strength over the entire surface of the lava lake. Small lava fountains, seen as a vigorous extension of seething magma, commonly last 20-120 s and reach 10-40 m above the lava free-surface. Strombolian explosions can last for less than a second in a single bubble burst that erupts mainly bombs, as seen at the lava lake of Mt. Erebus and Villarrica volcanoes, or for more than 30 seconds accompanied by large amounts of ash, as seen at Stromboli and Mt. Etna volcanoes. At Stromboli, the second case study volcano, gas puffing consists of small but repetitive bubble bursts with a generally stable eruption frequency in the range 0.2-1.2 s^{-1}. More vigorous explosive phenomena, such as hundreds-metres high lava fountains or very strong (paroxysmal) explosions, may occur during eruptions or episodes of elevated activity.

Correlations between seismicity and visual observations at Villarrica volcano indicate that the seismic tremor is mostly caused by explosive outgassing. Real-time Seismic Amplitude Measurements (RSAM) and SO_2 emission rates (measured by FLYSPEC) show a very good positive linear correlation between periods of background and elevated activity. Higher SO_2 emissions appear to be related to higher levels of the lava lake, stronger bubble bursting activity and changes in the morphology and texture of the crater floor. Background (low) levels of activity correspond to a lava lake located >80 m below the crater rim, small and/or blocky morphology of the roof, seismic amplitude (RSAM) lower than 25 units, few volcano-tectonic earthquakes, and daily averages of SO_2 emission below 600 Mg d^{-1}.

Convection of magma in the narrow conduits of the plumbing system can explain the sustained degassing with negligible effusion of lava, while supporting the variable outgassing styles at open-vent volcanoes. Theoretical analysis and laboratory experiments carried out with immiscible fluids in vertical and inclined pipes, constrain the convection in terms of a 'flux coefficient' that depends on the viscosity ratio between the liquids, flow regime, angle of inclination of the pipe, and position of the interface between the fluids. Prediction of the flux coefficient is possible within an acceptable range of error. Application of this model to Villarrica and Stromboli volcanoes, along with the analysis of the physical properties of the magma and gas data collated from the literature, allow the estimation of two parameters that constrain the dimensions of the convection: the magma flow rate and equivalent radius. Magma degassing at Villarrica is characterised by the ascent of a relatively degassed magma. Most of the gas exsolves at shallow levels in the system, leading to continuous bubble bursting activity at the lava lake. At Stromboli, magma degassing takes place in an inclined dyke (or dykes). Within this geometry, magma convection adopts a stratified regime of the gas-rich magma overlying the degassed melt, which favours coalescence of bubbles and an efficient convection. Interconnected conduits at the uppermost part of the system constrain the release of the large gas slugs observed during strombolian explosions.

A mi adorada abuela María,

que en paz descansa.

To Franziska and Liliana,

the two most important people in my life.

Acknowledgements

Thanks to my supervisors, Eliza Calder, Steve Blake and Dave Rothery for their support, valuable input and for believing in this work. I would also like to acknowledge The Open University for providing financial support.

Many thanks to Keith Horton for helping me with the software for processing the spectral (FLYSPEC's) data. Andy Harris, Maurizio Ripepe and colleagues are thanked for their support on Stromboli island. Thanks to Steve Self and Ashea Tambe and all the people working in the Volcano Dynamics Group (VDG-Open University).

Special thanks to Caco (Joaquin Cortés) and Eliza for their friendship and help in the good and rough times in England. A very special thank you goes to my family for their continuous and unconditional support. And thanks to my wife and daughter, Franziska and Liliana, for giving me the strength and support during the last months of my PhD, and for making me so happy.

Contents

List of Figures

List of Tables

Chapter 1

Introduction

1.1 Understanding open volcanic systems

Volcanoes of low silica content (e.g. basalt to basaltic andesite, phonolite) that exhibit open–vent activity are characterised by persistent gas emissions and recurrent explosive (typically strombolian-type) activity. Examples of volcanoes with these characteristics are Izu-Oshima in Japan (Kazahaya *et al.*, 1994; Ida, 1995), Stromboli in Italy (Giberti *et al.*, 1992; Rosi and Landi, 2000), Mt. Erebus in Antartica, (Kyle *et al.*, 1994; Rowe *et al.*, 1998), Villarrica in Chile (Fuentealba *et al.*, 2000; Calder *et al.*, 2004), Masaya in Nicaragua (Rymer *et al.*, 1998; Duffell *et al.*, 2003), and Ambrym in Vanuatu (Carniel *et al.*, 2003). Visible magmatic activity ranges from sluggish and slowly moving lava lakes, as seen at Erta Ale's summit caldera (Oppenheimer and Yirgu, 2002; Harris *et al.*, 2005), to intermittent explosive strombolian eruptions from multiple vents, as seen at Stromboli volcano (Ripepe, 1996; Ripepe *et al.*, 2005; Patrick *et al.*, 2007). In the former, the formation of a cooled lava crust on top of a convecting degassed magma is a common occurrence, with sporadic bubble-bursting also taking place. More explosive activity involves gas slugs rising through a magma-filled conduit and rupturing at the magma free–surface (Ripepe *et al.*, 2002; Aster *et al.*, 2003). Although not sustained for long periods of time, more vigorous phenomena such as lava fountains (e.g. Vergniolle, 1996; Andronico *et al.*, 2005) and abnormally strong (paroxysmal) explosions (e.g. Calvari *et al.*, 2006) can also occur during eruptions or periods of elevated activity.

The persistent gas emission accompanied by very low rates of lava extrusion, which is a characteristic of most open-vent volcanoes with low-viscosity magmas, has been interpreted and modelled by buoyancy-driven convection of magma within the plumbing system (Kaza-

haya *et al.*, 1994; Stevenson and Blake, 1998; Locke *et al.*, 2003). This convection allows the continual ascent and degassing of relatively gas-rich magma. Some of the most important variables controlling the characteristics of magma transport and volcanic activity are gas concentration, magma ascent velocity, gas segregation, and viscosity and density of the magma (Parfitt and Wilson, 1995; Spera, 2000; Sparks, 2003). Different approaches can be exploited in order to investigate these characteristics. Whilst petrography and chemical analysis of the products of the magmatic activity can provide valuable constraints regarding the properties of the magma (e.g. Métrich *et al.*, 2001; Gurenko *et al.*, 2005; Allard *et al.*, 2005), geophysical measurements improve the understanding of the activity observed at the surface (e.g. Williams-Jones *et al.*, 2001; Ripepe *et al.*, 2002; Harris and Ripepe, 2007a). However, characterisation of magma degassing and transport in volcanic conduits using these data is difficult to accomplish, and generally requires a multidisciplinary investigation (Andronico *et al.*, 2005). For instance, at Stromboli geophysical studies have shown that during the persistent activity there exist variable styles and frequency of explosive gas emissions (e.g. Ripepe *et al.*, 2002; Patrick *et al.*, 2007); the combination of multiple geophysical approaches offer valuable information for understanding the degassing processes in the shallow system (e.g. Harris and Ripepe, 2007a). Through analysis of melt inclusions, Métrich *et al.* (2001) showed that within the products of magmatic activity at Stromboli, two magmas with different volatile burdens (one crystal-poor and gas-rich and the other crystal-rich and gas-poor) can be responsible for the persistent mild explosive activity as well as more vigorous explosions; the different density and viscosity of these magmas favour the overturn and mechanical mixing between them, and may play a role in the rapid ascent of volatile-rich magma (Métrich *et al.*, 2001).

One of the aspects of these studies that has been given less attention is the interpretation of processes governing the convective motion of magma, or conditions that would make it change, based on the style of explosive activity observed at the surface. For instance, two contrasting models have been proposed to explain the explosion of large gas slugs (involving large bubbles) in strombolian and hawaiian-style activity (Parfitt, 2004): the rise speed dependent model (e.g. Head and Wilson, 1987; Parfitt and Wilson, 1995) and the collapsing foam model (e.g. Vergniolle and Jaupart, 1986; Jaupart and Vergniolle, 1989; Vergniolle, 1996). In the rise speed dependent model, the formation of gas slugs is achieved through gas exsolution, growth of bubbles and bubble coalescence during magma ascent (Parfitt, 2004). In the collapsing foam model, coalescence of bubbles occurs in a geometrical trap at the top

of a magma reservoir, and collapse of the foam into the conduit can develop a slug or annular flow that leads to strombolian- or hawaiian-style activity (Jaupart and Vergniolle, 1989). In these two models, however, the ascent of magma is not driven by convection within the conduits, and the conditions and characteristics of persistent degassing are not investigated. Furthermore, the wide range of strombolian activity observed at different volcanoes, such as the individual bubble bursts that take place at the lava lake of Mt. Erebus (Aster *et al.*, 2003) and the long bursting sequences observed at Stromboli (Patrick *et al.*, 2007), needs a more detailed explanation.

Although accepted as a viable mechanism for persistent degassing and mild explosive activity at open-vent volcanoes (e.g. Wallace and Anderson, 1998; Sparks, 2003; Locke *et al.*, 2003), the fluid mechanics of magma convection in the plumbing system has not been given much attention. Developed under specific and simplified conditions, analogue and numerical models are additional tools that can be used to constrain the convection of magma, dynamics of gas segregation, and style of eruptive activity (e.g. Jaupart and Vergniolle, 1988; Stevenson and Blake, 1998; Mastin and Ghiorso, 2000; James *et al.*, 2004). Advancing the understanding of convective ascent of fresh magma, Stevenson and Blake (1998) and Huppert and Hallworth (2007) carried out experiments in the laboratory to model the laminar countercurrent flow of immiscible fluids in narrow vertical pipes. Their results allow the estimation of magma degassing in terms of a flow rate, rather than degassing rate by mass, that better explains the dynamics of degassing by linking gas emissions with transport of magma. Only recently, Stix (2007) and Burton *et al.* (2007b) applied the idea of convection to model the dynamics of magma degassing at Masaya and Stromboli volcanoes, respectively, as carried out earlier by Kazahaya *et al.* (1994) and Stevenson and Blake (1998) on Izu-Oshima, Stromboli and Mt. St. Helens volcanoes.

This thesis presents a more detailed analysis of the explosive activity observed at two case study volcanoes: Villarrica and Stromboli. These volcanoes were selected because they are easily accessible and show contrasting styles and levels of explosivity. The results are used to interpret conditions of magma and gas ascent within the upper part of the plumbing system. In addition, and building upon the work of Stevenson and Blake (1998), the mechanics of magma convection are investigated in order to better constrain the transport of magma in volcanic conduits. Finally, both approaches are combined to interpret the characteristics and conditions of degassing of low-silica magma at open vent volcanoes.

1.1.1 The concepts of degassing and outgassing

In this thesis I make a distinction between the terms degassing and outgassing. I recognize three main processes responsible for the transfer of magmatic gas from deep magma chambers to the atmosphere: exsolution of gas from the melt, gas segregation, and outgassing. Gas exsolution involves bubble nucleation and bubble growth by diffusion of gas into it (Sparks, 2003). Once the gas has been separated from the melt and formed bubbles of sufficiently large size, it migrates upwards through a magma-filled plumbing system in the process that is commonly termed 'gas segregation'. Continuous bubble growth by decompression, gas diffusion, and coalescence occurs during this stage. 'Degassing' is a general term often implying any or all of these processes (e.g. Sparks, 2003). The term 'outgassing' has been previously used by Gerlach (1986); Ryan (1995); Adams *et al.* (2006); Lautze and Houghton (2007), among others, to describe the escape of gas from magma. However, despite a consensus on the main idea, a clear definition has not been provided.

Accordingly, 'outgassing' is here defined as the escape of gas (as a gas phase) from the magma either directly to the atmosphere, or to the permeable country rock or hydrothermal system surrounding a magma body. Hence, outgassing activity includes all the processes of bubble bursting, non-explosive gas emission, and sustained explosion by which gas escapes to the atmosphere. It also involves the direct escape of gas to the atmosphere by gas diffusion at the surface of a magma column.

1.2 Objectives and methodology

A main goal of this thesis is to improve the understanding of the processes operating in the magma plumbing system of open-vent low-silica volcanoes, that enable degassing of high volumes of magma along with the development of particular styles of explosive activity. The starting point for this investigation is the study of the characteristics of the outgassing activity observed at these volcanoes. To that end, I investigated the variable styles of bubble bursting activity observed at the lava lake of Villarrica volcano, and at the crater terrace of Stromboli volcano. Measurements of emissions of sulphur dioxide were carried out to better constrain the variable outgassing activity, and to correlate gas fluxes with seismicity and visual observations. At Villarrica, correlation of visual observations of the activity at the lava lake with the seismicity and SO_2 fluxes, allowed me to link the outgassing activity with the morphology of the crater, amplitude of the tremor, and magma degassing.

To investigate the dynamics of persistent degassing, I carried out laboratory experiments of convection in vertical and inclined pipes, that allowed me to extend the work of Stevenson and Blake (1998) and Huppert and Hallworth (2007). I also explored analytically the case of steady-state countercurrent flow of immiscible fluids, and developed a two-fluid model able to represent the results obtained from the laboratory experiments. Finally, in order to integrate the results obtained from observations and geophysical measurements, with those of the convective flow modelling, I describe a simple conceptual model of magma degassing (that does not need a numerical code to be solved) which I have applied to Villarrica and Stromboli volcanoes. I discuss the implications of these calculations in terms of the physical properties of the magma and the outgassing activity that magma degassing at these volcanoes generate at the surface.

1.3 Case study volcanoes

In this work two case study volcanoes are used: Villarrica and Stromboli. This section presents only a general introduction to these volcanoes. Additional geological background and results of previous studies on each of these volcanoes are presented along with analysis of their activity in the related chapters of this thesis.

1.3.1 Villarrica volcano

Villarrica is an active stratovolcano in the southern Andes of Chile (39.42° S, 71.93° W, 2847 m a.s.l), located on the northwest end of the volcanic chain Villarrica-Quetrupillán-Lanin, on the intersection of the Gastre and Liquiñe-Ofqui fault zones (Figure 1.1). The snow-covered cone is located on the northwest side of an 6.5 x 4.2 km elliptical caldera that was created during the Late Pleistocene (ca. 95 ka, Moreno *et al.*, 1994; Clavero and Moreno, 2004). Two basaltic andesite ignimbrites, Licán (ca. 14 ka BP, ~10 km^3) and Pucón (ca. 3.7 ka BP, ~5 km^3), have been associated by Moreno *et al.* (1994) and Clavero and Moreno (2004) with the collapse of a nested caldera (Stage I caldera, Figure 1.1) and the partial collapse or destruction of the postglacial stratocone (Stage II caldera, Figure 1.1). The predominant composition of lavas and pyroclastic deposits is basaltic to basaltic andesite, with 50-57 wt% SiO_2 (Moreno *et al.*, 1994; Witter *et al.*, 2004; Hickey-Vargas *et al.*, 2004), and the current whole-rock composition of the products is basaltic andesite, with ~52.6 wt% SiO_2 (Witter *et al.*, 2004). At the summit, a crater of ca. 200 m in diameter has been the site of the activity since, at least, the end of the XIX century (Casertano, 1963). Since the last eruption in 1984-1985, Villarrica has shown persistent gas plume emission and bubble-burst activity at the surface of an active lava lake, typically located less than 200 meters below the crater rim (Figure 1.2) (Fuentealba *et al.*, 2000; Calder *et al.*, 2004).

The tectonic setting has been described in López-Escobar *et al.* (1995); Lavenu and Cembrano (1999) and Ortiz *et al.* (2003), the geology and composition of the products in Moreno *et al.* (1994); Witter *et al.* (2004); Clavero and Moreno (2004) and Hickey-Vargas *et al.* (2004), gas plume composition in Witter *et al.* (2004); Witter and Calder (2004) and Shinohara and Witter (2005), and the recent eruptive activity in Fuentealba *et al.* (2000); Ortiz *et al.* (2003), Calder *et al.* (2004), and Chapter 4 of this thesis.

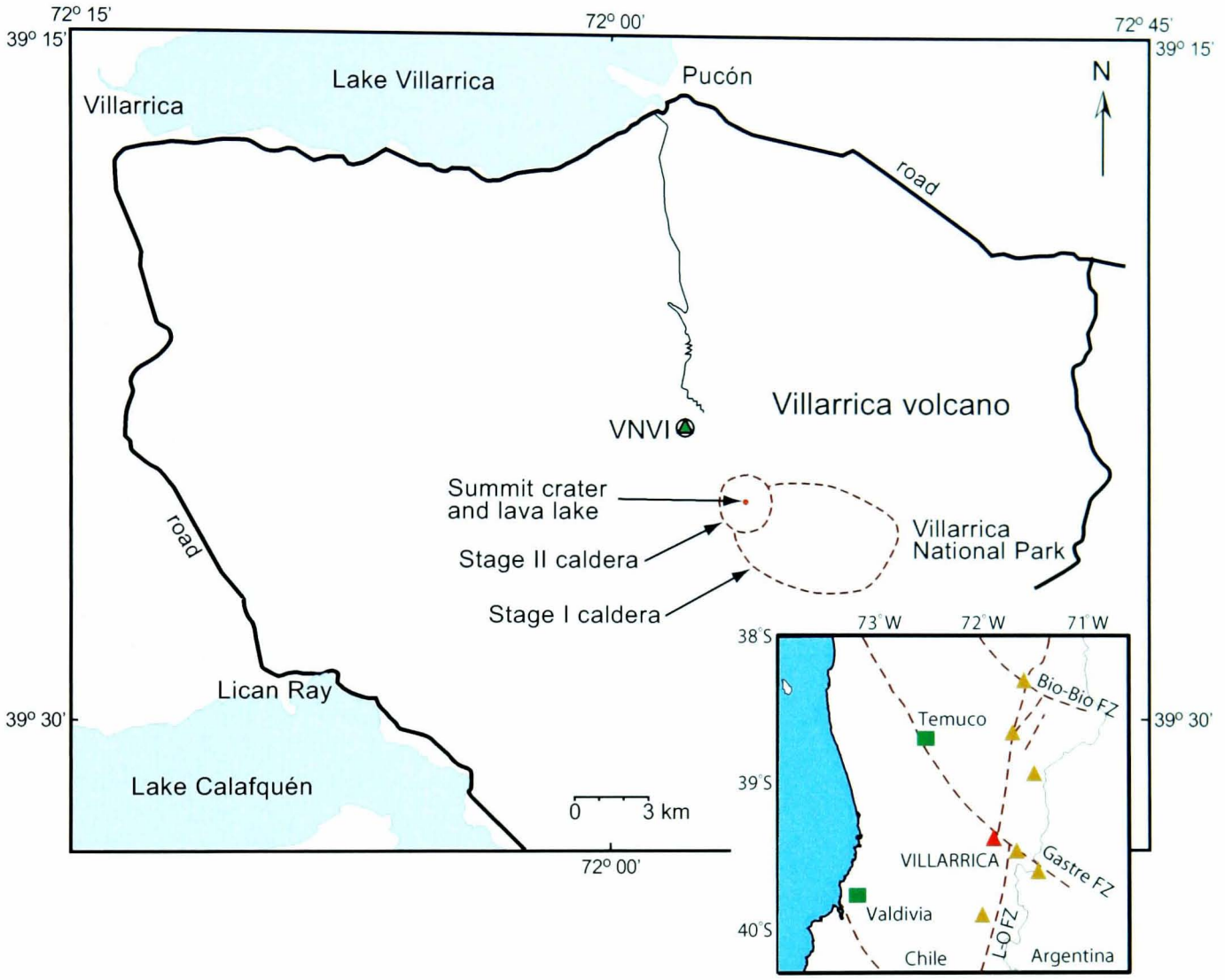

Figure 1.1: Location of Villarrica volcano in the southern Andes volcanic zone (33°- 46° S). The inset map shows some of the major regional tectonic structures (dashed lines, after Bohm *et al.* (2002)): Liquiñe-Ofqui (LOFZ), Gastre and Bio-Bio fault zones. It also shows the cities of Valdivia and Temuco (squares), and the location of other Quaternary volcanoes (triangles). Villarrica volcano is part of a NW-SE volcanic chain that also includes, to the SE, Quetrupillán and Lanín volcanoes. Stage I and Stage II calderas were created *ca.* 100 ka (14 ka) and 3.7 ka BP, respectively (Moreno *et al.*, 1994; Clavero and Moreno, 2004). The summit crater is ca. 200 m in external diameter with an active lava lake at the bottom. The roads surrounding the volcano on which the ground-based traverses were performed for SO_2 measurements are also shown. VNVI is the seismometer. Contours every 100 m.

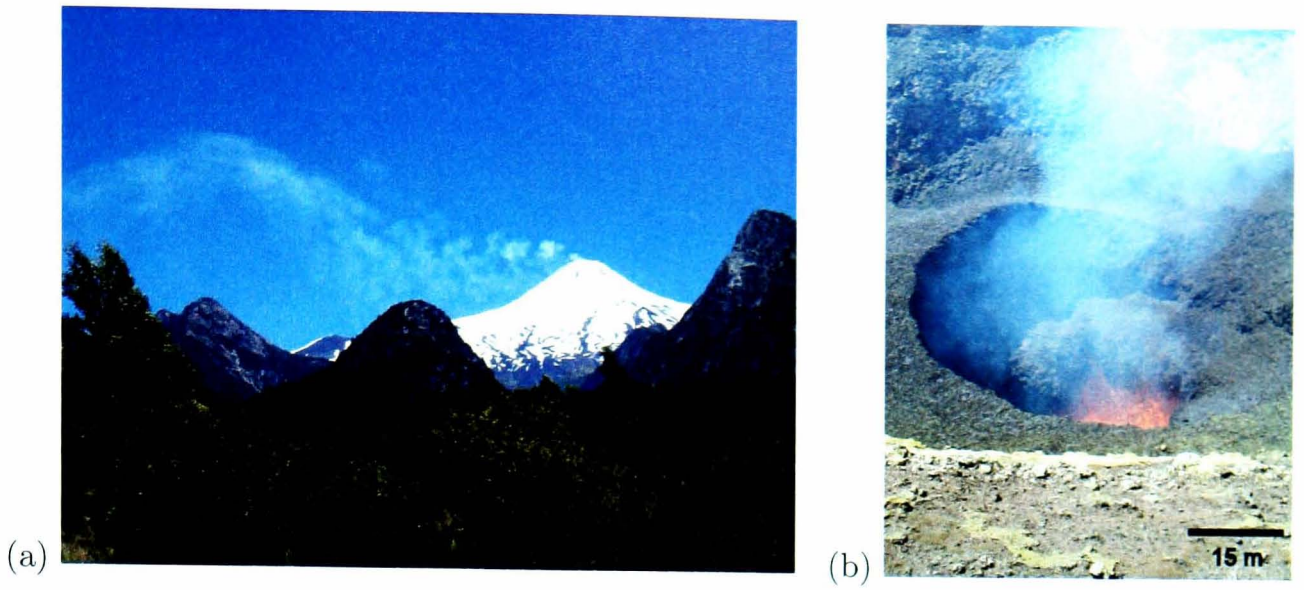

Figure 1.2: Photographs showing (a) the gas plume emitted at the crater of Villarrica volcano, and (b) the bottom of the crater where all the magmatic activity takes place. Scale is approximate.

1.3.2 Stromboli volcano

Stromboli is a stratovolcano located in the Aeolian Archipelago, in the southern Tyrrhenian Sea, southern Italy (38.79°N, 5.213°E, 924 m a.s.l., rising ~2500 m above the sea floor). The magmatic activity of Stromboli volcano comprises six main periods: Paleostromboli I, II, III, Vancori, Neostromboli and Recent, in which the magma composition ranged from calc-alkaline, to potassic-alkaline, through high-K calc-alkaline and shoshonitic types (Rosi and Landi, 2000; Francalanci *et al.*, 2005). The magma composition of the products of the current activity ranges between high-K basalts and shoshonitic basalts (49-53 wt% SiO_2) (Bertagnini *et al.*, 2003; Francalanci *et al.*, 2004). Stromboli is currently characterised by persistent gas emission and explosions from a summit crater-terrace which contains multiple vents. The vents are distributed inside three main craters aligned in a north-east direction (Ripepe *et al.*, 2004, 2001b; Settle and McGetchin, 1980) (Figure 1.3). This situation has lasted since at least the fourth century B.C. (Rosi and Landi, 2000),

Owing to the persistent activity and easy access to the summit of the volcano, from where this activity can be observed, a vast amount of literature has been dedicated to study the characteristics of the explosive outgassing through analysis of the dynamics of the eruptions and explosions (e.g. Chouet *et al.*, 1974; Blackburn *et al.*, 1976; Lautze and Houghton, 2007; Patrick *et al.*, 2007), seismicity (e.g. Ripepe, 1996; Chouet *et al.*, 1999; Ripepe *et al.*, 2001b), infrasound (e.g. Ripepe and Gordeev, 1999; Ripepe *et al.*, 2002; Ripepe and Marchetti, 2002), gas emissions (e.g. Allard *et al.*, 1994; McGonigle *et al.*, 2003; Burton *et al.*, 2007a), thermometry (e.g. Ripepe *et al.*, 2005; Calvari *et al.*, 2006; Harris and Ripepe, 2007b), stratig-

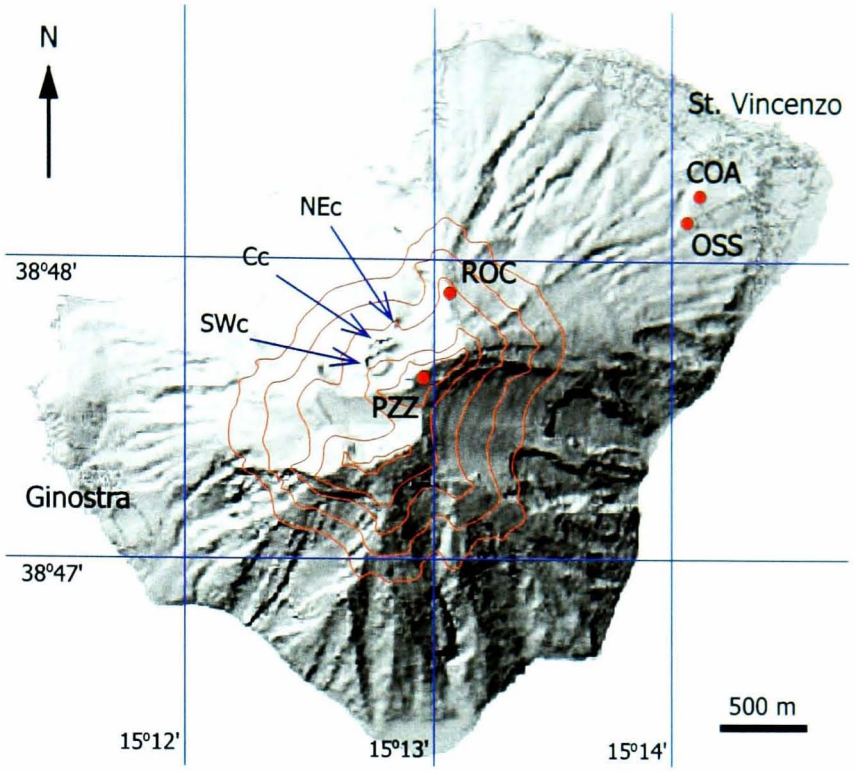

Figure 1.3: Stromboli island. The locations are: COA=Advanced Operational Centre (∼50 m a.s.l., 3848.1725 N, 01514.0118 E); OSS=Osservatorio (195 m a.s.l., 3847.9159 N, 01513.6338 E); ROC=Roccette (765 m a.s.l., 3847.8276 N, 01513.0250 E); PZZ=Pizzo (918 m a.s.l., 3847.5533 N, 01512.9893 E).

raphy and petrology of the products (e.g. Métrich *et al.*, 2001; Bertagnini *et al.*, 2003; Francalanci *et al.*, 2004, 2005), and analysis of multiparameter investigations (e.g. Ripepe *et al.*, 2004; Harris and Ripepe, 2007a).

1.4 Thesis Outline

Chapter 2 describes the theory and methodology developed in this thesis to process the raw spectra data collected with the spectrometer used in the field (FLYSPEC), and to calculate the path-length concentration of SO_2 (ppm m). Measurements of SO_2 emissions at Stromboli and Villarrica volcanoes (Chapters 3 and 4) were performed with FLYSPEC UV spectrometer and this new data-reduction algorithm.

Chapter 3 analyses the explosive outgassing activity of Villarrica and Stromboli volcanoes. At Villarrica, distinctive bubble bursting styles observed at the crater are described based on visual observations, videos and photographs. At Stromboli, explosion sequences observed at the north-east crater are studied using data collected with a Forward Looking Infrared Radiometer (FLIR). Further insights into the characteristics of the outgassing activity are presented through direct measurements of SO_2 concentrations from the summits of these volcanoes.

Chapter 4 describes the variations in volcanic activity at Villarrica during November 2004–April 2005, including observations of the morphology of the crater, explosive activity, and characteristics of the seismic tremor. Also, it presents correlations between SO_2 flux, seismicity and outgassing activity. The implications for volcano monitoring are discussed.

Chapter 5 investigates, analytically and with laboratory experiments, the convection of immiscible fluids in narrow conduits. The equations for the counter-current flow in a vertical pipe are developed, followed by a dimensional analysis and the introduction of the flux coefficient. The experiments involve the flow of two liquids with variable densities and viscosities. Convective flow in vertical and inclined pipes were analysed in terms of the flow regimes and volumetric flux. Two-fluid models for the cases of vertical and inclined pipes, able to represent the results from the experiments, are also developed.

Chapter 6 presents the basis of a simple degassing model that takes into account the properties of the magma, gas loss calculated from measurements of volatiles in melt inclusions and gas (sulphur dioxide) emissions, and the characteristics of the convection. This model is applied to Villarrica and Stromboli volcanoes. In addition, the characteristics and source of the different outgassing styles observed at open-vent volcanoes are discussed.

Chapter 7 summarizes the conclusions and achievements of this thesis.

Appendix A shows the equations that describe the counter-current flow in a vertical slot, which are analogous to those for vertical pipes.

Appendix B presents the description of a selected group of laboratory experiments, including notes and photographs.

Chapter 2

Modern Correlation UV Spectroscopy

2.1 Introduction

Remote sensing of SO_2 emanations from volcanoes is one of the most important monitoring tools in volcanology. It has contributed to (a) the estimation of the worldwide SO_2 flux from volcanoes, (b) determination of temporal variation of SO_2 flux from a specific volcano and its correlation with eruptive activity, and (c) delineation of the shapes and concentrations in volcanic plumes. Since the early 1970s the ultraviolet correlation spectrometer, COSPEC (initially developed by Barringer Research, Canada), has been used extensively for the quantification of volcanic gas flux emissions (e.g. Stoiber *et al.*, 1983). Measurements of SO_2 burden in gas plumes using COSPEC are still carried out as part of the monitoring system of volcano observatories (e.g. Andronico *et al.*, 2005; Elias and Sutton, 2007), as well as for research purposes (e.g. Allard *et al.*, 1994; Sutton *et al.*, 2001; Fischer *et al.*, 2002).

In addition to COSPEC, a new generation of portable ultraviolet spectrometers (PUVS) is currently in use for gas plume measurements (e.g. Galle *et al.*, 2002; Horton *et al.*, 2006), which improve upon the capabilities of the traditional COSPEC (Elias *et al.*, 2006). These new smaller, lighter, cheaper and computer-controlled instruments are able to reproduce the measurements carried out with COSPEC (Horton *et al.*, 2006; Elias *et al.*, 2006), and are easy to automate for specific tasks in the field (e.g. Edmonds *et al.* (2003)). The reader is referred to Galle *et al.* (2002), Horton *et al.* (2006) and Elias *et al.* (2006) for a description of the hardware and cross-correlation of the results obtained by similar instruments. McGonigle *et al.* (2003) and Edmonds *et al.* (2003) presented examples of the configuration

and deployment of UV spectrometers to perform automated tasks in the field. Although the methodology for the application of these instruments in the field has been described extensively (e.g. Stoiber *et al.*, 1983; McGonigle and Oppenheimer, 2003; McGonigle *et al.*, 2004; Williams-Jones *et al.*, 2007), details of the algorithms for spectra processing and evaluation of their quality and limitations had less attention. Descriptions of the hardware and procedure to calculate gas burden are better known for COSPEC and DOAS (e.g. Platt, 1994). For instance, Millán (2007) presented details of the instrument and the procedure carried out by the COSPEC for the calculation of gas concentrations.

In this chapter I describe the theory and spectra processing for the calculation of SO_2 burden in volcanic plumes using UV correlation spectroscopy, focusing on its implementation with the FLYSPEC (Horton *et al.*, 2006). One of the objectives is to present the algorithms I have developed that have been used to re-process the raw spectra data collected by the FLYSPEC[1]. This was necessary in order to obtain accurate values of the sulphur dioxide path-length concentration, that were incorrectly calculated by the instrument owing to calibration issues[2]. In addition, these new algorithms allowed me to improve the accuracy and precision (as signal to noise ratio) of the measurements and to explore new methodologies applied in the field for the study of explosive outgassing (see Chapter 3). This chapter starts with a brief description of the instrumentation used to acquired the UV spectra, followed by the theory and procedure for the calculation of gas absorption, and the description of the algorithms developed to obtain the final SO_2 path-length concentrations.

2.2 Instrumentation for remote sensing of SO_2 in gas plumes

The hardware design of the PUVS is based on fore-optics, electronics, the USB2000 or S2000 ultraviolet spectrometer (or the new USB4000)[3], and a computer for recording and processing of the acquired spectra (Figure 2.1). The USB2000 plugs directly into the computer by USB 1.1 connection, which supplies the spectrometer with the working power while allowing direct access to the spectra being measured. The USB2000 is the common option for human-controlled measurements such as vehicle traverses. In contrast, the S2000 is

[1] I have to acknowledge the help of Keith Horton for answering my questions about the operation of the instrument the first time I went to the field, and for showing me the FLYSPEC's original algorithm for the calculation of the SO_2 path-length concentration.

[2] To calibrate the instrument, the procedure requires the use of calibration cells with accurate values of previously measured sulphur dioxide concentrations. One of these calibration cells showed continuous depletion of the gas concentration, which caused incorrect calibrations and consequently erroneous measurements.

[3] Supplied by Ocean Optics. More information in the web site http://www.oceanoptics.com.

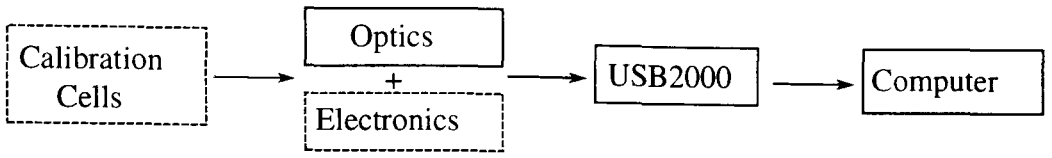

Figure 2.1: Hardware design of the new Portable UV Spectrometers (PUVS). The dashed boxes represent optional components. For vehicle-based traverses or static-mode scanning, FLYSPEC uses calibration cells but does not require extra electronic components. Automated tasks require electronic equipment to control part of the optics and the USB2000 spectrometer.

preferred for automated measurements, such as scanning systems, in part due to the RS232 (serial port) connection and independent power supply that allows more flexibility in the configuration and running of automated tasks in the field.

The procedure for SO_2 retrieval employed by two well known PUVS, the FLYSPEC and mini-DOAS, is based on Differential Optical Absorption Spectroscopy (DOAS) (Platt, 1994). These two instruments use slightly different approaches for the computerized processing of the light spectra collected by the spectrometer. Whereas the mini-DOAS applies laboratory-measured spectra to model the concentration-absorption spectra relationship, FLYSPEC incorporates an in-field calibration system. This calibration method is based on the insertion of two or more calibration cells with known SO_2 concentration into the optical path of the instrument (Horton *et al.*, 2006). Hence, FLYSPEC combines the advantageous calibration set up of COSPEC with the differential absorbance correlation of the DOAS methodology, creating a hybrid methodology that takes advantage of both techniques.

2.2.1 The FLYSPEC

The hardware of the FLYSPEC is based on an ultraviolet spectrometer and a portable computer. It uses a USB2000 Miniature Fiber Optic spectrometer built by Ocean Optics[4] that incorporates a monochromator based on an asymmetric crossed Czerny-Turner configuration (see Figure 2.2), and a 2048-element charge coupled device (CCD) linear silicon array (Horton *et al.*, 2006). Connected via a USB port the USB2000 gets its power from the host computer, eliminating the need for an external power supply. The spectrometer and two calibration cells are mounted inside a protective case, where a UV band-pass filter is inserted in front of the viewer. The case measures only 89 x 64 x 34 mm and weighs 200 g. The calibration cells can be rotated manually without opening the case to allow the calibration procedure and to

[4]More information at http://www.oceanoptics.com. Most of the characteristics of the hardware presented herein are collated from documents provided by the company and from Horton *et al.* (2006).

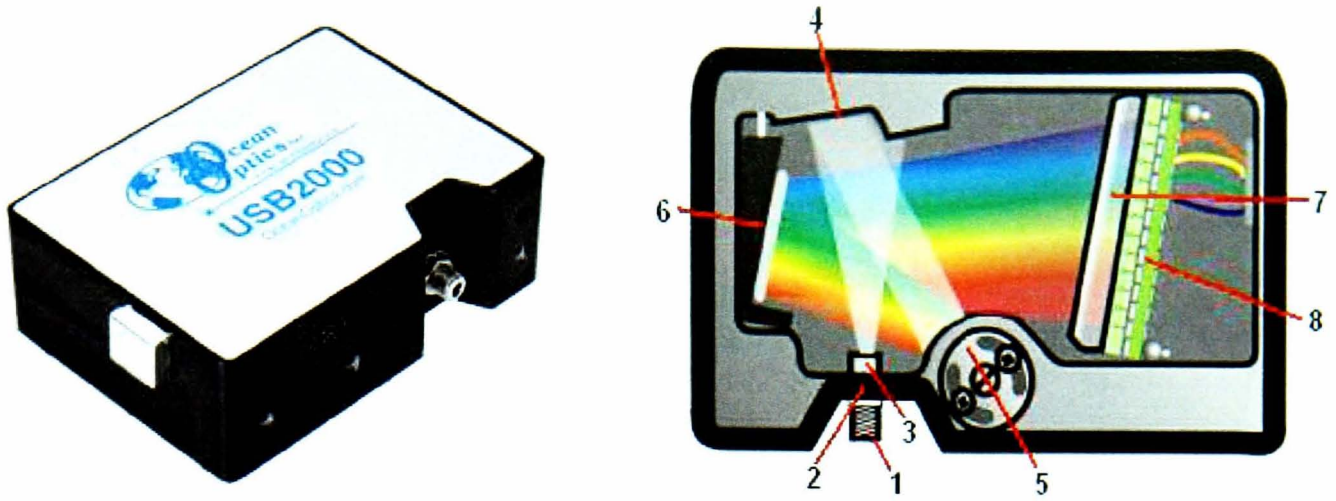

(a) (b)

Figure 2.2: Ocean Optics USB2000 Fiber Optic Spectrometer. (a) Oblique view of the instrument (b) Spectrometer's components: 1=SMA connector, 2=slit, 3=filter, 4=collimating mirror, 5=grating, 6=focusing mirror, 7=Optional L2 detector collection lens which is not present in the FLYSPEC, 8=CCD detector. See Table 2.1 for details.

leave the field of view free for direct measurements of the volcanic plume. The filter and case also reduce the amount of stray light reaching the spectrometer, while the case protects the spectrometer from harsh environments and vibration (Horton *et al.*, 2006).

At a specific user-defined 'integration time' the computer receives a spectrum in the wavelength range of 177-330 nm through the USB connection. At the same time, a small GPS plugged into the computer registers the time and location of the instrument for each data retrieval. Specialized software then processes the data in real-time and creates several binary files with the measured spectra and a file in ASCII format with the calculated concentration along with the location and time of every data point.

2.2.2 USB2000 Spectrometer

In the FLYSPEC, the USB2000 spectrometer combines a 2400 lines/mm plane grating with a 25 μm slit to get an optical resolution of 0.25 nm with sampling resolution of 0.1 nm across the array[5]. A small fiber-optic collimating lens is connected to the spectrometer input

[5]The optical resolution of a monochromatic source, measured as Full Width Half Maximum (FWHM), depends in the groove density of the grating and the diameter of the entrance optics (optical fiber or slit). Resolution increases with an increase in the groove density and as the slit width or fiber diameter decreases. However, a smaller optical entrance reduces the signal strength, the same for a higher groove density that also reduces the spectral range. The optical resolution can be calculated as follows:

$$opt.res.\ [nm] = dispersion\ [\frac{nm}{pixel}] \times pixel\ resolution\ [pixel]$$

where the dispersion is the spectral range of the grating divided by the number of detector pixel elements (2048 for the USB2000 CCD array); the pixel resolution depends on the value from slit size and the fiber diameter chart.

aperture which, in combination with the UV filter window located in the FLYSPEC's durable case, results in a field of view of 44 mrad (~2.5°) (Horton *et al.*, 2006). The integration time varies in the range 3 milliseconds-65 seconds with a data transfer rate for full scans (2048 wavelengths) into memory every 13 milliseconds. An external view of the USB2000 and the configuration of the monochromator are shown in Figure 2.2, and the characteristics and function of each component are listed in Table 2.1.

2.3 Theory and methodology of absorption retrieval

2.3.1 Scattered sunlight

The general equation that relates the intensity of light coming into the spectrometer (or the power carried by a light beam, Brown, 2000) to the gas absorption in the atmosphere can be expressed as follows (e.g. Platt, 1994):

$$I(\lambda) = I_0(\lambda)e^{-L[\Omega_S(\lambda)+\Omega_{RM}(\lambda)]} \tag{2.1}$$

where:

$I(\lambda)$ = transmitted intensity

$I_0(\lambda)$ = initial intensity

λ = wavelength

L = path length

$\Omega_S(\lambda)$ = molecular absorption over all gas species

$\Omega_{RM}(\lambda)$ = Rayleigh and Mie scattering

In this case $I_0(\lambda)$ is the unattenuated light spectrum, and $I(\lambda)$ is the absolute wavelength-dependent intensity obtained. The transmittance is the ratio between the light spectrum that is transmitted and acquired by the spectrometer, and the initial or source light spectrum:

$$T = I/I_0 \tag{2.2}$$

2.3.2 Absorption cross-section

The absorption, A, is defined as the logarithm of the ratio between a reference (without the sample) and transmitted (through the sample) intensity of light, with all other conditions

Table 2.1: USB2000 spectrometer's components used in the FLYSPEC

Item	Name	Description
1	SMA connector	The SMA Connector secures the input fiber to the spectrometer. The FLYSPEC has a small fiber-optic collimating lens (telescope) mounted to this point.
2	Slit	The Slit is a dark piece of material containing a rectangular aperture of 25 μm size, which is mounted directly behind the SMA Connector. It regulates the amount of light that enters the optical bench and controls spectral resolution.
3	Filter	The Filter is a device that restricts optical radiation to predetermined wavelength regions.
4	Collimating mirror	The Collimating Mirror focuses light entering the optical bench towards the Grating of the spectrometer.
5	Grating	The Grating diffracts light from the Collimating Mirror and directs the diffracted light onto the Focusing Mirror, allowing to specify wavelength coverage and resolution in the spectrometer. The FLYSPEC has a plane grating of 2400 lines/mm.
6	Focusing mirror	The Focusing Mirror receives light reflected from the Grating and focuses the light onto the CCD Detector or L2 Detector Collection Lens (depending on the spectrometer configuration).
7	L2 detector collection lens	The L2 Detector Collection Lens (optional and not present in FLYSPEC) focuses light from a tall slit onto the shorter CCD Detector elements. It should be used with large diameter slits or in applications with low light levels. It also improves efficiency by reducing the effects of stray light.
8	CCD detector	The CCD Detector (Sony ILX511, coated by Ocean-Optics) collects the light received from the Focusing Mirror or L2 Detector Collection Lens and converts the optical signal to a digital signal. Each pixel on the CCD Detector responds to the wavelength of light that strikes it, creating a digital response. The pixel size is 14μm x 200μm.

or variables constant (e.g. Thorburn, 1993; Smith, 2002):

$$A = -\ln(T) = -\ln(I/I_0) \tag{2.3}$$

In the laboratory, the main variables that must be controlled are temperature, pressure and intensity of the artificial (source) light. Likewise when studying volcanic plumes in the field it is important to be aware of the changing light and atmospheric conditions (Williams-Jones *et al.*, 2007).

As the volcanic plume moves and disperses in an area around the vent, it is possible to measure the background atmosphere in a path-length where the plume is not present (Figure 2.3). This measurement of the atmospheric background, along with the acquisition of calibration cells spectra, provides advantages when processing the spectra as radiative transfer modeling is not necessary, and most of the non-desirable scattering effects (e.g. inelastic Raman scattering) affecting the true molecular absorption can be separated (Horton *et al.*, 2006).

Rearranging Equation 2.1 to include the effect of the light passing through the volcanic plume:

$$I(\lambda) = I_0(\lambda)e^{-L\Omega_A}e^{-l\Omega_p} \tag{2.4}$$

where Ω_A considers the general atmospheric absorption without the plume ($\Omega_S + \Omega_{RM}$), Ω_p is the molecular absorption that takes place within the volcanic plume only, and l the path length (vertical thickness) of the volcanic plume ($l << L$). The reference light spectrum is defined as:

$$I_R(\lambda) = I_0(\lambda)e^{-L\Omega_A} \tag{2.5}$$

which must be measured away from the plume. Then, combining equations 2.4 and 2.5 the absorbance profile of the volcanic plume is obtained:

$$A_{plume}(\lambda) = -\ln\left(\frac{I(\lambda)}{I_R(\lambda)}\right) = l\ \Omega_p \tag{2.6}$$

2.3.3 Beer-Lambert Law

Assuming an ideal case in which the reference light spectrum does not change (I_R constant, equation 2.5), and the SO_2 is the only absorbing species in the wavelength range of interest, the Beer-Lambert law (or just Beer's law) expresses a linear relationship between

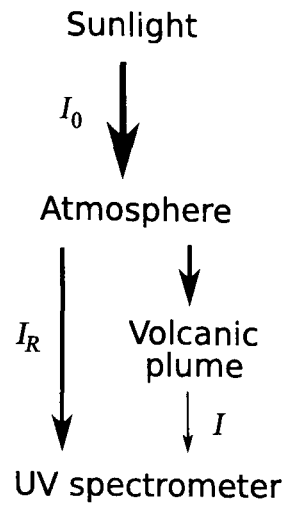

Figure 2.3: Basic model that accounts for the path and interaction of sunlight that is captured by the spectrometer. The thickness of the arrows represents the intensity of light that decreases as sunlight is scattered and absorbed within the atmosphere and volcanic plume.

the gas concentration and the absorbance (e.g. Thorburn, 1993; Smith, 2002):

$$A_{plume}(\lambda) = \sigma_{SO_2}(\lambda)\ c_{SO_2}\ l \tag{2.7}$$

where $\sigma_{SO_2}(\lambda)$ is the absorptivity coefficient, c_{SO_2} the concentration of sulphur dioxide, and l the path length of the plume. As the absorbance is dimensionless, the units of concentration of any species is inverse to the units of its absorptivity coefficient. Typically, the path-length concentration of SO_2 ($c_{SO_2}\ l$) is expressed in units of $ppm \cdot m$ (parts per million by metre). Gerlach (2003) pointed out that the calibration of the instrument in terms of 'column abundance' units [kg/m^2] instead of 'path-length concentration' units [ppm·m], might facilitate the calculation of gas emission rates[6]. This is achieved by re-scaling the units of the calibration cells (in ppm·m) by a factor $2.663{\cdot}10^{-6}$. In practice, this is the user's choice since the results obtained from calculating gas emission rate with either units are equivalent. The units ppm·m are used in this thesis throughout, and the terms column abundance and path-length concentration are used interchangeably.

In analytical chemistry the Beer-Lambert law is used to calculate the gas concentration from one or a few specific wavelengths of an absorbance profile (Smith, 2002). Deviations from the Beer-Lambert law can be present in UV and IR spectroscopy (Brown, 2000; Smith, 2002). Originally, this mathematical law was derived for monochromatic radiation (Brown, 2000) and assumes a constant intensity of light, no stray light coming into the system, no physico-chemical changes in the absorbing species as a function of its concentration, and

[6]For SO_2: 1 ppm·m = $2.663{\cdot}10^{-6}$ kg m^{-2} (Gerlach, 2003).

no other absorbing species affecting the wavelength range of interest (Massart *et al.*, 1988). Unlike studies performed in the laboratory, field measurements of SO_2 burden in volcanic plumes can be subject to variations in some of these assumptions such as changes in the environmental conditions and incoming sunlight (Figure 2.3). Furthermore, the acquisition system or transfer function of the instrument can introduce more uncertainties and deviations from the linearity in the Beer-Lambert law.

In the case of measurements of SO_2 in volcanic plumes, the linear relationship between gas concentration and absorption has been shown to be not always valid. For instance, Elias *et al.* (2006) has recently shown that using FLYSPEC the linear relationship between absorbance amplitude and sulphur dioxide path-length concentration is not valid at concentrations above ca. 1500 ppm·m. In fact, the different properties of the COSPEC and USB2000 (and the new USB4000), as well as the optics and concentration retrieval algorithms used in different PUVS, means that each instrument user must evaluate independently the validity of measuring high SO_2 concentrations. Those instruments that use calibration cells can assume correct values up to about 10% above the gas concentration of the concentration cell with the highest concentration, although it depends on the number of calibration cells used for the calibration[7]. More care must be taken with instruments that rely completely on the original DOAS algorithm.

2.3.4 Differential absorbance

Molecular absorption can be split into two parameters relating the slowly varying trend in the absorption spectrum and the narrow differential features (typically less than 10 nm). The former trend is due to a softer wavelength dependance, which means that in closely spaced wavelengths the difference in attenuation of light intensity is low. For instance, the Rayleigh and Mie scattering contribute only as slowly varying components of the light intensity. Thus, within the UV wavelength range where sulphur dioxide is absorbed, Equation 2.6 can be expressed as follows:

$$A_{plume}(\lambda) = A_{slow}(\lambda) + A_{SO_2}(\lambda) \tag{2.8}$$

where A_{slow} characterizes the source light spectrum modified by the slowly varying component of the molecular absorption spectra, as well as by Rayleigh and Mie scattering; A_{SO_2}

[7]This statement is completely empirical, as no exhaustive analysis has been performed, and it relies on the fact that variations to the linearity in the calibration curve with high gas concentrations have been observed to occur rather smoothly.

represents the narrow molecular absorption features characteristic of the SO_2. Equation 2.8 is the basis of the differential optical absorption spectroscopy (DOAS) technique, which compares the narrow (or high frequency) changes in amplitude of the spectra (Platt, 1994). This technique is useful since the Beer-Lambert law is generally considered for the narrow as well as slowly varying features of the spectrum.

By using absorbance spectra measured in the laboratory, the DOAS technique has the ability to measure trace gas species that are always present in the atmosphere (Platt, 1994). On the one hand, PUVS that rely completely on this technique (e.g. mini-DOAS, Galle *et al.* (2002)) need to take into account the slit function of the instrument as well as atmospheric effects, such as Ring-effect and Fraunhofer lines (Horton *et al.*, 2006). Thus, the accuracy of the measurements depends greatly on the correction of these effects. On the other hand, the combination of the DOAS technique with a calibration performed in the field allows a better constraint of the properties of the scattered light reaching the spectrometer (Figure 2.3) and facilitates the processing of the data. In this case, the accuracy of the measurements depends mainly on the characteristics and quality of the correlation that allows the calculation of gas column abundance from the absorbance spectra.

The first step in the development of the spectral processing is the acquisition of the calibration data set and the calculation of the differential absorption.

2.3.5 Procedure to calculate the differential absorbance

An example of the raw spectra collected by FLYSPEC is shown in Figure 2.4. It includes the average of 100 individual samples of the reference, low and high calibration cells, and dark spectra. The reference spectrum (I_R) and the calibration cells spectra are acquired away from the volcanic plume (Figure 2.3). In this example only two calibration cells were used, with known low and high concentrations of SO_2. The dark spectrum is acquired by blocking the view of the fore-optics of the instrument, ensuring that no light gets into the spectrometer. In general terms, the dark current is the background signal continuously generated by the instrument, and contributes to the noise (variance) of the resulting path length concentrations. In the calculation of the absorbance from the spectra acquired by the USB2000, it is necessary to extract the instrument noise (dark spectra) from each spectrum.

The procedure to calculate the differential absorbance consists of the following steps:

1. Subtraction of the dark signal and a 'background' light difference.

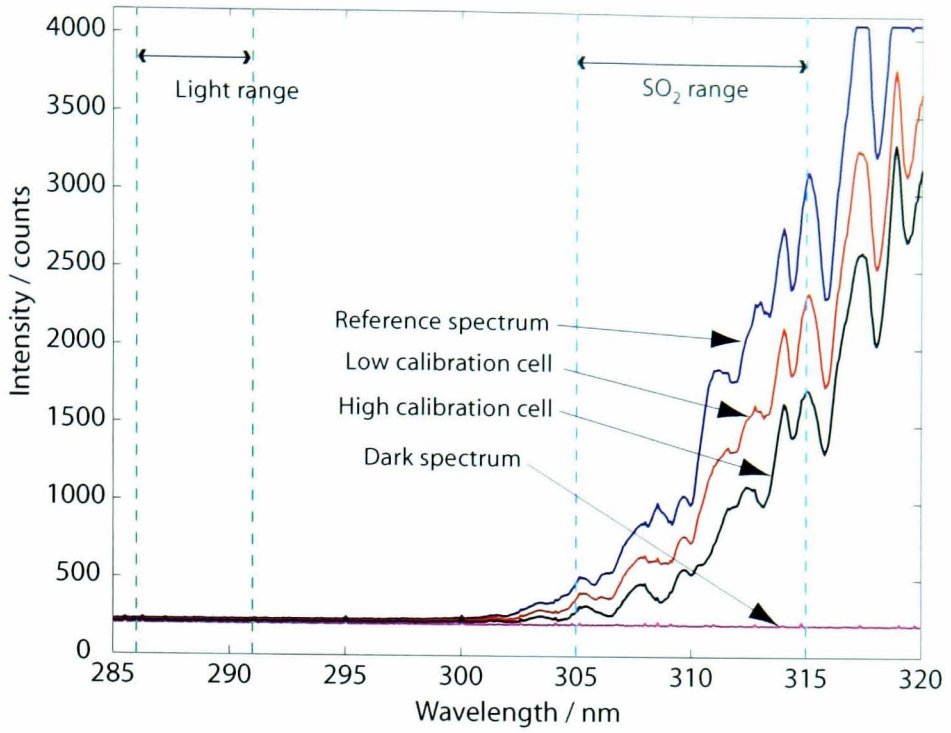

Figure 2.4: Radiance spectra collected by the USB2000 spectrometer (FLYSPEC). From the highest to lowest amplitude it shows the Reference, Low and High calibration cells, and Dark spectra. Vertical lines define the wavelength ranges used for light intensity correction (286-291 nm in this example) and SO_2 calculation (305-315 nm).

2. Calculation of the absorbance cross-section.

3. Filtering of the absorbance profile to get only the narrow features of the spectrum for comparison.

Light intensity changes

As pointed put previously, several environmental conditions can change during the measurements of gas burden in volcanic plumes. One of them is the background light intensity (I_R). The change in light intensity, relative to the original reference spectrum measured during the calibration, will affect the absolute value of the absorbance (Equation 2.6). For instance, acquisition of the same light spectrum at different integration times (duration of the exposure), or small variations in the spectrum acquisition-time inherent in the spectrometer, will have an amplitude proportional to this time difference. Hence, the amplitude of a radiance spectrum acquired with an integration time of 200 ms would be roughly twice as high as the amplitude of the same spectrum acquired with an integration time of 100 ms. The following set of equivalences describes this effect in the absorbance:

$$A(\lambda) = -\ln\left(\frac{I^A(\lambda)}{I_R(\lambda)}\right) = -\ln\left(\frac{\frac{t_A}{t_B}\, I^B(\lambda)}{I_R(\lambda)}\right) = -\ln\left(\frac{I^B(\lambda)}{I_R(\lambda)}\right) - \ln\left(\frac{t_A}{t_B}\right) \tag{2.9}$$

where I^A and I^B are two spectra acquired with integration times of t_A and t_B, respectively. Therefore, if t_A/t_B times spectrum B is a good approximation of spectrum A, within some specific frequency range, the absorbance profile will show a wavelength-independent amplitude change given by $\ln(t_A/t_B)$. This approximation is, however, difficult to implement owing to the difficulty of getting an accurate estimation of the light change. Nevertheless, the technique is useful when the integration time of the measuring spectra is different, but known, to the one used during the calibration.[8]

An easier approach to estimate the light intensity variation, that is useful to minimize the effect of changing light conditions, consists in averaging the amplitude of a specific frequency range of the spectrum outside the range under the influence of the SO_2 (Figure 2.4). This estimate is then removed along with the instrumental noise. Thus, the calculation of the absorbance cross-section is expressed as:

$$A(\lambda) = -\ln\left(\frac{I(\lambda) - D(\lambda) - dI_R}{I_R(\lambda) - D(\lambda) - dI_R}\right) \tag{2.10}$$

where D is the dark spectrum and dI_R the estimation of the background light intensity change, which can be modelled as a wavelength independent parameter, although it does show small variations on different wavelength ranges:

$$dI_R = (\lambda_2 - \lambda_1)^{-1} \sum_{\lambda_1}^{\lambda_2} (I(\lambda) - D(\lambda)) \tag{2.11}$$

The wavelength range $\lambda_1 \rightarrow \lambda_2$ is chosen below 295 nm, where the total light extinction by ozone absorption (Hartley band, Burrows *et al.* 1999), and to some extent by the fore-optics (UV filter and fiber optics lens), is high enough to generate a very low transmittance of light and a flat radiance amplitude (Figure 2.4).

In theory, the extraction of the extra radiance outside the range where the SO_2 is evaluated, is not equivalent to the adjustment to the background light level. However, this step helps in the comparison of the narrow absorption features. In fact, it proves to be very useful in avoiding sharp changes in the slope of the absorbance profile. These changes, with no careful treatment in the filtering step, can introduce anomalous differential absorption amplitudes.

[8] The Dark spectrum needs to be multiplied by the same factor when extracting it from the measured spectrum.

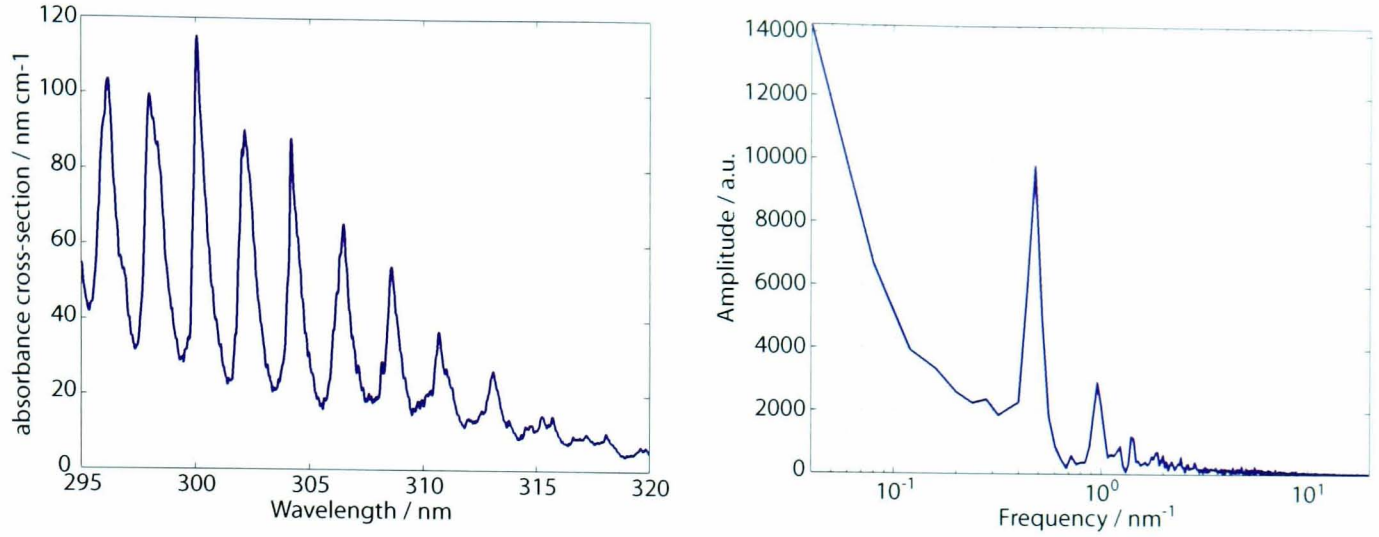

Figure 2.5: Example of sulphur dioxide absorption profile acquired by Hearn and Joens (1991) (left) and the frequency spectrum of the absorption features (right). Note that the decreasing trend of the total gas absorption is reflected in the frequency spectrum with high values at frequencies below 0.1 nm^{-1}. The narrow features exhibit a frequency peak at about 0.5 nm^{-1} and another peak at about 0.95 nm^{-1}.

Filtering the narrow variations

The absorbance profile of pure sulphur dioxide in the ultraviolet consists of several peaks and troughs with different amplitudes (Figure 2.5). These features are regularly spaced at about 2.1 nm. Between 290-325 nm the absorbance of SO_2, measured in the laboratory (Hearn and Joens, 1991), shows a general trend in which the amplitude decreases towards longer wavelengths (Figure 2.5). The absolute amplitude and decreasing trend will change if the background light changes (Equations 2.3,2.6). However, the trough-peak amplitude will stay unaltered under such changes.

There are several options for extracting the slowly varying (or low frequency) part of the absorbance profile. Two techniques have been explored in this work: the extraction of a 5th order polynomial fit and FIR (Finite Impulse Response) filtering. Figure 2.6 depicts an example and comparison of the results of both techniques. Polynomial fitting and Fourier filtering show similar waveforms. In practice, the order of the polynomial that can be used ranges between 3 and 7, where the difference depends on the slope of the absorbance profile in the region of SO_2 absorption. For instance, a higher order polynomial yields better results in long traverses where the light conditions can change considerably. A zero-phase FIR filter is also a good option for extraction of the differential absorption. The characteristics of the absorption features, as seen in Figure 2.5, suggest that a band-pass filter in the range 0.35–2.5 nm^{-1} is a good candidate to extract the long-wavelength trend as well as high-frequency noise. The filter selected in this work is a high-order zero-phase FIR filter implemented with

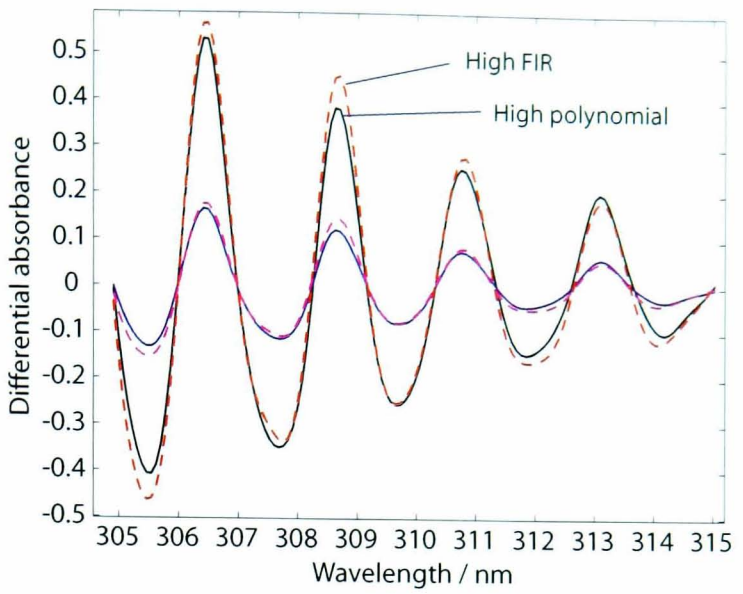

Figure 2.6: Differential absorption of sulphur dioxide (305–315 nm) of two concentrations obtained by extracting a 5th order polynomial curve (fitted with a least square minimization) to the original absorbance cross-section (continuous line), and with a gaussian-based FIR filter (dashed line). The measurements were performed in the field with calibration cells of SO_2 path-length concentrations of 1504 (High) and 438 (Low) ppm·m.

a gaussian window (see Chapter 7 in Ingle and Proakis, 2000). Unless specified otherwise, this is the filter used by default in the calculations below. In both cases (polynomial and FIR filter), for the extraction of the slow trend it is convenient to use a wavelength range a little wider than the range chosen for SO_2 evaluation.

2.3.6 Light extinction by particles

Another cause of changes in the intensity of the light spectra acquired during measurements of volcanic plumes is the presence of pyroclasts in the field of view of the instrument. As discussed above, the light absorbed by the sulphur dioxide in the gas plume decreases the transmittance in the ultraviolet wavelength range. Pyroclasts in the field of view of the instrument also decrease the level of transmittance, but mainly due to extinction and backscattering of light as the particle radii are much larger than the wavelength in the UV range. Thus, both SO_2 and big particles contribute to the modification of a slowly varying (or low frequency) component of the absorbance.

The total extinction of light caused by the plume is wavelength dependent and it can be split into gas absorption (and extinction) and pyroclastic extinction:

$$\Omega_p(\lambda) = \Omega_{gas}(\lambda) + \Omega_{pyro}(\lambda) \tag{2.12}$$

where Ω_{gas} refers to the light absorption by the gas in the plume, Ω_{pyro} is the extinction caused

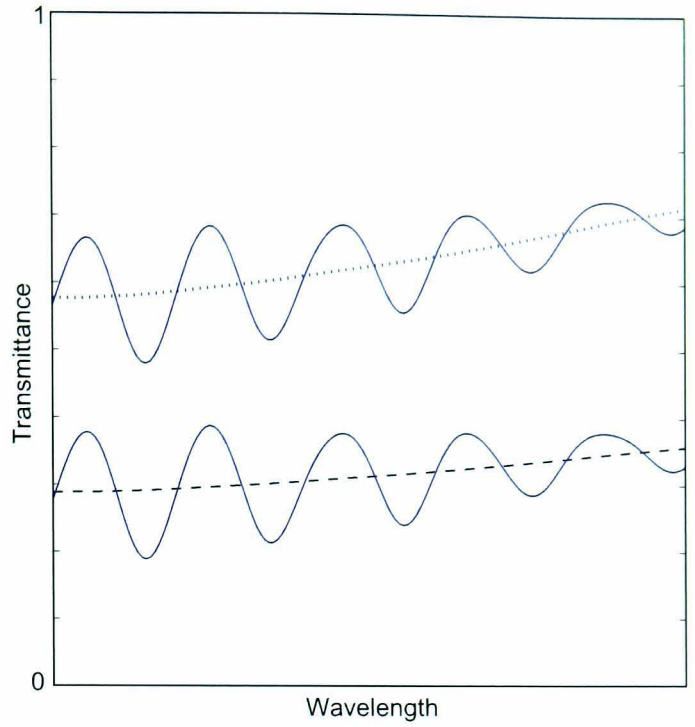

Figure 2.7: Sketch of the changes in transmittance in a volcanic plume that contains pyroclasts. The upper solid line represents the total gas extinction showing the narrow features used to calculate the SO_2 concentration. The bottom solid line has the same narrow features but higher light extinction (lower transmittance) which is due to the pyroclastic mass in the field of view of the instrument. The dotted and dashed lines represent the slowly varying component of the previous cases, respectively.

only by the pyroclastic particles, and λ refers to the wavelength dependance of the total extinction. Considering a relatively dry atmosphere, it can be assumed that the gas extinction is mainly dependent on the sulphur dioxide concentration, $\Omega_{gas}(\lambda) = \sigma_{SO_2}(\lambda)\, c_{SO_2}$ (Equation 2.7). The pyroclastic extinction depends on the scattering properties of the medium, the pyroclastic mass and its size distribution, and the pattern of their arrangement within the line of sight. Both extinctions affect the slowly varying component of the transmittance (Figure 2.7). Thus, the total transmittance can be expressed as:

$$T = \frac{I}{I_R} = e^{-(\Omega_{gas}+\Omega_{pyro})\, l} \tag{2.13}$$

where I_R and I are, respectively, the intensities of the incident light (Equation 2.5) and of the light passed through a volcanic plume of thickness l. T is the transmittance which can also be expressed as:

$$T = e^{-A_{SO_2}} - \Delta I_p \tag{2.14}$$

where A_{SO_2} corresponds to the light absorption by sulphur dioxide (Equation 2.7), and ΔI_p

is the fraction of light lost due to the big particles within the field of view (Figure 2.7):

$$\Delta I_p = e^{-A_{SO_2}}(1 - e^{-\Omega_{pyro}\, l}) \tag{2.15}$$

Since the SO_2 concentration is calculated independently with the methodology described in Section 2.4, by using the spectra of the calibration cells to model the slowly varying component of the gas absorption, the extinction due to a different concentration of sulphur dioxide can be calculated, and it is used as an estimation of the total gas extinction. Then, ΔI_p is obtained from the measure of the total transmittance (Equation 2.14). It is worth mentioning that, although the SO_2 path-length concentration might not be representative of the gas concentration in the gas plume, the pyroclastic extinction is independent of that inaccuracy, since it measures the changes in light intensity (in the field of view of the instrument) that reached the spectrometer, regardless of whether the scattered light crossed through the whole gas plume or only part of it. This approach yields a parameter (ΔI_p) that estimates only relative concentrations of pyroclasts in the volcanic plume (for a given size and spatial distribution of the particles). Moreover, the calculation of the absolute amount (volume fraction or mass) of pyroclastic material in the field of view of the instrument cannot be performed without information about the size distribution of the pyroclasts, their spatial distribution within the field of view, and a relation between the amount of solid material and transmittance change (or light lost, ΔI_p) due to the particles. Corrections to the measured path-length concentrations of sulphur dioxide would require an additional model of light extinction as it passes through the plume.

2.4 Processing of the absorption spectra

2.4.1 General algorithm

In this section, the algorithm for the calculation of SO_2 path-length concentration from measurements of the differential absorption is described. The data used are taken mainly from an experiment where three pairs of calibration cells[9] were combined to get ten known gas concentrations (Table 2.2). The measurements were conducted by placing the cells directly in front of the lens of the spectrometer, without the UV band-pass filter.

The basis of the procedure for SO_2 calculation from the spectra data is as follow:

[9]The cells OUl, OUh, HMl and HMh belong to the Open University, and the calibration cells UHl and UHh belong to the University of Hawaii.

Table 2.2: List of the calibration cells and SO_2 path-concentration of the experiment.

Cells	Concentration [ppm m]
OUl	438
UHl	448
OUl+UHl	886
UHh	1375
OUh	1504
OUl+UHh	1813
OUh+UHl	1915
OUh+UHh	2878
OUh+UHh+HMl	3048
OUh+UHh+HMh	3568

1. Specification of the spectrometer and algorithm parameters.

2. Calibration set up.

3. (Optional) Checking for waveform shifts of the instrument.

4. Correlation of the differential absorption spectra to calculate gas path-length concentrations.

5. Save results

Two sets of parameters need to be specified before the start of the processing algorithm. The first one is related to the configuration of the spectrometer: the background light correction and gas-fitting pixel ranges. The second set of parameters describes the characteristics of the filtering step such as the order of the fitting polynomial or frequency band for the FIR filter. In addition, if the same set of calibration cells is to be used, the number of cells and their path-length concentrations can be specified as part of the initial set up; otherwise, they will have to be entered on each run of the algorithm.

An optional checking of the waveform is recommended to be carried out at least every few months. The purpose of this checking is to correct for shifts in the wavelength-pixel relation of the spectrometer, that can modify the position of the narrow features. This can be performed by cross-correlating two normalized differential absorption profiles acquired at different times. Another optional step is the identification and correction of spikes in the signal. The occurrence of spikes is commonly produced by objects covering the field of view. Thereby, their identification can be performed by a combination of the amount of gas

calculated with respect to previous data points, and the absolute amplitude of the absorbance (or transmittance) at a specific wavelength.

2.4.2 Calibration set up

Measuring known concentrations before each experiment allows the calibration of the instrument under any new set of environmental conditions. Some conditions which control the amplitude of the transmittance, and to some degree the accuracy of the measurements are: the position of the sun relative to the line of sight of the instrument, the integration time of the acquisition, amount and type of clouds in the line of sight, ambient temperature, etc. Thus, it is desirable to measure the calibration cells under the same (or very similar) conditions encountered in the measurements of the volcanic plume. More on the atmospheric variables that need to be considered at the time of calibration and measurements can be found in Williams-Jones *et al.* (2007).

The calibration is carried out with two or more calibration cells with known SO_2 path-length concentrations. The absorbance cross-section of the cells are used as calibration values for the interpolation of the new measured absorbance profiles from light that passes through the volcanic plume. Unknown concentrations can be obtained by fitting a curve (polynomial model) in an absorption-gas concentration empirical relationship. In order to avoid extrapolation, the gas concentration being measured must be in the same concentration range as the calibration cells. As pointed out previously, the empirical relationship between absorbance amplitude and gas concentration is not necessarily linear as stated by the Beer-Lambert law (Equation 2.7, Section 2.4.3).

The calibration set up is executed as follows:

1. Read reference (background) and dark (instrument offset) files
2. Read spectra and concentrations of the calibration cells
3. Calculate and store the differential absorbance of the calibration cells

Storing the differential absorbance (DA) spectra of all the calibration cells is not needed if a 'passive' correlation is applied. In passive correlation, a mathematical model that describes the relation between the amplitude of the DA features of the calibration cells and their path-length concentrations can be obtained immediately after the calibration procedure. The calculation of these amplitudes can involve any linear combination of the amplitudes of the DA spectrum at specific wavelengths. For instance, Horton *et al.* (2006) relate the

path-length concentrations of the calibration cells with the peak-trough difference of the narrow features of their DA spectra[10]. This mathematical model is usually a quadratic polynomial, although a third order polynomial can be more appropriate when dealing with high concentrations (above 1500 ppm·m, Elias *et al.* (2006)). Thus, the DA profile amplitude derived from a new light spectrum (related to an unknown gas concentration) can be entered in the model to get the concentration of SO_2. An 'active' correlation involves the creation and application of the polynomial fitting model for each new calculated DA spectrum. Details of the model to correlate the differential absorbance amplitude with gas concentrations are described in the next section.

2.4.3 Correlating the differential absorbance with gas concentrations

There are several alternatives to extract absolute values from the differential absorbance (DA) cross-section, in order to enter them in the mathematical model created in the calibration set up, and to perform the subsequent calculation of gas concentrations. In effect, it is possible to use a single pixel (specific wavelength), peak to trough differences, area of the curve, or any average or linear combination of them. As each value in the absorption profile is potentially useful in the calibrated model of gas concentration–absorption amplitude, the choice of a 'good' set of parameters relies on the improvement of the final interpolation and of the signal-to-noise ratio. According to the Beer-Lambert law (Equation 2.7), any wavelength (pixel) could be used to calculate gas concentration. However, this relationship does not apply in the same manner with the differential absorbance, as at a finite number of wavelengths the DA amplitude can be zero (Figure 2.6), and thus the correlation model cannot be applied at those wavelengths. Nevertheless, the idea behind the Beer-Lambert law is still valid and, theoretically, any wavelength other than the ones with zero amplitude can be used in the correlation model. This relation between the DA amplitude and gas concentration is similar to that of Equation 2.7:

$$DA(\lambda) = \sigma'_{SO_2}(\lambda)\ c_{SO_2}\ l \tag{2.16}$$

where $\sigma'_{SO_2}(\lambda)$ is a modified absorptivity coefficient that contributes to the amplitude of the narrow features in the absorption profile only. Equation 2.16 is the basis of the DOAS technique (Platt, 1994).

[10] Actually, from a theoretical point of view, the use of the peak-trough amplitude difference does not require the filtering of the absorbance profile.

A note about noise

Another aspect that needs attention is the noise-related fluctuations that, in practice, appear in the whole wavelength range of total and differential absorbance spectra. The amplitude of this noise depends mainly on the environmental intensity of the light that is received by the instrument, and contributes to a variable percentage of the DA profile. Low DA amplitude profiles (related to lower gas concentrations) are affected further by this noise than relatively high DA amplitude profiles. Thereby, the contribution of this noise to the amplitude of the absorbance is lower at wavelengths with higher absolute DA amplitudes. As described above, a band pass FIR filtering can reduce the noise-related variations of the calculated gas concentrations, and improves the signal-to-noise ratio. In fact, in order to improve the signal-to-noise ratio it is desirable to use as many pixels (wavelengths) in the calculation of the gas concentration as possible. Averaging gas concentrations (gas column abundance) obtained at different wavelengths from the same DA spectrum can also reduce noise. Averaging of the raw light spectra with the aim of reducing the noise of (or to smooth) the final gas concentration time series should be avoided, since the relation between the amplitude of the light intensity and gas concentration is non–linear. This practice is common when keeping a backup of the light spectra for post–processing is needed. In order to reduce the amount of data for storage, this averaging should be performed over the total or differential absorption spectra; the dark and reference light spectra can be also stored, so the original light spectra can be restored later on. If the goal of the spectral averaging is to smooth the final gas concentration time series only, the best option is to calculate the gas column abundance from each light spectrum captured by the instrument, and then apply a moving average over that time series. Moreover, using every individual light spectrum to calculate the absorbance and gas concentration also allows the recognition (and correction) of 'spikes' or other rapid deviations from the genuine light absorption and gas column abundance obtained from the volcanic plume

Relation between differential absorption profiles

Since in the wavelength dependent DA profile the variation in amplitude of the narrow features depends on the gas path-length concentration only, and that the absorptivity coefficient in Equation 2.16 is independent of the gas concentration, it follows that wavelengths with similar DA amplitude should have similar absorptivity coefficients. Thus, any pair of DA profiles can be correlated so that one profile can be obtained from the other through

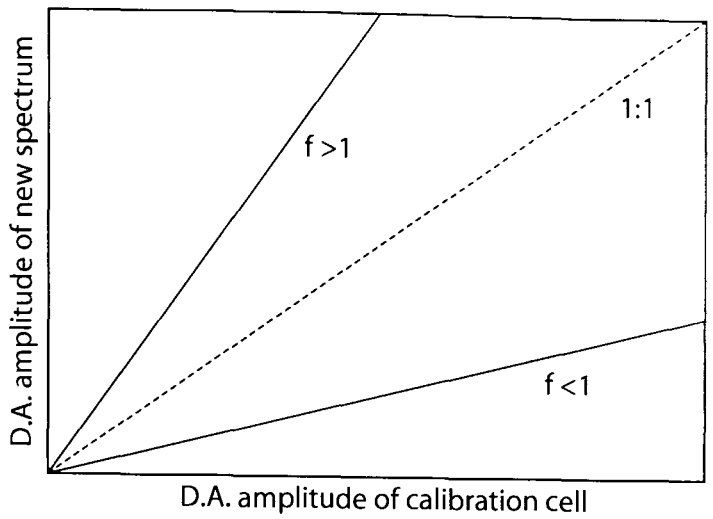

Figure 2.8: Theoretical comparison of the amplitude of two differential absorption spectra. It yields a slope (multiplication factor, f) higher than one when the narrow features of the new spectrum are larger than the spectrum of the calibration cell, and lower than one on the contrary. Thus, when $f > 1$ and $f < 1$ the new spectrum is associated to higher and lower gas concentrations, respectively.

a multiplication factor f, that is related to the difference in gas path-length concentrations only (Figure 2.8). Indeed, since for higher gas concentrations the narrow features of the differential absorbance are larger, in order to get the DA profile associated with a relatively high gas concentration from a profile associated with a relatively lower gas concentration, the former can theoretically be obtained from the latter by multiplying it by a factor f, that is higher than unity and close to the ratio of the gas concentrations[11]:

$$DA_h(\lambda) = f \cdot DA_l(\lambda) \qquad f > 1 \tag{2.17}$$

where DA_h and DA_l are the differential absorption spectra associated to a relatively high and a low gas concentration, respectively (Figure 2.8).

Active correlation between absorption amplitude and gas concentrations

From the calibration procedure, the DA spectra and corresponding known gas path-length concentrations of the calibration cells are required to calculate the parameters of the correlation model, and to obtain the unknown concentration. To perform the active correlation between DA profiles, a Bisquare Weighed Least Square (BWLS) is applied to each pair of profiles corresponding to the new spectrum (of unknown concentration) and the calibration cells DA spectra. The advantage of this technique is that it minimizes the effect

[11] An example: a DA profile of a gas sample with 10 ppm·m SO_2 can be obtained from a second DA profile of a sample of 5 ppm·m, by multiplying the later by a factor f of about 2. It would be exactly 2 only if the relationship between the absorption values and the gas concentration is perfectly linear.

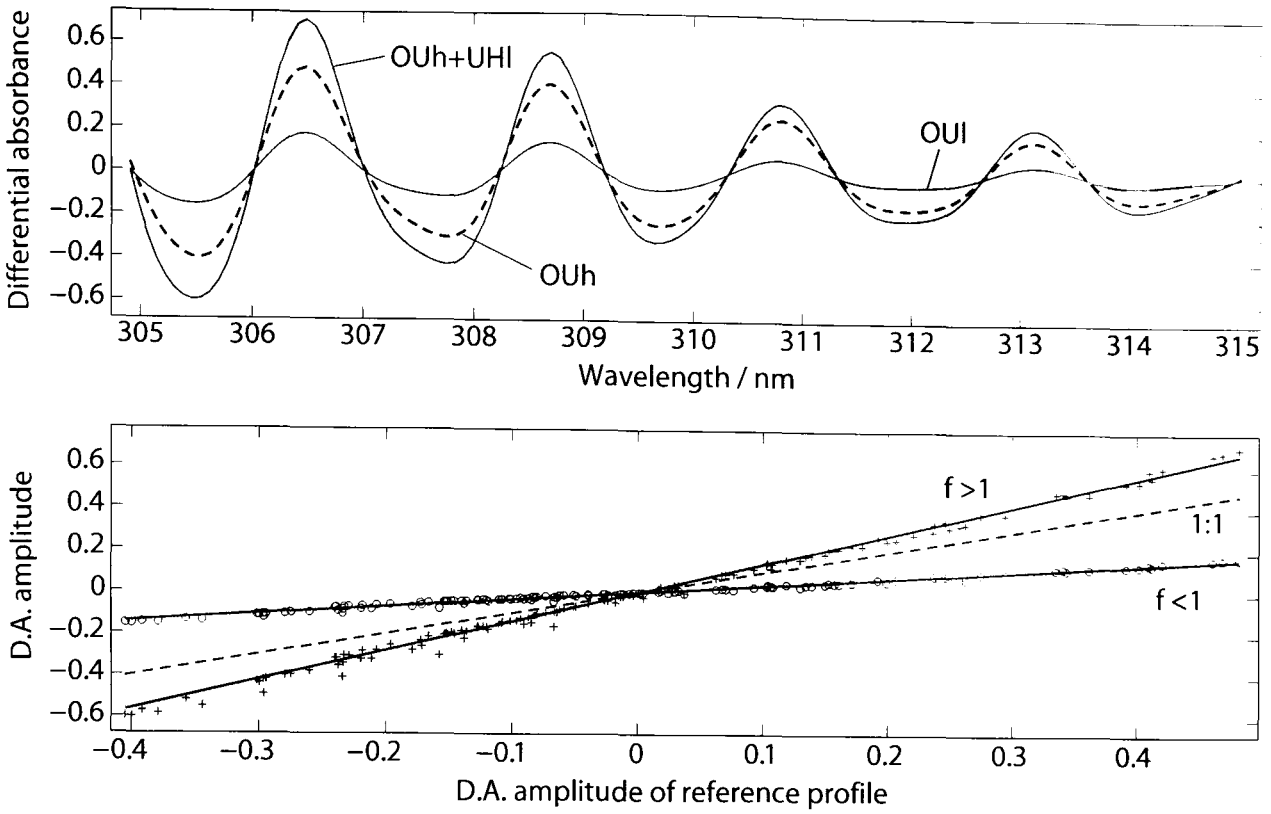

Figure 2.9: Comparison of three differential absorbance profiles associated to three different gas concentrations. The upper plot shows the profiles of OUh (dashed line), OUl (lower amplitude), and OUh+UHl (higher amplitude) (see Table 2.2). The lower plot depicts the correlation of the profiles and the weighted linear least square (BWLS) fit from which the multiplication factor f is obtained. OUh is used as reference. Note that $f(OUh, OUl) = 0.3516$ and $f(OUh, OUh + UHl) = 1.3956$ whereas the ratio of the concentrations are 0.2912 and 1.2733, respectively.

of outliers by iterative calculation of the weights of each data point, based on how far they are from the fitted line[12]. Thereby, it also reduces the inherent noise of the DA spectrum. An example of the correlation between three absorption profiles is shown in Figure 2.9. The comparison of each pair of DA profiles requires the choice of one of the profiles as a reference profile, which is compared to all the others profiles. The resulting amplitude factors represent a linear estimation of the DA amplitude, relative to the reference DA profile (which gets assigned a value of 1).

The result of this approach in the experiment with ten known concentrations (Table 2.3) is depicted in Figure 2.10. In this case, the whole set of calibration cells exhibited a non-linear relationship between the DA amplitude and SO_2 path-length concentration. This deviation from linearity is particularly stronger with cells of gas concentrations higher than 2000 ppm·m. Using all the calibration cells (up to 3560 ppm·m), it is found that a third-order polynomial model (model B) fits the data better than a quadratic polynomial (model A) (Table 2.3). The stronger deviation from linearity at high gas concentrations is also evi-

[12]See MATLAB's Help

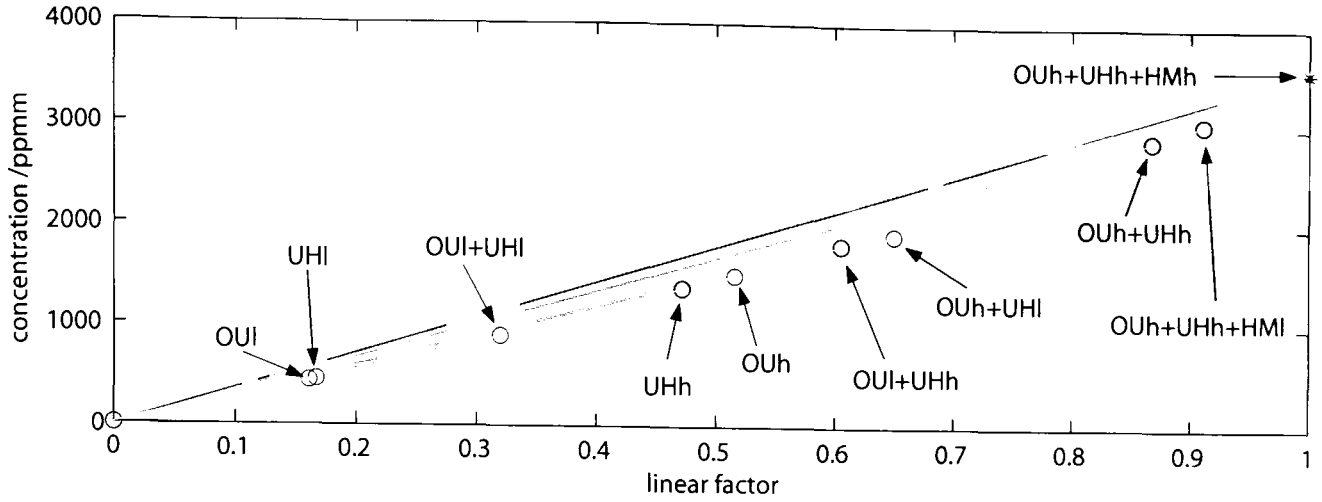

Figure 2.10: Non-linear relationship between the differential absorbance amplitudes and SO_2 path-length concentrations for a set of 10 calibration cells (Table 2.2). The linear factor in the abscissa is the amplitude factor calculated with the BWLS technique where the highest concentration was used as the reference profile.

denced by the good correlation that a quadratic model yields when only two calibration cells, with path-length concentrations lower than 1500 ppm·m, are used in the model (model C in Table 2.3). This model does not, however, represent well the cells with concentrations higher than 2000 ppm·m. Modeling the gas concentrations lower than 2000 ppm·m only with a linear relation (model D) shows relatively large errors, but the correlation improves with a quadratic model (model E). Looking at both quadratic models that use calibration cells of concentrations lower than 2000 ppm·m only (models C and E), it appears that the deviations from linearity are stronger with concentrations higher than about 1500 ppm·m. Thus, these results indicate that a quadratic polynomial that relates the DA amplitudes with gas path-length concentrations is a good model for concentrations of up to 1500 ppm·m, and still acceptable for gas concentrations of up to 2000 ppm·m, regardless of the number of calibration cells used in the derivation of the model. A third-order polynomial might improve the correlation in the latter case, but it seems to be necessary in the case of measuring gas concentrations higher than 2000 ppm·m[13].

The FLYSPEC is commonly operated with just two calibration cells, a low- and a high–concentration cell (Lc and Hc, respectively). Those are sufficient to create a reliable quadratic model to cover the whole gas concentration range from zero to, at least, the concentration of the Hc cell (e.g. model C in Table 2.3).

In active correlation, the DA profile of the new sample of unknown concentration is

[13]It is important to mention here that these results cannot be generalized to other instruments. Although similar, other FLYSPEC instruments can exhibit a different relationship between absorbance amplitude and measured gas concentrations. It is likely to expect only small variations but, in practice, this type of analysis should be carried out on every single instrument in order to constrain their own characteristics and capabilities.

Table 2.3: Error of the quadratic models. Models A and B are quadratic and third–order polynomial models, respectively, that use all cells. Model C is a quadratic model using only two calibration cells (UHl and UHh). Models D and E are linear and quadratic models, respectively, that only use cells with concentrations lower than 2000 ppm·m. All these models were calculated with a zero–intercept condition. The error is calculated as concentration minus model value.

Cells	Concentration [ppm m]	Error of the model A	B	C	D	E
none	0	0.0	0.0	0.0	0.0	0.0
OUl	438	45.3	-15.7	6.1	-35.9	0.4
UHl	448	40.1	-21.5	0.0	-42.7	-5.7
OUl+UHl	886	38.6	-7.9	-10.5	-53.4	-11.5
UHh	1375	32.0	31.8	0.0	-7.0	12.7
OUh	1504	3.9	18.4	-18.2	-7.8	0.4
OUl+UHh	1813	-15.6	24.1	-11.4	42.8	20.9
OUh+UHl	1915	-82.6	-34.0	-62.3	17.9	-22.0
OUh+UHh	2878	-30.8	-3.6	100.6		
OUh+UHh+HMl	3048	-46.5	-40.5	111.7		
OUh+UHh+HMh	3568	90.0	32.2	307.0		

compared to those of the Lc and Hc cells, as depicted in Figure 2.8. As an example, and simply to illustrate this procedure, it will be assumed that the gas concentration of the new sample is higher than that of the Lc cell and lower than that of the Hc cell. Thus, the two amplitude factors obtained from these comparisons are $f_l = f(low, new) > 1$ and $f_h = f(high, new) < 1$ (Equation 2.17, Figure 2.8). If DA_{new}, DA_{high} and DA_{low} are the differential absorbance profiles of the new gas sample, high and low calibration cells, respectively, the relations between them can be expressed as follow:

$$\begin{aligned} DA_{new} &= f_h \cdot DA_{high} \quad f_h < 1 \\ DA_{new} &= f_l \cdot DA_{low} \quad f_l > 1 \end{aligned} \tag{2.18}$$

With these amplitude factors and the concentrations of the calibration cells, a quadratic model with zero (0,0) intercept can be formulated (Figure 2.11):

$$C_i = a \cdot \tilde{f}_i^2 + b \cdot \tilde{f}_i \tag{2.19}$$

where C_i is the gas concentration of the cell, $\tilde{f}_i = 1/f_i$ is the inverse of the amplitude factor, the subscript $i = l, h$ represents the calibration cells, and a, b are the constants of the model. The above equation can be re-arranged (dividing it by the factor $\tilde{f}_i$) to obtain the equation

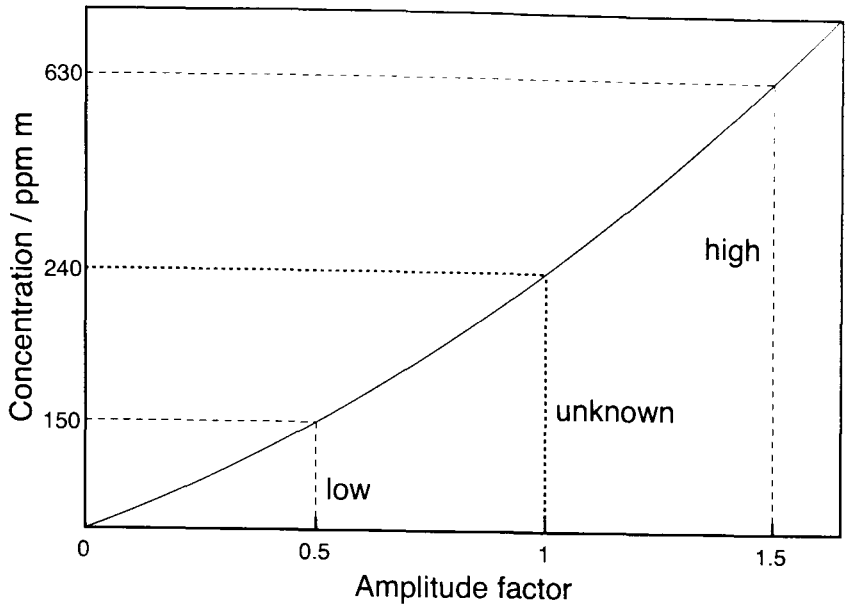

Figure 2.11: Fictitious example of a quadratic model calculated with the amplitude factors $\tilde{f}_h = 1.5$ and $\tilde{f}_l = 0.5$, that is used to obtain the gas path-length concentration of an unknown sample (Equations 2.19-2.21). In this example, the gas concentration of the low and high calibration cells are 150 and 630 ppm·m, respectively.

of a straight line,

$$C_i \cdot f_i = a\frac{1}{f_i} + b \tag{2.20}$$

which can be easily solved for the parameters a and b. Thus, the concentration of the new gas sample can be calculated as:

$$C_{new} = a + b \tag{2.21}$$

In passive correlation, the relation between the DA amplitude and gas path-length concentration is obtained by using the low–concentration (Lc) cell as the reference cell, and calculating the factor $f(low, high) > 1$ with the high–concentration (Hc) cell. Thus, the quadratic model is calculated with the set of amplitude factors $x = \{0, 1, f(low, high)\}$ and corresponding concentrations $y = \{0, C(low), C(high)\}$, where C is the concentration of the calibration cell. The coefficients of this model have to be stored during the calibration set up, along with the DA profile of the Lc cell. Then, to calculate the concentration of a new (unknown) gas sample, the new DA profile is compared to the DA profile of the low concentration cell with the weighted least square (BWLS) algorithm. Finally, the calculated amplitude factor $f(low, new)$ is entered into the model to obtain the new gas concentration.

Residuals

In addition to the deviations from linearity observed in the wavelength-independent relation between DA amplitude and gas path-length concentration (Figure 2.10), the residuals

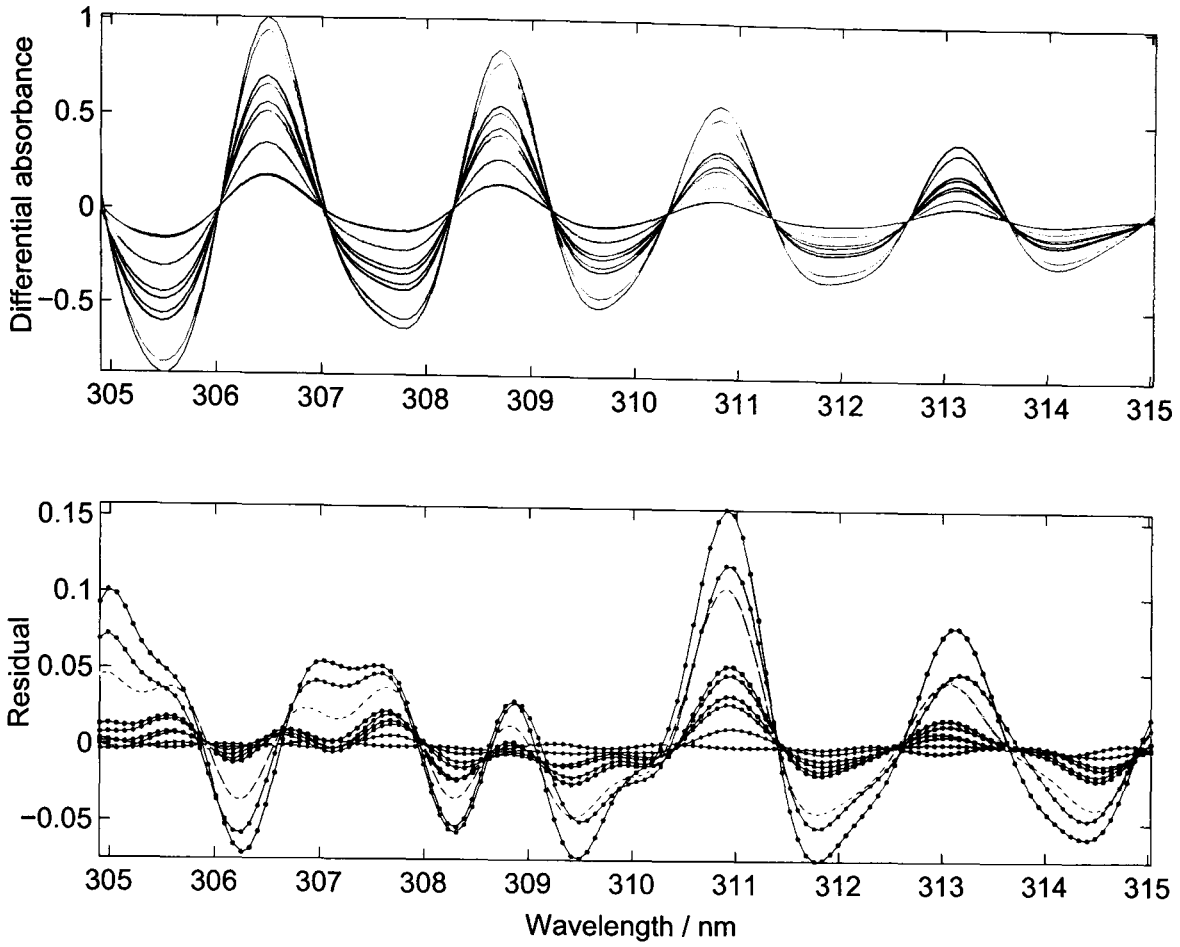

Figure 2.12: Differential absorbance profile of all the calibration cells (top figure), and the residuals obtained after the comparison between them using the weighted least square method (bottom figure) (Figure 2.10).

obtained from the comparison of the profiles evidence a wavelength–dependent non-linearity in the absorbance recorded by the instrument (Figure 2.12). These residuals were calculated by subtracting the original DA profile of the calibration cells, from the theoretical DA profile obtained with the reference cell and amplitude factor associated with that pair of cells; in this example the profile of the calibration cell with the lowest gas concentration (OUl) was used as reference. It appears that the amplitude of the residual can be relatively very high (Figure 2.12). For instance, the highest residual value at ~311 nm is reached in the comparison between the calibration cells with the lowest and highest gas concentrations (OUl=438 ppm·m and OUh+UHh+HMh=3568 ppm·m, respectively), with an amplitude that is about 25% of the DA amplitude of the second cell. To some extent, these residuals are consistently (in the whole wavelength range) related to the gas concentration of the cells. Therefore, the correlation model described herein can potentially be expanded to incorporate these residuals. This extended model could help to analyse the quality of the correlation and to check for anomalies in the recorded absorbance; it could also, perhaps, improve the correlation between DA amplitude and gas concentration.

Whether these residuals are real features observed in the absorbance of sulphur dioxide under normal outdoor–environmental conditions, or a result of the acquisition system (calibration cells and/or USB2000 spectrometer) is unknown. However, the existence of residuals in the correlation procedure developed herein should not alter the accuracy of the model greatly. In effect, as long as the measurements are within the gas concentration range of the calibration cells, and that a reasonable number of cells is used to cover that range, the results can be considered of high accuracy. (The accuracy of the results is constrained by the calibration model.) The model examples presented in Table 2.3 indicate that this is the case when the measurements are performed with two calibration cells and concentrations of up to 2000 ppm·m.

2.5 Test on Mount Etna

2.5.1 Description of the experiment

In May 2005, during the 9th IAVCEI gas workshop held in Sicily, Italy, a field experiment was carried out to measure, simultaneously, the gas plume emanating from the summit of Mount Etna. This experiment involved several groups working with remote sensing techniques. In one of these groups, T. Caltabiano from INGV, T. Mori from Tokyo University, and myself (Open University), performed traverses on the south flank of the volcano. We installed, in the same car, a COSPEC and a mini-DOAS (INGV), a home–made ultraviolet spectrometer (Tokyo U.), and a FLYSPEC (OU). The hardware of the UV spectrometer belonging to Tokyo U. was similar to that of FLYSPEC (T. Mori, personal communication), with the main difference that five calibration cells were available for calibration of the instrument. Also, the algorithm to calculate the SO_2 column amount was similar to that of the LapFly software that came with the FLYSPEC (Horton *et al.*, 2006)[14], which calculated the peak–trough height difference in the wavelength range 305–317 nm. Details of the COSPEC can be found, for example, in Stoiber *et al.* (1983); Williams-Jones *et al.* (2007), and the characteristics of the mini-DOAS can be found in Galle *et al.* (2002); McGonigle and Oppenheimer (2003). The mini-DOAS was the only instrument that did not utilize calibration cells, since the methodology employed by this instrument is very similar to that of the DOAS technique (Platt, 1994).

[14]There is a second version of the software that processes the raw spectra data in the FLYSPEC, which now uses a higher number of wavelengths in the correlation absorption–gas concentration (Keith Horton, personal communication).

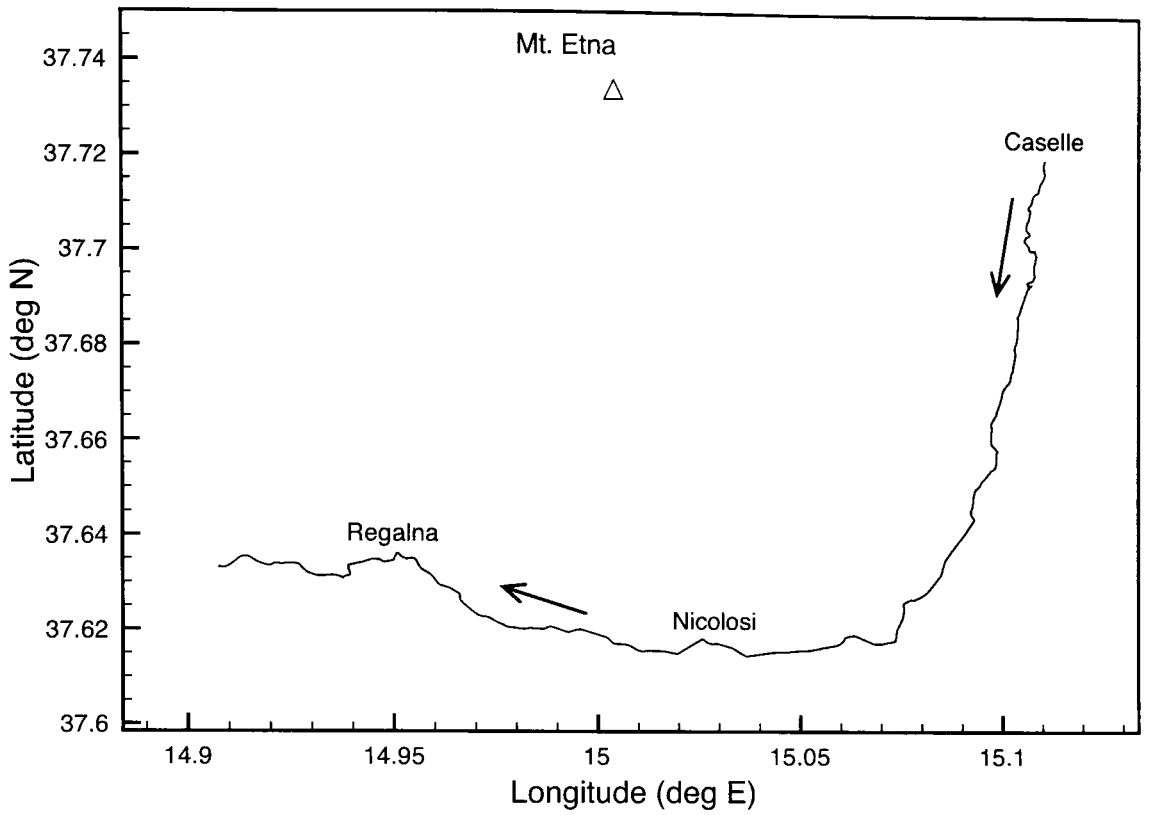

Figure 2.13: Sketch map of the second car traverse carried out on the south flank of Mount Etna, driving from east to west starting at the town named Caselle. The volcanic plume was flowing to the south. The triangle symbol represents the summit area of the volcano (coordinates gathered from the Global Volcanism Program website).

Seven car traverses were performed between the morning and afternoon of the 7 May 2005. Five of them were between the towns of Caselle and Santa Maria de Licodia, between 10 and 15 km from the summit craters (Figure 2.13). Two traverses were performed closer to the volcano, finishing or starting at Refugio Sapienza (about 5.5 km from the summit craters), ensuring that the plume concentration profile was complete (Figure 2.14).

2.5.2 Results

One of the main objectives of this experiment was to compare the results obtained from standard procedures to measure the SO_2 gas flux emitted by volcanoes, using slightly different techniques (instrumentation). As expected, the measurements carried out with all the instruments yielded similar results. Examples of the SO_2 column abundance profiles are presented in Figure 2.15. This example illustrates the good results (in agreement with other instruments) obtained with the FLYSPEC and the algorithm described in this chapter. The most prominent feature in these profiles are the spikes observed in the whole profile obtained with the COSPEC. These spikes are caused mainly by trees hanging over the road which block part of the field of view of the instrument, or direct sunlight coming into the

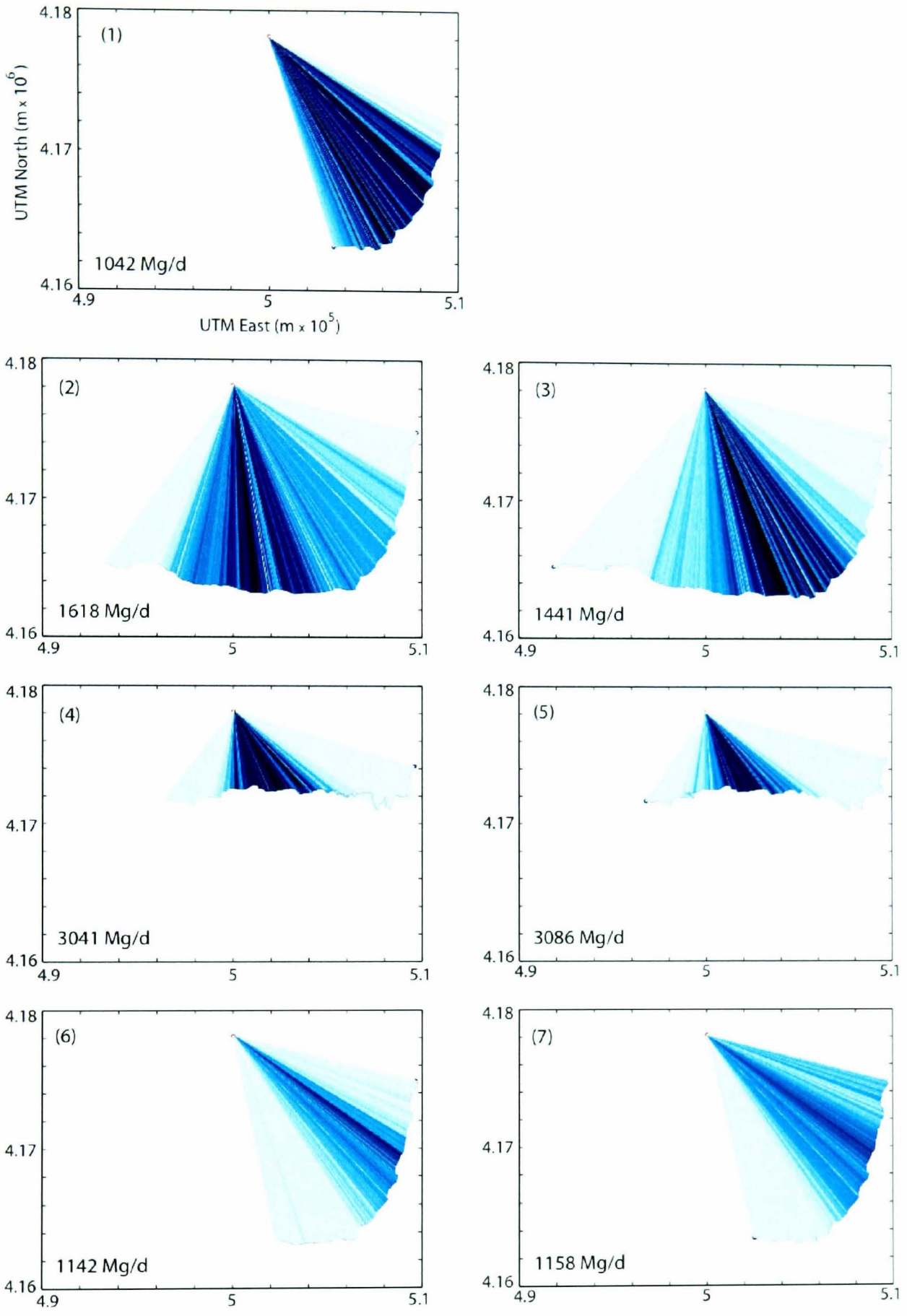

Figure 2.14: Maps of the seven road traverses carried out on the south flank of Mount Etna. Lines were drawn from the crater to the GPS locations within the traverse; the darkness of the lines indicates relative higher column abundance of SO_2. Note that traverses (4) and (5) were performed on a different road, closer to the summit of the volcano. All the maps are in Universal Transverse Mercator coordinate system; axes labels as in map (1). The calculated emission rate of SO_2 for each traverse is given in the bottom left of the maps.

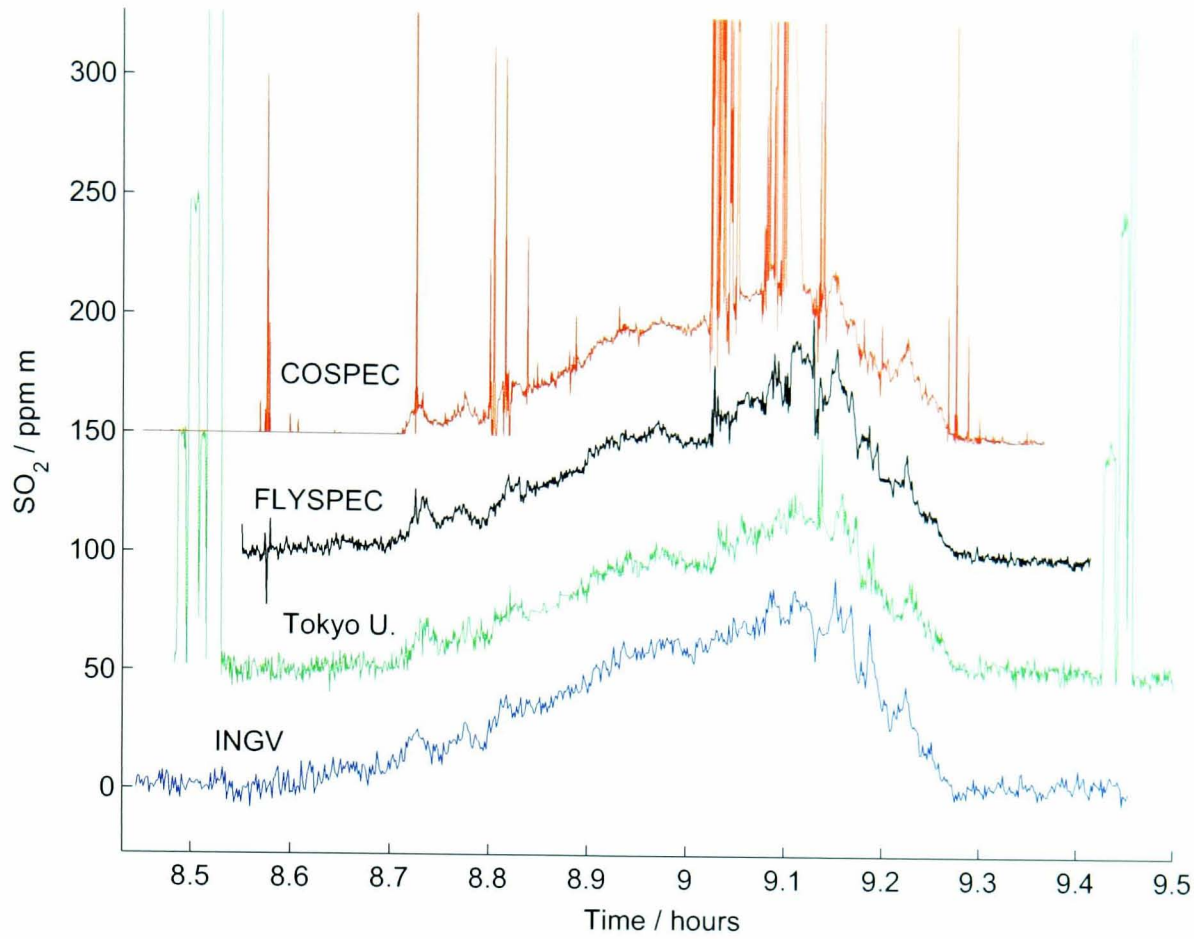

Figure 2.15: Comparison of the measurements of four instruments, from top to bottom: COSPEC (INGV), FLYSPEC, USB2000-Tokyo U., and mini-DOAS (INGV). In order to facilitate the comparison of the measurements, the profiles of SO_2 path-length concentrations are displaced 150, 100, 50 and 0 ppm·m, respectively. These results correspond to the second car traverse performed on the south flank of Mount Etna (Figure 2.13).

spectrometer. Only a few spikes are observed in the profiles of the other instruments. (The high values at the beginning and end of the profile acquired with the Tokyo U. spectrometer correspond to readings of the calibration cells.) In terms of the absolute values of path-length concentrations, the COSPEC, FLYSPEC and Tokyo U. spectrometer are in very good agreement, over both the slow and more rapid changes. The mini-DOAS (INGV), however, exhibited a tendency to yield slightly higher values of path-length concentrations when the thickness of the plume (or gas column abundance) increased. This effect might be related to different correlation methodology of the instrument. A quantitative comparison of these results is presented in Table 2.4. In order to be consistent with a value per value comparison, the profiles measured by the four instruments were re-sampled to a sampling rate of one datum every second. The sum of the path-length concentrations over the profiles (Figure 2.15) were calculated to check for general deviations, to relative higher or lower values, in the total SO_2 column abundance (Table 2.4, 'Sum' column). The result from the mini-DOAS instrument presented the highest value, consistent with the slightly higher path-length concentrations

Table 2.4: Comparison of results of all the instruments in second car traverse. The first column shows the sum of the SO_2 path-length concentrations over the entire profile, as seen in Figure 2.15. Within the second to fifth columns, the upper and lower triangular matrices show, respectively, the mean and standard deviation of the difference between the profiles of the instrument on the left and the instrument on top of the table (in ppm m).

Instrument	Sum	COSPEC	DOAS	Tokio U.	FLYSPEC
COSPEC	9.70E+04	-	-1.0	5.3	3.6
DOAS	1.00E+05	36.3	-	6.4	4.7
Tokio U.	8.14E+04	36.9	7.0	-	-1.7
FLYSPEC	8.64E+04	37.3	6.4	6.8	-

observed in Figure 2.15, whereas the also relatively high value calculated for the COSPEC is caused by the high number of anomalous spikes. Calculations of the mean and standard deviation of the difference between the profiles of any two instruments show that there is an overall very good agreement between their measurements. The difference between the results of the four instruments is, on average, less than ten ppm m (Table 2.4). Only the COSPEC shows greater variations caused by the spikes in its profile. Comparison of the results from all the road traverses revealed that the four instruments presented relative variations in the path-length concentration on short segments of the column abundance profiles. These variations can be caused by the different hardware and methodology to reduce the spectral data as well as by the slightly different line of sight of the instruments installed in the car.

Another relevant observation is the variance of the measurements. Although each data point in the profile of the mini-DOAS was calculated by co-adding 50 spectra (collected with an integration time of 100 ms), the signal-to-noise ratio is relatively lower in comparison to that of the FLYSPEC and COSPEC. The Tokyo U. spectrometer co-added 30 spectral samples. With the FLYSPEC, every single light spectrum was analysed and used to calculate the path-concentration, and the resulting profile, shown in Figure 2.15, was obtained by applying a moving average window of only 10 samples to the original column abundance profile. Thereby, the good signal-to-noise ratio of the FLYSPEC is comparable to that of the COSPEC.

SO_2 fluxes were calculated from the data collected with the FLYSPEC for the seven car traverses (Figure 2.14). The gas flux is obtained by integrating the column abundance in the profile following the position of the instrument recorded with a computer-connected GPS. The profiles were splitted in segments of five path-length concentrations which were acquired in a time span of one second (associated with an integration time of 200 ms). Each segment was integrated using the length of the segment calculated from the GPS data and

corrected by deviations from perpendicularity between the orientations of the segment and the plume transport from the craters of the volcano. The result of this integration is then multiplied by the plume transport speed and converted from units of ppm $m^3 s^{-1}$ to units of mega-grams per day (Mg/d). The methodology used in these calculations is similar to that used in measurements of gas emissions at other volcanoes (and by other research groups); more details of this methodology can be found in Stoiber *et al.* (1983) and Williams-Jones *et al.* (2007). Using a fixed plume speed of 10.3 $m s^{-1}$ (measured by INGV) the fluxes of sulphur dioxide obtained for the seven car traverses are 1042, 1618, 1441, 3041, 3086, 1142 and 1158 Mg/d, respectively. Most of the variations in these results can be attributed to variable gas emissions from the crater, variations in plume speed, and errors related to the methodology used to measure the column abundance of SO_2 in a cross section of the plume. However, the two-times higher gas fluxes obtained from measurements made on a road closer to the volcano (car traverses 4 and 5, Figure 2.14) show column abundances of up to 350 ppm m, which is considerable higher than the maxima of 80-120 ppm m measured in traverses 1-3 and 6-7. This indicates that during traverses 4 and 5, either there was a sudden increase in gas emissions or that closer to the craters the plume was optically thicker. Other participants of the IAVCEI workshop observed that the gas plume was flowing downslope on the upper parts of the south flank of the volcano (Patricia Nadeau, personal communication). Thus, it is likely that the lower gas fluxes obtained from the car traverses performed on the Caselle-Regalna road (Figure 2.13) are bounded by measurements of only part of the gas plume. If this is the case, SO_2 fluxes of 3050 Mg/d are more representative of the real volcanic emissions than the average 1280 Mg/d calculated from the data obtained on the Caselle-Regalna road.

2.6 Conclusions

I have described the characteristics of the FLYSPEC instrument along with the theory and spectra processing algorithm used in the calculation of SO_2 column abundance in volcanic plumes. The instrumentation and methodology are based on the UV correlation spectroscopy technique, which was originally developed for the COSPEC. The capabilities of the FLYSPEC and its comparison with other techniques and instruments were presented by Horton *et al.* (2006); Elias *et al.* (2006). The implementation of a new algorithm for the re–processing of the raw spectra data in the FLYSPEC (developed herein) also showed good agreement with measurements performed with the COSPEC, mini-DOAS and a UV spectrometer built by

Tokyo University. This new algorithm has also shown improvements in the quality of the measurements, such as higher signal-to-noise ratio and extraction of spikes.

The detailed procedure for calculation of the SO_2 path-length concentration from raw light spectra data is as follows:

1. Set parameters of the spectrometer (light correction and fitting ranges) and calculations.
2. Set the calibration
   (a) Read reference (background) and dark (instrument offset) files
   (b) Read spectra and get concentrations of calibration cells
   (c) Calculate and store the differential absorbance of the calibration cells
3. Read files with new measurements
   (a) Read dark and reference files if they are different to the corresponding calibration files
   (b) Open the file with new measurements
4. (Optional) Check for waveform shifts of the instrument
5. Loop over the spectra in the new scan file
   (a) Read a single spectrum
   (b) Get the differential absorbance of the new spectrum
   (c) Correlate the differential absorbances of the calibration cells with the new spectrum, and calculate the concentration of SO_2
6. (Optional) Identify and label spikes end loop.
7. Plot and save the results

Chapter 3

Outgassing activity at Villarrica and Stromboli volcanoes

3.1 Introduction

Persistent degassing at many open–vent volcanoes, such as Villarrica (Chile), Stromboli (Italy), Mt. Erebus (Antartic), Masaya (Nicaragua), Mt. Etna (Italy), among others, is characterised by both passive gas emissions and explosive outgassing. However, the styles of outgassing activity observed on these volcanoes can be very different. For instance, Villarrica and Mt. Erebus are characterised by an active lava lake inside the summit crater, in which lava overturn and strombolian explosions take place (Calder *et al.*, 2004; Witter *et al.*, 2004; Kyle *et al.*, 1994; Aster *et al.*, 2003). At Stromboli and Mt. Etna, however, direct visualization of the top of the magma column is not possible, although they exhibit manifestations of shallow magmatic activity (Ripepe *et al.*, 2001a,b; Carbone *et al.*, 2003; Harris and Ripepe, 2007a). Whilst Mt. Etna displays strong explosive activity only during eruptive phases, such as fire fountaining, strombolian and vulcanian explosions (e.g. Taddeucci *et al.*, 2004; Andronico *et al.*, 2005), Stromboli exhibits continual mild to moderate explosive outgassing, of diverse characteristics, at several active vents (e.g. Ripepe *et al.*, 2002; Ripepe and Marchetti, 2002; Harris and Ripepe, 2007b; Patrick *et al.*, 2007).

In this chapter, I describe the characteristics of the outgassing activity of Villarrica and Stromboli volcanoes, and show the differences in the bubble bursting activity observed between them. At Villarrica, video recordings, photographs, and direct observations of the lava lake activity within the crater allowed, for the first time, the detailed identification of different styles of bubble bursting, and the description of some distinct activity which can be

considered unique to this particular volcano with its visible active lava lake. At Stromboli, the explosive outgassing has been characterised previously by Chouet *et al.* (1974); Blackburn *et al.* (1976); Ripepe *et al.* (2001b, 2002); Ripepe and Marchetti (2002); Lautze and Houghton (2007); Patrick *et al.* (2007); Harris and Ripepe (2007b), among others, and it is much better constrained and understood. Based on a field campaign carried out during June–July 2004, and building upon the work of Patrick *et al.* (2007) and Harris and Ripepe (2007b), the different styles of bubble bursting are described. The classification and description of the explosive activity presented herein, in agreement with that of Patrick *et al.* (2007), include a qualitative analysis of the bursting sequence. In addition, further insights about the outgassing activity, as well as the dispersion of the gas plume, were gained from measurements of gas emissions performed with the FLYSPEC at the summit of Villarrica and Stromboli volcanoes.

3.2 Observed outgassing styles at Villarrica volcano

Since the eruption of 1984-1985, continuous shallow magmatic activity has been seen inside the crater at the summit of the volcano. The interior of the crater has a funnel shape and steep inner walls, with an internal diameter of approximately 150±10 metres at the crater rim (Figure 3.1). Visual observations account for persistent outgassing that involves mild strombolian activity taking place at the surface of a highly dynamic lava lake, which represents the top of the magma column within the main conduit (Witter *et al.*, 2004; Calder *et al.*, 2004). The depth of the lava free–surface ranges from >150 m to about 50 m below the summit. Because of the changing morphology of the crater floor, the lava lake is not always visible from the crater rim (Figure 3.1). The reader is referred to Section 4.2.4 for more details on the morphology of the crater floor. Descriptions of the activity at the lava lake by Fuentealba *et al.* (2000) and Calder *et al.* (2004) mention the rapid crusting-over of a relatively tranquil lava surface as well as vigorous ~5-30 m high fountaining.

3.2.1 Bubble burst activity at the lava lake

The observations summarised in this section were made myself from the crater rim of Villarrica volcano during November 2004-January 2005 and January-February 2006. Mild strombolian explosions are, perhaps, the most common explosive activity observed at the crater. However, five distinct types of bubble burst have been observed during periods with different levels of activity[1]. Here, the term 'bubble bursting' refers to the processes involved in gas-bubble rupture at the magma free–surface, fragmentation and subsequent ejection of pyroclastic material.

Seething magma

This distinctive bubble bursting style is distinguishable only when the lava free–surface is visible. The activity at the surface of the lava lake resembles the dynamics of boiling water, as medium-size bubbles (~0.5-3 m in diameter) burst continuously across the magma free–surface (Figure 3.2). Bubbles can be seen to rupture at the same location within the space of a few seconds. This style of activity induces the magma surface to experience continual wave-like undulations. The vigour of seething magma is variable: at the lower end of the scale only a few bubble bursts occur per minute and gentle roll-over of the magma surface can

[1] More of my photos and videos at http://picasaweb.google.com/jose.luis.palma/Villarrica

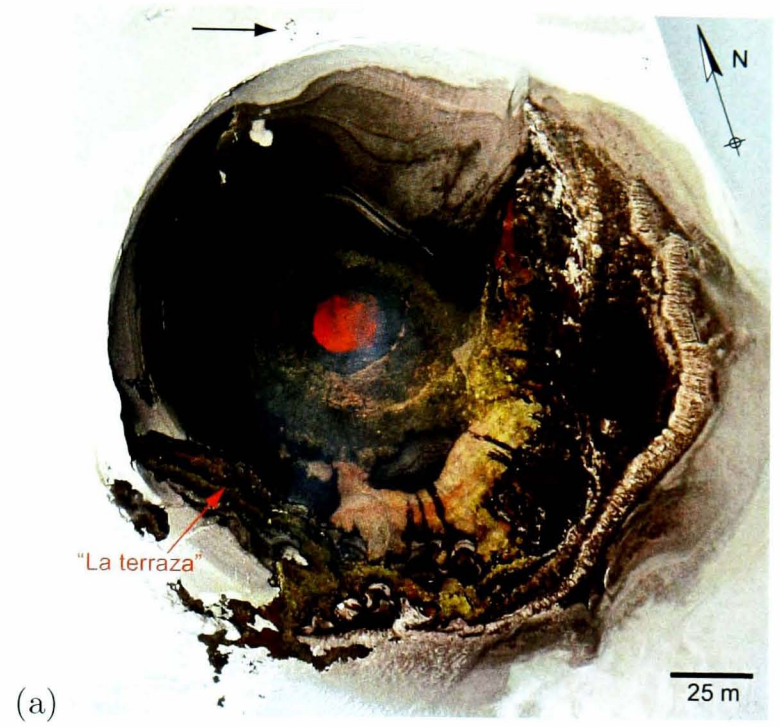

(a)

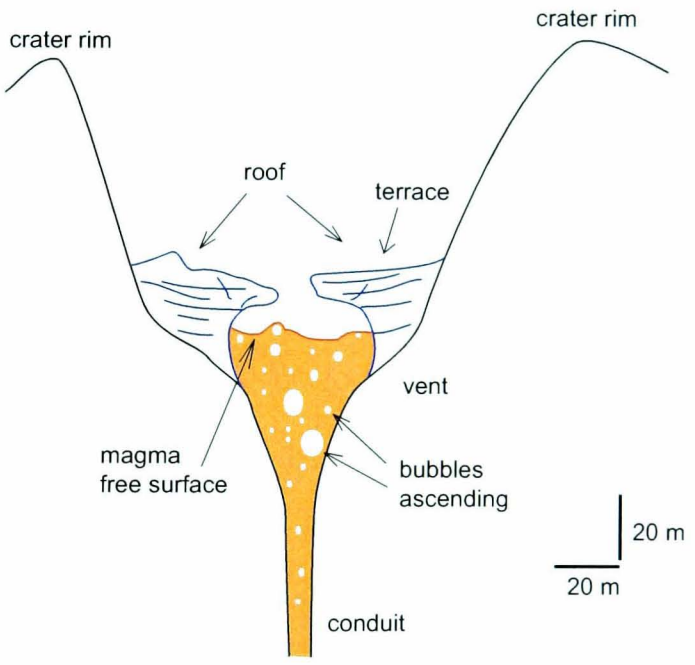

(b)

Figure 3.1: (a) Near vertical view of the crater of Villarrica volcano in November 2004 (courtesy of C.J.Tanguy). The arrow at the top indicates people (black dots) walking on the snow-covered crater rim. The interior of the crater has a diameter of 150±10 metres, whereas the outer rim is *ca.* 200 m across. (b) Schematic cross-section of Villarrica crater. The active lava lake represents the top of the magma column. The spatter roof adheres to the inner crater walls by accumulation of ejected spatter. A terrace (with a relatively flat surface) can be formed by accumulation of tephra during periods of elevated explosive activity.

be easily identified; at the more vigorous end of the spectrum, there are single bubble bursts almost every second ejecting pyroclasts more than 5 m above the lava lake. Perhaps the only volcano, apart from Villarrica, where a similar style of bubble bursting has been observed is Erta Ale, Ethiopia, although the scale and origin of the activity are different (Burgi *et al.*, 2002, note that the authors call this activity 'bubbling activity'). At Erta Ale, this activity generally occurs when the encrusted surface of the lava lake breaks and opens up to allow the escape of bubbles[2].

Small lava fountains

Fountains of lava occur through a relatively wide roof opening. Compared with the more classic hawaiian style of activity observed at Kilauea volcano (e.g. Parfitt, 2004), in which fountains reach tens to a few hundred metres high, these lava fountains are very small and are sustained only briefly (Figure 3.3). They normally last between 20 and 90 seconds, and reach 10 to 40 metres high. To some extent, a small lava fountain resembles a very strong variety of seething magma, with a much greater concentration of bubbles continuously reaching the surface. Although difficult to quantify, it is apparent that most of the pyroclastic material is centimeter-to-decimeter-sized clots of magma. Small lava fountains are less common than both seething magma and strombolian explosions. Lava fountains have also been observed at the lava lakes of Erta Ale, Ethiopia (Tazieff, 1994; Burgi *et al.*, 2002; Harris *et al.*, 2005), and Nyiragongo volcano, Democratic Republic of Congo (Zaire) (Tazieff, 1994). At Erta Ale, most of the lava fountains observed by Burgi *et al.* (2002) in February 2001 lasted less than 3 minutes and were 5 to 10 m high.

Strombolian explosions

This type of bubble bursting, named after the activity at Stromboli volcano, has been described as mild explosions caused by the rise and rupture of large gas bubbles or slugs at the top of the magma column (Vergniolle and Mangan, 2000; Parfitt, 2004). The magnitude and frequency of strombolian explosions at Villarrica volcano are both variable. Strong explosions ejecting pyroclastic material over 100 m above the vent are seen mostly when the general level of the observed and seismic activity is high, whereas during periods of reduced activity, when the level of magma is low within the crater, it is very rare to see

[2]See photos and videos at http://www.swisseduc.ch/stromboli/perm/erta/index-en.html (last visit on 2 February 2008). Note that the authors of this webpage call the this activity 'fountain', even though when the bubbly activity is very mild.

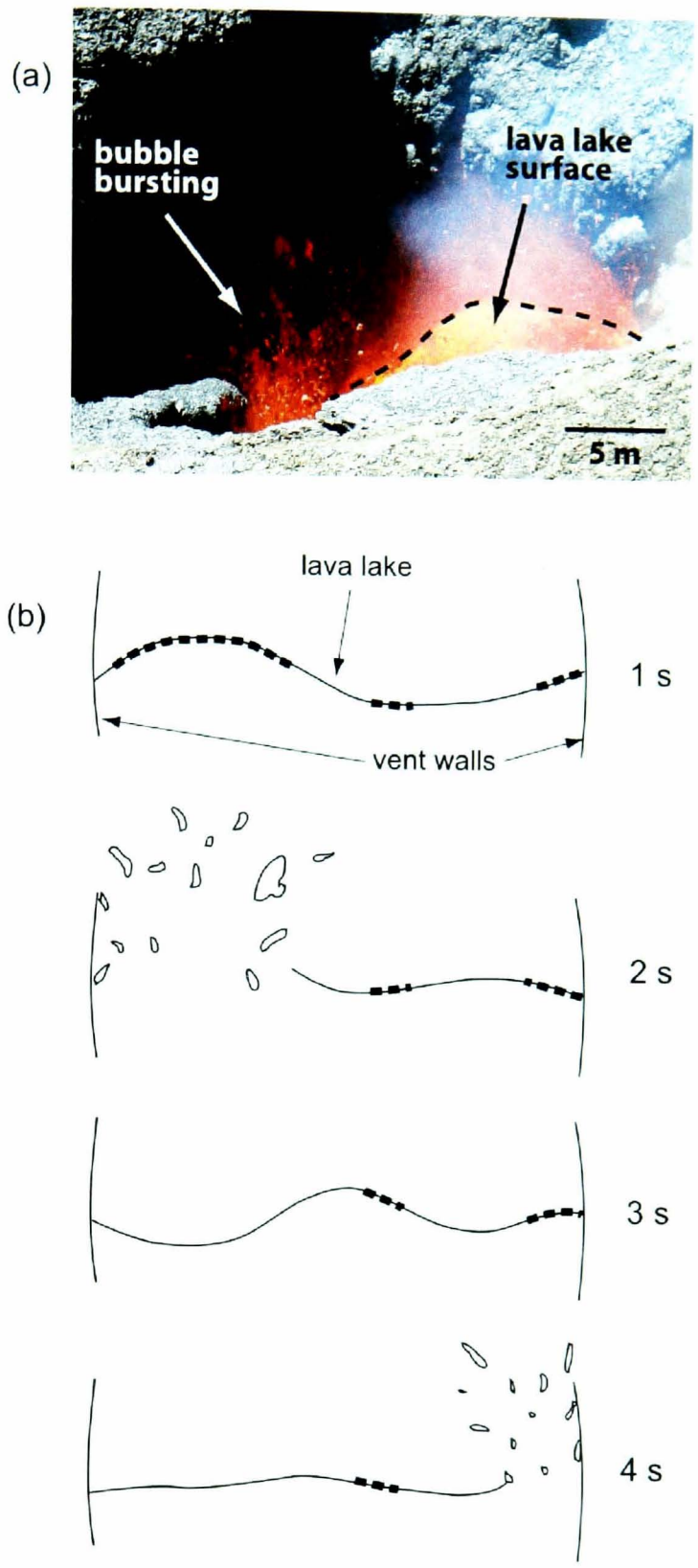

Figure 3.2: Seething magma bursting style. a) Photograph of the orifice in the spatter roof that shows part of the lava lake's free–surface with a bubble bursting on one side. The dashed black line indicates the margin of the lake. Photo from 8 February 2006, taken from the south-west side of the crater rim with the camera at about 95 m from the crater floor and using a zoom. The scale is approximate. b) Schematic of the seething magma activity, in which undulations occur in a partly encrusted lava lake (thick dash line) due to the bubbles that constantly reach the surface. In this case, two bubble bursts occur in a time frame of four seconds.

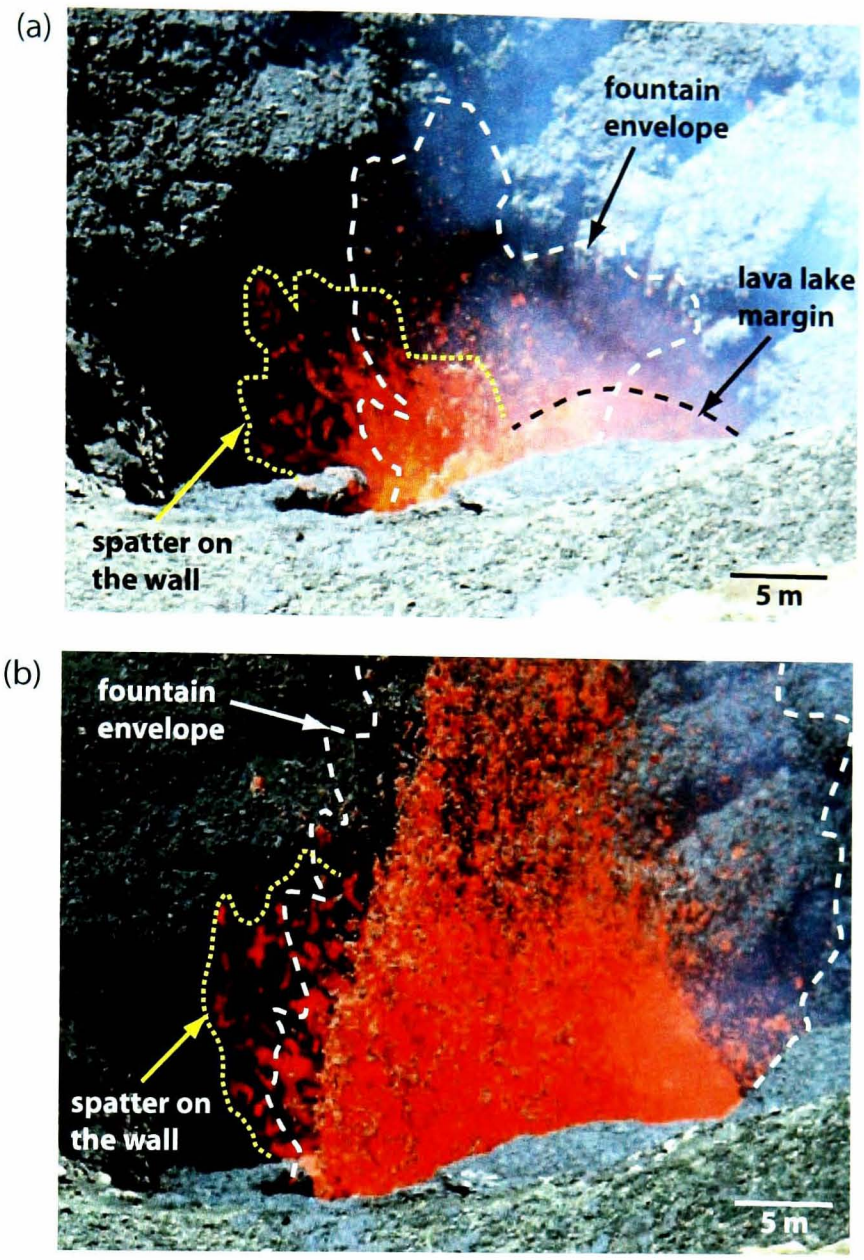

Figure 3.3: Photographs of the small lava fountain activity. a) The beginning of the fountain displays a few bubbles bursting simultaneously. b) Six seconds later, the fountain reaches more than 25 m high. Photos from 8 February 2006, taken from the south-west side of the crater rim using a zoom. Scales are approximate.

such explosions (Figure 3.4). The duration of an explosion ranges from a fraction of a second, involving a single strong burst, to more than 15 seconds when the explosion is composed of rapid sequences of pyroclastic ejections. Due to the morphology of the vent (Section 3.2.4), some explosions do not exhibit pyroclastic ejection through the orifice in the spatter roof, but a sudden and relatively rapid gas emanation that ascends as a distinctive thermal plume. Sometimes, when no spatter is emitted, the spurt of gas is the only evidence of explosions or a strong bubble burst. Strombolian explosions observed at Villarrica are similar to Stromboli type 1 eruptions described by Patrick *et al.* (2007), essentially by virtue of the dominance of coarse particles and lack of a dense ash plume (Figure 3.4). There have been observations of atypical explosions at Villarrica that are accompanied by a brownish ash plume. They are associated with partial collapses of the spatter roof or avalanches from the inner crater walls.

Figure 3.4: Photograph of a strombolian explosion observed from the crater rim of Villarrica volcano. Photo taken 18 January 2005 from the west side of the crater rim.

which is consistent with the idea of backfilling of loose material for the type 2 eruptions at Stromboli (Patrick *et al.*, 2007).

Gas jetting

Gas jets are strong exhalations of gas and relatively fine (ash-lapilli size) pyroclastic material. Their duration is normally longer than that of strombolian explosions. None of them have been observed directly generated from the lava lake surface, but instead they originate through an opening in the spatter roof or spatter cone. If the hole in the roof is small relative to the surface area of the lava lake underneath, it is likely that during an explosion or small lava fountain only the fine fraction of the ejecta vents through the hole, generating the impression of an exhalation of gas with only a small amount of coarse material. There have been observations of near simultaneous explosions and gas jetting events at two adjacent openings (less than 20 metres apart). In that case, the gas jet occurs in the smaller hole (in effect, a blow-hole), and commonly lasts as long as the explosion. Gas jet-like activity has also been observed during periods of elevated activity, when a scoria cone has built up on top of the spatter roof, and whose opening is generally narrow. In these instances, the gas jet resembles an energetic narrow fountain whose spatter, ash to bomb in size, can reach a hundred or more metres in height.

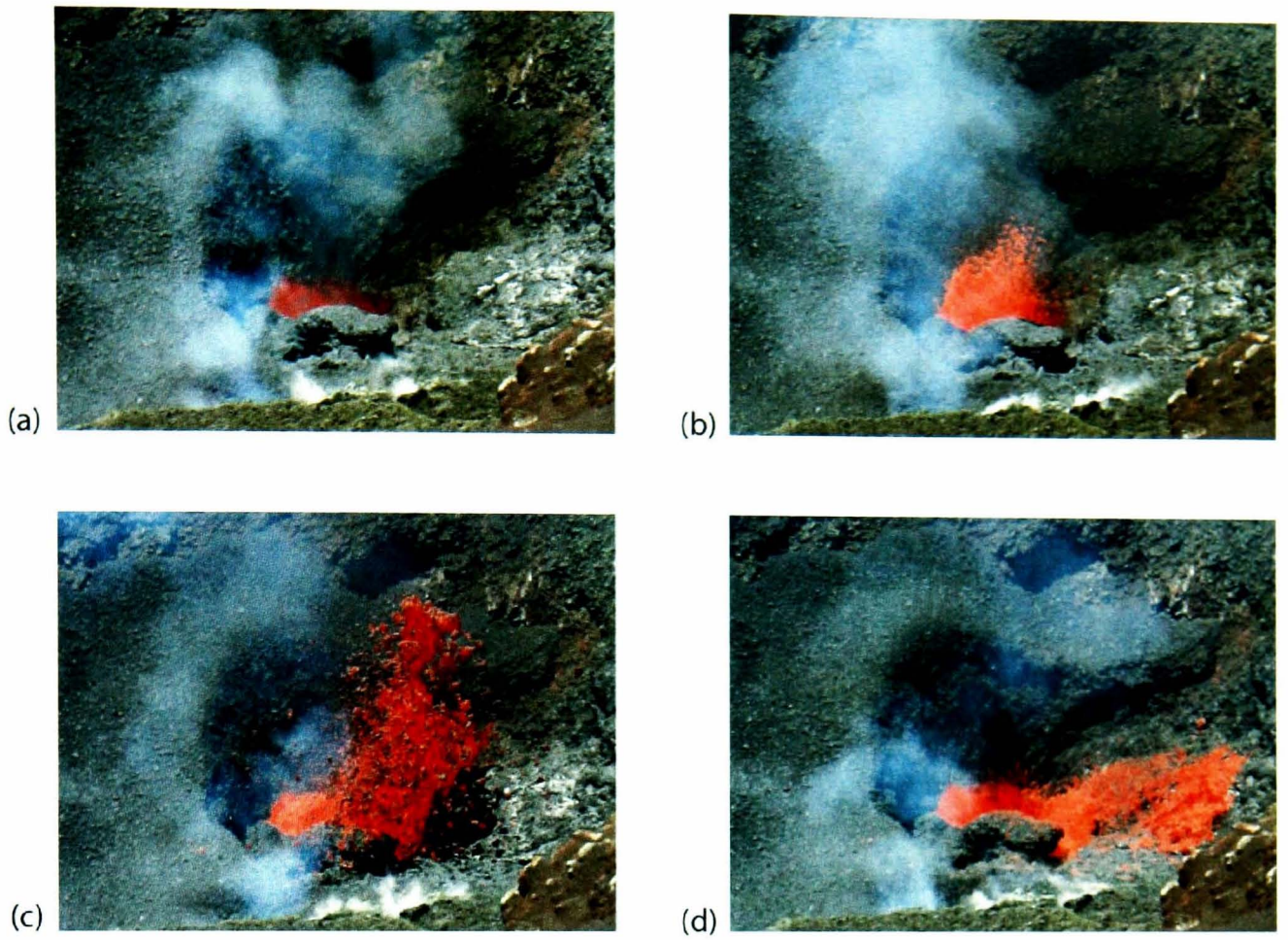

Figure 3.5: A 'splashing lava' event observed from the crater rim of Villarrica volcano. The video sequence shows: a) explosion, b) partly fragmented lava appears, c) the bulk of the material comes out through the orifice, and d) the lava splashed on to the crater wall. Note that the orifice in the spatter roof is next to the crater wall (on the right).

Splashing lava

A fifth type of activity, indirectly related to bubble bursting, has been observed occurring particularly when the spatter roof covers a big part of the lava lake. In this case, the roof prevents the explosions from sending pyroclastic material out of the vent. Often, shortly after an explosion is heard or a gas spurt is observed, a considerable amount of spatter is expelled through the roof orifice (Figure 3.5). It is characteristically coarse spatter that fragments on exit and accumulates around the vent. I believe that this material is not derived from primary fragmentation of magma during bubble rupturing, but is caused by subsequent splashing of lava associated with waves generated on the lava free–surface in the aftermath of an explosion.

Frequency and products of the explosive outgassing

These descriptions recognize different mechanisms for the origin of the explosive events. Whilst seething magma, strombolian explosions and small lava fountains represent types of

primary bubble bursting activity at the surface of the lava lake, gas jetting appears to result from a combination of bubble burst activity and subsequent interaction with the spatter roof. This interaction modifies the development of the bursting activity and ejection of pyroclastic material as it leaves the vent. This would explain why the size distribution of pyroclasts ejected during gas jetting appears skewed towards smaller fractions compared with that generated as a result of the primary fragmentation. Spatter generated from splashing magma activity is derived directly from the lava lake, although again the fragmentation is not caused by bubble bursting directly.

Timing of the explosive events observed from the crater rim during 6 days of January-February 2006, yielded a mean frequency of 32 events per hour with variations between 20 and 46 events per hour. This result considered all the styles of bubble bursting activity of episodic nature, i.e. did not consider seething magma. Since the spatter roof hindered the observation of every major bursting event, this frequency is considered a minimum[3].

Pyroclasts derived from explosions exhibit vesicles with a broad size distribution. Two examples of typical pyroclasts found on the crater rim of Villarrica volcano are shown in (Figure 3.6). Reticulite is common among this material (Figure 3.6a). General textural characteristics of scoria found on the crater rim include high vesicularity (>60% in the most vesicular samples) with vesicle radii up to a few centimeters (Figure 3.6b), irregular and iridescent surface with adhered Pele's hair, or spatter with cowpat-like form (elongated and flat) in some products of big explosions. Often after an explosion, it is only the more dense material that remains on the crater rim as the highly vesicular ejecta is easily dispersed by the wind. Although not quantified in this work, observations of the high vesicularity of the pyroclastic material along with observations of the bubble bursting activity at the lava lake, are an indication of a very broad bubble-size distribution in the gas phase reaching the magma free–surface.

3.2.2 Variable outgassing and plume dispersion

As mentioned earlier, Villarrica volcano is characterized by the continuous emission of a gas plume from the summit. This is the background degassing activity observed at the crater. It has persisted since the end of the last eruption in 1985, although a gas plume has been observed recurrently since the end of the 19th century (Casertano, 1963).

[3]The observation time varied between about 2 and 4 hours, and the total number of events amounted to 262. The estimated frequency of these events is constrained by the few number of days with observations, the limited time during which observations were made, and influence of the spatter roof.

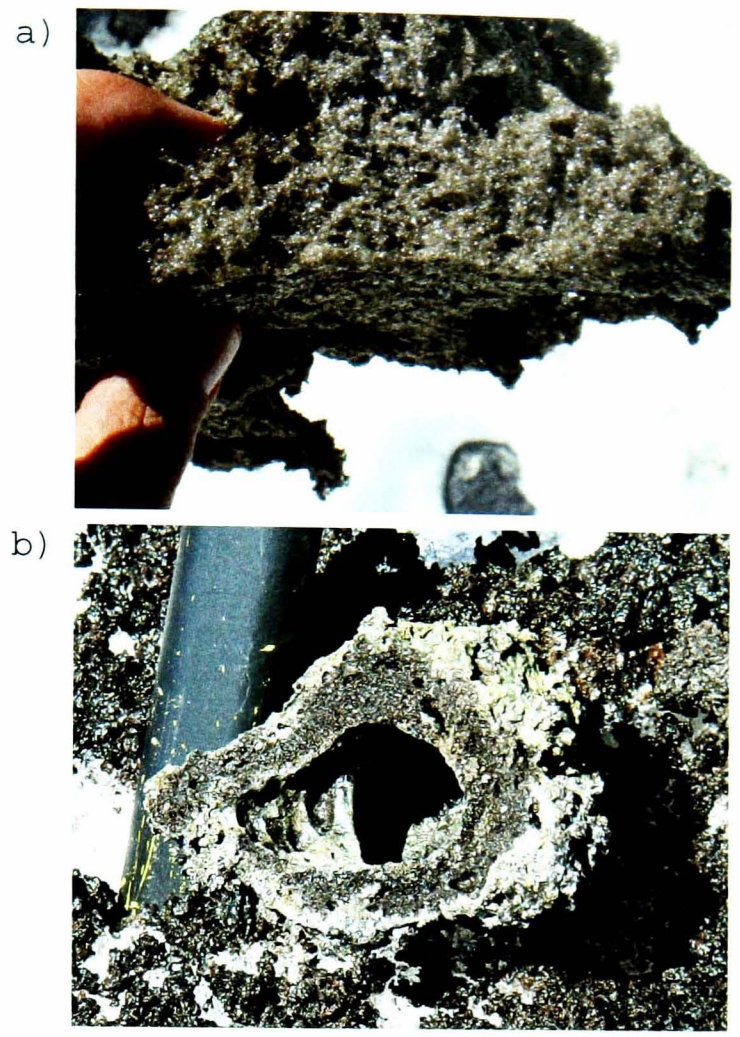

Figure 3.6: Photographs of two characteristic samples found on the crater rim, generated by explosions that occurred in December 2004 and January 2005. (a) Reticulite scoria that was part of the pyroclastic material thrown >100 m above the crater floor (19/Dec/2004 17:24 local time); by the next day, no scoria with that texture remained on the crater rim. (b) Scoria sample showing the wide vesicle-size distribution commonly found in Villarrica scoria samples (ice axe handle for scale).

The gas plume observed at Villarrica is emitted from the lava lake, the top surface of the magma column within the conduit, through passive and explosive outgassing. The unsteady emission of the gas and the dispersion of the plume as it is blown away from the source, contribute to strong fluctuations in gas concentrations within distinct parcels of plume and, therefore, high amplitude fluctuations in the gas fluxes measured downwind. For instance, using a UV gas–imaging video camera Bluth *et al.* (2007) showed measurements of SO_2 fluxes of the gas plume of Villarrica volcano, up to 3500 m away from the crater, with fluctuations that ranged over a factor of three (between 197 and 640 Mg/d; see Figure 2 in Bluth *et al.* (2007)). Similar fluctuations were observed with measurements of SO_2 path-length concentrations acquired with the FLYSPEC (Figure 3.7). In this example, the gas concentration exhibited peaks and troughs that were associated with big puffs and relatively discontinuous flux (observed as a thinner and/or more diluted plume), respectively (Figure 3.7).

a)

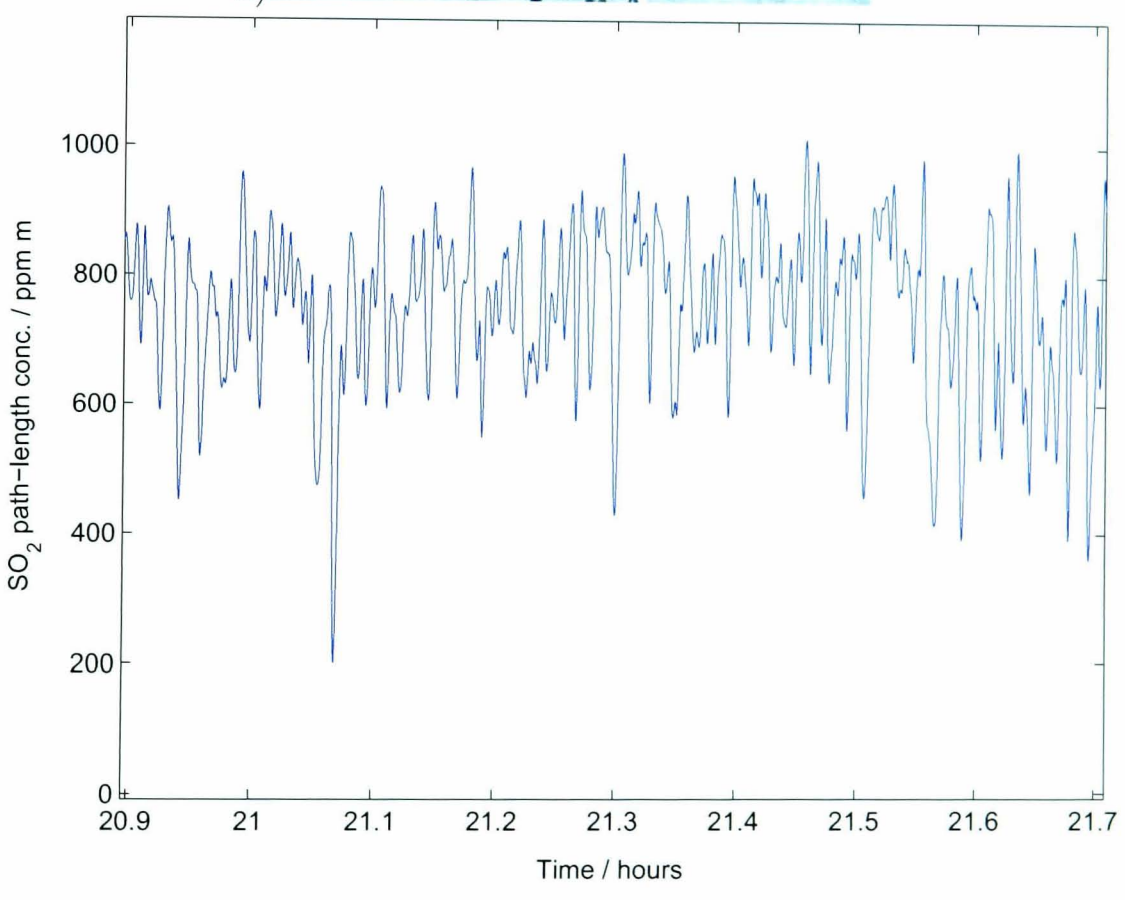

b)

Figure 3.7: Measurements of the SO_2 path-length concentration of the gas plume as it leaves the crater, from 17 November 2004, made from the north flank of the volcano at 1250 m from the crater. a) Photograph of the deployment of the FLYSPEC and the approximate field of view (~60 m diameter); the line of sight of the FLYSPEC was nearly perpendicular to the flow direction of the gas plume. b) time series of the measurements.

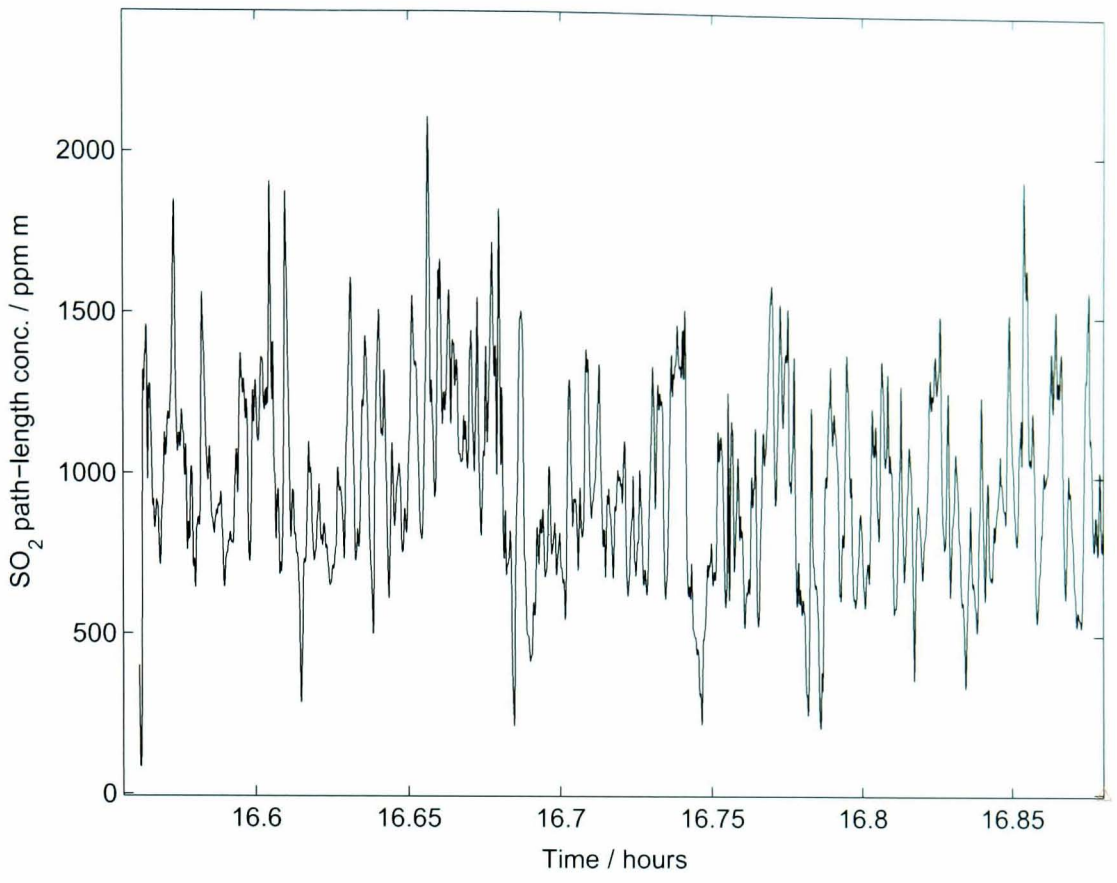

Figure 3.8: Example of the variable path-length concentration of sulphur dioxide in the gas plume leaving the crater, as measured on the 31 December 2005 with the FLYSPEC from the southeast side of crater rim (sampling frequency 5 Hz). The line of sight of the instrument was perpendicular to the direction of flow of the gas plume (towards the southwest), and the field of view at the plume, only a few metres above the crater rim, was about 6-7 metres in diameter.

Direct visual observations from the crater rim along with measurements of SO_2 path-length concentrations evidence the variable emissions from the bottom of the crater. Measurements of gas concentration in the plume as it leaves the crater exhibited fluctuations from 500 ppm·m up to about 1000 ppm·m of SO_2, in a time span of tens of seconds (Figure 3.8). That is equivalent to about 50–100% of the mean path-length concentration of the gas plume. Although the field of view of the instrument was too small for the measurement of the entire plume profile, which at the level of the crater rim exhibited a width between about 10 and 30 metres, by targeting the instrument on the area of maximum SO_2 concentration the variance in these measurements is related to variations in the emission rate of gas from the vent. Thus, these measurements are thought to yield a fairly good estimate of the plume heterogeneity next to the vent.

Several factors can contribute to these variations, such as the accumulation of gas inside the lava lake-spatter roof cavity, and the sudden release of higher fluxes of gas through explosive activity (in which the gas is vented at higher speeds). As a consequence, small gas puffs can be seen rising with irregular periodicity from the crater floor. Wind entering the

crater intensifies the gas circulation and contributes to further variations in the gas fluxes observed outside the crater.

To assess the contribution of the bubble bursting activity and the influence of the spatter roof on the variations of gas emanated from the crater floor, the FLYSPEC was pointed lower down in the crater in order to measure the path-length concentration of SO_2 in the gas plume, expelled through an opening in the spatter roof (Figure 3.1). An example of the resulting time series, from 2 January 2006, is depicted in Figure 3.9. This time series illustrates the continuous emission of gas as well as the appearance of gas puffs. Although at the time of the measurements there was a second smaller orifice from which more gas was being released, most of the gas plume (emitted continuously) was emanated from the targeted orifice. That day (2 January 2006) was particularly good for this type of measurement since not much wind-induced re–circulation of the gas plume occurred in the crater. Visual observations of the explosive events coincided with peaks in the SO_2 path-length concentrations measured by the FLYSPEC[4] (Figure 3.9). However, many other peaks in amplitude appeared in this time series that were not related to these discrete events. It is worth recalling that the spatter roof prevents thorough observation of the activity taking place at the lava lake and, considering the seething magma activity, it is likely that only major explosions were observed. The frequent but irregular peaks in the amplitude of gas concentration, as well as short periods of slightly higher gas concentrations, suggest that the continuous bubble bursting activity might not be the only source of these variations, but also temporal entrainment and circulation of gas between the surface of the lava lake and the spatter roof (Figure 3.1).

A similar experiment was carried out on another day (8 February 2006) in which the spatter roof had a large opening that allowed visual observations of the seething magma activity at the lake. With the FLYSPEC pointing just a few tens of metres above the crater floor, measurements of the gas concentration in the plume were less influenced by the spatter roof (Figure 3.10). The time series of SO_2 path-length concentrations showed relatively low and high frequency fluctuations, both of over 100% of the mean concentration. In this case, the gas emission from the lava lake ascended freely inside the crater, maintaining a more steady gas flux and more dense plume with higher concentrations than in the case shown in Figure 3.9. Low and high frequency fluctuations observed in Figure 3.10 are mostly caused by the bubble bursting activity, wind-induced gas circulation, and the narrow field of view

[4]The negative values are a result of the line of sight of the instrument, which pointed to the ground instead of the sky. Consequently, the absolute values are not accurate.

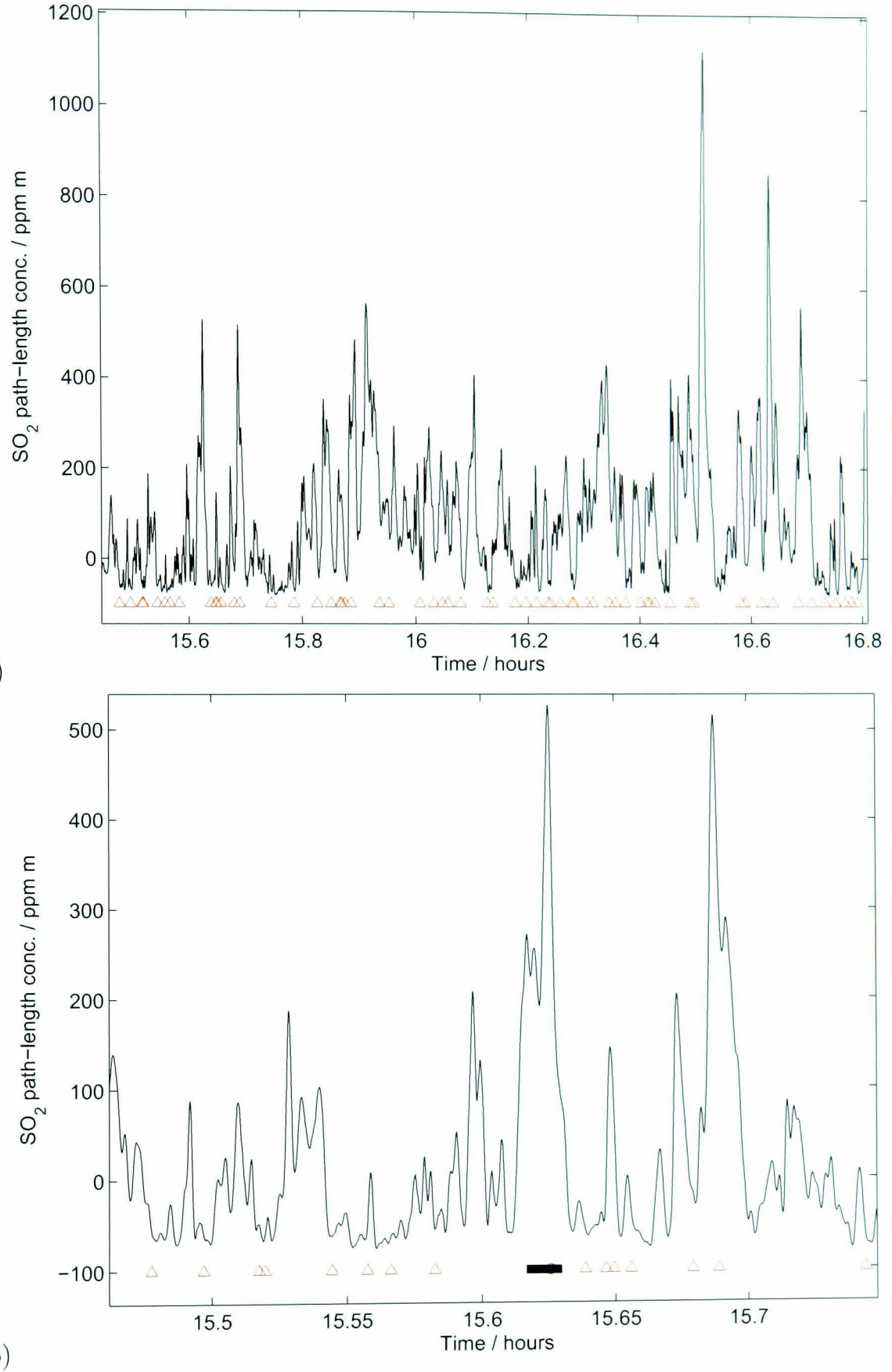

Figure 3.9: Time series SO_2 path-length concentration of the gas plume coming from the orifice in the spatter roof at the bottom of the crater. Example from 2 January 2006. The timing of the explosive activity observed from the crater rim is also included (triangles). The hole was about 15–20 m wide, and the field of view (FOV) of the instrument about 4.5 m in diameter. The bottom figure (b) shows details of part of the same time series in the top figure (a). The black horizontal bar indicates a period with gas re-circulation clearly visible.

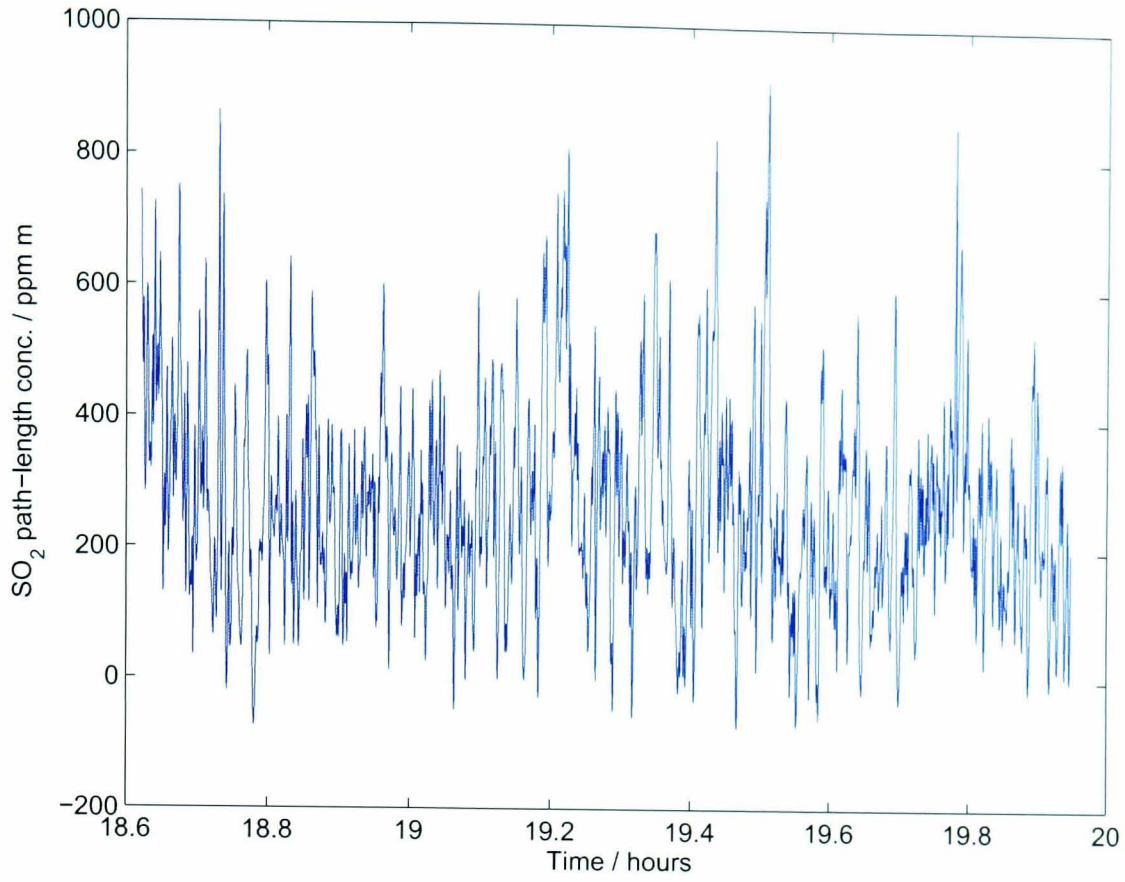

Figure 3.10: Measurements of SO_2 path-length concentration of the gas plume at a level between the crater floor and crater rim. At the time of the measurements the spatter roof exhibited a large opening ($\sim$ 25 m across) through which seething magma activity could be observed.

(FOV) of the instrument compared to the width of the plume (generally wider than 20 m).

The indirect measurements of the temporal variations in gas emissions at the crater presented herein show that the variation in the SO_2 path-length concentration of the gas plume can be higher than 50% in a time span of a few minutes; it can be higher than 100% over longer time periods. Since the FLYSPEC was targeting the center of the gas plume where the gas path-length concentrations reached maximum values, and because similar variations can be expected towards the edges of the plume, these fluctuations can be representative of the whole plume. Moreover, since the rise velocity of the gas plume inside the crater in the examples shown was mainly constrained by the buoyancy of the plume, with not much influence of wind entering the crater, the rise velocity can reasonably be approximated by a constant value. Gas puffs or spurts of gas emitted through the spatter roof, which show higher gas path-length concentrations, may exhibit higher rise speeds, and thus an even greater variation in SO_2 emission rate. Therefore, despite the limitations of the methodology employed, the measurements of SO_2 path-length concentrations presented in this section indicate that fluctuations in the gas flux emitted by the volcano can exceed 50% of total (time averaged) emissions.

3.3 Explosive activity of Stromboli volcano

In this section, I describe the characteristics of different styles of explosions observed at the crater terrace of Stromboli volcano. The data used in this study consist of my own visual observations, photographs and short videos gathered during June–July 2004. I also analysed video recordings performed with a Forward Looking Infrared Radiometer (FLIR) thermal video camera, manufactured by FLIR^{TM} Systems and operated by M. Patrick during the same period near the summit of the volcano. Since I had access to the same FLIR data, courtesy of M. Patrick and A. Harris (HIGP), I use that to illustrate the descriptions. To date, two publications use these data to describe in detail the different styles of explosive outgassing activity, with emphasis on the characteristics of the pyroclastic ejecta (Patrick *et al.*, 2007) and persistent gas puffing emission (Harris and Ripepe, 2007b). The descriptions included herein are based on my own observations, which are in agreement with most of what was presented in those papers, and citations to those papers accompany any information gathered from them.

The model of the FLIR used in the field is a ThermaCAM^{TM} S40, which has a thermal response in the wavelength range 7.5–14 μm, a field of view of 24°x18°, image size of 320x240 pixels, and a frame (image) output frequency of 30 Hz (Patrick *et al.*, 2007; Harris and Ripepe, 2007b). The FLIR automatically corrects for atmospheric effects using a LOWTRAN atmospheric model and user-specified parameters for target emissivity, distance to the target, relative humidity and ambient temperature. Thus, the temperature distribution of the plume could be obtained using an emissivity coefficient of 0.95, as adopted for basalt within the range 8-14 μm (Salisbury and D'Aria, 1992). The resolution of the videos achieved at the site of recording, about 450 m to the northeast of the crater terrace, yielded a pixel width of about 59 cm. This resolution allowed the identification of bomb-sized pyroclasts in the video sequence and, due to the temperature contrast with the surrounding material, it was possible to track their trajectories. Particles of smaller sizes, however, were mainly distinguishable as a mass of material with a particular 'opacity', which exhibited a contrasting temperature controlled by the amount of material, its size distribution, and absolute temperature (thermal radiation) of the pyroclasts. With the software ThermaCAM^{TM} Researcher, temperature time series of the pyroclastic plume measured above the crater rim allowed tracking of thermal changes associated with bubble bursting activity.

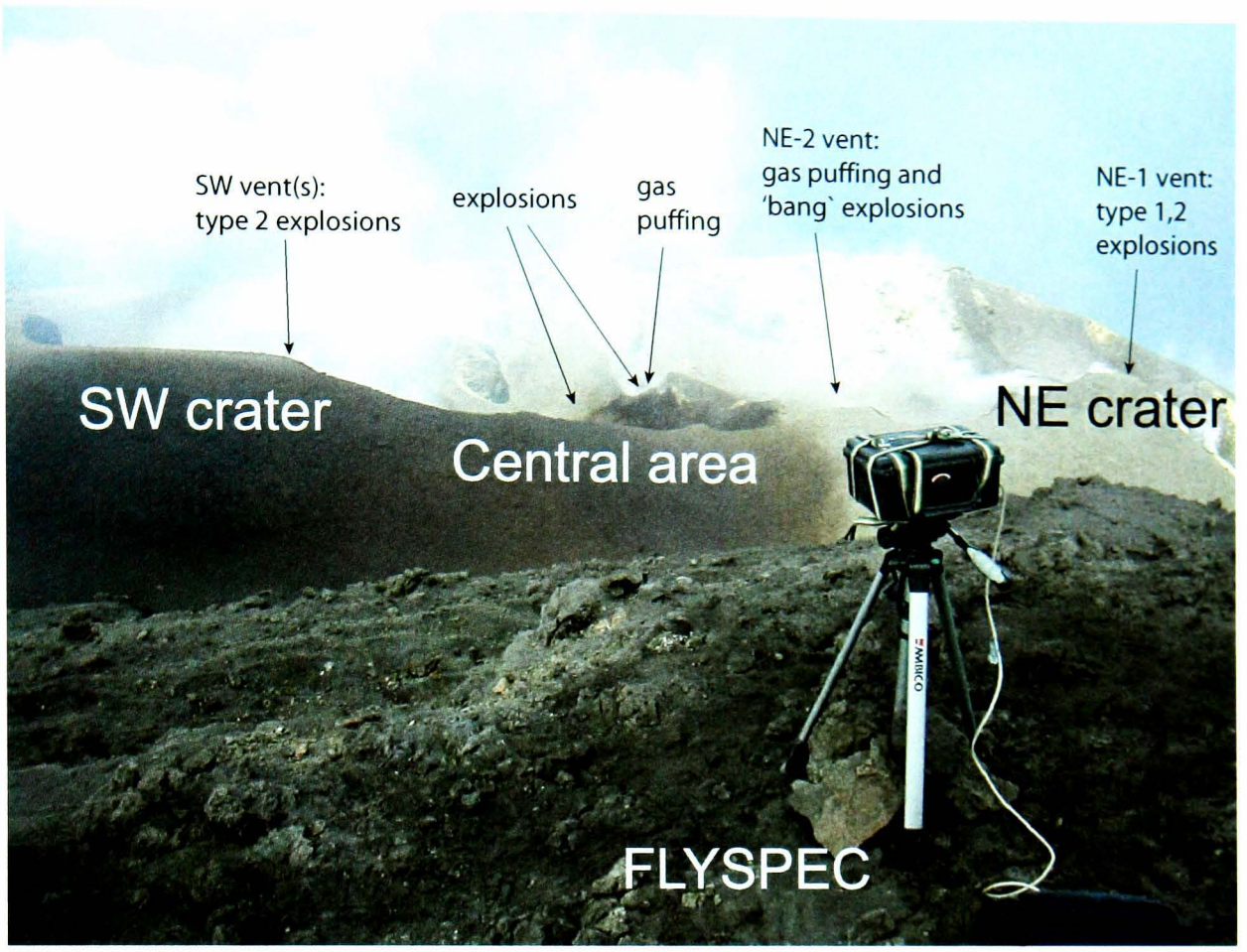

Figure 3.11: Photograph of the crater-terrace view from the summit of Stromboli volcano (Pizzo). From left to right the craters are South-West crater (SW), Central crater (Cc, or central area) and North-East crater (NE). The position and type of bubble bursting activity of the main vents are indicated with arrows.

3.3.1 'Strombolian' explosions and gas puffing

At Stromboli, the explosive activity is characterized and identified by pressure and seismic waves, gas coming out of the vent, and variable amounts of pyroclastic fragments ranging from ash to bomb in size (Ripepe *et al.*, 2002; Harris and Ripepe, 2007b; Patrick *et al.*, 2007). Strombolian explosions take place most frequently at the southwest (SW) and northeast (NE) craters (Figure 3.11). Within these craters there are at least two vents that exhibit explosions with different characteristics. For instance, during June–July 2004 in the NE-1 vent (Figure 3.11) the explosions had durations between 6 and 41 seconds (average 15 seconds) and involved variable amounts of ash and coarse material (Patrick *et al.*, 2007). In the NE-2 vent, however, the explosions were generally ash-poor and with durations of less than 1-2 seconds (Figure 3.11). These explosions were so short that in the field they were identified as 'bang' explosions, essentially due to their gun shoot-like sound.

Using a Forward Looking Infrared Radiometer (FLIR), Patrick *et al.* (2007) analysed 170 explosions that occurred during the same period. They characterised two main types of eruptions based on the amount of ballistic (coarse) particles and ash within the plume: Type

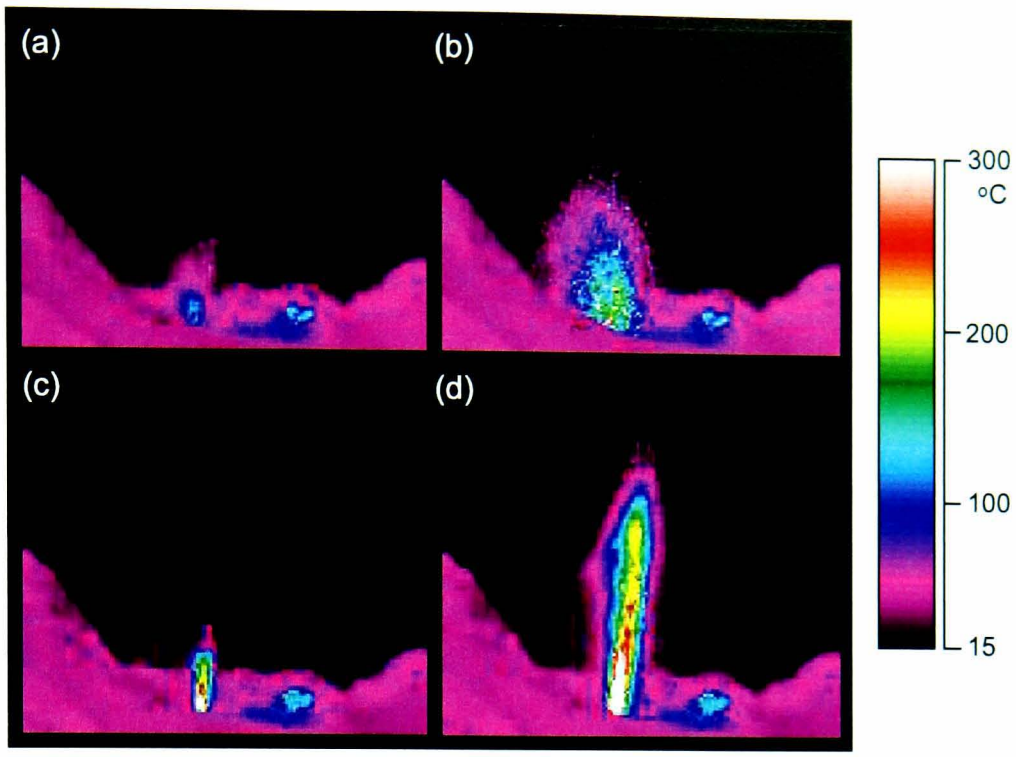

Figure 3.12: FLIR still images of the beginning of two (a-b and c-d) spatter-rich (Type 1) explosions. At the very beginning both explosions (a and c) had a narrow and directed jet. In the second explosion (c-d) this jet activity lasted longer and reached higher altitudes than in the first explosion, before it adopted a fountain shape as in (b).

1 and Type 2 explosions.

Type 1 explosions

Type 1 explosions were dominated by coarse particles (lapilli to bomb size pyroclasts or spatter) with only minor amounts of ash (Figure 3.12). At the beginning, some of these explosions exhibited a jet-like ejection of pyroclastic material that evolved into a fountain shape with most of the material following a ballistic trajectory (Figure 3.12) (Chouet *et al.*, 1974). Some other explosions exhibited this pyroclastic fountain structure (or less collimated explosion, following the nomenclature of Chouet *et al.*, 1974 and Patrick *et al.*, 2007) almost from the beginning. The velocity of the ballistic (coarse) particles, measured by Patrick *et al.* (2007) at the height of the crater rim, ranged between 9 and 101 m/s (with a mean of 34 m/s). The maximum height and degree of collimation in the trajectory of the pyroclasts was variable. In Figure 3.12, it can be observed that the front of the pyroclastic cloud consisted of a dilute cluster of bombs, whose velocity was essentially sub-vertical. Behind the front of bombs and spatter, the dense cloud of coarse material of explosions with a jet-like envelope (Figure 3.12c-d) initially ascended with similar velocity, as indicated by the trajectory of large particles. After a few seconds, and supported by the loss of momentum, the pyroclastic column spread laterally and adopted a fountain shape with the larger particles following

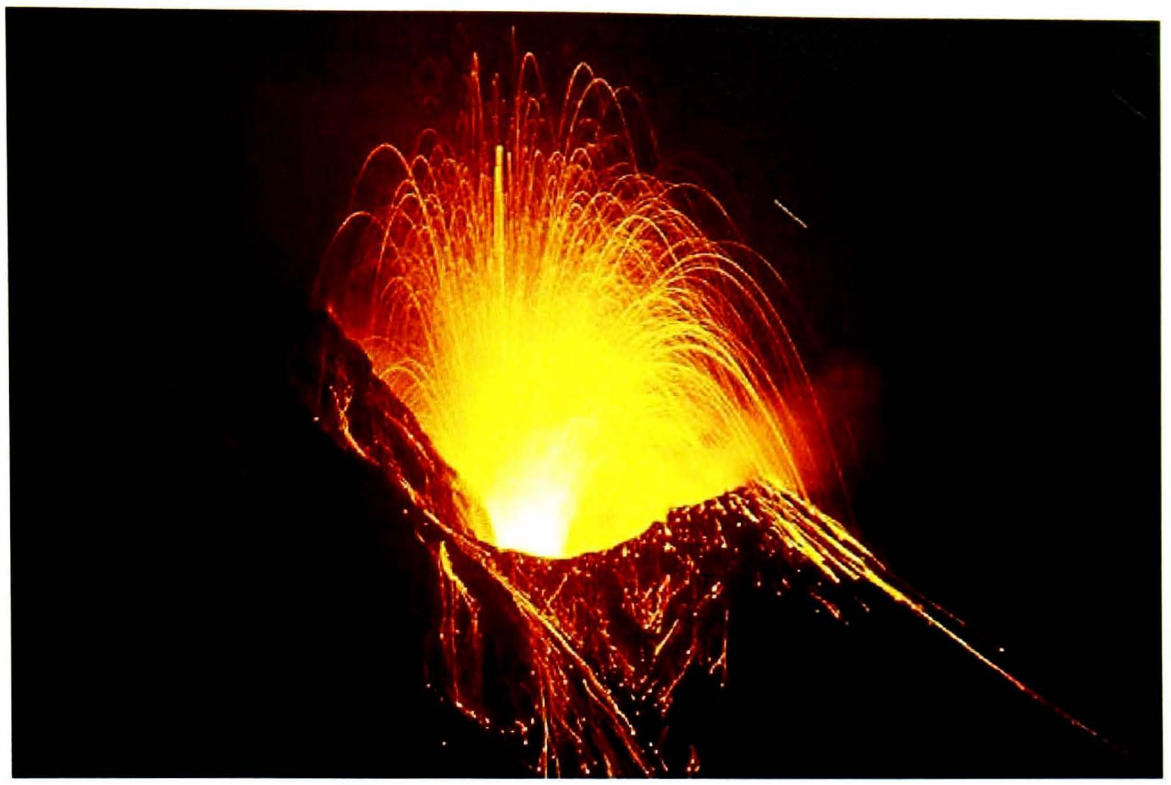

Figure 3.13: Photograph of an explosion that occurred in the NE crater showing the ballistic trajectory of the bomb-sized particles. This photo was taken by Tom Pfeiffer in September 2003, and gathered from the website http://www.decadevolcano.net in December 2007.

ballistic trajectories. During the widening of the pyroclastic column in long explosions, some bombs on the outer rim exhibit a higher radial velocity, compared with what is expected for particles following a ballistic trajectory initiated inside the crater. This deviation is likely to be caused by collision between the pyroclasts ascending in the core of the fountain, falling pyroclasts, and those previously ejected coarse fragments that at the time have lower speed, modifying their velocity and trajectory. Nevertheless, based on visual observations of the FLIR video sequences, it was noted that most of the coarse material followed ballistic trajectories (Figure 3.13).

Type 2 explosions

Type 2 explosions are characterised by high amounts of ash within the plume, such that the pyroclastic cloud looks optically thick (Figures 3.14-3.15) (Patrick *et al.*, 2007). Variable amounts of coarse (lapilli to bomb size) pyroclasts are also part of the ejected material. Explosions in which most of the pyroclastic material is ash in size, and with negligible amounts of bombs, were subcategorized by Patrick *et al.* (2007) as Type 2b (Figure 3.15). Explosions rich in ash and spatter bombs were subcategorized as Type 2a (Figure 3.14). Measurements of the velocity of the pyroclastic material at the level of the crater rim, performed by Patrick *et al.* (2007), yielded mean values of 31 and 7 m/s for Type 2a and type 2b explosions,

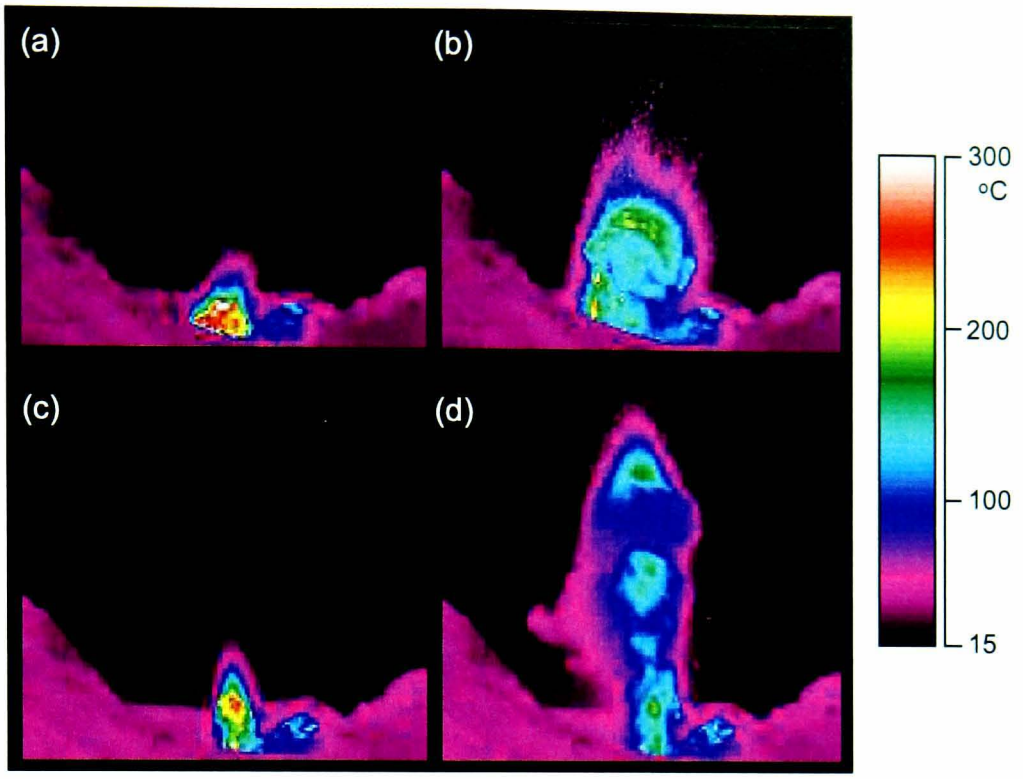

Figure 3.14: FLIR images of the beginning of two separate large (a-b and c-d) ash-rich explosions (Type 2a). These involve lots of bomb-size pyroclasts as well, mainly as ballistics on the outer part of the column.

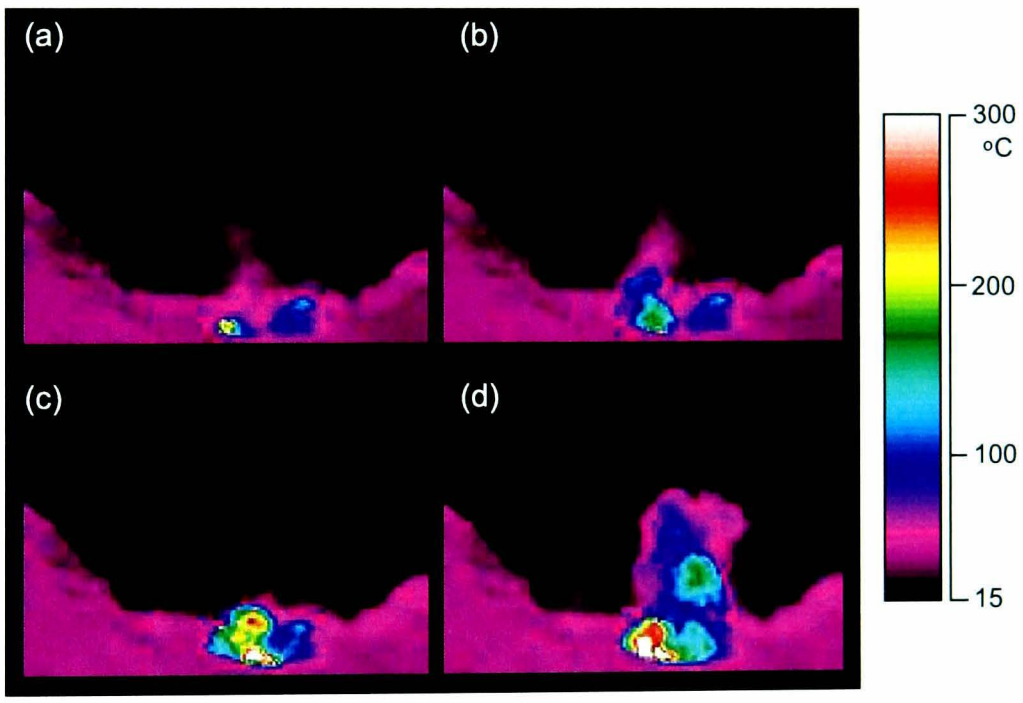

Figure 3.15: FLIR images of the beginning of two separate (a-b and c-d) small ash-rich explosions (Type 2b). No bomb-size pyroclasts are visible. The inner crater wall on the right has been warmed up by deposits in the previous explosion.

respectively. In Type 2a explosions, the front of the column usually consisted of bomb-sized pyroclasts that, owing to the higher velocity of the ballistic particles, preceded the bulk of the ash-rich cloud. Generally, bombs were continually ejected throughout the eruption. Type 2b explosions were considered of lower energy, essentially due to the absence of coarse particles and low velocities of the pyroclastic material observed, although their duration is comparable

Table 3.1: Statistics of the explosions observed at NE crater from the ROC station (Figure 1.3). This data set was obtained by processing FLIR video sequences of the explosions on days with available direct visual observations.

	7-June	11-June	13-June	27-June	7-July	20-July
Number	14	16	14	16	14	8
Type[a]	2a	2a+2b(56%)	2a+2b(50%)	2a+2b(50%)	1	2a+2b(88%)
Explosions/hr	3.9	5.29	5.02	5.26	5.12	3.6
Bursting time [s]						
average	15.52	17.55	14.64	17.1	15.14	19.81
min	9.7	7.9	5.4	6.5	6.94	13.48
max	24.29	34.1	33.93	41.37	25.42	32.36
Repose time [min]						
average	15.48	11.49	12.6	11.66	10.28	16.63
min	2.65	0.87	0.64	1.19	2.28	1.97
max	42.3	31.41	34.67	28.93	26.39	64.28

[a] The number between brackets corresponds to the percentage of explosions of the type 2b.

to that of Type 1 and Type 2a explosions (Patrick *et al.*, 2007).

The statistics of the explosions observed in the NE crater from ROC (765 m a.s.l, 450 m to the northeast of the craters; Figure 1.3), on 6 days between June-July 2004, are shown in Table 3.1. During that period the activity remained at similar levels, with an average bursting time of 16.6 seconds, and an average repose time of 13 minutes. Although the descriptions herein are based on observations of explosions taking place in the NE crater, the descriptions can be extended to those occurring in the SW crater, which have similar characteristics as Type-2 explosions. Perhaps, one of the few differences is that the fine pyroclastic content of explosions that occurred in the SW crater had a distinctive brownish colour, whereas Type 2 explosion in NE crater generally exhibited a darker or black color.

Bubble bursting sequences

In order to gain better insights into the dynamics of the different bubble bursting styles observed at Stromboli, a set of three areas of about 50 m^2 on the crater rim of NE crater were used to track the variations in temperature of the rising pyroclastic column. The position of the three square areas and temperature scale are shown in Figure 3.16(1). Because of the low spatial resolution of the FLIR images and the size of the target areas, not only radiance from hot pyroclasts but also radiance from the background crater wall can contribute to the total radiance recorded by the FLIR. Thus, dilute pyroclastic columns yield and apparent

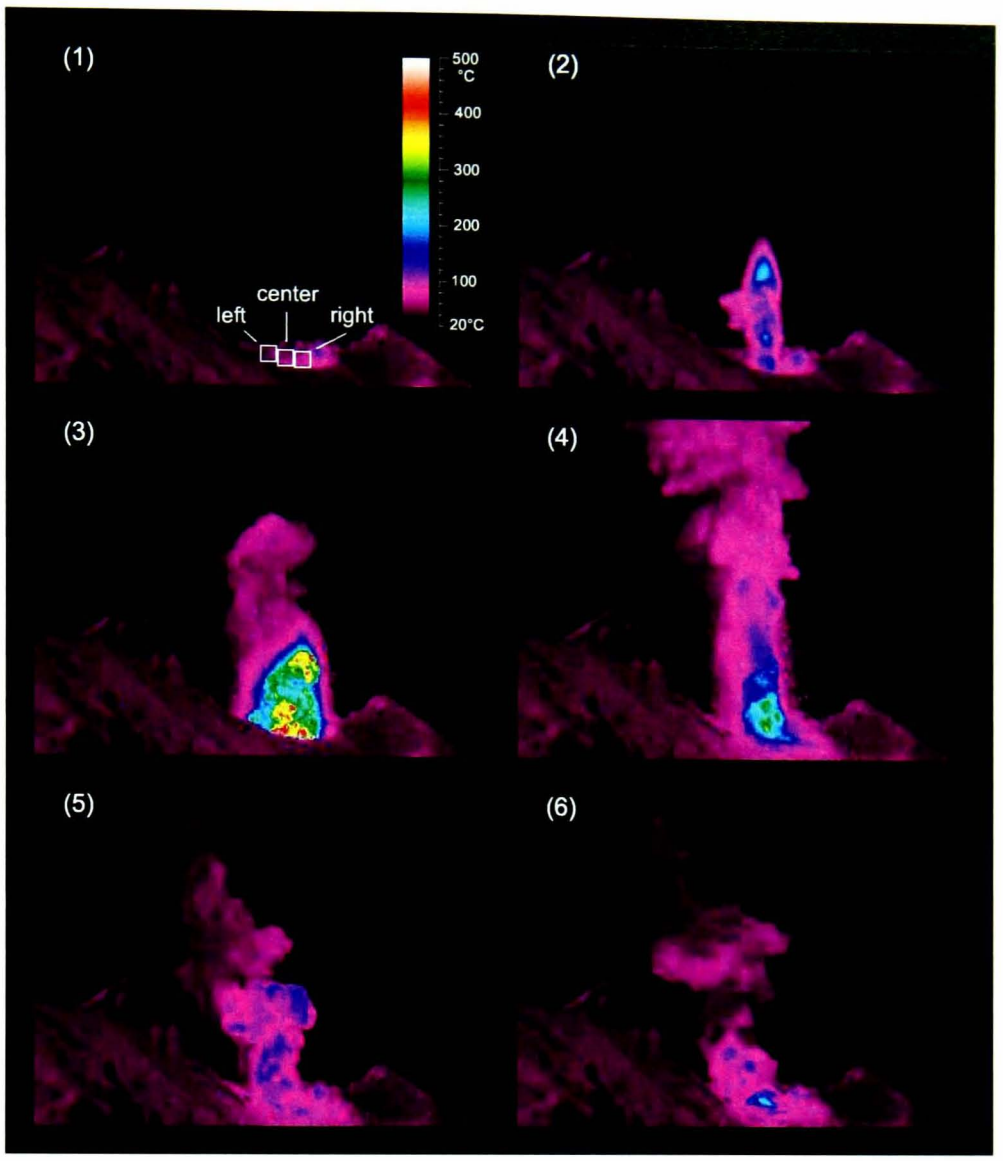

Figure 3.16: FLIR video stills showing the evolution of a Type 2a explosion, which described in Figure 3.17. Areas with higher temperature represent the bursting of single (or close packed) bubbles. For example, in (2) there are at least three main bursts that can be identified in the rising column.

temperature that is generally lower than that of the pyroclastic material. Therefore, higher temperatures are obtained when a relatively dense ash plume or more and hotter coarse material appear in the field of view. To some extent, this temperature time series reflects the evolution and intensity of the bursting sequence during the explosions. The intensity of the bursts are related here to the absolute value and gradient of the temperature time series. After a single bubble burst the measured temperatures in the target areas decrease owing to the rise and dilution of the plume and fall of coarse material. Continual bursts of bubbles, however, contributes to make the plume optically thicker and increases the amount of hot pyroclasts in the field of view, particularly if that material is lapilli to bomb in size. Thus, higher bubble bursting rates and the presence of hotter and/or coarse material lead to a positive and higher gradient in the temperature time series.

As an example, the evolution of one individual Type 2a explosion is depicted with

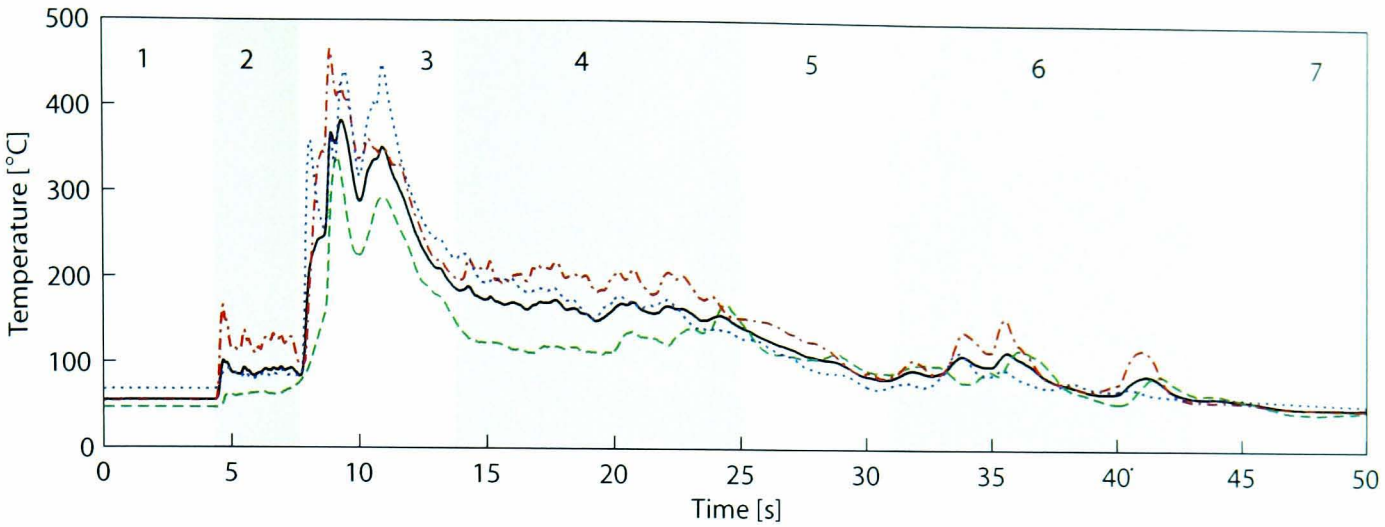

Figure 3.17: Example of the temperature evolution of a big ash (and spatter)-rich explosion (Type 2a) from the NE crater, as extracted from FLIR videos. The dot-dashed, dashed and dotted lines represent the average temperature of the central, left and right adjacent areas (~7 m wide each) above the crater rim, respectively. The solid line is the average temperature of these three areas together, which covers most of the width of the jet (Figure 3.16). The thermal evolution is as follows: 1) background temperature before the explosion, 2) an initial upward-directed bursting sequence, 3) the main vigourous sequence of explosions with large amounts of ash to bomb-size pyroclasts ejected upwards and sideways, including three main bursts concentrated on the right-centre of the crater, 4) continuous but less strong bursting sequence, 5) gap or strong decreasing in the bursting intensity, 6) a final weak gas slug, and 7) end of the explosion and dilution of the ash plume (not many bombs falling as in spatter-rich explosions).

FLIR video stills in Figure 3.16, with the associated temperatures shown in Figure 3.17. In this example, the duration of the complete bursting sequence was about 40 seconds (one of the longest recorded explosions, Table 3.1). It started with a few bursts that ejected relatively small amounts of pyroclastic material (stage 2), followed by the main part of the explosion in which a large amounts of ash to bomb-sized pyroclasts formed a wide column that reached temperatures of about 450° C (stage 3). During stage 3 the main bursting sequence lasted only about 5 seconds. Note that the three areas tracked show peaks in temperature at slightly different times. This could indicate the nearly simultaneous bursts of bubbles at slightly different positions, although the rapidly moving convective ash cloud could influence the appearance of hotter material in the field of view of the camera. Although continual, the latter bursts involved decreasing intensities (stage 4), and a strong detachment of the ballistic particles from the buoyant ash-rich plume was observed. Then, an interruption of the bursting sequence, perhaps with some very low intensity bursts, led to the rapid cooling of the ash-rich cloud that convectively rose while allowing the sedimentation of relatively heavy particles (stage 5). The end of the explosive sequence (stage 6) was characterised by a few scattered bursts of low intensity over a time span of about 12 seconds, accompanied

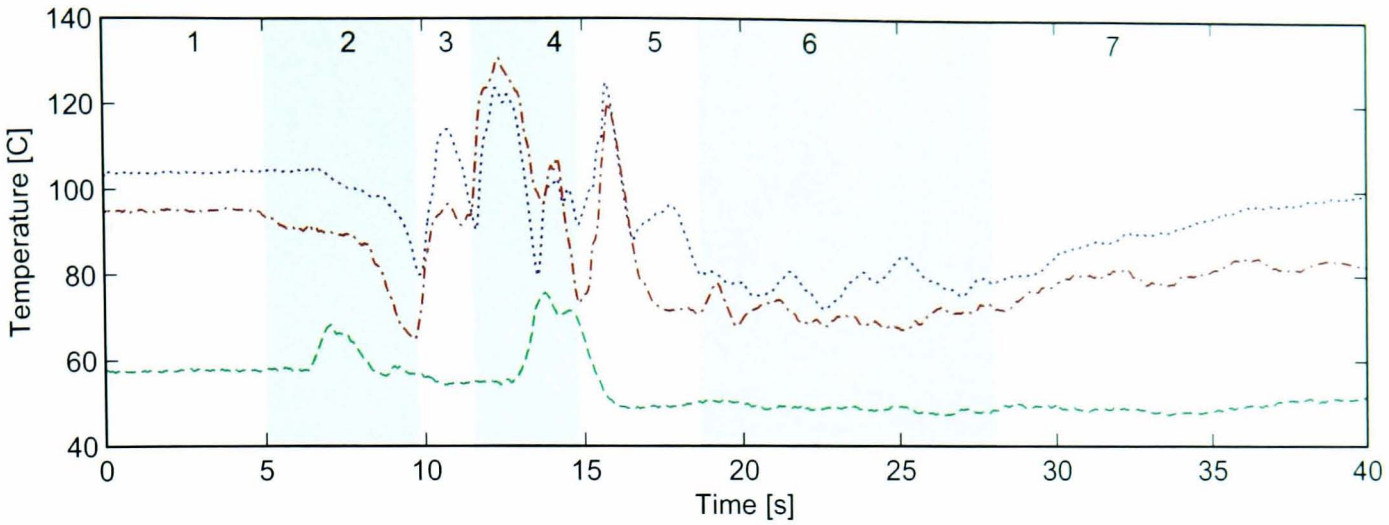

Figure 3.18: Time series of a small ash-rich explosion (type 2b) from NE crater extracted from FLIR videos. The dashed, dot-dashed and dotted lines represent the maximum temperatures at three adjacent areas above the crater rim (~7 m wide) identified as left, central and right, respectively (Figure 3.16). The temperature evolution is: 1) background temperature in crater wall, 2) dilute ash plume raising on the left and hiding the crater wall on the center-right, 3) first big thermal ash plume raising on the right-center, 4) two more bursts on the central area with the second one moving to the left, 5) another burst predominantly on the center-right, 6) rising of the remaining thermal plumes, and 7) dilution of the ash plume until it uncovers the crater wall on the background.

by the dilution and dispersion of the tall (more than 120 m high) ash plume. After the last bursting stage, the ash cloud mixed with the gas plume emitted from the crater terrace and dispersed further, following the prevailing winds on top of the volcano.

Compared with Type 2a explosions, the bursting sequence of Type 2b explosions was characterised by lower intensity bursts and temperature variations of the pyroclastic material generally lower than 200 °C (Figure 3.18). In this case, the absolute temperature of the ash cloud measured with the FLIR results from a combination of the temperature of the gas and ash expelled from the vent, plus the atmospheric air entrained in the pyroclastic plume. For instance, the bursting sequence shown in Figure 3.18 is comparable to stage 6 of the Type 2a explosion shown in Figure 3.17; if that stage was considered independent of the Type 2a explosion, it would be classified as Type 2b owing to the lack of bomb-sized ejecta. Although the crater wall behind the pyroclastic plume exhibited relatively high temperatures due to the fall of juvenile material during previous eruptions, the ash cloud was thick (opaque) enough to not permit the recording of its temperature. The explosion depicted in Figure 3.18 consisted of a series of bursts recorded at different positions near the crater rim (left, central and right areas). Stages 3 to 5 comprise the main part of the eruption, with at least 5 pulses of bubble bursting, in which the temperature of the ash cloud rose less than 70 °C. The lower recorded temperature of the pyroclastic material is likely to be a consequence of the relatively more

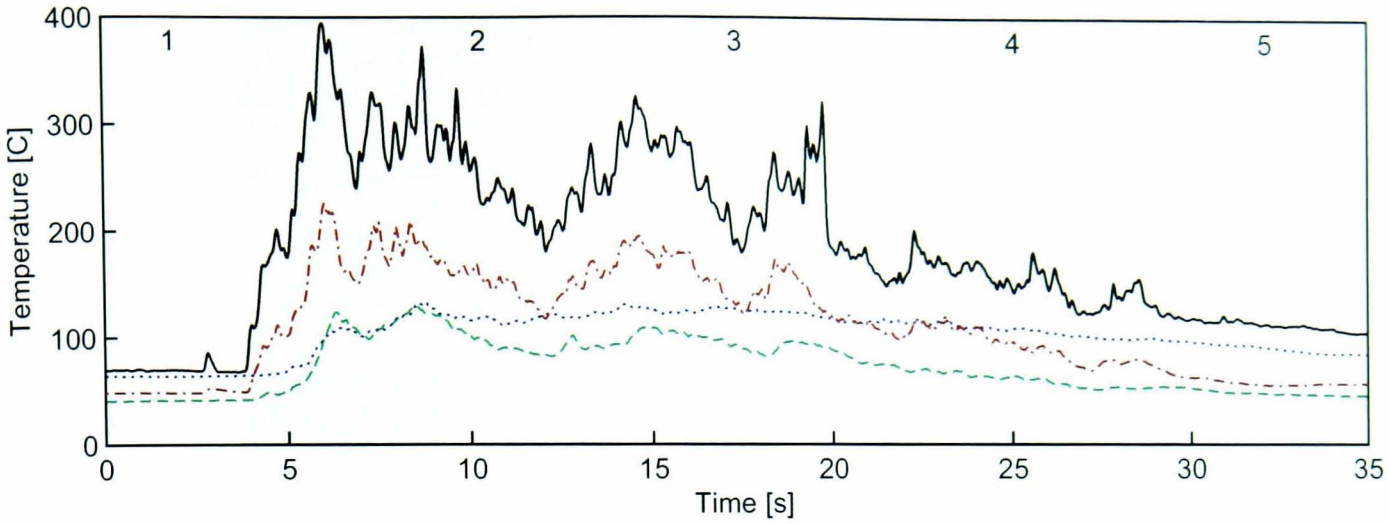

Figure 3.19: Example of the temperature time series of a spatter-rich explosion (type 1) from NE crater extracted from FLIR videos. The solid line represents the maximum temperature of the central area, and the dashed, dot-dashed and dotted lines are the average temperature of the left, central and right areas (~7 m wide) above the crater rim, respectively (Figure 3.16). The temperature evolution comprises: 1) background temperature with a small ash plume (initial bursting) rising at the end, 2) fountain of pyroclastic bombs with an impulsive start and subsequent slow decrease in intensity, 3) continual pulses of spatter ejecta, 4) slow decrease in intensity of the explosion, and 5) end of the fountain with pyroclasts falling inside and around the crater. The different trend of the dotted line (right area average temperature) is due to the continued warming up of the crater wall in the background due to the falling spatter.

dilute ash cloud and lack of coarse spatter.

An example of the bursting sequence of a spatter-rich and ash-poor explosion (Type 1) is shown in Figure 3.19. In this explosion the source of the pyroclastic material is well delimited by the central area of analysis. The explosion started adopting a fountain shape only after 3-4 seconds, at which time the highly dense core of the fountain reached the maximum temperature. For the rest of stage 2 and during stage 3 the bursting sequence continued with relatively high intensity. During stage 4 the intensity decreased although maintaining the ejection of spatter and the shape of the fountain. In stage 5 the eruption started to wane slowly with only mild bursts, as seen at the crater rim, with the last bubble bursts observed after about 40 seconds of the start of the eruption.

Gas puffing

Stromboli also exhibits a characteristic style of bubble bursting known as 'gas puffing' (Ripepe *et al.*, 2002; Harris and Ripepe, 2007b). Compared with strombolian explosions, gas puffing implies relatively small (weak, with infrasonic pressures of <1 Pa) and short bubble bursts occurring almost rhythmically with a frequency that ranges between 0.2 and 1.2 s^{-1} (every 0.8-5 s) (Ripepe, 1996; Ripepe and Gordeev, 1999; Ripepe *et al.*, 2002; McGreger and

Lees, 2004). Harris and Ripepe (2007b) showed that gas puffing is stable in the long-term outgassing activity of Stromboli volcano, although it experiences short-term variations in frequency and intensity at individual vents. Gas puffing has been observed in vents located within the NE or central craters of the crater terrace (Ripepe *et al.*, 2002; Harris and Ripepe, 2007b); in June–July 2004 it occurred between the central area and NE crater (Figure 3.11). An interesting characteristic of this activity is that it commonly takes place in only one vent at the time, but it can switch to another vent within a time span of minutes (Harris and Ripepe, 2007b). Based on its persistence and frequency, gas puffing appears to account for 2-45% of the total gas flux emitted by the volcano (Harris and Ripepe, 2007b). This contribution, however, has not been corroborated by direct measurements of gas flux.

3.3.2 Measuring SO_2 emissions

Measurements of gas emissions at the summit of Stromboli volcano were carried out to study the outgassing variations on short time and spatial scales. They involved the direct measurements of sulphur dioxide released during strombolian explosions at the NE crater, and gas puffing from the central area of the crater terrace (Figure 3.11). The data were collected with the FLYSPEC from the locations known as Roccette (ROC, 765 m a.s.l.) and Pizzo (PZZ, 918 m a.s.l.) (Figure 1.2).

Gas emissions from the crater terrace

Measurements of the gas plume from Pizzo were carried out with the FLYSPEC, in static mode, targeting the plume at a level slightly above the horizon (Figure 3.20), and also pointing directly to the central area (Figure 3.21), where gas puffing and outgassing from the walls combined to form the gas plume (Figure 3.11). Owing to the multiple sources of gas along the crater terrace and the proximity of the instrument, with this methodology it was possible to measure only part of the gas plume. The results are in path-length concentrations and cannot be used to estimate gas fluxes. Since it is not possible to perform a quantitative analysis of the outgassing, corrections for the different conditions of pressure and temperature of the plume were not necessary. Fluctuations in the measured gas concentration, however, can be considered representative of the unsteady and irregular gas emission. In part, this is a consequence of the style of activity of Stromboli volcano, with outgassing occurring from the crater walls as well as several vents displaying puffing and discrete explosions.

The example of Figure 3.20 shows the timing of explosions observed from Pizzo, and

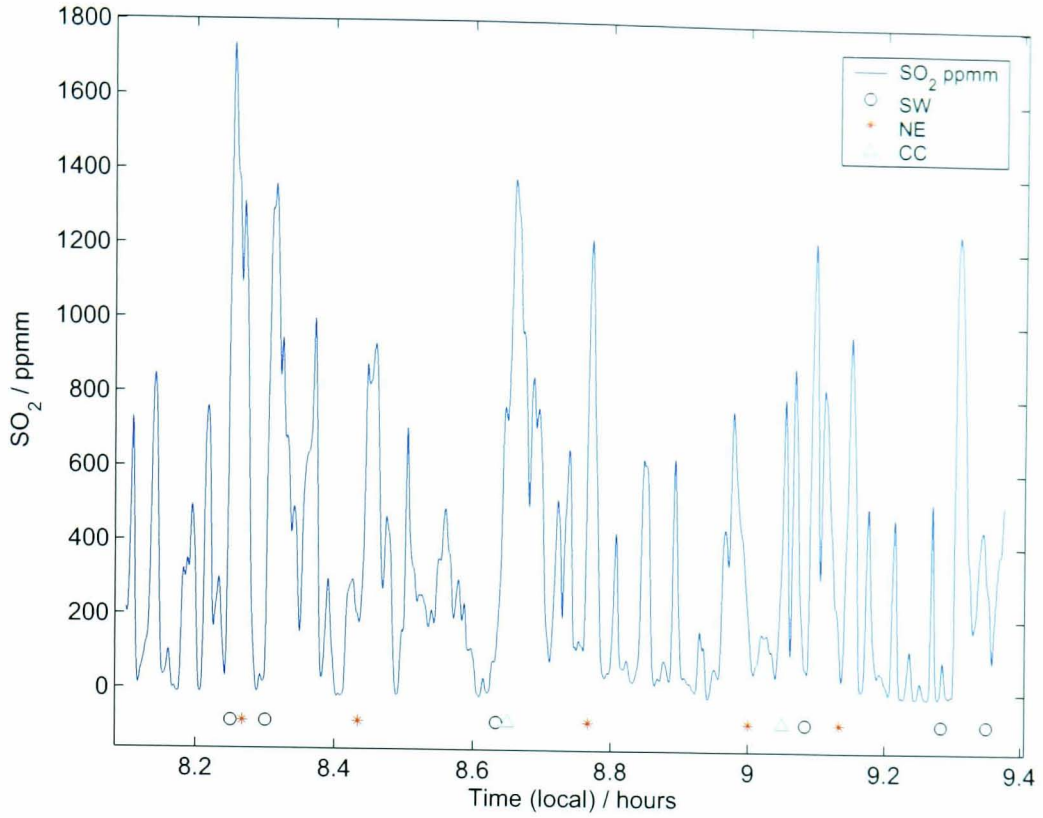

Figure 3.20: Measurements of SO_2 path-length concentrations of the gas plume emitted from the crater terrace of Stromboli volcano (25 July 2004). The FLYSPEC was pointing to the central area and slightly above the horizon; the sampling frequency was 0.5 Hz. The timing of the explosions observed at the southwest (SW), central (CC) and northeast (NE) craters is also included.

the fluctuations in SO_2 path-length concentration measured with the FLYSPEC on the 25 July 2004. The gas plume was flowing at low altitudes towards the northeast. The FLYSPEC was aimed at the central area in order to capture the variations in gas concentration during explosions that took place in the southwest and central craters. Increments of SO_2 were associated with individual explosions. However, considering the whole time series, the correlation between explosions and high concentrations is poor. This is essentially caused by the non-uniform circulation of the gas plume above the crater terrace, which is created by changes in the wind field (and enhanced by the irregular topography), as well as the irregular emission of relatively hot gas. With the aim of minimizing these effects, measurements with the FLYSPEC pointing directly above the vents were also performed. An example of these measurements is depicted in Figure 3.21. The drawback of this method is that the integration time of the instrument needs to be increased owing to the lower amount of scattered sunlight received by the spectrometer. (This means that the sampling frequency needs to be reduced.) In this case the measurements reflect the variations in the persistent passive outgassing from the central area of the crater terrace. The time series of SO_2 path-length concentration seemed to be more steady, but with variations between 25 and 100% of the mean that were

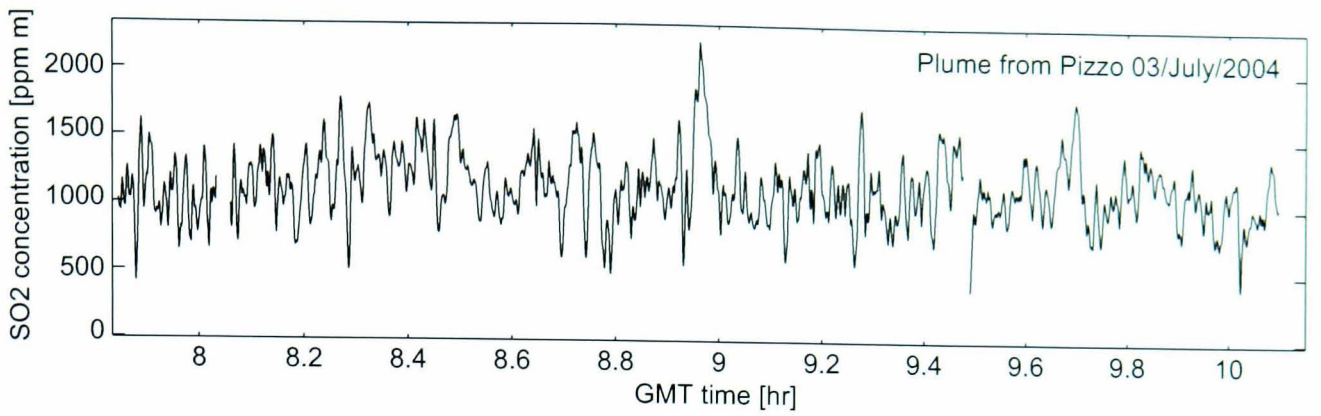

Figure 3.21: Example of the SO_2 path-length concentration measured from Pizzo and looking at the gas plume between the central and NE craters. The sampling frequency used in this measurement was 0.33 Hz. The bulk of the gas plume was being dispersed by the wind towards the northeast.

related to variable gas emissions from the southwest and central craters (Figure 3.21).

Gas released during strombolian explosions

During June–July 2004 a field experiment was carried out with the aim of estimating the gas emitted during individual strombolian explosions. With two FLYSPECs located in Roccette (ROC), ~450 metres to the northeast of the NE crater, the evolution of the SO_2 absorption and light extinction were measured during Type 1 and Type 2 explosions from NE-1 vent (Figure 3.22). The two instruments were targeting the NE crater, just above the crater rim, but one of them had a line of sight slightly higher than the other. An example of the results of these measurements is presented in Figure 3.23. In this example, the timing of explosions obtained from visual observations coincide with an increase in the SO_2 path–length concentration. However, not all the peaks in gas concentration were related to explosions occurring in the NE crater (Figure 3.23a). SO_2 peaks not associated with explosions are likely to be caused by the circulation of the gas plume in the crater terrace, behind the NE crater. The principal difference between the peaks associated with explosions and those associated with circulation of the gas plume, is the waveform of the SO_2 time series (Figure 3.23b). At the start of an explosion, the gas concentration measured by both instruments increased abruptly, and is followed by a relatively slow decrease with a nearly exponential form. In contrast, the peaks not related to the explosions did not resemble this waveform; in addition, they have a longer and non-uniform delay time between the measurements from the two FLYSPEC instruments (Figure 3.23b).

Figure 3.22: Photograph with the FLYSPEC located at ROC and the view of the northeast crater during a small type-2 explosion.

Effect of pyroclastic particles

Ash-size particles in the field of view of the instrument can scatter or block the incoming UV radiation, generating anomalous SO_2 burdens. Andres and Schmid (2001) investigated the effect of ash within the gas plume in the measurements of SO_2 burden using a COSPEC instrument. In their experiments, the initial drop of ash in front of a COSPEC caused a sudden decrease in SO_2 path-length concentration measured by the instrument. A similar effect was observed at Stromboli, originating from the rapid release of gas and mixed pyroclastic material during explosions. A particular example of SO_2 concentration of the volcanic plume measured from Roccette, in front of the north-east crater, is shown in Figure 3.24. In this case, the wind was blowing in the north-east direction and, as a consequence, the FLYSPEC was partly measuring the outgassing from other craters. During the explosions in the NE crater, the ejected material blocked part of the scattered ultraviolet radiation coming from behind the NE crater, causing a decrease in the measured gas absorption (Figure 3.24). The presence of pyroclasts can have the same effect on measurements of sulphur dioxide within the explosion plume. Conversely, it has also been observed that high ash concentrations can increase the SO_2 burden measured with COSPEC (Andres and Schmid, 2001). Although the underestimation of the SO_2 burden can be explained by a blocking light effect, the effect of the high amounts of ash and bigger size pyroclasts when they are mixed within the gas plume is poorly understood. The problem of sub- or over-estimation of SO_2 concentration related

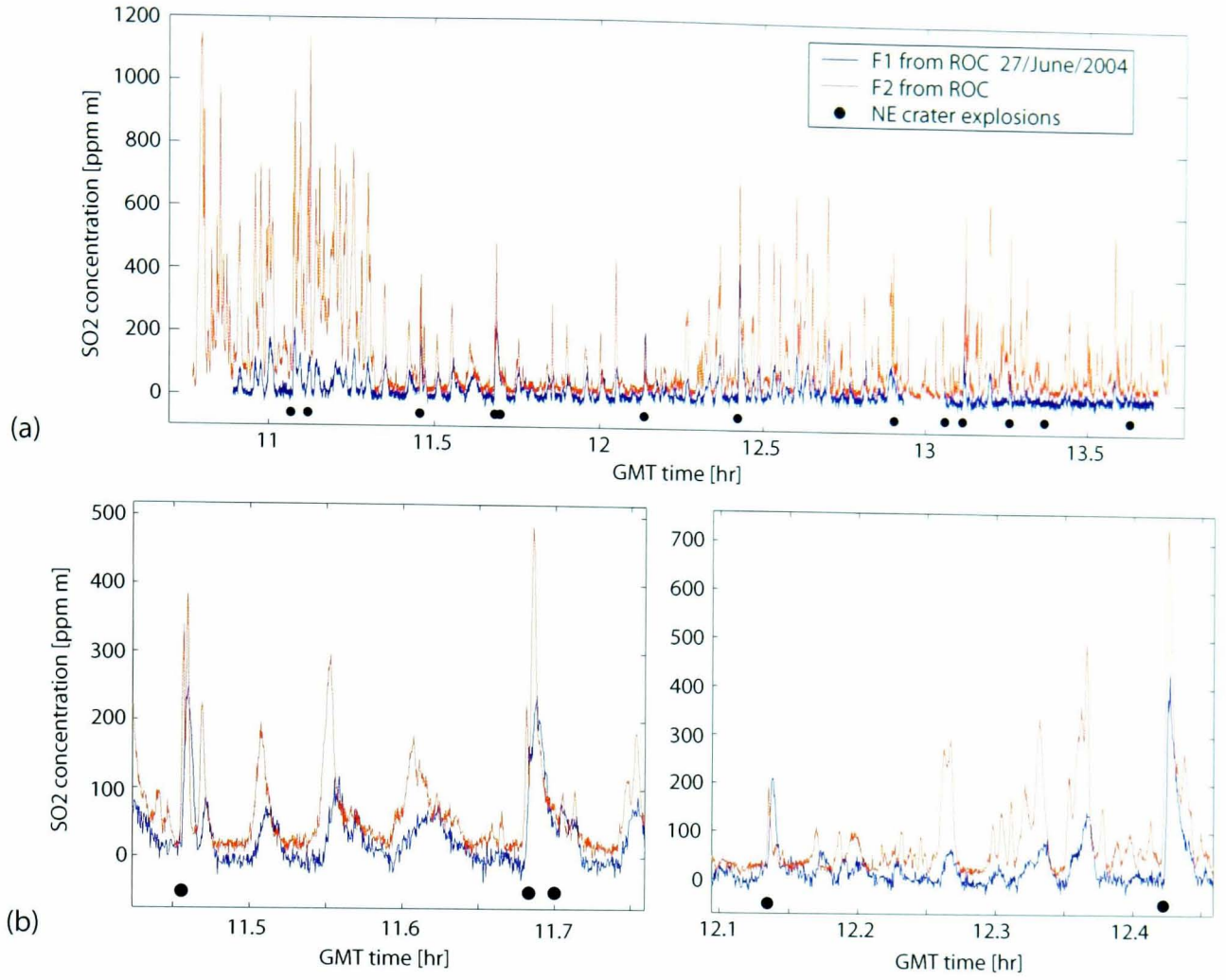

Figure 3.23: An example of the measurements of outgassing during strombolian explosions at the NE crater, along with the timing of the explosions. FLYSPEC F2 was pointing just above the crater rim and FLYSPEC F1 pointing slightly higher. The figures in (b) show details of the signal in (a).

to the presence of pyroclastic material in the gas plume has not been solved in this work.

In Chapter 2 it was shown that particles within the field of view of the spectrometer (FLYSPEC) affect the transmittance of light. The light extinction caused by the particles can be expressed by the fraction of light lost (ΔI_p) measured by the spectrometer (Section 2.3.6). Examples of the calculated pyroclastic extinction for 5 explosions of the Type 1 and Type 2 explosions are shown in Figure 3.25. Owing to the higher content of fine material in Type 2 explosions, the maximum and total (integrated) extinction produced during those explosions is generally greater than in ash-poor explosions (Type 1). The smaller Type 2b explosions reached lower values of pyroclastic extinction than Type 2a eruption. An example of the measured SO_2 path-length concentration, calculated pyroclastic extinction, and maximum temperature of an ash and spatter-rich explosion (Type 2a) is shown in Figure 3.26. Compared with the relatively short temperature signal, which is related to the bubble bursting sequence, the long-lasting extinction reflects not only the ejection of material but also the rise and dispersion of the ash–gas cloud. In fact, the maximum extinction occurs more than 10

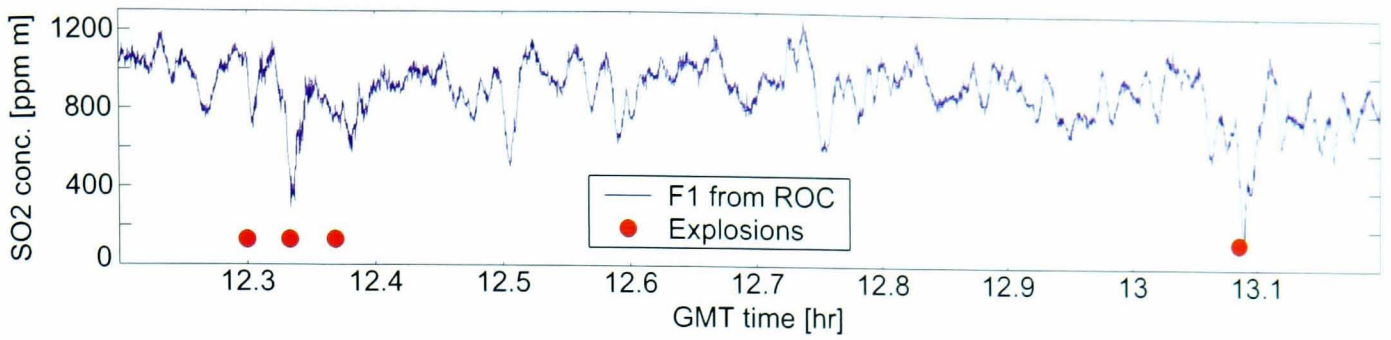

Figure 3.24: Example of a measurement from Roccette on 19 June 2004, where a decrease in SO_2 concentration is caused by the appearance of high amounts of pyroclastic material in front of the FOV, during the explosions. This decrease in SO_2 burden resembles the experimental results of Andres and Schmid (2001).

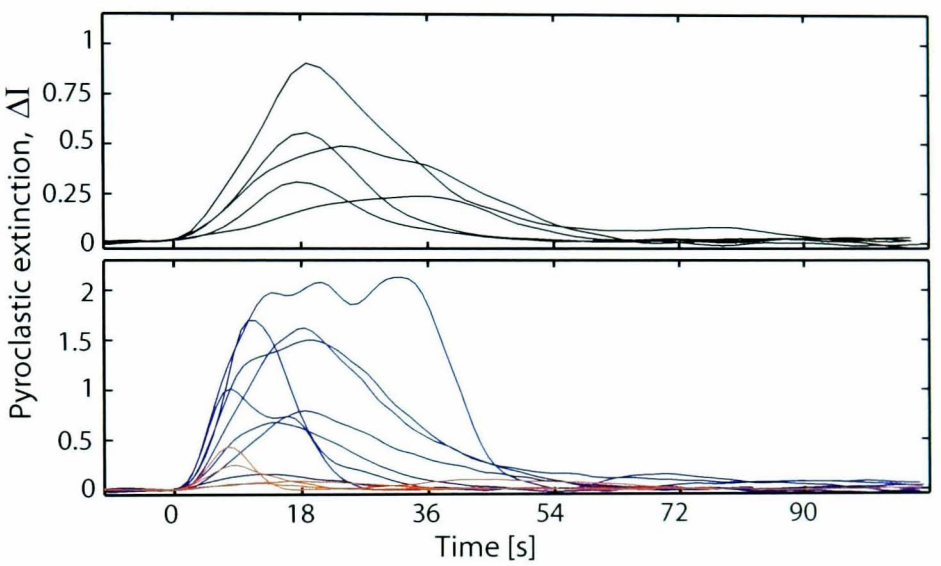

Figure 3.25: Examples of light extinction waveforms for the spatter-rich explosions (Type 1, top figure) and ash-rich explosions (Type 2, bottom figure). Note the different scales for both type of explosions. Ash-rich extinctions include Type 2a (highest amplitude) and 2b (low amplitude).

seconds after the start of the eruption, caused by the rise of pyroclastic material and the different positions of the crater-plume at which the FLYSPEC and FLIR were measuring.

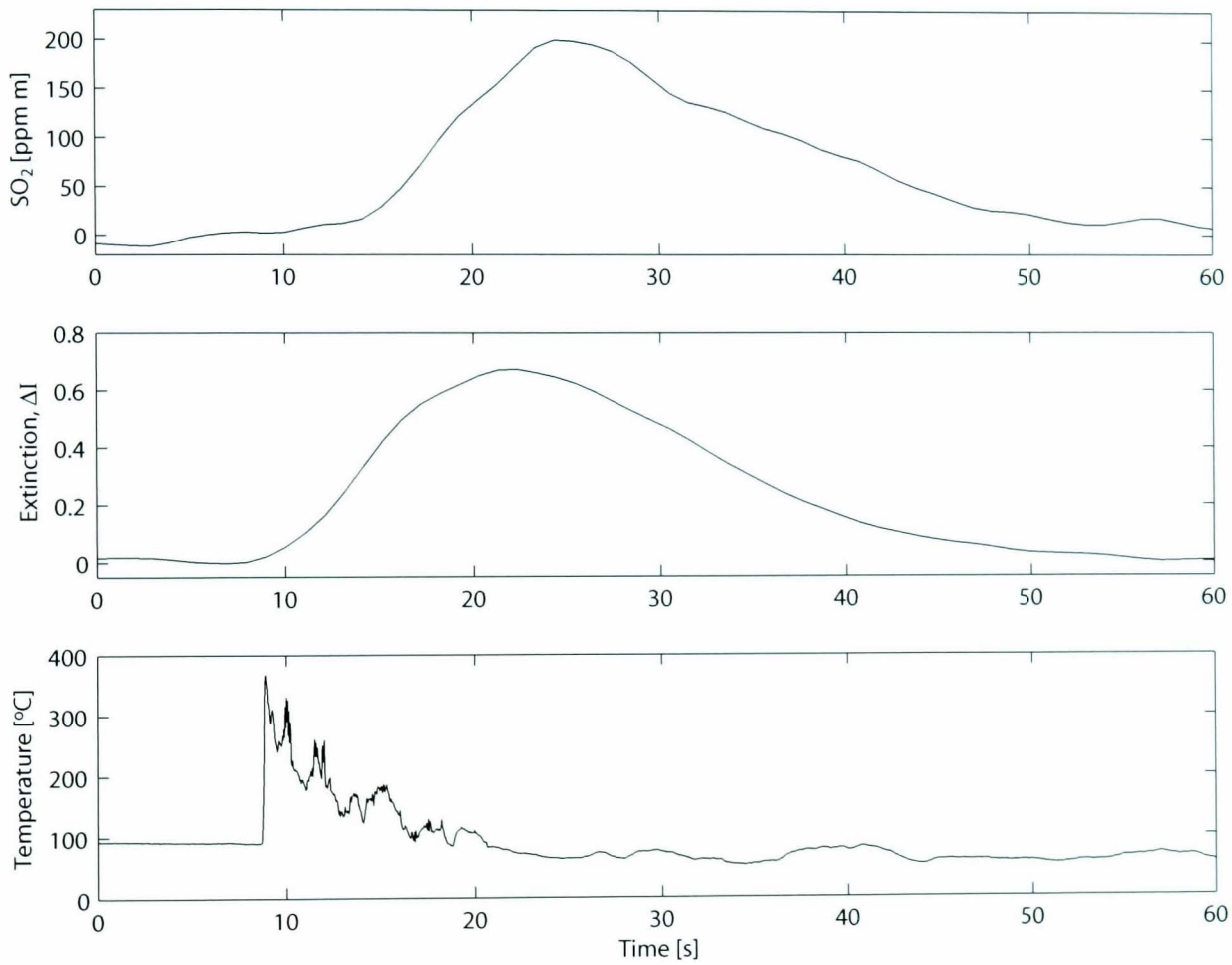

Figure 3.26: Example of SO_2 (top), pyroclastic extinction (middle) and temperature (bottom) measurements of an ash-rich (Type 2a) explosion. The gas and extinction have been measured with a FOV of ~20 m in diameter, whereas the temperature time series corresponds to the maximum temperature measured in an area of 20 m width x 7 m height just above the crater rim.

3.4 Discussion and conclusions

3.4.1 Bubble bursting styles

Strombolian explosions

The term 'Strombolian activity' has been largely used to describe a particular type of mild explosive activity taking place at several open-vent volcanoes (e.g. Blackburn *et al.*, 1976; Patrick *et al.*, 2007; Rowe *et al.*, 1998; Witter *et al.*, 2004). A rather simplified concept of a strombolian explosion illustrates the ejection of spatter following ballistic trajectories, caused by the rupture of gas bubbles at the magma free surface. A good example of this activity is observed at the lava lake of Mt. Erebus, Antartica (Aster *et al.*, 2003; Kaminuma *et al.*, 1988). At Mt. Erebus, single bubbles reaching the surface of the lava lake explode, disrupt the film of lava encapsulating the bubble, and throw the spatter in radial directions (Aster *et al.*, 2003)[5]. Descriptions of strombolian explosions at Stromboli volcano, however, include a much wider spectrum of bubble bursting styles (e.g. Chouet *et al.*, 1974; Blackburn *et al.*, 1976; Settle and McGetchin, 1980; Patrick *et al.*, 2007). At Stromboli, the length of the bubble bursting sequence and size distribution of the ejected material vary according to the crater or vent where they occur, as well as the period or characteristics of the activity (Patrick *et al.*, 2007; Harris and Ripepe, 2007a). Explosions taking place in the northeast crater exhibited durations that ranged from 5 to more than 40 seconds. While Type 2a explosions exhibited high amounts of ash to bomb-size pyroclasts, Type 1 eruptions exhibited ejection of mostly coarse material that can adopt a jet or fountain-like form. Patrick *et al.* (2007) explained the different style of Type 1 and Type 2 eruptions by either rheological changes in the magma, or backfilling of the conduit with previously erupted material. Another possible explanation for this different behaviour is the existence of two vents, less than 10 m apart, at which these two types of eruptions occur. This alternative has not been explored yet, and its analysis would require a precise location of the eruptions with, for example, the infrasonic array deployed at the summit of the volcano (Ripepe and Marchetti, 2002).

Time series of the temperature measured at the level of the crater rim with the FLIR, which were used to track the evolution of the bubble bursting sequence during explosions, indicate that in Type 1 and Type 2a explosions the intensity of the bursts is highest within the first stages of the eruption (and generally not at the very beginning). On some occasions, there was a second pulse or bursts of high intensity, although not as high as the first one.

[5]See videos of this explosions at http://erebus.nmt.edu/video/eruptions_stromb.html.

before the intensity and frequency of the bubble bursting sequence slowly waned. Type 2b explosions exhibited a more irregular bursting sequence.

At Villarrica, strombolian explosions can be variable in duration, from a single bubble burst (although rare) to a longer bursting sequence (>15 s) derived from the ascent of major gas slugs. They are more similar to Stromboli Type 1 eruptions, mainly by virtue of the lack of a dense ash plume. There have been observations of atypical explosions at Villarrica that are accompanied by a brownish ash plume. They have been attributed to partial collapses of the spatter roof or avalanches from the inner crater walls, which is consistent with the idea of backfilling of loose material for the Type 2 eruptions at Stromboli (Patrick *et al.*, 2007; Booth and Walker, 1973). Nevertheless, based on my observations, strombolian explosions at Villarrica are rather short and only small lava fountains could last as long as 20-60 s.

Other styles of bubble bursting

Observations of gas puffing at Stromboli revealed extremely mild bubble bursting activity that takes place alongside stronger strombolian explosions, although at different vents (Harris and Ripepe, 2007b). The source of this activity is the repetitive burst of bubbles within one of the conduits of the crater terrace (Ripepe *et al.*, 2002; Harris and Ripepe, 2007b). It is worth noting here that the terminology used to characterise this particular activity of Stromboli volcano, gas puffing, could be used elsewhere to describe the ascent of gas in puffs (rather than as a continuous gas stream) but whose source can be completely different to that interpreted at Stromboli. For instance, spurts of gas and gas puffs have been observed at the crater floor of Villarrica volcano, but they have been associated with the interaction between the bursting activity that takes place at the surface of the lava lake, and the spatter roof above it.

Two other styles of bubble bursting occurring at the lava lake of Villarrica volcano have been described in this chapter: seething magma and small lava fountains. Seething magma is a distinctive activity of Villarrica volcano, which may contrast to the activity observed at other open-vent volcanoes, that involves the continuous arrival and bursting of gas bubbles with radii generally lower than 5 m. The sequence of bursting events in seething magma is characterised by irregular frequency, strength, and location at the lava surface. Small lava fountains are intermediate in style, length and strength of the bursting event, between seething magma and strombolian explosions. The source of this activity is similar to that of seething magma, but involves a greater concentration of gas bubbles with, perhaps, larger size

and higher velocity. Thus, small lava fountains can be regarded as a vigorous manifestation of seething magma. Long duration lava fountains (>45 s) must result from large gas pockets that reach the surface of the lava lake.

Influence of the morphology of the vent

At Villarrica, the interaction of bubble bursting activity with the spatter roof can be manifested by two other types of event: gas jetting and 'splashing' magma. Gas jetting events have an analog at Stromboli volcano. Jet-like explosions have been observed coming from a hornito structure in the central crater of Stromboli terrace (McGreger and Lees, 2004). At both volcanoes, they are characterized by a clear acoustic signal and little (or no) coarse material. It is likely that these events are the result of the interaction between a primary type of bubble bursting with the solid structure above (partly concealing) the magma-filled conduit. This structure corresponds to the spatter roof in the case of Villarrica, and the hornito in the case of Stromboli. The splashing of lava out of the opening in the spatter roof at Villarrica can sometimes be mistaken for the ejection of material directly from strombolian explosions. Lava ejected in splashing magma events is generally poorly fragmented and, commonly, the spatter is thrown only a few metres to tens of metres away from the orifice, which contributes to the building of the spatter roof.

The existence of the spatter roof at Villarrica but not at other open-vent volcanoes with a lava lake, such as Erta Ale or Mt. Erebus, could be explained by the size of the lava lake, morphology of the crater interior, and style of activity. To build the spatter roof, the lava lake must exhibit a continuous mild bursting activity that could send spatter towards the walls of the crater (or the spatter roof itself), and also avoid encrusting of its surface. Seething magma, small lava fountains and splashing lava contribute to these two conditions. The contribution of strombolian explosions is generally minor, in part because of their lower frequency of occurrence. During periods of elevated volcanic activity, however, strombolian explosions contribute to the deposition of tephra on top of the spatter roof, and thus the creation of terraces. The funnel shape of the interior of the crater favours the construction of the roof, as it gets narrower with depth facilitating the adherence of the spatter on to the wall of the crater, so it does not collapse back down into the lava lake, as would happen if the internal walls of the crater were vertical. Besides, since the lava lake constitutes the top of the magma column, the relatively small area of the lava lake, at least a few tens of metres below the crater rim, permits the bubble bursting activity to take place across the entire

surface.

3.4.2 Variations in SO_2 emissions during explosive outgassing

At Stromboli, Allard *et al.* (1994) measured a mean total SO_2 flux of 809 Mg/day (with daily averages between 340 and 1420 Mg/day), and found that emissions from eruptive episodes increased the flux of sulphur dioxide between 40 and 400%. However, owing to the short duration of the eruptions as a whole, the contribution of strombolian explosions is less than 10% of that from passive degassing (Allard *et al.*, 1994; Harris and Ripepe, 2007b). Indirect estimates of the gas flux emitted in gas puffing activity, carried out with thermal infrared sensors, yielded contributions between 2 and 45% of the total gas flux (Harris and Ripepe, 2007b). Although the range is wide, this result suggests that persistent mild bubble bursting activity can be an important source of outgassing.

At the summit of Villarrica volcano, most of the outgassing takes place at the lava lake. Due to the persistent seething magma activity, it is difficult to estimate the gas emission rate contributed by passive emission only. Nevertheless, the high frequency of single bubble bursts at the surface of the lava lake, observed during seething magma, suggests that gas emission contributed by this activity at Villarrica is comparable or even higher than that of gas puffing at Stromboli. Thus, it is likely that the contribution to outgassing from bubble bursting at Villarrica is higher than at Stromboli, and perhaps higher than the contribution from passive degassing.

Chapter 4

Monitoring the degassing activity of Villarrica volcano

4.1 Introduction

Open–vent volcanic systems, such as Stromboli (Ripepe, 1996; Bertagnini *et al.*, 2003), Mount Erebus (Rowe *et al.*, 2000; Aster *et al.*, 2003), Masaya (Duffell *et al.*, 2003; Williams-Jones *et al.*, 2003), and Villarrica (Calder *et al.*, 2004), are characterized by persistent gas emission and sustained seismicity. Understanding the characteristics of volcano degassing using integrated geophysical and petrological studies during eruptive episodes, as well as the evolution of the activity with time, is fundamental for the purposes of volcano monitoring and research (e.g. Andronico *et al.*, 2005; Harris and Ripepe, 2007a). For instance, measurements of SO_2 concentrations using correlation spectroscopy have proved to be a valuable tool in volcano monitoring, and in the investigation of the dynamics of magma degassing (Stoiber *et al.*, 1983; Fischer *et al.*, 2002; Young *et al.*, 2003). At Villarrica, there are only a few periods with SO_2 flux measurements. They were mostly carried out by Witter *et al.* (2004) during early 2000 and 2001 to constrain the total gas emission and analyze the dynamics of degassing within the system. Other measurements have been also carried out by the Volcano Observatory of the Southern Andes (OVDAS) as part of their monitoring program. Daily averages of SO_2 flux typically revealed moderate emissions of ca. 100-700 Mg/day. Combining SO_2 emission rates with measurements of sulphur and other gas species within the gas plume (as molar ratios) and glass inclusions, Witter *et al.* (2004) and Shinohara and Witter (2005) showed that: i) magma ascending to the surface is almost completely degassed, ii) the relative abundance of gas species in the gas plume remains constant during spattering of lava at the

vent, which implies that bubbles bursting at the lava lake are in equilibrium with the magma, and that iii) on average, ca. 2.2 m^3/s of magma is degassed. They concluded that convection within the conduit is the most appropriate model of degassing for Villarrica volcano.

Volcanic tremor is one type of seismic signal that characteristically accompanies the activity of open-vent volcanoes. It may last for minutes, days, or even months (McNutt, 2000; Zobin, 2003; Ripepe, 1996; Falsaperla *et al.*, 2005). Several studies have shown a correlation between tremor amplitude and volcanic activity (e.g. Mount Etna, Falsaperla *et al.*, 2005; Kilauea, Koyanagi *et al.*, 1987). For instance, the continuous tremor recorded on Etna during the eruption of July-August 2001 showed amplitude and frequency variations that can be linked to the level and style of activity: phreatomagmatic explosions, lava fountains, lava effusion and strombolian explosions (Falsaperla *et al.*, 2005). Since the start of the seismic monitoring of Villarrica volcano in 1982, permanent tremor and variable amounts of long-period events have been the dominant seismicity recorded (Fuentealba and Peña, 1998). Other types of signals present in Villarrica seismicity have been classified as explosion events, hybrid signals and volcano-tectonic earthquakes (Fuentealba and Peña, 1998; Calder *et al.*, 2004). One of the main tools utilised by OVDAS to track the level of volcanic activity is the Real time Seismic AMplitude Measurement (RSAM, Endo and Murray, 1991). The RSAM is the absolute amplitude of the seismic signal typically calculated in windows of 10 minutes duration, although the length of the window vary depending on the time resolution needed for the analysis.

In this chapter, the main characteristics and variations of the continuous activity of Villarrica volcano are identified, and the relationship between seismicity, degassing and observed activity at the summit is established. This was achieved through new measurements of SO_2 flux, seismic data and visual observations in the period November 2004 to February 2006. In addition, total SO_2 emission rates were correlated with volcanic tremor.

4.2 Historical and recent activity of Villarrica volcano

4.2.1 Persistent activity

Based on more than 60 years of observations, Casertano (1963) describes the activity of Villarrica volcano as "...rather continuous through the central crater with quite frequent eruptive crisis." It is likely that the outgassing activity inside the crater has been ongoing for at least the 20^{th} century. Observations of historic activity highlight some similarities in

the eruptive behavior of Villarrica volcano (Casertano, 1963; Petit-Breuilh, 1994). Eruptions were generally preceded by a noticeable increase of volcanic activity, manifest by strombolian explosions, medium intensity earthquakes (felt by people living in towns nearby), and/or scoria cones and very active lava lakes. These observations suggest the rise of the magma level and strong outgassing activity taking place before and during the early stages of the eruptions. Some examples of different types of eruptive activity observed at Villarrica volcano in the 20^{th} century are (Casertano, 1963; Petit-Breuilh, 1994): a) lava flows from the main crater or from the side of the volcano ca. 250 m below the crater rim, while keeping the explosive activity at the summit (e.g. in 1963, 1984); b) 'agitated' lava lakes with strombolian explosions (e.g. in 1948); c) very strong explosions creating a pyroclastic cloud that rises more than 1000 m above the crater (in 1908, 1948, 1964, 1971); d) high lava fountains at the summit (in 1949, 1964, 1971). Hence, the historical record of observations shows persistent degassing activity and associated eruptions. In many cases, eruptive episodes showed precursor signs of increasing magmatic activity. At Villarrica, the activity is considered an eruption only when there is extrusion of lava outside the crater.

4.2.2 Background activity

At least for the last 10 years, background (low to moderate) levels of activity at Villarrica volcano were commonly characterized by the surface of the lava lake being located more than 90 metres below the crater rim. Gentle roll-over with brief moments of quiescence of the lava lake (as observed by Calder *et al.*, 2004) is likely to mark the lowest strength in activity of the visible lava lake. Strombolian explosions rarely reach 100 metres above the lava free–surface. In addition, during low levels of activity the tremor amplitude rarely reaches values above 20 RSAM units (persisting for more than one day), and the seismicity lacks significant numbers of volcano tectonic-type earthquakes.

Although these characteristics typify the predominant volcanic activity observed since 1985, Villarrica volcano displays continuous variations in seismicity, activity observed at the crater, and amount and style of outgassing.

4.2.3 The 1999 and 2000 crises

Three different episodes of high activity have been observed recently: in 1999, 2000 and 2005. These three periods developed with abnormal types of both visible and seismic activity but did not culminate in eruptions. The first two are documented by Calder *et al.*

(2004) and Ortiz *et al.* (2003), respectively, whereas the activity exhibited in 2005 is described in this chapter (Section 4.3).

Between August and December 1999, Villarrica showed a significant increase in seismic activity, a rise in the level of the lava lake, several large but discrete explosions, and morphological changes of the crater floor (Calder *et al.*, 2004). Several episodes of sudden increase in seismic amplitude (two or three-fold) lasting for several hours occurred in August, November and December. As a result of the explosive activity, scoria bombs up to 50 cm in diameter were found on the crater rim and tephra fall deposits extended up to 5 km from the vent (Calder *et al.*, 2004).

During September 2000, several tectonic earthquakes occurred in the region, including a magnitude 3.8 earthquake that took place less than 70 km from the volcano on 20 September. Subsequently, the tremor spectrum exhibited a frequency shift of its dominant peak from 1 to 2 Hz (Ortiz *et al.*, 2003). This seismic activity was associated with a sudden decrease in the fumarolic activity observed at the crater, and an apparent crusting-over of the lava lake that concealed the nature of magmatic activity. Reestablishment of the activity at the crater was accompanied by pahoehoe flows on the crater floor and the construction of a spatter cone.

4.2.4 Morphology of the crater floor: the spatter roof

Cooling at the surface of the lava lake creates partly solidified patches of crust that stay afloat temporarily on the lava surface. At Villarrica, slowly moving crust plates, as seen at Erta Ale (e.g. Oppenheimer and Yirgu, 2002; Harris *et al.*, 2005), are not observed. Instead, continually ejected spatter adheres to the inner walls of the vent and forms a spatter roof that grows by accretion and agglutination of the pyroclastic material (Figures 3.1, 4.1a). The spatter roof can partly or completely conceal the activity of the lava lake, so the location of this roof effectively defines the depth of the observable crater floor. The roof is commonly unstable and experiences frequent collapses depending on the intensity of the lava lake activity underneath; when the explosive activity increases, the roof thickens by accumulation of material on its upper surface, eventually creating terraces (relatively flat surfaces, Figure 4.1b), or even forming a small scoria cone (Figure 4.1c). The collapse of the roof or terraces may occur mainly due to the increasing overburden, but also by thermal erosion of its lower surface by the hot magma. Terraces can display concentric fractures which subsequently accommodate collapses. In turn, the outer concentric fracture observed on 16 January (Figure 4.1b) was the site of a small collapse that occurred within two days after the

photograph was taken (16-18 January 2005). On 26 January 2005, another small collapse was witnessed by mountain guides. This time, pyroclastic material that had accumulated around an elongated aperture in the spatter roof, not more than 10 m wide, collapsed and left an almost circular opening about 25 m in diameter. When the magma column withdraws and the free surface height lowers, the unstable roof usually collapses, often within a time span of hours.

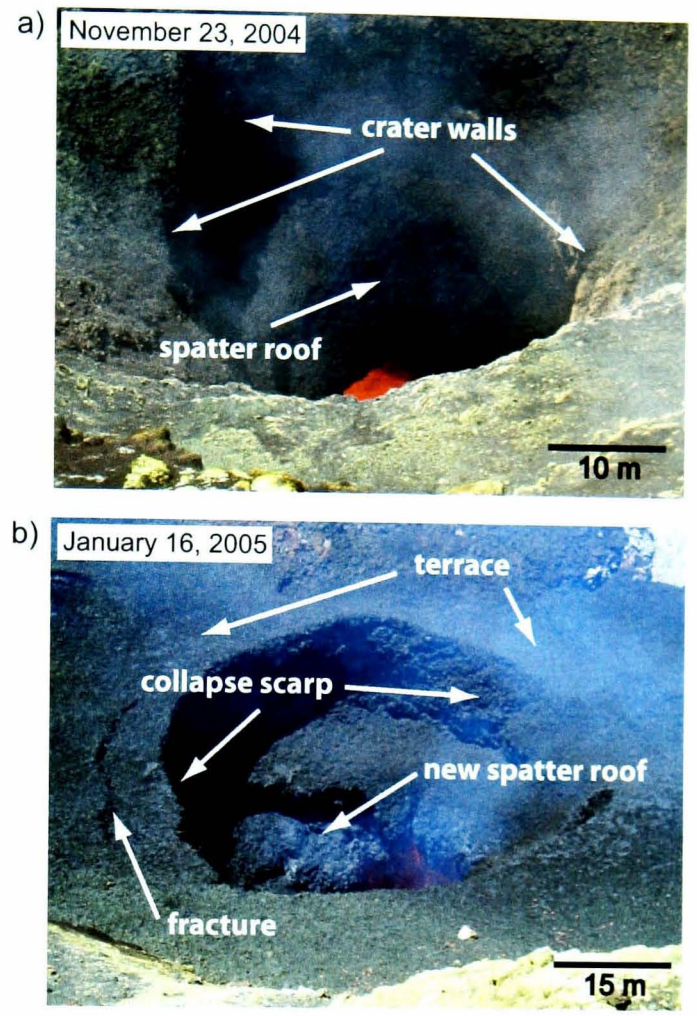

Figure 4.1: Sequence of photographs that shows the morphological evolution of the vent during the period November 2004–April 2005: spatter roof and terraces on the crater floor a) at the end of November 2004, b) middle of January 2005, and c) end of April 2005. The position of the roof was approximately 90 m, 50 m and 30 m below the crater rim, respectively. The roof adheres to the walls of the crater above the lava free surface. In (b) a set of three terraces with concentric fractures can be seen; the outer fracture was the site of a small collapse within the next two days. Photographs a) and b) were taken from 'La terraza' on the southwest side of the crater rim. Scales are approximate.

4.3 Activity and seismicity of Villarrica volcano during November 2004-April 2005

4.3.1 Chronology

From the end of 2004 until June 2005, the volcano showed an increase in activity as recorded by seismicity as well as visual observations. A summary of the chronology of the principal events and dates is given in Table 4.1. The rise in activity levels was accompanied by frequent changes in the morphology of the crater floor (Figure 4.1). In November 2004, the bottom of the crater was >90 m below the crater rim, and the lava lake was out of direct view. Spatter from small strombolian explosions could be seen but rarely reached more than 20 m above the spatter roof. By the end of November, a new small spatter roof had formed at the bottom of the crater (Figure 4.1a). Subsequently, the activity increased gradually and, by the middle of December, some explosions were sending bombs and spatter up to 100 m above the crater floor. Increasing amounts of new tephra were observed around the vent and also on the crater rim.

During January 2005, the intensity of the strombolian activity continued to increase, accumulating abundant material on top of the spatter roof and crater walls. Although it was unusual to see large explosions during the time spent at the summit of the volcano (usually between 1.5-3 hours), by the middle of January it was more common to find new pyroclastic material (lapilli-bomb sized) on the north-east side of the crater rim. During this period, the morphology of the crater floor was evolving rapidly and showed evidence of repeated construction and partial collapse cycles. A prominent upper terrace formed only ~50 metres below the crater rim, suggesting the rise of the magma free–surface. The second half of January was characterized by a rapid increase in the level of activity and, by the end of month, explosions were ejecting centimeter-sized pyroclasts up to ca. 100 meters above the bottom of the crater (~50 m above the crater rim).

There were no further substantial changes until late February and early March when the upper terrace increased in thickness by accumulation of pyroclastic material. By the end of March, a small spatter cone started to grow on top of the roof with an orifice less than 10 m in diameter on its top (Figure 4.1c). This acted as a nozzle generating narrow, vertically–directed jet–like explosions. The most vigorous explosions had durations of the order of 3-10 seconds and ejected bomb-sized pyroclasts at least 150 m above the crater floor. During April the roof morphology kept changing, notably the size of the cone and diameter

Table 4.1: Summary of visual observations and seismicity during November 2004-April 2005.

Date	Visual Observations	Seismicity[a]
9-17 November	Lava lake >100 m below crater rim; not visible. Ejected spatter rarely reached more than 20 m above the crater floor.	RSAM 10-20 units (average 15).
23 November	New spatter agglutinated to the inner wall of the vent.	Slowly increasing RSAM: up to 20 units
12-19 December	Explosions send pyroclasts onto the crater rim (>100 m above the lava lake).	RSAM over 20 units and increasing. Banded tremor appears interlaced with pulsating tremor.
3-12 January	Apparent increase in frequency of explosions ejecting material out of the vent.	Highly variable RSAM: 20-35 units and up to 40 on 8 and 9 January.
14-18 January	Spatter roof ca. 40 m higher than in November. Terrace built up with pyroclastic material falling on top of the roof. Evidence of partial concentric collapses of the roof around the vent.	Rapid increase in seismic amplitude: RSAM up to 50 units. Seismic signal shows high frequency.
21-26 January	New accumulation of spatter at the interior of the central opening. Big explosions sending bombs above crater rim. Partial concentric collapses.	RSAM 20-35 units.
February	Morphology of the spatter roof is more stable. Explosive activity similar to January. By the end of February, increase in accumulation of pyroclastic material around the vent is evident.	Average RSAM ca. 25 by the middle of Feb, but decreases to 15-22 towards the end of the month.
5-11 March	Pyroclastic material accumulating on the NE-E side of the vent. Two holes in the spatter roof.	RSAM shows positive trend, recovering values >20 units (on average).
24-30 March	Opening in the roof has consolidated into one small (ca. 5 m) circular hole. Pyroclasts ejected >100 m above the crater rim.	RSAM more stable at 20-27 units on average. Increasing amounts of VT earthquakes.
April	A spatter cone is developed on top of the roof with a hole <15 m in diameter. Explosions send bombs >150 m above the crater rim. Spatter appears around the vent on 19-20 of April.	Average RSAM stable at 20-30 units. Amount of VT earthquakes well above background (36 in the whole month).

[a] RSAM calculated over a time window of 10 minutes. Unless otherwise specified, all calculations and observations are my own.

of its vent. Explosions ejecting material above the height of the crater rim were seen until July. By the end of July–early August the lava roof (and magma free–surface) had retracted to about 70 m below the crater rim, which was accompanied by a decline of the activity, marking the end of the 2004-2005 episode.

4.3.2 Characteristics of the seismic tremor

During November 2004-April 2005, two short-period vertical component seismic stations were operating near the volcano, at 3.7 km (station VNVI) and 19 km (station CVVI) to the NW and W of the crater, respectively (Figure 1.1). Both are part of the volcano monitoring seismic array operated by the Southern Andes Volcano Observatory (OVDAS-SERNAGEOMIN). In this study, I used data from the VNVI station, which is the closest station to the volcano. Corrections for the frequency response of the seismometer, which is flat above the corner frequency of 1 Hz, were not made. This limits the quantitative analysis of frequency peak amplitude and dominance below 1 Hz, but it does not affect the temporal analysis of amplitude and frequency variations.

Tremor at Villarrica contributes more than 90% of the total seismic energy. It is commonly a continuous, irregular and low amplitude seismic signal. Its waveform generally has a pulsating pattern in which short tremor bursts of higher amplitude occur as often as once per minute (Figure 4.2). The frequency of occurrence of the higher amplitude bursts varies with the level of activity (Calder *et al.*, 2004, reported 10 events per hour in 1999). Periods of elevated observed volcanic activity have an overall higher occurrence of these events. If viewed as individual discrete events, these higher amplitude bursts normally last less than 50 seconds, are generally characterized by emergent starts and ends (gradual increase and decrease in amplitude, respectively), and show a wide range of amplitudes and durations (Figure 4.2). They have been previously described as low-frequency events generated by strombolian explosions (Fuentealba and Peña, 1998; Fuentealba *et al.*, 2000). Examples of the waveform and frequency content of the background tremor as well as some high amplitude events are shown in Figure 4.3. Among them, high amplitude tremor bursts with similar frequency content to the background low amplitude tremor (or similar to low-frequency events) are predominant in the signal. Other event types, similar to hybrid and volcano-tectonic events are also embedded in the tremor but they are less frequent. Most of these high amplitude events are composed of low frequencies with peaks that coincide with those of background tremor (Figure 4.3), making difficult the distinction between events and tremor itself. Indeed, and

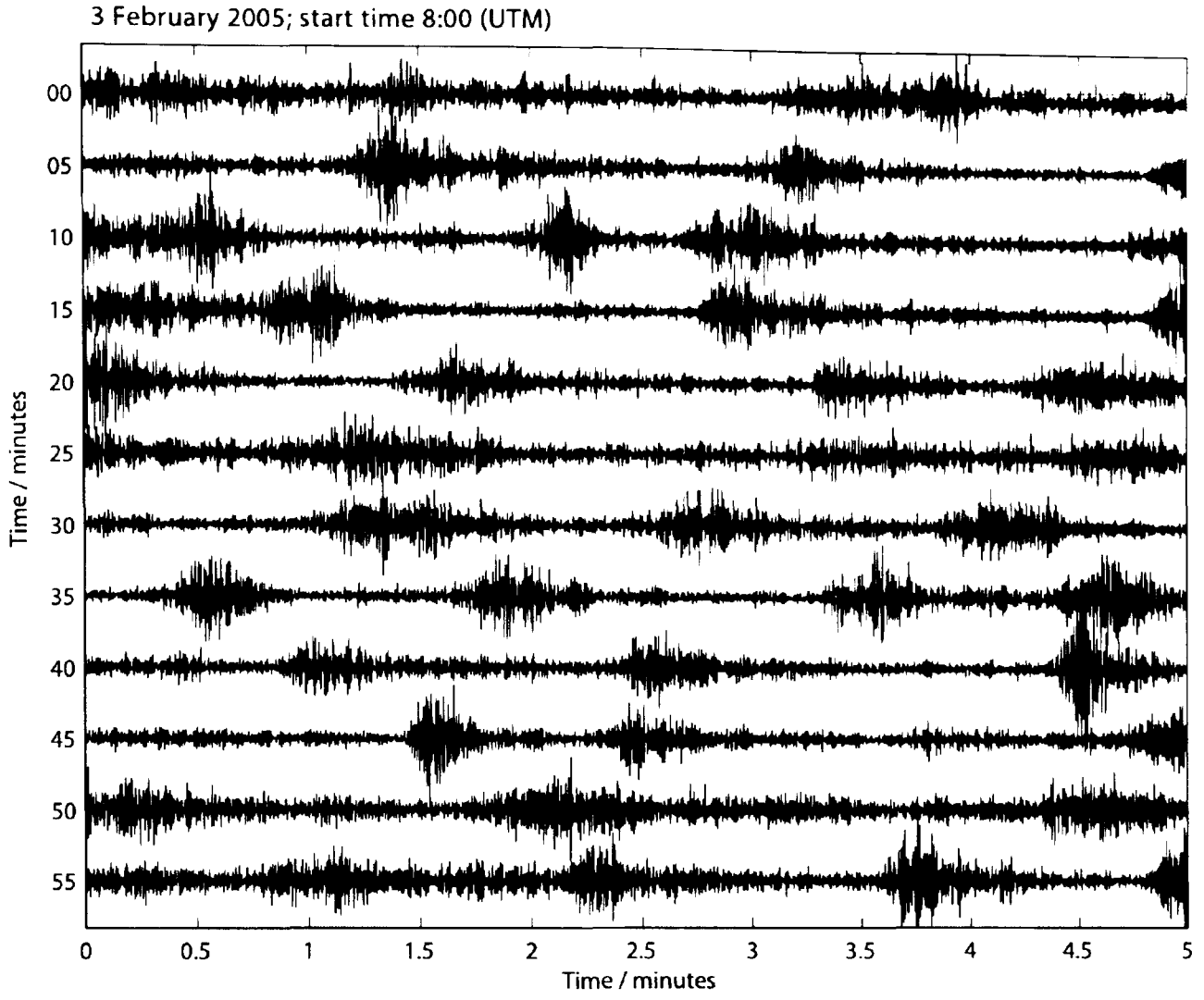

Figure 4.2: One hour of seismicity from 03-Feb-2005 beginning at 8 am (GMT). The vertical axis shows the start of the signal at 5-minute increment. Individual bursts have a wide range of amplitudes and durations, as well as emergent starts and ends.

as it will be shown later, inspection of the seismic signal does not reveal any consistent (and persistent) difference between the frequency content of background low amplitude tremor and high amplitude bursts. The identification of all the individual types of events over a long period of time is beyond the scope of this work. Yet, the analysis of the tremor as a continuous signal, irrespective of the appearance of distinguishable events, will be useful to study the changes in activity and degassing of Villarrica volcano.

Banded tremor, characterised by tremor packets of higher amplitude, is also part of the seismicity of Villarrica volcano. Such higher amplitude tremor can last minutes to days, but commonly has a duration of a few hours. Typically, it preserves the spectral features of the lower amplitude tremor preceding it. Banded tremor repeats during the period of study and has been described during the 1999 crisis (Calder *et al.*, 2004), as well as at other volcanoes of low-silica composition such as Miyakejima (Fujita, 2008) and Kilauea (Barker *et al.*, 2003).

One of the main tools employed by the Southern Andes Chilean Volcano Observatory

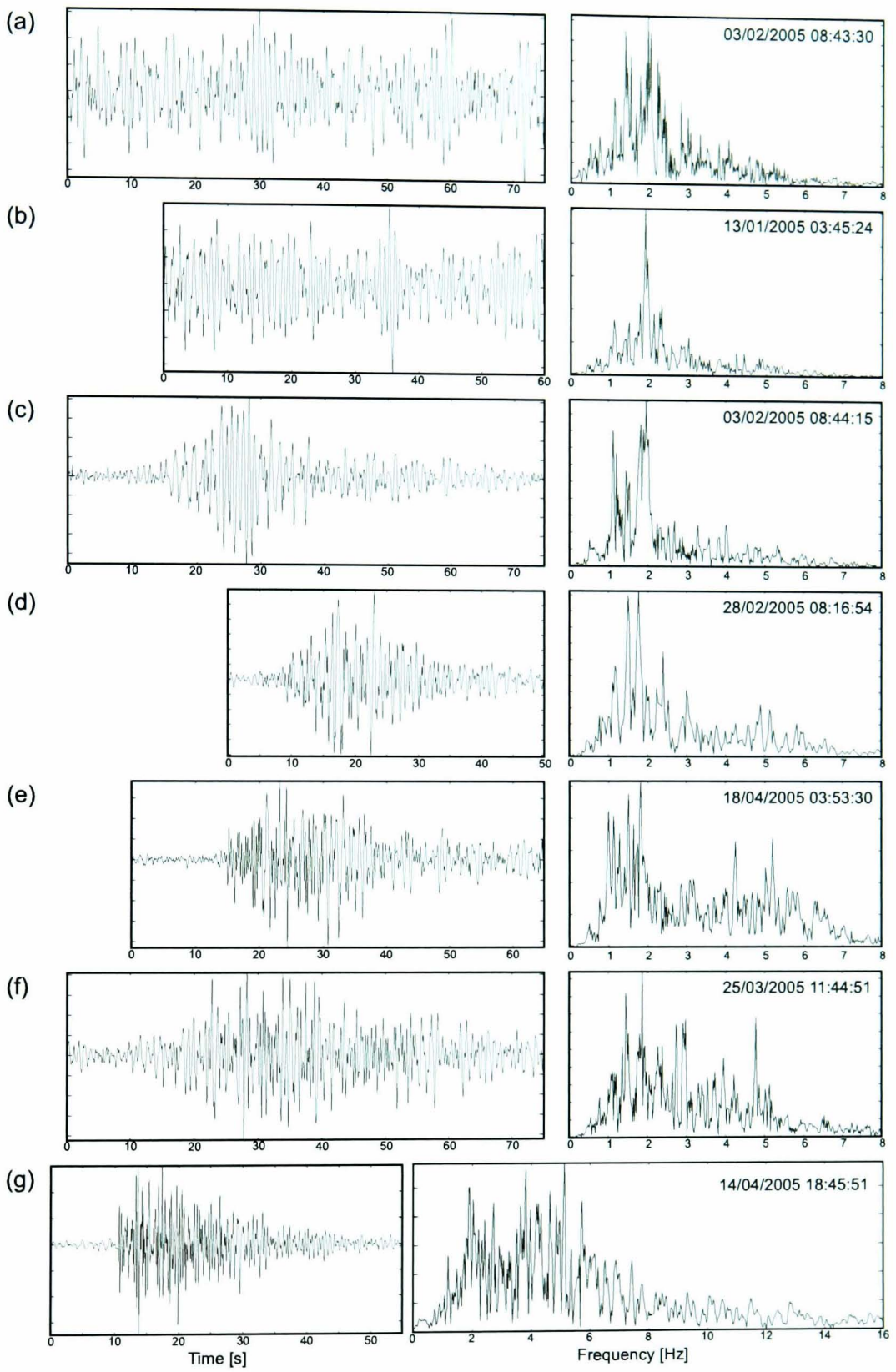

Figure 4.3: Waveform (left) and spectrum (right) of tremor high amplitude events. (a) and (b) are examples of background tremor, (c) resembles an explosion quake, (d) a long period event, (e) and (f) are two different types of hybrid events, and (g) is a volcano tectonic quake. Waveforms on the left plots were normalised by the maximum amplitude range. Dates and times of the start of each signal are in the top right corner of the spectra plots.

(OVDAS), to routinely monitor the activity of Villarrica volcano, is the amplitude of the seismic signal, which is measured as RSAM units (Endo and Murray. 1991). Changes and trends in seismic amplitude (RSAM) for the period November 2004-April 2005 correlate well with the volcanic activity described above (Table 4.1 and Figure 4.4a). RSAM started increasing in December and continued increasing until the end of January, reaching values of between 40 and 50 RSAM counts. There was a decrease in amplitude at the beginning of February, although remaining higher than 20 counts, and a further sudden decrease that was followed by a slow increase starting the last week of February, reaching values of 30 counts by the middle of March. During the second half of March and April, the RSAM values remained fairly constant between 20 and 30 counts. In general, these variations are manifested by the total range and maximum values of the RSAM amplitude (Figure 4.4a). In addition to the long monthly trend in seismic amplitude there are some short episodes, normally just a few days, where the overall RSAM amplitude changes abruptly to higher or lower values (e.g. 14-19 and 29-30 January 2005). One of these episodes, in the middle of January, was correlated with increasing gas emissions (Section 4.4.2).

Throughout the analysed period most of the seismic energy is concentrated within the frequency range 1-7.2 Hz, with the highest peaks commonly between 1-2.15 Hz (Figures 4.4b, 4.5). Along with the increasing activity from November 2004 to January 2005, the associated tremor displayed gradual variations in the relative amplitude of the dominant peaks in the frequency domain: the amplitude in the frequency band 1.65-2.15 Hz increased whereas in the frequency bands 1-1.35 and 2.55-7.2 Hz the relative amplitude decreased (Figures 4.4b, 4.5). Sharp changes in amplitude within the range 2.55-5.5 Hz, occurring on 14-19 and 29-30 January 2005, strongly contribute to the sudden increases in RSAM values (Figures 4.4, 4.5, 4.6). These variations last for a few hours or days and do not represent individual transient events. The relationship between these short periods of higher amplitude and the activity observed at the summit of the volcano is not clear. Although environmental effects such as high winds cannot be ruled out, weather reports and observations in the field did not point to any particular meteorological conditions that would coincide with the timing of these variations. Moreover, a closer look at the signal reveals different amplitudes and start times of these peaks at low and high frequencies (Figure 4.6). The onset of the tremor with highest amplitudes in the band 2.15-7.2 Hz coincides with a decrease in the amplitude of the band 1-2.15 Hz. Only a few hours later, when the amplitude of the relatively high frequency band (2.15-7.2 Hz) is in a waning stage, the low frequency band (1-2.15 Hz) recovers its

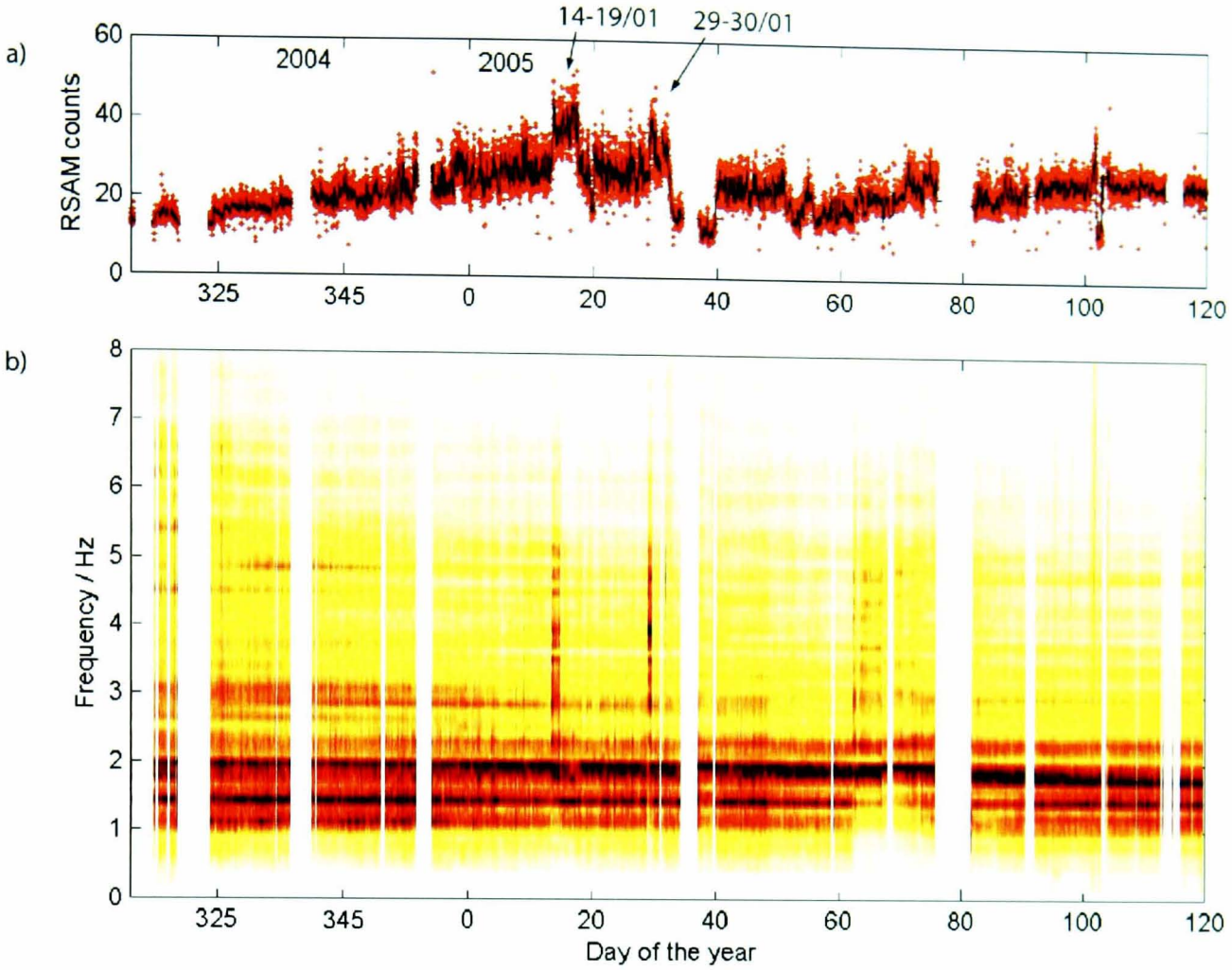

Figure 4.4: a) Real-time Seismic Amplitude Measurements (RSAM) and b) spectrogram of the tremor for the period November 2004–April 2005. RSAM is calculated over a moving window of length and step of 10 minutes. The spectrogram is normalized to the maximum value of the energy for every 10 min window, so it shows the relative changes in frequency distribution and dominant spectral peaks. Empty spaces represent data gaps.

previous amplitude (Figure 4.6). Unfortunately, detailed visual observations of the crater on some of these days (16 and 18 January 2005) were not sufficient to allow the correlation of these variations with the volcanic activity. It is interesting to note that the background low amplitude tremor follows a similar trend in RSAM and frequency content (Figure 4.7). Although the frequency peaks do not look as prominent as in the case of considering the whole seismic signal, similar features such as the higher energy in the frequency band 1-2.15 and the higher frequency content during 14-19 and 29-30 January 2005 are present in both cases. The same tendency was found in the other months pertaining to the period of study.

During periods of elevated seismic activity, such as in December 2004 and January 2005, the daily RSAM exhibited a broad range of values with a fast increase and subsequent slow fall in amplitude (Figure 4.8a). These fluctuations had a periodicity of about 1.9 to 5 hours, but the most prominent saw–tooth cycles commonly had a duration between 2 and

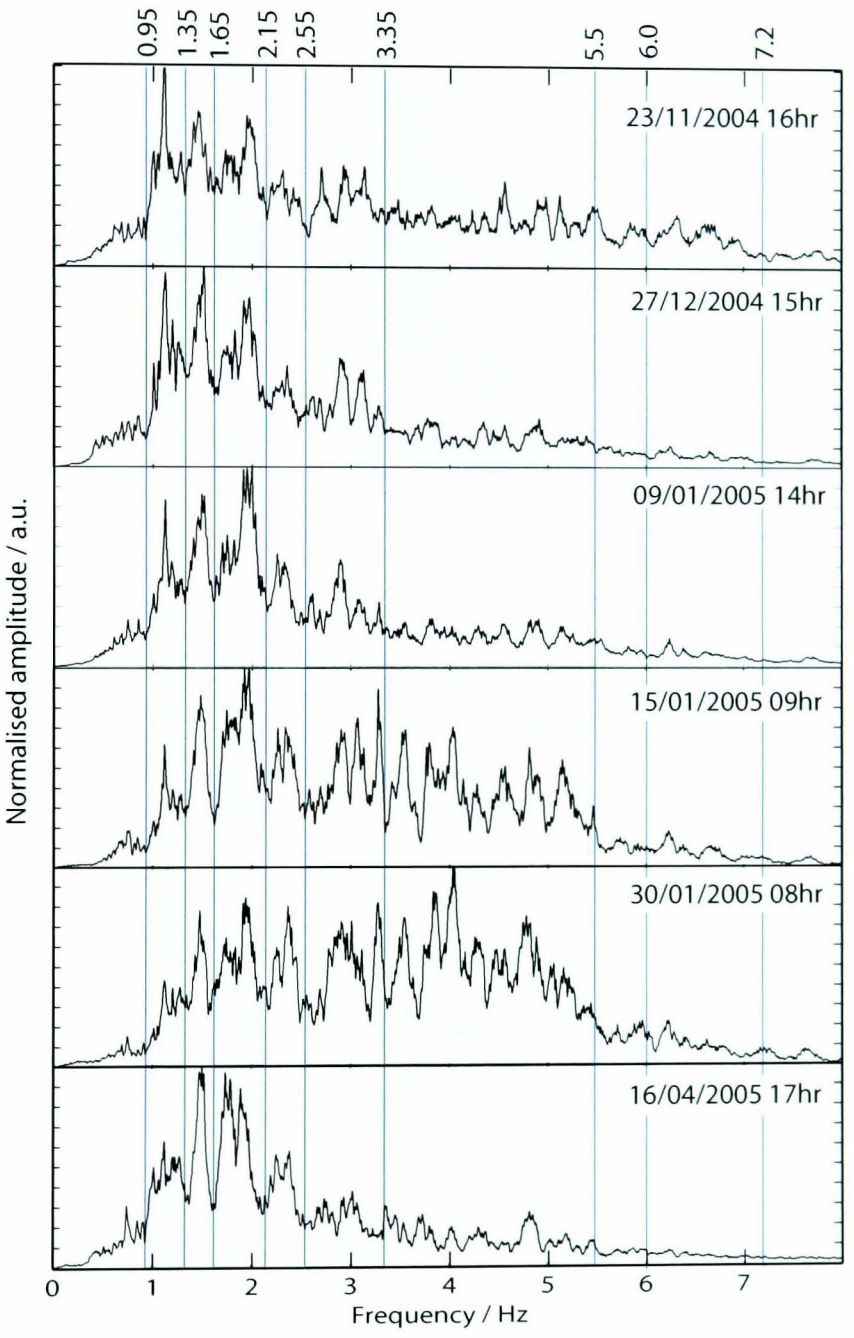

Figure 4.5: Spectra of six one-hour long seismic signals that show the changes in the amplitude of the predominant peaks between November 2004 and April 2005. Vertical lines divide the spectra at frequencies 0.95, 1.35, 1.65, 2.15, 2.55, 2.85, 3.35, 5.5, 6 and 7.2 Hz. These lines were chosen in order to highlight the variations in amplitude of particular frequency ranges. Grey areas correspond to frequency bands 0.95-1.35, 1.65-2.15 and 2.55-5.5 Hz.

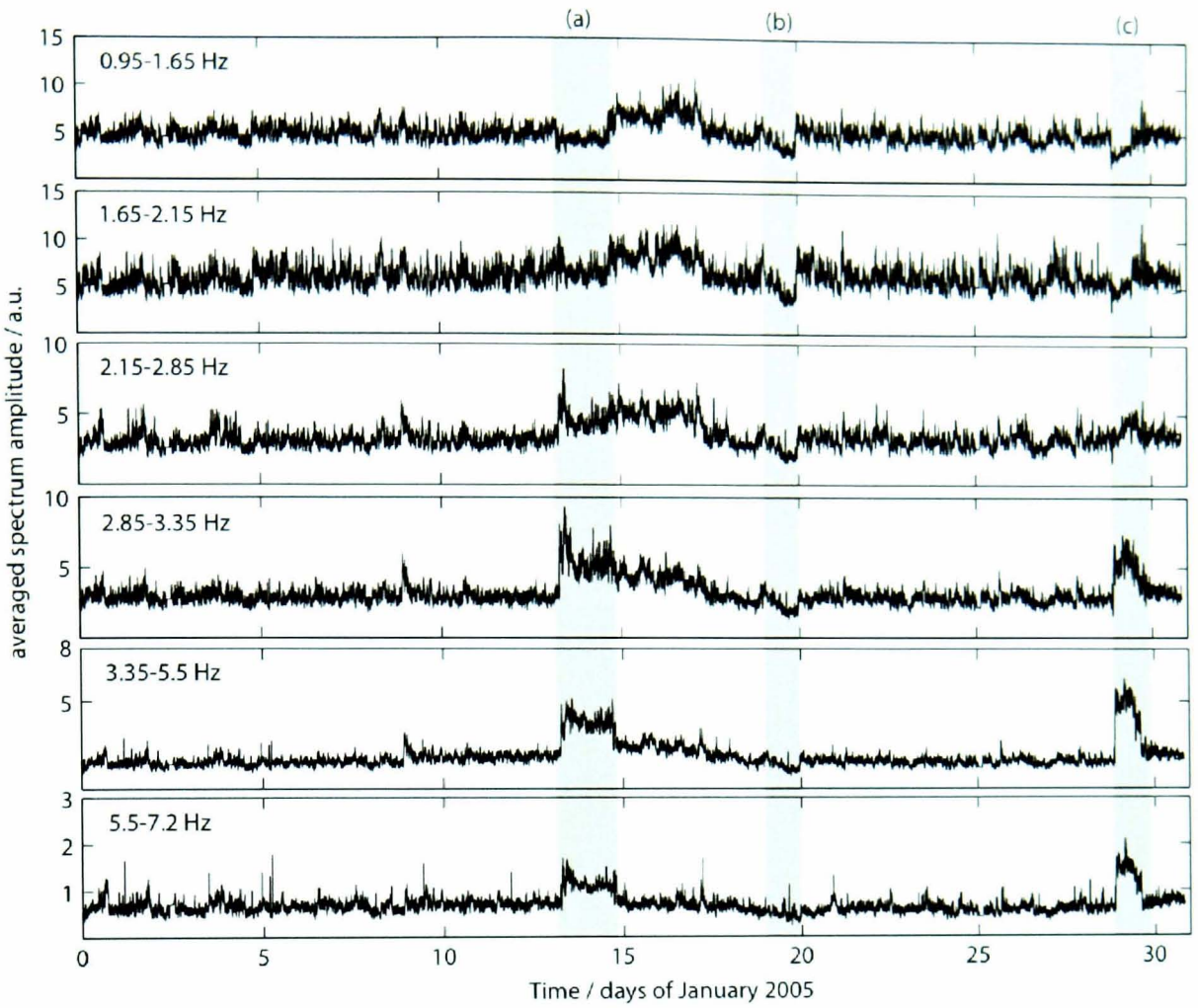

Figure 4.6: Amplitude variations in the frequency of the tremor during January 2005. Each trace was obtained by calculating the Fast Fourier Transform (FFT) and averaging the spectral amplitude of a 30 minutes long window moving with a step of 15 minutes. Frequency bands were chosen based on the distribution of peaks and troughs in the spectra after inspection of the whole data set. Notice the different scales on the vertical axes. Although the absolute amplitudes are in arbitrary units, values between bands can be compared.

3.5 hours. Seismic traces coincident with high RSAM units evidence a higher frequency and amplitude of the tremor bursts (Figure 4.8b), although the frequency content of the tremor is similar on both RSAM peaks and RSAM troughs (Figure 4.8c). During periods where the RSAM was low (< 20 units), these features were absent or appeared more erratic and less frequent.

4.3.3 Correlation between outgassing activity and tremor magnitude

Simple experiments were carried out between January-February 2006 in order to correlate the seismic signal with the observed activity at the summit of Villarrica volcano. From the crater rim, we made timed observations of the explosions and other outgassing related events (Figure 4.9). During this period the level of activity was considered low, with the bottom of the crater located more than 80 m below the crater rim. The diameter of the orifice in the roof was no greater than 15 m and so the lava lake was not directly visible. A second small

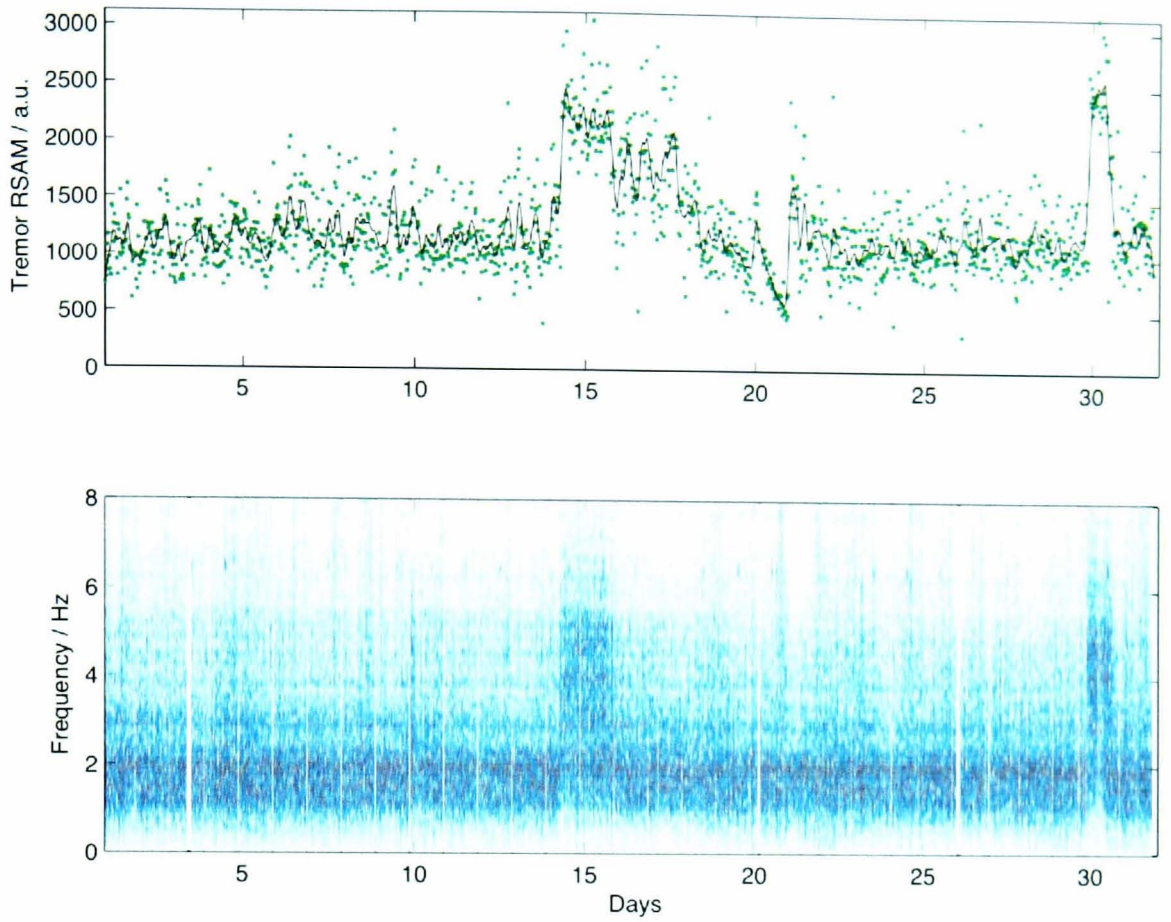

Figure 4.7: RSAM and spectrogram of low amplitude tremor registered in January 2005. Both the RSAM and spectrogram were calculated choosing the segment of tremor (10.24 seconds duration) with the lowest amplitude in a moving window of 30 minutes duration. Every spectrum calculated in the spectrogram was normalised by the maximum amplitude. (unlike the other plots, the time starts from 1 instead of 0)

hole was present on the west side of the roof and showed continuous gas emission with only sporadic pyroclastic activity. Owing to morphological restrictions, not every bursting event could be observed. In spite of that, the results show a good correlation between the timing of the observed bubble bursts and that of higher amplitude tremor transients (Figure 4.9a). Moreover, the frequency content of the seismic signal, evaluated as the relative contribution of bands 0.95-2.15, 2.15-3.35 and 3.35-5.5 Hz, was observed to change slightly with time. This was particularly evident on high amplitude tremor bursts (Figure 4.9a). However, despite the apparent higher component of low frequency energy on tremor peaks, there was no consistent variation in the frequency content of low and high amplitude tremor (Figure 4.9b). This characteristic has also been observed during other periods, such as December 2004-January 2005. Hence, the higher amplitude tremor transients are not distinguishable based upon their frequency content alone.

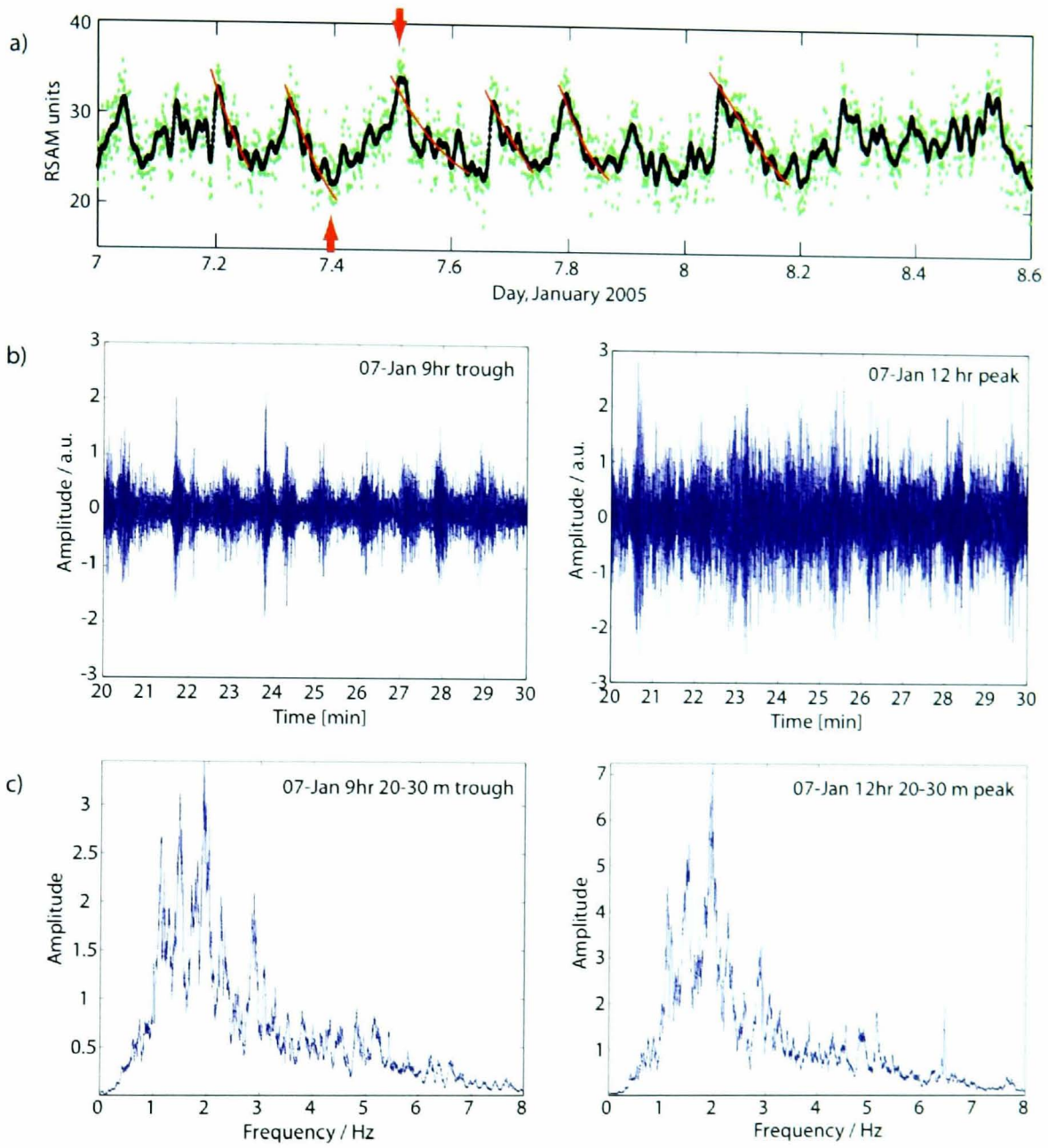

Figure 4.8: (a) Fluctuation patterns in seismic amplitude (RSAM). This example is from 7-8 January 2005. Many of the fluctuations display a saw-tooth shape, with a fast increase in amplitude followed by a slow decrease. (b) Waveform plots of one-hour of seismic signal coincident with an RSAM peak and RSAM trough (indicated with arrows in (a)). (c) Their associated frequency distribution (Fourier Transform, normalised amplitude).

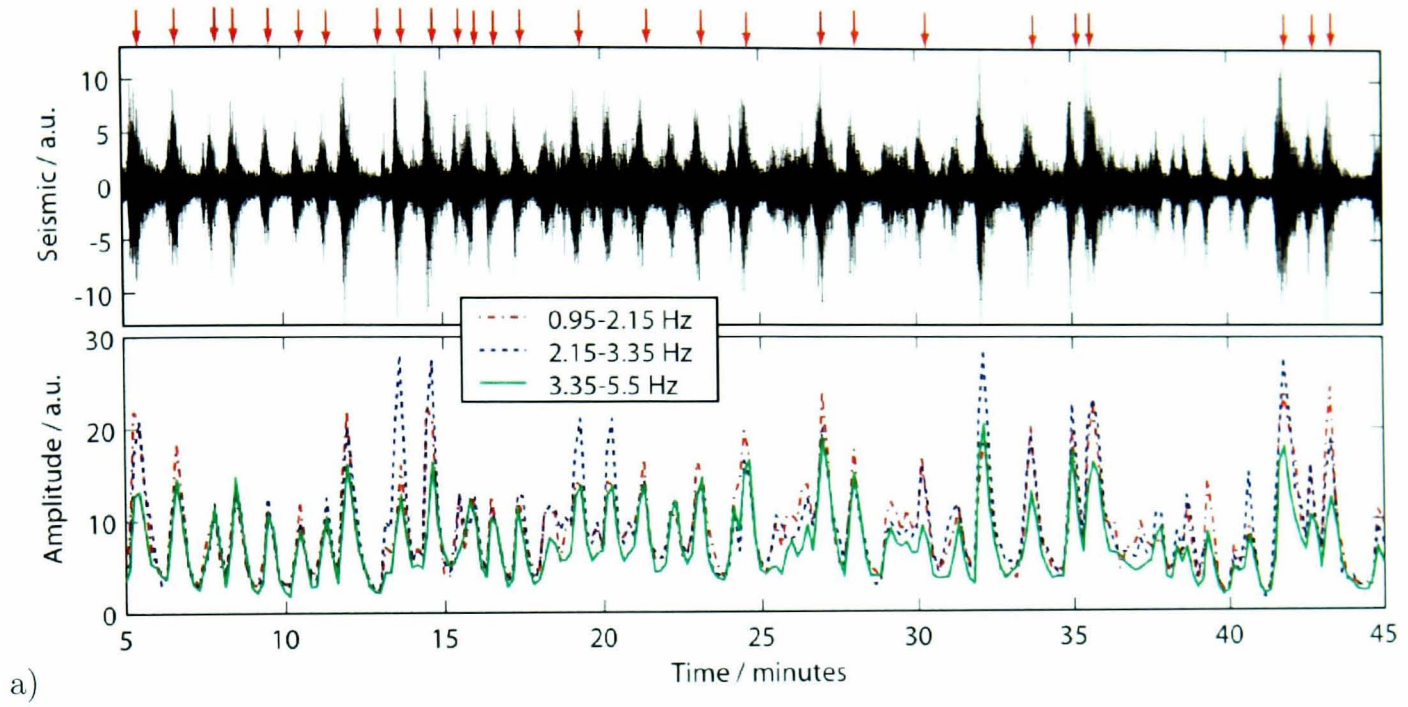

a)

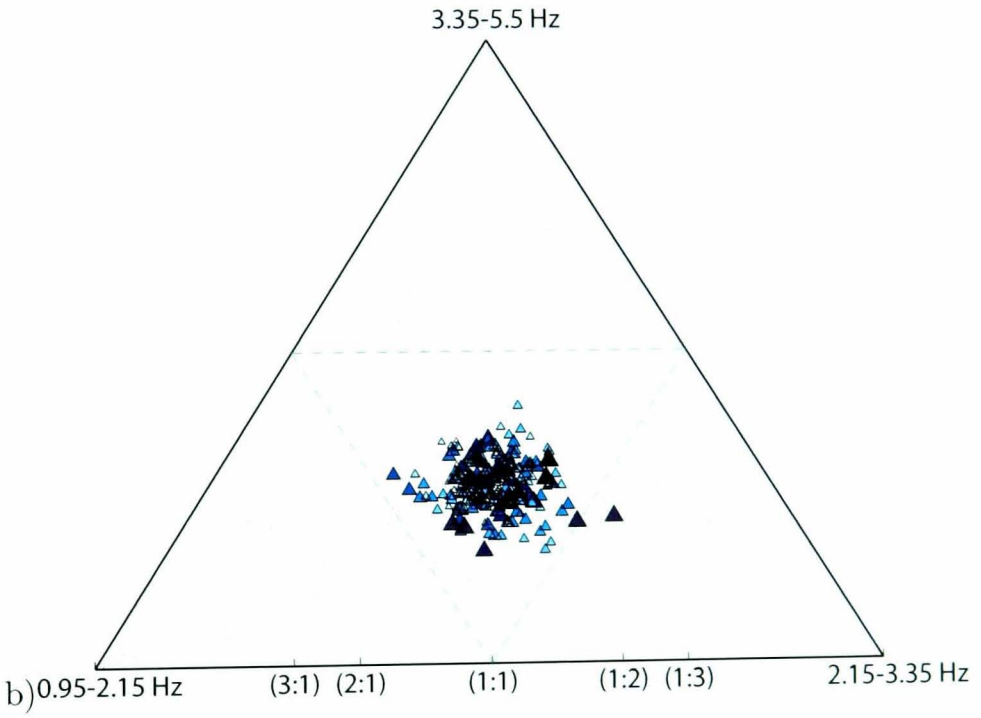

Figure 4.9: Example of the correlation between visual observations of explosions and seismicity at Villarrica volcano. a) Seismic tremor and amplitude of three frequency bands are illustrated for 40 minutes of data of 17 January 2006. Arrows on top of the figure mark the time of explosions observed from the summit of the volcano. The amplitude of the frequencies was calculated with a 15 second long moving window with a step of 10 seconds. b) Distribution of the frequency content for the same signal. Higher amplitude tremor is represented by darker and bigger triangles.

Table 4.2: Monthly volcano-tectonic (VT) earthquakes detected at Villarrica volcano.

Month	Number of VT
December 2004	2
January 2005	4
February 2005	2
March 2005	10
April 2005	36
May 2005	5
June 2005	5
July 2005	0

4.3.4 Volcano-tectonic earthquakes

Volcano-tectonic (VT) earthquakes, also called high-frequency events (McNutt, 2000, 2005), are uncommon in the seismicity of Villarrica volcano. Only a few such events are reported every month during periods of low (background) activity (between 1-3, Calder *et al.*, 2004). During the elevated volcanic activity of December 2004–July 2005, however, as many as 10 and 36 VT earthquakes were identified in March and April, respectively (Table 4.2). The small number of stations in the local seismic network operating during that time period did not allow the location of these events to be determined. Nevertheless, three major VT earthquakes that occurred on 6 April 2005 were clearly recorded by the seismic network located at neighboring active volcanoes (Llaima, Lonquimay and Calbuco volcanoes) as well as in the city of Temuco. Analysis of data from 9 stations located between approximately 4 to 220 km away from the volcano, using the Hypo 71 algorithm under the software SEISAN, allowed the localization of these events within 8 km to the northeast of Villarrica crater[1]. These results support the idea of a change in the stress state of the volcanic system. To better constrain the evolution of such changes, however, an adequate seismic array is needed around Villarrica volcano.

4.3.5 Statistical characteristics of the tremor

In order to assess the fluctuations in amplitude of the seismic tremor, three statistical parameters were calculated from a high resolution RSAM of the seismic signal: 1) RSAM mean ($\overline{rsam}$), 2) RSAM standard deviation (σ), and 3) rate of high amplitude tremor burst (#events). I have chosen this set of parameters because when combined they describe the waveform of the tremor. In addition, from a statistical point of view they can be used to track changes in the seismicity, and so the evolution of the volcanic activity.

[1]This localisation analysis was carried out by the volcano observatory (OVDAS)

Calculations

The Real time Seismic AMplitude (RSAM) is calculated over the whole time series by means of a moving average window in the time domain. For a particular time, t, the RSAM is calculated as follows:

$$RSAM(t) = \frac{1}{T} \sum_{l=t-\frac{T}{2}}^{t+\frac{T}{2}} |s(l)| \tag{4.1}$$

where T is the duration of the moving time-window and $|s(t)|$ corresponds to the absolute value of the seismic signal. The length of the resulting RSAM time series depends on the overlap (or time step) of the moving window. The selection of both the duration (T) and time step determines the resolution of the RSAM and affects the results and meaning of the analysis. In particular, it is desirable to be able to identify each of the higher amplitude transients (or events) of the tremor, thereby the rate of events can be calculated. Accordingly, values of 10 and 7.5 seconds (25% overlap) for the duration of the window and time step, respectively, have been found appropriate for the statistical analysis of tremor amplitude at Villarrica volcano (Figures 4.10-4.11).

Once the RSAM(t) has been obtained, another moving window is applied over the RSAM time series in which the mean ($\overline{rsam}$) and standard deviation (σ) are calculated. The duration (ΔT) and time step (δt) of this window are dependent on the objective of the analysis. For instance, the study of the characteristics and waveform of the tremor, as well as the hourly fluctuations in its amplitude, were carried out using $\Delta T = 300\ s$ and $\delta t = 180\ s$ (Figure 4.10). To study long-term variations, $\Delta T = 900\ s$ and $\delta t = 600\ s$ were chosen (Figure 4.11).

A third parameter, the rate of higher amplitude events, was calculated by counting the amount of these events over a time-window of duration equivalent to ΔT. An event corresponds to a peak in the RSAM time series whose magnitude is above the average ($\overline{rsam}$) calculated for that window. To identify the peaks, a forward finite difference was performed beforehand in the RSAM time series, that was used to find those elements of the series with a preceding positive derivative and followed by a negative derivative.

Results

One of the advantages of processing the seismicity based on a high resolution RSAM time series, obtained from time-windows of 10 seconds duration, is that it allowed the identification and counting of the higher amplitude tremor transients (herein also called events). In

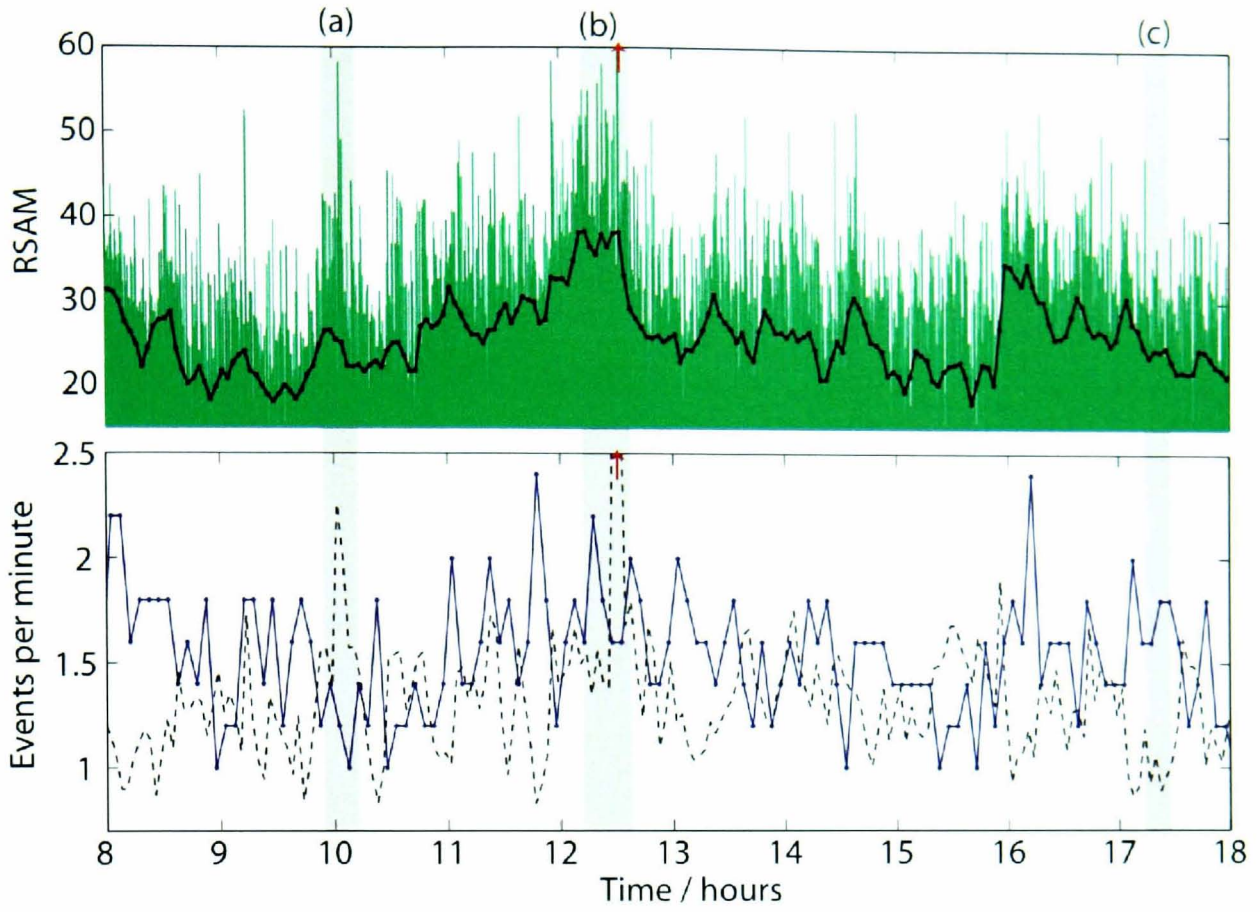

Figure 4.10: Statistical characteristics and event counting of the tremor. The top graph displays a high resolution RSAM (bars) calculated with a 10 seconds long window moving with a step of 7.5 seconds. The continuous line is the average RSAM. The bottom graph shows the number of higher amplitude transients (#events) per minute (continuous line) and the standard deviation (σ) of the RSAM divided by 5 (dashed line). The number of events was counted every five minutes. The average and standard deviation of the RSAM were calculated with a moving window with a duration and step of 5 and 3 minutes, respectively. Grey areas indicate example time periods with (a) high σ and low #events, (b) relatively high σ and high #events, and (c) with low σ but high #events. This example is from 7 January 2005. Compare with the two examples of tremor waveform and their spectra in Figure 4.8.

addition, the RSAM mean and standard deviation yielded information about the difference in amplitude of the background low amplitude tremor and higher amplitude tremor bursts, as well as the occurrence of exceptional bigger events. As shown in the example of Figure 4.10, all three parameters vary greatly, $\overline{rsam}$ from 16 to 36, σ from 4 to more than 8, and #events from 1 to 2.4 per minute. Also, the combination of their values varies continuously with time. These variations indicate that, unlike the more steady frequency content of the tremor (Figure 4.8), its amplitude can change considerably over a short time span. Further, the combination of these parameters can describe relevant characteristics of the tremor waveform. For instance, low events rate along with low RSAM mean and high standard deviation (e.g. area (a) in Figure 4.10) represent relatively less frequent high amplitude discrete events with well defined starts and ends (not overlapping with each other). It is noteworthy that owing to the short duration of the window used in the calculations of the statistics, one single

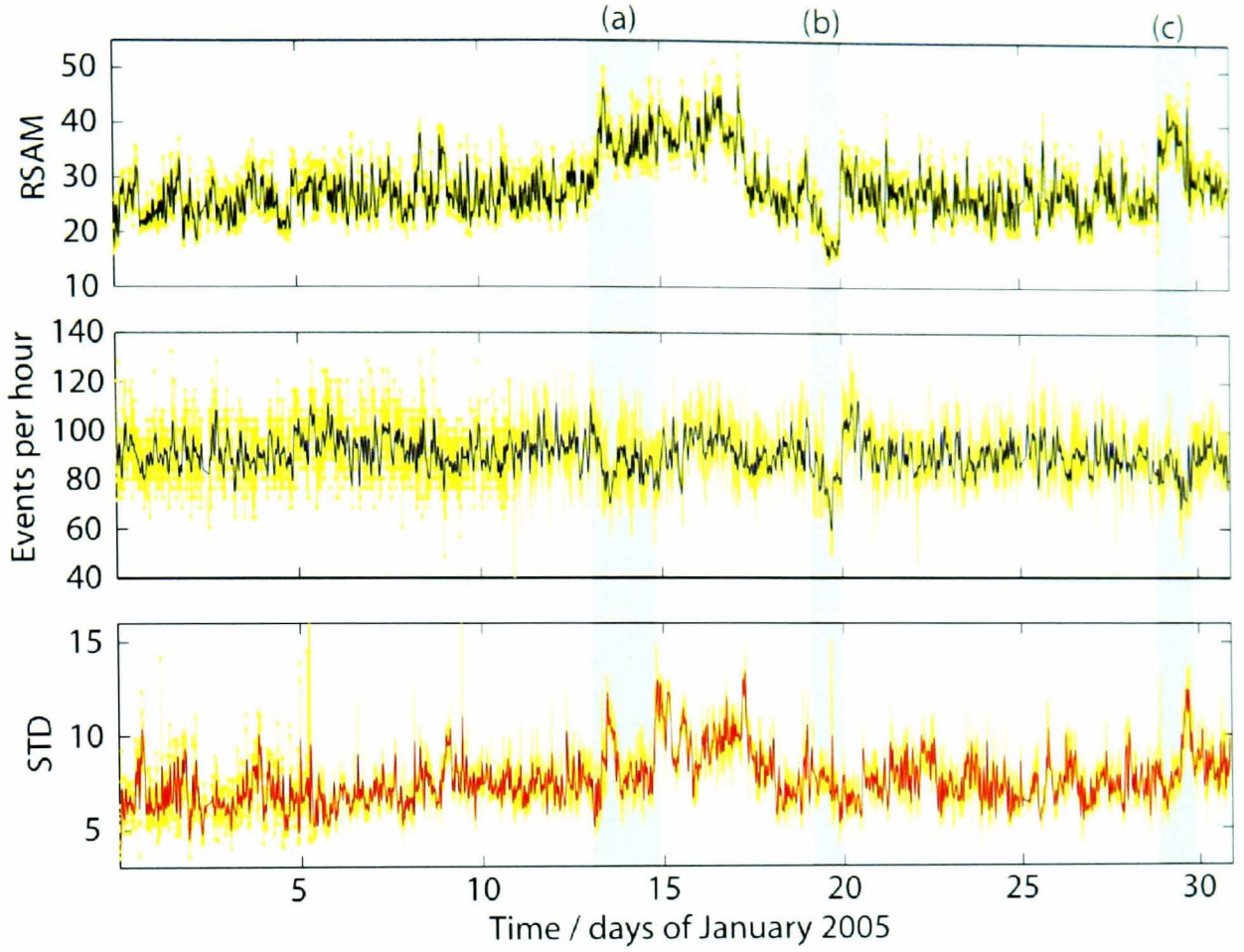

Figure 4.11: RSAM amplitude (top), number of events per hour (middle) and RSAM standard deviation (bottom) of the tremor signal in January 2005. The RSAM was calculated with a moving window with duration and step of 10 and 7.5 seconds, respectively. RSAM average and standard deviation were calculated in a 15 minutes long window moving with a step of 10 minutes. In each case, a moving average (four data points) was applied (dark line). Grey areas mark time periods with abrupt changes in RSAM amplitude, and coincide with areas marked in Figure 4.6.

big event can increase the standard deviation substantially (as observed in area (b) of Figure 4.10). The opposite arrangement, with high event rate and very low standard deviation (e.g. area (c) in Figure 4.10), represents tremor with a steady envelope in which events of similar amplitude occur more frequently; the amplitude of these events can be determined by the magnitude of the RSAM mean.

Although the overall trend of events per minute might display a rough correlation with the amplitude of the RSAM (e.g. Figure 4.10), during November 2004–April 2005 neither the RSAM standard deviation nor the events rate showed a consistent correlation with the RSAM amplitude. An example of this is shown in Figure 4.11. During the distinct changes in RSAM amplitude in January 2005, both the standard deviation and the event rate showed patterns different to that of the RSAM mean. Some noteworthy features are those that occurred on the 14–15 and 29–30 January (areas (a) and (c) in Figure 4.11, respectively), in which the number of events per hour increased and subsequently decreased sharply, and

correlated with the inverse fluctuations in standard deviation; the RSAM displayed a rather different behavior. In turn, the peaks in RSAM amplitude and standard deviation denote the occurrence of relatively high amplitude tremor events on a time span of a few hours (e.g. 9-12hrs 14 January, 15-16hrs 30 January). The trough in standard deviation accompanied by higher RSAM denotes banded tremor (e.g. 29–30 Jan). On the 20 January (area (b) in Figure 4.11), however, the tremor event rate followed the decrease in RSAM mean amplitude, in the same manner as all frequency bands did (Figure 4.6), denoting a considerable drop in seismic activity.

The evolution of the seismic activity analysed on a monthly basis is shown in Figure 4.12 for the period November 2004–April 2005. In this case, the time series of statistical parameters, calculated over a time window of 900 seconds duration (as shown above Figure 4.11), were reduced to daily averages of each parameter. Several interpretations can be formulated from this analysis, on the basis of the information that each parameter yields on its own and when combined with others, as well as the information about the seismic waveform and its correlation with the volcanic activity described in Section 4.3.3. For instance, the days on which the volcano showed low levels of activity, such as during November 2004, can be clearly identified. It is somewhat surprising, however, to find such consistent high event rate during November 2004, given the low levels of seismicity and activity at the crater. That could be the result of the very low variance in amplitude of the signal, and the lack of a threshold in the algorithm for the determination (and identification) of high amplitude events. In effect, using a short time window for the calculation of the RSAM favours the detection of small fluctuations in amplitude of the tremor; those fluctuations are picked up as events by the algorithm. A second observation is the gradual increase in seismic activity from November 2004 to January 2005, which is in agreement with visual observations, and that is reflected in the simultaneous increase of RSAM and standard deviation (STD) (Figure 4.12). Six days in January with very high RSAM, STD and event rate are also evident, in which the explosions were not on average more frequent but perhaps stronger. February, on the other hand, shows scattered values of all three parameters, suggesting significant alterations in the volcanic activity that changed the frequency of explosions and the overall seismic energy. The lower event rate and higher STD observed in March 2005 suggest that the explosions became less frequent but the energy released by such outgassing activity was somehow stronger. April 2005 shows similar characteristics to January, but with more episodes of long-lasting tremor bands of higher amplitude.

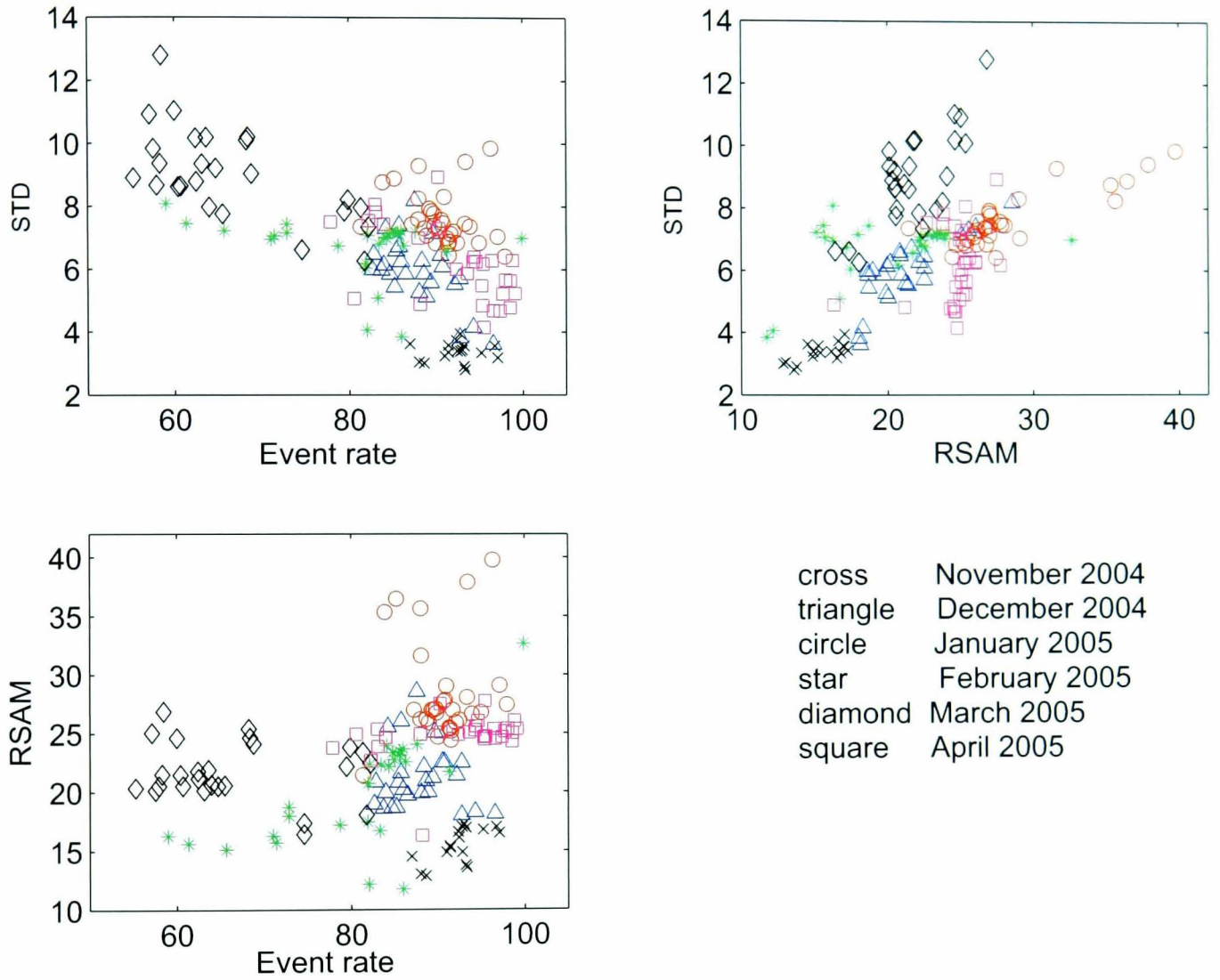

Figure 4.12: Variation in the statistical parameters of the seismic tremor between November 2004 and April 2005. Every month was represented with a distinct symbol. The event rate, RSAM average and standard deviation (STD) were calculated with a moving window of 15 minutes duration and step of 10 minutes. The data points correspond to the daily average of these parameters.

4.4 Measurements of magma degassing at Villarrica volcano

4.4.1 SO_2 flux measurements

Despite the persistent passive degassing exhibited for more than 20 years, measurements of gas composition and emission rates have not been made regularly at Villarrica volcano. Witter *et al.* (2004) and Witter and Calder (2004) contributed most of the data available on SO_2 fluxes and on the gas composition of the plume. They measured sulphur dioxide fluxes using ground-based correlation spectroscopy (COSPEC) in early 2000 and 2001. For this work, the new ultraviolet spectrometer (UVS) known as FLYSPEC (Horton *et al.*, 2006) was utilised. The FLYSPEC, and another UVS known as mini-DOAS (Galle *et al.*, 2002), share and improve upon the capabilities of the traditional COSPEC (Elias *et al.*, 2006). The new UVS are smaller, lighter, cheaper, and easy to automate for specific tasks in the field (e.g. Edmonds *et al.*, 2003). The hardware design of this UVS is based on fore-optics, electronics, the USB2000 ultraviolet spectrometer from Ocean Optics, and a computer for recording and processing of the acquired spectra. See Galle *et al.* (2002); Horton *et al.* (2006); Elias *et al.* (2006); Edmonds *et al.* (2003) and references therein for more details on the design and capabilities of these instruments. The procedure for gas concentration retrieval is based on Differential Optical Absorption Spectroscopy (DOAS) (Platt, 1994), and has been described in Horton *et al.* (2006), Elias *et al.* (2006) and in Appendix A. Software designed specially for FLYSPEC allows the user to calibrate the instrument in the field and to get real-time SO_2 path-length concentrations. The theory and algorithm to process the raw spectral data, from which the SO_2 path-length concentration is obtained, is described in Appendix A.

In order to estimate the SO_2 flux from Villarrica volcano, ground-based traverses were carried out on the roads that surround the volcano, between 10 and 20 km away from the crater (Figure 1.1). These traverses were performed on six days between November 2004 and January 2005, and on three days in January-February 2006 (Table 4.3). Measurements on the southeast side of the volcano, that coincide with the direction of the prevailing winds, could not be completed owing to the unsuitable conditions of the road for traverses; those measurements yielded lower integrated values of total gas concentration than those obtained on other segments of the road where the complete plume could be measured, and so they were not included in this work. The calibration of the FLYSPEC instrument was performed using a pair of calibration cells with concentrations 438 and 1504 ppm m and, on some occasions,

was additionally complemented with calibration cells of 170 and 704 ppm m. An example of these measurements is depicted in Figure 4.13. Note the good definition of the plume and low levels of transverse dispersion on that day.

The estimation of plume velocity is one of the primary sources of error in SO_2 flux measurements (Stoiber *et al.*, 1983). For this work, the National Centers for Environmental Prediction (NCEP) Reanalysis data (Kalnay *et al.*, 1996), provided by NOAA-CIRES (Climate Diagnostics Center, Boulder, Colorado, USA; available at http://www.cdc.noaa.gov/), were used for wind velocity estimates (Table 4.3). These estimates are generated by using a state-of-the-art analysis system to perform data assimilation using past data from numerical models as well as from direct observations of atmospheric conditions (Kalnay *et al.*, 1996). Comparison of our observations of plume dispersion and wind direction obtained from the NCEP Reanalysis data show very good agreement. At Villarrica volcano, a few estimates of plume speed were made by recording the movement of the plume with a digital photo-camera up to 5 km away from the crater. The comparison of these estimates with the interpolated wind field extracted from the NCEP Reanalysis data yielded differences of less than 50% in wind speed. However, it is not possible to accurately quantify the error using this method. Therefore, for these results I estimate an overall error of 10%-40%, similar to those considered in previous studies that performed similar methodologies for SO_2 flux measurements (Stoiber *et al.*, 1983; Kyle *et al.*, 1994; Williams-Jones *et al.*, 2003; Witter *et al.*, 2004; Rodríguez *et al.*, 2004). It is worth noting that, in any reported gas flux estimate lacking direct measurement of plume speed, this error can be much higher (Rodríguez *et al.*, 2004; Williams-Jones *et al.*, 2006).

4.4.2 Results and correlation between SO_2 flux and RSAM

Sulfur dioxide emitted from the crater of Villarrica volcano during November 2004 to January 2005, on individual traverses, ranged between 180 and 1500 metric tonnes per day (Mg/d) (Table 4.3, Figure 4.14). Daily averages ranged between 260 and 1300 Mg/d; that is a 5-fold difference. These values are clearly higher than those obtained in previous studies (in 2000-2001 and 2003; Witter *et al.*, 2004; Mather *et al.*, 2004). During the period January-February 2006 the gas fluxes were considerably lower, with daily averages no higher than 300 Mg/d. These new results highlight the variability of gas emissions at Villarrica volcano. Further, they were obtained at periods with different levels of activity, which contributes to a more representative analysis and correlation with seismicity and the observable activity of

Table 4.3: Summary of the results of ground-based traverses carried out to estimate SO_2 emissions [Mg/d] at Villarrica volcano, along with RSAM averages for the same periods. The wind speeds [m/s] utilised in this work for the calculation of SO_2 fluxes are also included.

Date	RSAM			SO_2 flux			Wind	No. runs
	min	mean	max	min	mean	max	speed	
February-March 2000 [a]								
29 Jan	14.7	15.9	17.6		178			1
30 Jan	12.3	13.6	14.8	327	353	379		2
02 Feb	13.5	14.9	16.2	203	274	338		6
05 Feb	14.6	17.6	19.5	95	209	352		11
07 Feb	14.9	16.5	19.8		121			1
13 Feb	14.8	16.4	17.9	177	204	231		2
14 Feb	13.4	16.1	20.1	126	151	195		7
03 Mar	12.9	14	15.1	127	149	163		5
07 Mar	11.9	13.7	17.8		174			1
18 Mar	11.5	13.1	15.8	241	374	614		3
21 Mar	10	12.2	14.3	429	694	1115		8
April-June 2000 [b]								
01 Apr	12.3	15.4	18.3	152	269	333		9
04 May	9.3	11.2	12.7	47	171	298		7
01 Jun	9	10.2	11.6		80			1
January-February 2001 [a]								
15 Jan	12.2	17.3	22.8	87	118	176		8
25 Jan	20.9	24.6	30.3	257	441	961		6
28 Jan	22.2	24.7	28.6	324	564	705		7
02 Feb	24.5	28.9	30.5	565	732	939		7
February 2003 [c]								
08 Feb		15.1		277	397	518		2
12 Feb		15.1		190	281	363		4
November 2004								
10 Nov	12.0	14.5	17.8	178	261	356	2.5	10
January 2005								
13 Jan	23.4	28.3	33.4	553	735	993	10.5	6
15 Jan	32.4	37.6	42.9	1176	1299	1482	11.0	4
17 Jan	36.5	40	44.6	706	951	1080	6.2	4
19 Jan	21.8	26.5	30	384	603	742	9.1	6
24 Jan	22.6	26.7	34.2	772	996	1164	10.0	4
January-February 2006								
17 Jan	6.2	6.8	7.5	78	122	154	2.6	8
09 Feb	8.3	9.2	10	233	262	343	3.0	6
13 Feb	9.6	11.2	12.5	86	149	232	4.5	4

[a] Gas data from Witter *et al.* (2004). They used a COSPEC.
[b] Gas data from Witter and Calder (2004). They used a COSPEC.
[c] Gas data from Mather *et al.* (2004). They used a mini-DOAS. RSAM values from 12 November 2004.

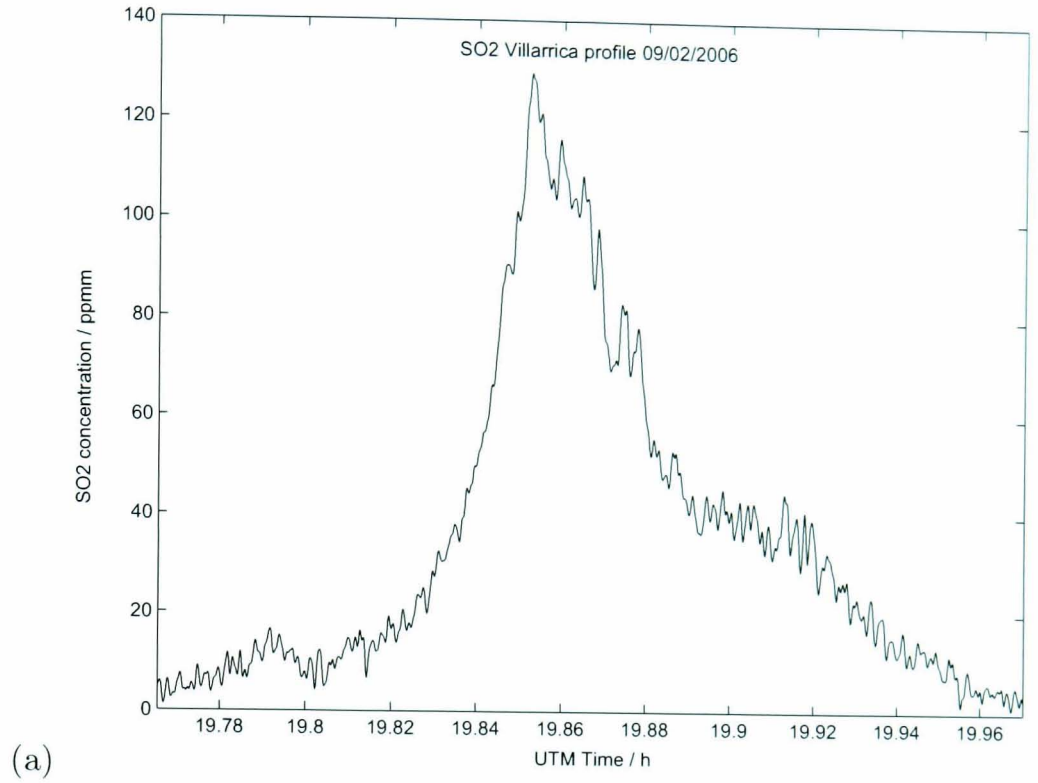

(a)

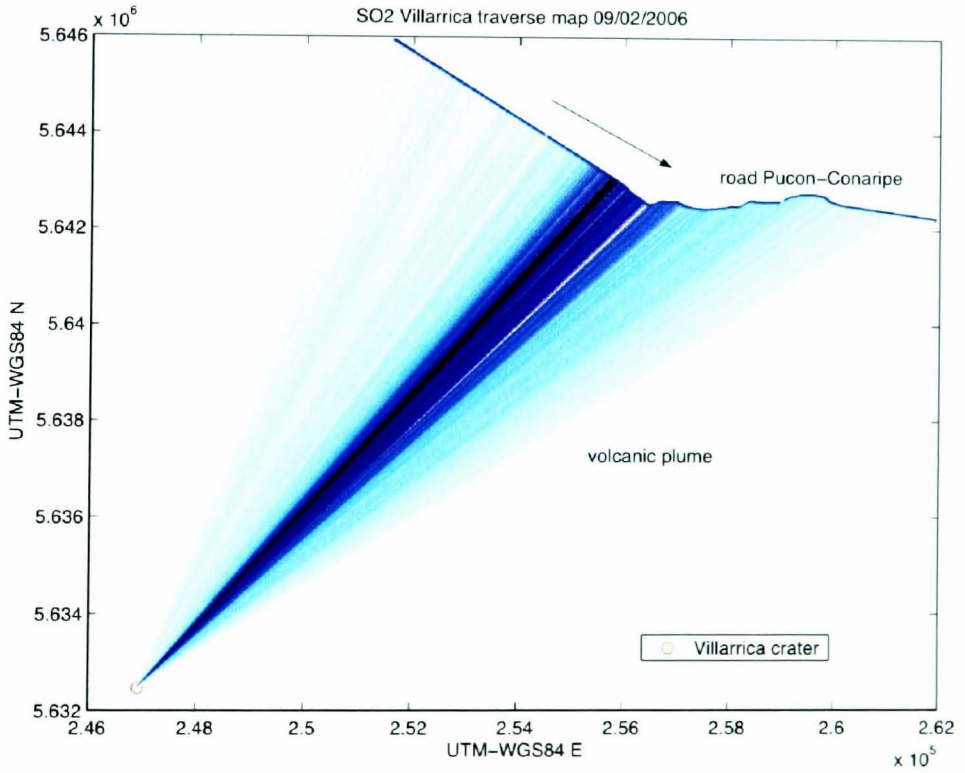

(b)

Figure 4.13: Example of the measured (a) SO_2 path-length concentration profile and (b) map of a car traverse carried out to the northeast of Villarrica volcano. In the map, lines connecting the road and the crater, whose darkness is proportional to the gas concentration, were drawn to represent the SO_2 column abundance of the plume.

the lava lake. The highest SO_2 flux measured coincides with high levels of activity on 15–17 January 2005 and high values of RSAM. Conversely, the lowest fluxes were measured during periods of background (low) levels of volcanic activity: February–March 2000, February 2003 and January–February 2006 (Figure 4.14).

Considering SO_2 emission rates of 200-500 Mg/d as representative of background levels of volcanic activity, degassing at Villarrica is lower than at similar open-vent systems such as Masaya (350–1800 Mg/d, Duffell *et al.*, 2003), Stromboli (300–1200 Mg/d, Allard *et al.*, 1994), Yasur (216–1665 Mg/d, Bani and Lardi, 2007), and Pacaya (350–2400 Mg/d, Rodríguez *et al.*, 2004), but higher than Erebus (16–71(up to 230) Mg/d, Kyle *et al.*, 1994). (Andres and Kasgnoc, 1998, reported time-averaged values of 790, 730, 900, 510 and 79 Mg/d for Masaya, Stromboli, Yasur, Pacaya and Erebus, respectively.) It is noteworthy that the total emission of sulfur dioxide is subject to the variations in SO_2 fluxes that these volcanoes can manifest during periods with different levels of activity. For instance, at Yasur and Villarrica the emission of sulfur dioxide can exhibit more than a 5-fold increase between low and high activity phases.

Measured SO_2 emission rates of individual traverses exhibit a high variability on any particular day (Table 4.3). These fluctuations are the consequence of the combination of four phenomena: 1) the unsteady emission from the lava lake, in part owing to the concurrence of 'passive' and explosive outgassing, 2) accumulation of gas between the magma free surface and the spatter roof, 3) the gas plume-air turbulent mixing and circulation caused by the combination of the rise of the thermal plume and wind velocity fluctuations inside the crater, and 4) non-uniform dispersion of the gas plume between the crater and the location where it is measured. In addition, a single traverse spans a time period in which the transport and dispersion of the gas plume continues and, therefore, the final gas column-abundance profile measured might not be representative of the actual plume cross-section at a specific time. All these variables contribute to the scattered results of daily SO_2 flux measurements.

SO_2 flux data acquired herein (2004-2006) complemented by available measurements from previous studies (Witter *et al.*, 2004 and Witter and Calder, 2004, in 2000-2001; Mather *et al.*, 2004, in 2003) show a good positive correlation with seismic amplitude (RSAM) (Table 4.3, Figure 4.14). Similar to gas flux measurements, the one-hour averaged RSAM (calculated from 9 to 21 hours, local time) exhibits daily fluctuations. These variations in seismic amplitude are explained by the occurrence of banded tremor and changes in the frequency, length and amplitude of the higher amplitude seismic transients. In particular, on days when

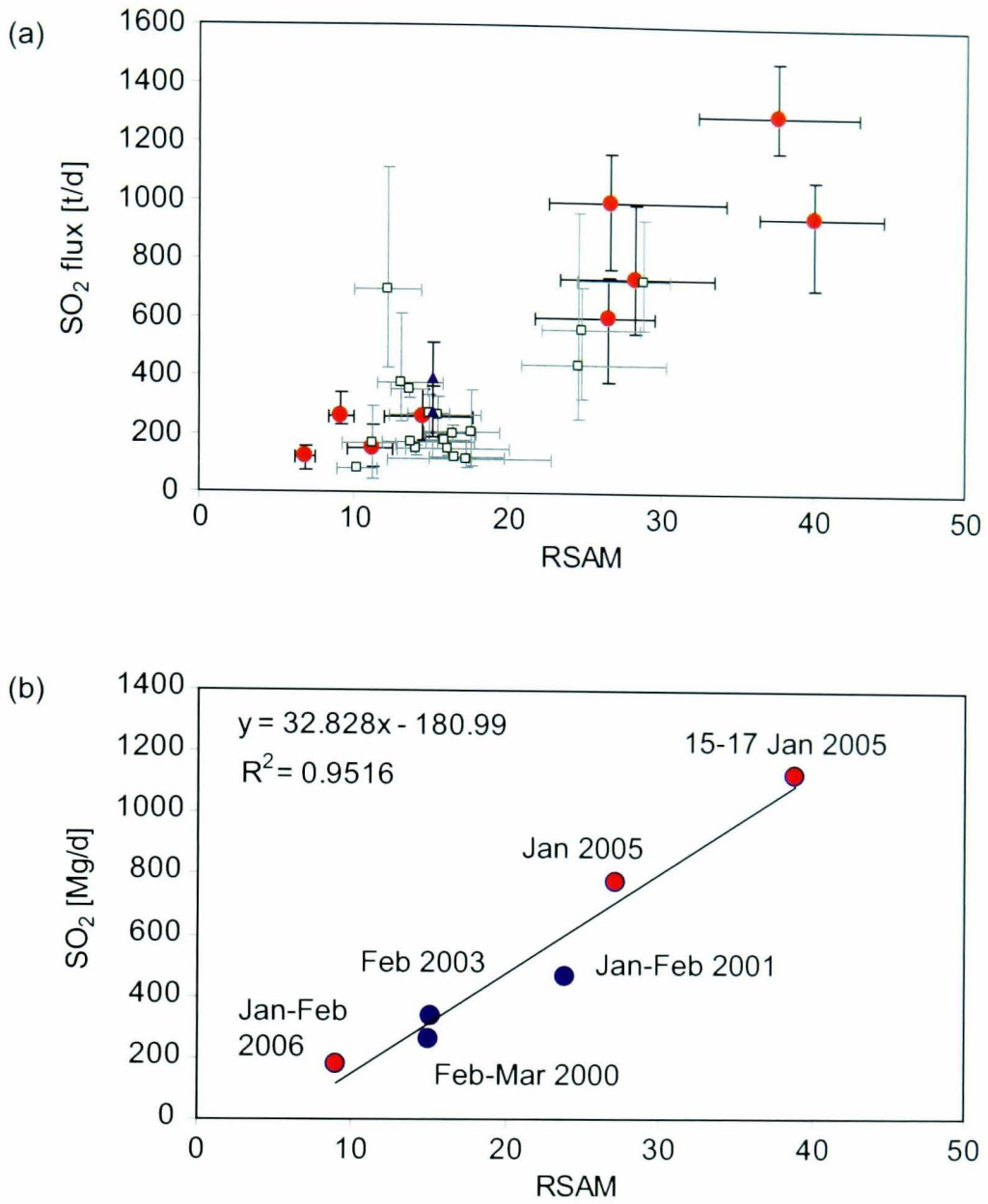

Figure 4.14: Correlation between RSAM and SO_2 flux observed at Villarrica volcano. (a) Daily averages; the vertical and horizontal bars show the minimum and maximum for individual traverses and hourly RSAM, respectively (Table 4.3). Square symbols from Witter *et al.* (2004) and triangles from Mather *et al.* (2004). (b) Average seismic and gas data for different periods (of a few days to weeks) with available SO_2 flux measurements (Table 4.2).

Table 4.4: Time averaged SO_2 emissions [Mg/d] at Villarrica volcano alongside RSAM averages for selected periods, and the number of days over which the average was made.

Period	RSAM	SO_2	No. days
Feb-Mar 2000	14.9	263	12
Jan-Feb 2001	23.9	464	4
Feb 2003	15.1	339	2
Jan 2005	27.1	778	3
15-17 Jan 2005	38.8	1125	2
Jan-Feb 2006	9.1	178	3

the volcano showed elevated levels of activity (e.g. 13, 15, 17 January 2005), as recognized by visual observations and high RSAM values, the emission of SO_2 was consistently higher (Figure 4.14a). This relation establishes a strong link between the generation of seismic tremor and outgassing activity. Moreover, variations between minima and maxima of RSAM and SO_2 fluxes observed in Figure 4.14a also seem to be correlated, with smaller variations during periods of low activity (RSAM <15) and greater variations in periods of higher gas emissions. Similar correlations between SO_2 emissions and seismic amplitude have been found at Mount Etna (Leonardi *et al.*, 2000) and Yasur (Bani and Lardi, 2007) volcanoes.

Selected time periods in which Villarrica volcano exhibited sustained levels of activity allowed a better correlation between degassing and seismicity (Figure 4.14b, Table 4.4). During these periods, the activity observed at the crater remained unchanging along with the RSAM values. Assuming a uniform emission of SO_2 for each one of these periods, the average of daily results improves the precision of the measurements. Hence, a linear relationship between SO_2 flux and RSAM is obtained (Figure 4.14b):

$$SO_2\,[Mg/d] = 32.8 \cdot RSAM - 181 \tag{4.2}$$

The negative value of the ordinate-intercept (second value on the right hand side) of this linear equation implies a lateral displacement of the regression line to the right, meaning an abscissa-intercept (at SO_2=0 Mg/d) of 5.5 RSAM units. Even though this value represents very low levels of volcano seismicity, it is within 30% of the RSAM values measured during background activity. Some plausible explanations for this displacement are: 1) tremor is not only caused by outgassing activity but also by another volcano-related or non-volcanic phenomenon, 2) towards very low levels of outgassing and tremor magnitude the relationship turns non-linear and the curve goes through the origin, or 3) this relationship is non-linear but there is not enough data (or it is not accurate enough) to define it. As a first approximation, this relationship certainly serves as an estimation of the gas emitted from Villarrica volcano based on measurements of tremor magnitude.

4.5 Discussion and conclusions

4.5.1 Volcanic activity and crater morphology

Currently, the interior of the crater is characterized by a spatter roof built above the surface of the lava lake, which constitutes the bottom of the crater. The descriptions presented herein illustrate how the depth and morphology of the spatter roof in the crater of the volcano change according to the degree of volcanic activity. Elevated or increasing activity levels are characterized by scoria terraces, spatter cones or pahoehoe lavas flooding the crater. The roof itself is very unstable and can experience major changes in morphology on a time span of hours to days. Low levels (or decreasing levels) of volcanic activity are commonly linked to a partly or totally collapsed roof, deep crater floor (perhaps with no roof), or a deep funnel shaped crater with no magmatic activity directly visible from the crater rim. The latter case implies that the top of the magma column is more than 100-150 m deep below the crater rim. Hence, the position, morphology and texture of the roof can give important information regarding changes in the depth of the magma column, and the intensity and type of activity taking place during the previous few days to weeks.

The visibility of the lava lake is not directly related to the level of activity but instead to the depth of the lava free–surface, morphology of the spatter roof, and the occurrence of roof collapses. Although strong explosions can affect the stability of the overlying roof, visual observations suggest a poor correlation between its collapses and the magnitude of explosions. However, the morphology of the spatter roof does have an effect on the apparent magnitude of explosions: they look stronger when the opening is big, by allowing pyroclastic material to be ejected freely out of the vent. Explosions also look stronger when a narrow cone-shape vent is built on top of the spatter roof during elevated levels of activity, probably owing to the high level of the lava lake.

4.5.2 Summary of the recent activity

The activity at the crater of Villarrica volcano shows fluctuations on the scale of months to years. Slow increase in activity at Villarrica, as observed during November 2004 and May 2005, exhibited a rise in the magma column of at least 60 m reflected in the position of the spatter roof, higher SO_2 fluxes (I measured up to 1500 tons/day), and an increase in the frequency and strength of strombolian explosions. This evolution was also evidenced in the higher tremor amplitude as well as the presence of VT-earthquakes. Hence, typical

background (low) levels of activity correspond to a lava lake located >80 m below the crater rim, small and/or blocky morphology of the roof, seismic amplitude (RSAM) lower than 25 units, few VT-earthquakes, and daily averages of SO_2 emissions lower than 600 tons/day. Elevated levels of activity show fluctuations in the height of the magma column, changes in the morphology of the spatter roof, and changes in the characteristics of the bubble bursting activity. Available SO_2 flux data also suggest an increase in gas emission rates during periods of elevated activity.

It is noteworthy that the historic record of the activity of Villarrica volcano, comprising more than 100 years, mentions gas plume emissions, active lava lakes and strong explosions before the eruptions. That is an important consideration on the longevity of Villarrica as an open vent system.

4.5.3 The relationship between outgassing and seismicity

Although we have no geophysical data appropriate to study the seismic source of the tremor, we have presented evidence that supports the relationship between the seismicity and volcanic activity observed at the crater:

1. the close correlation between visual observations of bursting events and rapid changes in tremor amplitude (transient events) (Figure 4.9a),
2. the predominance of low frequencies within the tremor (Figures 4.4, 4.6),
3. the consistent frequency content of the low and higher amplitude tremor (Figure 4.9b), and
4. the positive correlation between RSAM and SO_2 flux (Table 4.3, Figure 4.14).

Much work carried out at other basaltic open-vent volcanoes supports the link between tremor and outgassing activity (Ripepe *et al.*, 1996; McGreger and Lees, 2004; Ripepe *et al.*, 2001a; Métaxian *et al.*, 1997; Ripepe, 1996; Ripepe *et al.*, 2002). For instance, by using small aperture seismic arrays, Métaxian *et al.* (1997) analysed the wavefield of the tremor at Masaya volcano. At the time of their study, lava lake activity was characterised by minor fountaining and audible outgassing. They concluded that the source of the tremor was surface waves linked to superficial magmatic activity in Santiago crater. Ripepe *et al.* (2001a) combined infrasound and seismicity to study a phase of vigorous strombolian activity at Mt Etna, and concluded that the tremor was generated by a superposition of small point sources, lasting

1-2 s, due to pressure flux instability induced by magma degassing in the shallow portion of the magma column. At Stromboli, combination of seismicity with infrasound and thermal recording has demonstrated that the source of tremor resides in the explosive outgassing activity (Ripepe *et al.*, 1996; Ripepe and Gordeev, 1999; Ripepe *et al.*, 2002).

The results presented herein on the activity of Villarrica volcano yield complementary insights into the results obtained from the analysis of tremor source at similar open-vent volcanoes, which provide the rationale for the interpretation of our data. Therefore, we suggest that the tremor at Villarrica volcano, in particular the higher amplitude transients, is produced by surface waves resulting from gas ascent and outgassing activity taking place at the top of the magma column.

4.5.4 Volcano monitoring

Seismic tremor is the most common and continuous type of seismicity related to the activity of Villarrica volcano. Its amplitude, evaluated as RSAM units, has been shown to correlate well with the level of the activity observed at the summit. For instance, the different features shown in Figure 4.4 between January and April 2005 correlate with the increase in activity and evolution of the spatter roof (Table 4.1). Changes in seismic amplitude were also part of the elevated activity of 1999 (Calder *et al.*, 2004), as well as of the rapid changes in the level of the magma column observed at the end of 2000 (Ortiz *et al.*, 2003). In addition, the extraction of statistical parameters describing the tremor waveform has proved to be a good alternative to track changes in seismicity and volcanic activity (Section 4.3.5).

The abnormal sequence of events that took place in 2000 (Ortiz *et al.*, 2003) is an example of variations in the type of volcanic activity accompanied by clear changes in the frequency distribution of the seismicity. These results and our analysis of the activity during November 2004–April 2005 show that the amplitude and frequency distribution of the tremor can be good indicators of the variations in the activity of Villarrica volcano. However, during this time the relationship between the variations in frequency content and type or evolution of the volcanic activity was not straightforward. We hypothesize that elevated high frequencies (2.15–5.5 Hz) are caused by a rise in the level of the lava lake, perhaps interacting strongly with the spatter roof. Support for this idea comes from the positive correlation between gas flux and seismic amplitude that is in accordance with stronger levels of degassing, and therefore, with vertical expansion of the magma column. Moreover, during one of the periods that exhibit high frequencies, 15-19 January, instability and collapse of the roof was directly

observed.

Volcano-tectonic (VT) earthquakes are uncommon in the background seismicity at Villarrica volcano. VT-type seismicity is the result of rock failure caused by an increase in pressure within the magmatic system that is transferred to the country rock (McNutt, 2005). Such a pressure increase can occur due to new inputs of magma into the system and/or increasing degassing. The eruption in 1971, which involved the opening of a fracture in the upper part of the edifice and the generation of fissure-fed lava flows, is an example of this pressure rise and subsequent magma intrusion. If this fracturing occurs at deeper levels, it can lead to emplacement of magma as dikes or sills, which may reach the surface and initiate a flank eruption. Furthermore, because of the open state of the system, the occurrence of a shallow magma intrusion or increasing degassing will be accompanied by variations in the activity observed at the summit. The elevated SO_2 flux measured during January and the appearance of VT earthquakes during March-April 2005, were strong evidence of an increase in the pressure of the system related to stronger degassing. It is not possible to know, however, how close the volcano was from starting a renewed eruptive episode. This anomalous episode did not last for long, as the VT earthquakes vanished in June and towards the end of July the activity at the crater declined to background levels (Table 4.4).

In addition to seismic characteristics, visual observations of the activity in the crater give valuable information regarding the level of the magma column and its variations, as well as the style of activity taking place. Some important parameters worth considering are the position and morphology of the spatter roof, the texture of its surface, presence and texture of new material on the crater rim, frequency of the big explosions and the height above the crater floor that ejected pyroclasts can reach. Furthermore, continual measurements of SO_2 fluxes would be a significant contribution to the monitoring of degassing levels at Villarrica. The correlation of these gas data with seismicity and visual observations of activity in the crater offer a fuller appreciation of the current state and variations of the volcanic activity, and help to understand the evolution of the magmatic system.

Chapter 5

Convection of immiscible fluids in narrow conduits

5.1 Introduction

Basaltic systems are characterised by relatively large chambers and long feeding conduits where magma ascends from a deep source to the surface. Due to the difference in density between the melt and the surrounding country rock, the general or average magma transport is upwards. However, within the chamber and plumbing system there is no reason to restrict this movement to any particular direction. For example, many investigations in the field as well as in the laboratory support the idea of convection of magma in large reservoirs (Sparks *et al.*, 1984; Weinstein *et al.*, 1988; Tait and Jaupart, 1989; Rudman, 1992; Koyaguchi *et al.*, 1993; Simakin and Botcharnikov, 2001). This convection can be the result of crystalisation (e.g. Brandeis and Jaupart, 1986; Worster *et al.*, 1990), gas exsolution (e.g Cardoso and Woods, 1999; Simakin and Botcharnikov, 2001), or new inputs of magma (e.g. Snyder, 2000), among other causes.

An interesting case where convection of magma is likely to take place is in open basaltic systems such as Villarrica, Mount Etna, Stromboli and Mount Erebus. In these type of volcanoes, density and viscosity differences arise owing to cooling and degassing of magma, generating natural convection driven by buoyancy contrast. Typical dimensions of the feeding conduits at basaltic volcanoes are lengths of several hundreds to thousands of metres and radii of just a few to tens of metres. Hence, the plumbing in which magma flows has very high aspect ratios. Since natural convection in long dykes or cylindrical enclosures can involve a great variety of three-dimensional phenomena, such as stratified flow, slug flow,

helical flow, turbulent flow (e.g. Arakeri *et al.*, 2000; Debacq *et al.*, 2003; Mandal *et al.*, 2007; Huppert and Hallworth, 2007), the understanding of this process requires the investigation of more simplified systems.

The scope of this chapter is to present a theoretical analysis of the dynamics of convection of basaltic magmas in narrow conduits. Flow instabilities shall be briefly analysed as they have an effect on the fluctuations and total out-flux of gas. Other important variables, such as temperature and crystalisation rate, are not incorporated directly in this analysis in order to keep the model as simple as possible. However, temperature variations are implicitly considered as the source of changes in density and viscosity of the melt.

The assumptions considered to simplify the problem are that magma convects in a laminar regime inside a vertical cylinder. This is the same problem investigated by Kazahaya *et al.* (1994) and Stevenson and Blake (1998) to estimate the rate of magma flow, degassing and radii of the conduits in volcanic systems. They assumed that the fresh gas-rich magma ascended in the core of the pipe and that degassed and more dense magma descended in the annulus. The equations and dynamics of core-annular flow in vertical pipes have been analysed previously by Hickox (1971), Arney *et al.* (1993) and Huppert and Hallworth (2007), among others. In this thesis, the case of tilted tubes and different flow patterns will be also investigated, an aspect of the problem which has not been addressed in relation to volcanic systems before. Specific assumptions will be mentioned along with the formulation and solution of the problems. Section 5.2 analyses, from an analytical point of view, the characteristics of steady core–annular flow in a vertical pipe, followed by a dimensional analysis of the problem and the specification of dimensionless coefficients (Section 5.3). Section 5.4 describes the experiments carried out in the laboratory with the aim of investigating some of the dynamics of fluid convection in narrow tubes, in vertical and tilted pipes, and to obtain flow rate measurements that constrain the amount of magma degassing. Section 5.5 takes advantage of the two-fluid model approach to find solutions for the laminar core–annular flow in vertical pipes and laminar stratified flow in tilted pipes, both of which constrain the fluid flow rate found in the experiments. Finally, Section 5.6 summarises and discusses the most relevant results of this chapter. Applications of the results to Villarrica and Stromboli volcanoes are presented in Chapter 6.

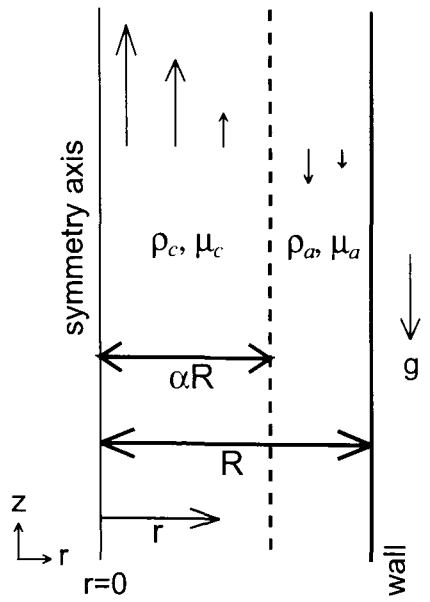

Figure 5.1: Definition of the geometry in cylindrical coordinates and the parameters for the problem of laminar convection in a vertical tube.

5.2 Steady-state laminar core-annular flow in vertical pipes

In order to calculate the velocity profile and volumetric flow rate of the convecting magma, I consider the problem of two-fluid viscous laminar flows within a vertical cylindrical tube under steady-state conditions. The geometry and variables of the problem are shown in Figure 5.1. It is necessary to specify a tube length large compared with the tube radius, so that end-effects are unimportant and not considered throughout the analysed geometry. Only Newtonian fluids with constant viscosity and density are considered (isothermal). Surface tension effects are neglected. An axisymmetric solution where one fluid flows inside (inner fluid) and the other next to the wall (outer fluid) surrounding the inner fluid is assumed. The following formulation is valid only in the case of flow of immiscible and incompressible fluids flowing with straight vertical streamlines. This is achieved at low Reynolds number[1]. Small variations in the last conditions, however, do not change the solution greatly.

5.2.1 Velocity profiles

The general solution of the Navier-Stokes equations under the previous assumptions is, in cylindrical coordinates (e.g. Batchelor, 1967; Hickox, 1971):

$$v(r) = -\frac{P}{4\mu} r^2 + C_1 \ln r + C_2 \tag{5.1}$$

[1]The transition from laminar to turbulent flow in pipes is Re~2100 in the case of one isoviscous liquid flowing in the pipe (Massey, 2006). However, Blake and Campbell (1986) showed that in concurrent liquid-liquid flow of miscible fluids with similar density and variable viscosity, the transition to turbulence is achieved at much lower Re numbers (Re=3 in their experiments). Thus, the transition laminar-turbulent flow in buoyancy driven counter-current flows needs to be determined.

where v is the vertical velocity, r the radial distance, $P = -dp/dz - \rho g$ is the combination of pressure gradient and gravitational force per unit length[2], and μ is the viscosity of the fluid. The constants C_1 and C_2 need to be determined by using the appropriate boundary conditions. Equation 5.1 can be obtained from the general continuity and momentum equations in cylindrical coordinates using the conditions of steady-state axisymmetric flow, or directly through a stress balance at the interfaces between liquids and at the wall of the cylinder[3].

In the particular case of only one fluid of constant density and viscosity the solution of Equation 5.1 is the well known Hagen-Poiseuille flow (Bird *et al.*, 1960; Massey, 2006), which exhibits a parabolic velocity profile:

$$v^{HP}(r) = P\frac{R^2 - r^2}{4\mu} \tag{5.2}$$

In the two-fluid problem the solution of Equation 5.1 is obtained separately for both fluids considering the following boundary conditions: the velocity of the inner fluid is finite at the cylindrical axis ($v(r = 0) < \infty$), continuity of shear stresses and velocity across the interface, and zero velocity of the outer fluid at the wall. Hence, the velocity profile for the two-fluid problem becomes

$$v_c(r) = \left[\frac{\Delta p}{h} - \rho_c g\right]\frac{(\alpha R)^2 - r^2}{4\mu_c} + v_a(\alpha R) \qquad 0 \le r \le \alpha R \tag{5.3}$$

$$v_a(r) = \left[\frac{\Delta p}{h} - \rho_a g\right]\frac{R^2 - r^2}{4\mu_a} - \frac{\Delta\rho\, g}{2\mu_a}(\alpha R)^2 \ln\left(\frac{r}{R}\right) \qquad \alpha R \le r \le R \tag{5.4}$$

where the superscripts c and a refer to the core and annular fluids, respectively, μ is the viscosity, ρ the density, R is the radius of the cylinder, αR is the radius of the core liquid flow and defines the position of the interface, $\Delta\rho = \rho_a - \rho_c$ is the density difference, $\Delta p = p_b - p_t$ is the difference between the pressure at the bottom and top of the fluid column[4], h the depth (length) of the column, and g is the absolute value of gravity.

It is clear that the first term in the right-hand side of Equations 5.3-5.4 is the Hagen-Poiseuille velocity (Equation 5.2) for the corresponding radial section of the cylinder. Then,

[2]It can also be seen as the variation with length of the modified (or piezometric) pressure, $p^* = p + \rho g z$

[3]In this case the stress at the interface is defined by Newton's law of viscosity:

$$\tau_{rz} = -\mu\frac{dv_z}{dr}$$

where τ_{rz} is the force per unit area on z-direction perpendicular to unit area of r-direction, v_z is the vertical velocity, and μ is the viscosity of the liquid; τ_{rz} represents the flux of z-momentum in the positive r-direction.

[4]Note that $P = -\left(\frac{dp^*}{dz}\right) = \frac{\Delta p}{L} - \rho\, g$; also, $P_c - P_a = \Delta\rho\, g$.

the core fluid is the only one that develops such velocity profile (Figure 5.2). This shows that the velocity at the fluid interface is not zero. This velocity, $v_a(\alpha R) \neq 0$. depends on the positions of the fluid interface (α), pressure drop, density difference and viscosity of the annular fluid:

$$v_a(\alpha R) = \frac{P_a R^2(1-\alpha^2)}{4\mu_a} - \frac{(P_c - P_a)(\alpha R)^2 \ln \alpha}{2\mu_a} \tag{5.5}$$

When $\alpha = 1$, Equation 5.3 reduces to the Hagen-Poiseuille velocity profile (Equation 5.2). in which the core fluid occupies the whole cylinder[5].

The average velocities can be calculated by dividing the volumetric fluxes (Equations 5.11-5.12), which are obtained by integrating the velocities across the radius and angle in the cylindrical domain, by the cross-sectional area occupied by the liquids. Details of the derivation of the volumetric fluxes are given in Section 5.2.3. Hence, the average velocities for the core and annular flows are, respectively,

$$\langle v_c \rangle = \frac{P_c(\alpha R)^2}{8\mu_c} + v_a(\alpha R) \tag{5.6}$$

$$\langle v_a \rangle = \frac{1}{2} v_a(\alpha R) + \frac{(P_c - P_a)(\alpha R)^2}{4\mu_a} \left[1 + \frac{(1+\alpha^2)}{(1-\alpha^2)} \ln \alpha\right] \tag{5.7}$$

The velocity profile of the convective core–annular flow and associated momentum flux (viscous shear stress, $\tau_{rz} = -\mu\, dv_z/dr$) are shown in Figure 5.2. In these examples the unknown pressure gradient has been modeled with two approximations: 1) by setting the position of the interface (α) at 0.6 of the radius, and 2) with the value that maximizes the flow rate. The first approximation is based on the experimental results of Stevenson and Blake (1998) and a relationship between α and the pressure drop (Equation 5.15) which will be presented in the following section of this chapter. The second approximation has been considered in models of lubricating pipelines of water and oil (Joseph and Renardy, 1993b), and it has been proposed by Huppert and Hallworth (2007) to explain their experimental results. Huppert and Hallworth (2007) pointed out that since in steady-state flow the dissipation equals the rate of release of potential energy (which is proportional to the flux of fluid),

[5]Equation 5.4 also shows that the velocity of the annular fluid is different from that in steady-state laminar flow in a cylindrical annulus ($v^{annular}$, Bird *et al.* 1960) with fixed walls:

$$v_a(r) = v^{annular} + \frac{(1-\alpha^2)}{\ln \alpha} \ln\left(\frac{r}{R}\right) \left[1 + \frac{v_a(\alpha R)}{(1-\alpha^2)} - \frac{P_a R^2}{4\mu_a}\right]$$

In part, this is consequence of the non-zero velocity of the annular liquid at the interface with the core liquid.

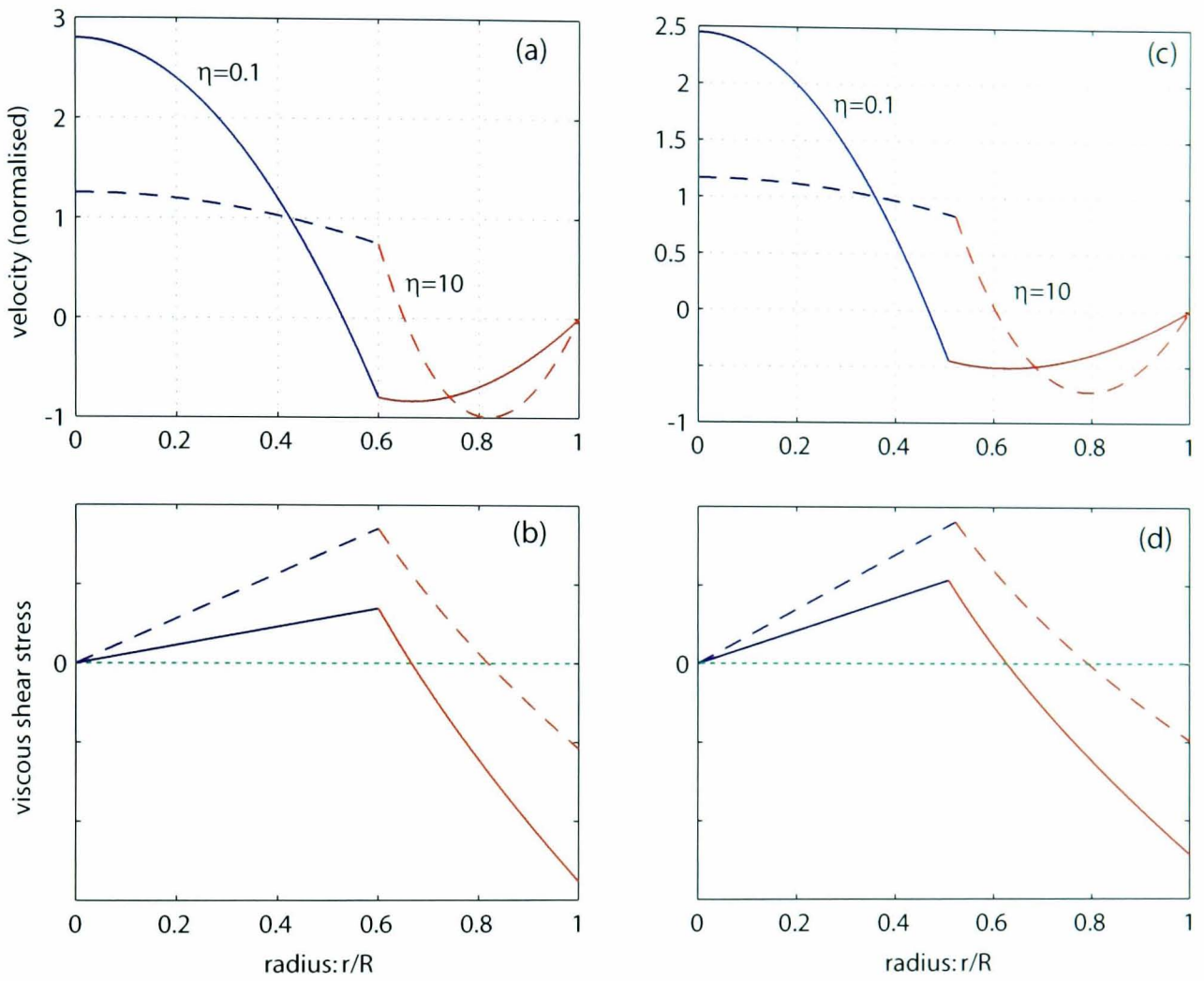

Figure 5.2: Examples of velocity profiles (a, c) and shear stresses (b, d) in counter–current core–annular flow with different density and viscosity contrast. The velocities are normalized by the average velocity of the core fluid $\langle v_c \rangle$ (Equation 5.6). Velocity profiles in (a) with the corresponding shear stresses in (b) calculated for a fixed position of the interface at $\alpha = 0.6$, whereas the profiles in (c,d) correspond to the solutions that maximize the volumetric flux (Q). Two examples, with $\eta = \mu_c/\mu_a = 0.1$ (solid line) and $\eta = 10$ (dashed line), are shown in each case. The densities used in all the examples are $\rho_c = 2250, \rho_a = 2500\ kg/m^3$. Setting an inverse density contrast, that is with the annular fluid being the lighter one, the resulting profiles are symmetric along the horizontal line at zero. In (a, b) the parameters are: for $\eta = 0.1, \alpha = 0.6, \phi = 0.189, \langle v_c \rangle = 28.96$; for $\eta = 10, \alpha = 0.6, \phi = 0.464, \langle v_c \rangle = 50.38$. In (c, d) the parameters are: for $\eta = 0.1, \alpha = 0.508, \phi = 0.344, \langle v_c \rangle = 47.02$; for $\eta = 10, \alpha = 0.522, \phi = 0.567, \langle v_c \rangle = 72.15$. The parameters ϕ and α are defined in Equations 5.8-5.15.

the maximum flux condition is equivalent to maximise the dissipation. Several interesting features can be observed in both approximations:

- the velocity gradient changes abruptly at the interface between the two liquids;
- in the case of maximum flow rate, the position of the interface is nearly half way between the middle and the wall of the pipe (regardless of the value of the viscosity ratio);
- the velocity at the interface is lower than zero with $\eta = 0.1$ and greater than zero with $\eta = 10$, as a consequence of the drag imposed by the more viscous fluid;
- the average velocity in the case of maximum flux of fluid (Figure 5.2c) is greater than in the case of fixed position of the interface ($\alpha = 0.6$) (Figure 5.2a);
- the average velocity of the liquid flowing in the core is greater when its viscosity is greater than the viscosity of the annular liquid (when $\eta = 10$);
- the momentum flux (shear stress), which by definition is zero at the radial distance where the velocity is maximum (zero velocity gradient), exhibits one peak at the interface and another maximum (in absolute sense) at the wall;
- the shear stress at the wall is greater than the shear stress at the interface for $\eta = 0.1$, whereas the opposite is found with $\eta = 10$;
- the magnitude of the momentum fluxes are slightly greater at the interface in Figure 5.2d and slightly smaller at the wall than in Figure 5.2b.

5.2.2 Pressure drop

In general, the total pressure gradient in a liquid-liquid system (and in a two-phase flow) results from the contribution of three components due to gravity, friction and acceleration. The latter, however, is neglected here due to the steady-state of the problem. The pressure drop of flows that involve more than one phase or constituent has to be calculated with semi-empirical methods (e.g. Wongwises *et al.*, 1998). For instance, the establishment of the liquid volume fraction (related to α in this work) and pressure loss in pipes is one of the main goals in the investigation of two-phase flows (Oliemans and Pots, 2006). Likewise, viscous shear stresses at the wall of the tube and at the interface of a liquid-liquid system whose flows exhibit different velocities need to be estimated. The approach utilized to constrain such variables will be presented in section 5.5.

For convenience in the calculations, the pressure drop is expressed here as a combination of the weights of the individual liquids in the cylinder,

$$\Delta p = [\phi\rho_a + (1-\phi)\rho_c]gh \tag{5.8}$$

where ϕ is a parameter that represents the fluid weight fraction of the annular liquid. This expression is only a mathematical substitution and it does not mean any modification to the solution of the problem. A priori, the range of values that ϕ can adopt is not constrained. However, if the Hagen-Poiseuille velocity term is considered the dominant term in Equations 5.3-5.4, it follows that in order to have a convective (counter–current) flow, with the core and annular liquids flowing in opposite direction, the pressure drop within the column must range between the weight of the fluids:

$$\rho_l gh \leq \Delta p \leq \rho_h gh \qquad \rho_l \leq \rho_h \tag{5.9}$$

with the subscripts l and h representing the lighter and heavier fluids, respectively. In that case, ϕ would range between 0 and 1.

5.2.3 Volumetric flux

Assuming that this two-fluids flow is a consequence of convection within the cylinder with no loss of mass (or at least it can be neglected), and with interminable availability and influx of the two liquids at both ends of the tube, the volume of the system must be conserved and it is stated as

$$Q_c + Q_a = 0 \tag{5.10}$$

where Q_c and Q_a are the volumetric flow rates of the liquids in the core and annulus, respectively. Q_c is given by

$$\begin{aligned}
Q_c &= \int_0^{2\pi}\int_0^{\alpha R} v_c(r) r dr d\theta \\
&= \int_0^{2\pi}\int_0^{\alpha R}\left[P_c\frac{(\alpha R)^2 - r^2}{4\mu_c} + P_a\frac{R^2-(\alpha R)^2}{4\mu_a} - \frac{\Delta\rho g}{2\mu_a}(\alpha R)^2\ln(\alpha)\right] r dr d\theta \\
&= \int_0^{2\pi}\left[\frac{P_c(\alpha R)^4}{8\mu_c} - \frac{P_c(\alpha R)^4}{16\mu_c} + P_a\frac{R^2(1-\alpha^2)(\alpha R)^2}{8\mu_a} - \frac{\Delta\rho g}{4\mu_a}(\alpha R)^4\ln(\alpha)\right] d\theta \\
&= 2\pi\left[P_c\frac{(\alpha R)^4}{16\mu_c} + P_a\frac{(1-\alpha^2)\alpha^2 R^4}{8\mu_a} - \frac{P_c - P_a}{4\mu_a}(\alpha R)^4\ln(\alpha)\right] \\
&= \frac{\pi(\alpha R)^4}{8\mu_c}\left[P_c + 2\eta P_a\frac{(1-\alpha^2)}{\alpha^2} - 4\eta(P_c - P_a)\ln\alpha\right] \qquad (5.11)
\end{aligned}$$

where $\eta = \mu_c/\mu_a$ is the viscosity ratio. Q_a is given by

$$\begin{aligned}
Q_a &= \int_0^{2\pi}\int_{\alpha R}^{R} v_a(r) r dr d\theta \\
&= \int_0^{2\pi}\int_{\alpha R}^{R}\left[P_a\frac{R^2 - r^2}{4\mu_a} - \frac{\Delta\rho g}{2\mu_a}(\alpha R)^2\ln\left(\frac{r}{R}\right)\right] r dr d\theta \\
&= \int_0^{2\pi}\left[\frac{P_a}{4\mu_a}\left(\frac{R^4}{2} - \frac{R^2(\alpha R)^2}{2} - \frac{R^4}{4} + \frac{(\alpha R)^4}{4}\right)\right. \\
&\quad \left. -\frac{\Delta\rho g}{2\mu_a}(\alpha R)^2\left(\frac{R^2}{2}\ln(R) - \frac{R^2}{4} - \frac{(\alpha R)^2}{2}\ln(\alpha R) + \frac{(\alpha R)^2}{4} - \ln(R)\frac{R^2}{2} + \ln(R)\frac{(\alpha R)^2}{2}\right) d\theta \right. \\
&= 2\pi\left[\frac{P_a R^4}{16\mu_a}\left(1 - 2\alpha^2 + \alpha^4\right) - \frac{\Delta\rho g R^4\alpha^2}{8\mu_a}\left(\alpha^2 - 1 - 2\alpha^2\ln(\alpha)\right)\right] \\
&= \frac{\pi R^4}{8\mu_a}\left[P_a(1-\alpha^2)^2 + 2(P_c - P_a)\alpha^2(1 - \alpha^2 + 2\alpha^2\ln\alpha)\right] \qquad (5.12)
\end{aligned}$$

Combining Equations 5.10-5.12 we get an expression for α:

$$\left(\frac{1}{\eta}P_c - 2P_c + P_a\right)\alpha^4 + 2(P_c - P_a)\alpha^2 + P_o = 0 \qquad (5.13)$$

As pointed out previously, the values of α that solve Equation 5.13 might lie within the

space of solutions that satisfy Equations 5.8-5.9. Using ϕ to represent the pressure gradient (Equation 5.8), Equation 5.13 becomes

$$\left(\phi(1-\eta^{-1})+1\right)\alpha^4 - 2\alpha^2 + (1-\phi) = 0 \tag{5.14}$$

which is independent of the fluid densities. Hence, the position of the interface only depends on the fluid viscosity ratio, but varies with the pressure drop along the cylinder[6]. Equation 5.14 can be re-written to get an expression for the pressure drop in terms of ϕ:

$$\phi = \frac{2\alpha^2 - \alpha^4 - 1}{(1-\eta^{-1})\alpha^4 - 1} \tag{5.15}$$

The solution to this equation is shown in Figure 5.3. It is worth noticing that the volumetric fluxes of the uprising and sinking fluids (Equations 5.11-5.12) are different to the expressions presented by Kazahaya *et al.* (1994) that assume Hagen-Poiseuille flow for both fluids with zero velocity at the interface.

The expressions of the volumetric flux (Equations 5.10-5.12) are now re-arranged to obtain the following dimensionless parameters:

$$Q_c = \widehat{Q}_c\, Q^*, \qquad Q_a = \widehat{Q}_a\, Q^* \tag{5.16}$$

with

$$Q^* = \frac{\pi g \Delta\rho R^4}{8\mu_a} \tag{5.17}$$

$$\widehat{Q}_c(\phi,\alpha,\eta) = \alpha^4\left[\frac{\phi}{\eta} - 2(1-\phi)\left(\frac{1-\alpha^2}{\alpha^2}\right) - 4\ln\alpha\right] \tag{5.18}$$

$$\widehat{Q}_a(\phi,\alpha) = (\phi-1)(1-\alpha^2)^2 + 2\alpha^2(1-\alpha^2) + 4\alpha^4\ln\alpha \tag{5.19}$$

where $\widehat{Q}_c$ and $\widehat{Q}_a$ represent the dimensionless volumetric flux (normalized by Q^*) of the fluids in the core and annulus, respectively. I recall that the condition of volume conservation holds: $\widehat{Q}_c + \widehat{Q}_a = 0$. In a similar way to the velocity profile, the volumetric flux depends on the pressure drop (Δp) and position of the interface (α). The latter strongly depends on

[6]The case of upward core flow and downward annular flow means that the average velocities of the fluids must be greater and lower than zero, respectively. By imposing these conditions, it can be shown that the range of values for the pressure drop gets more restricted, and Equation 5.9 becomes

$$\rho_c g h + f_l \Delta\rho g h \leq (p_b - p_t) \leq \rho_a g h - f_u \Delta\rho g h$$

where $f_l > 0$ and $f_u > 0$ are two different functions that depend on α. Replacing the pressure drop with Equation 5.8, the last condition reduces to $f_l \leq \phi, f_u \leq 1-\phi$. However, within the space of solutions for (α,ϕ) (Equation 5.14), the pressure drop adopts the same range of values previously assumed (Equation 5.9).

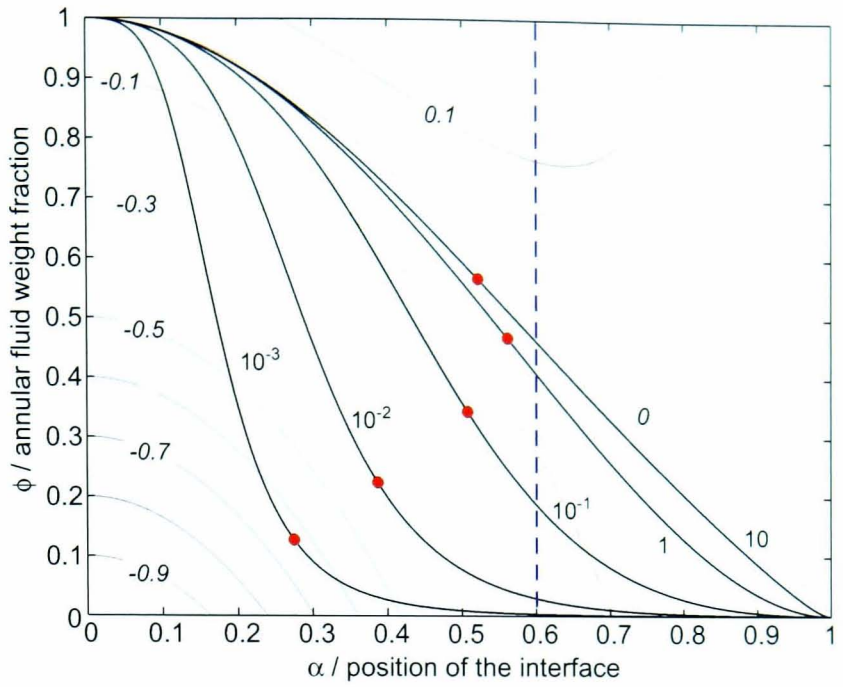

Figure 5.3: Solution of Equations 5.14-5.15 for different values of $\eta = 10^{-3}, 10^{-2}, 10^{-1}, 10^{0}, 10^{1}$ (solid dark lines). It also shows the contour lines of the dimensionless volumetric flux $\widehat{Q}_a$ (Equation 5.19) for values between -0.9 and 0.1. The dots represent the values that maximize the volumetric flux, and the vertical dashed line constrains the solution when the position of the interface at $\alpha = 0.6$ is set.

the viscosity ratio (Figures 5.3-5.4). Figure 5.4 shows the position of the interface when the volumetric flux reaches its maximum value, an idea introduced by Huppert and Hallworth (2007). It is noteworthy that in this model the position of the more dense or more viscous liquid in the pipe is not constrained. Thus, the solution presented in Equations 5.16-5.19 is valid for the cases when the rising (lighter) fluid flows in the core or annulus of the tube.

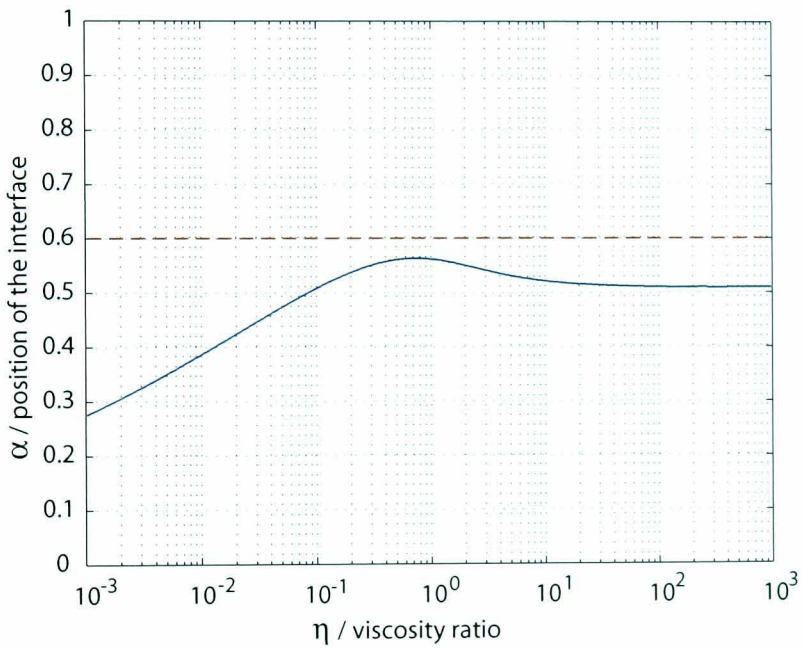

Figure 5.4: Position of the interface for different values of the viscosity ratio ($\eta = \mu_c/\mu_a$) for the hydrostatic (dark continuous line) and maximum volumetric flux (dashed line) solutions.

5.3 Dimensionless coefficients

5.3.1 Dimensional analysis

To start with the dimensional analysis of the core–annular flow described above, seven variables and four dimensions have been considered (Table 5.1). Three primary dimensions: mass, length and time are essential for this analysis. In addition, the premise of laminar steady flow allowed the selection of 'force' as an additional dimension by neglecting inertial forces and instabilities at the interface between the liquids and at the pipe wall (Taylor, 1974). As stated in the previous section, the flow rate during convection of two immiscible liquids in a conduit is governed by the balance between buoyancy and viscous forces, where the buoyancy force depends on the density difference between the two fluids. Thus, the volumetric flux, density difference, gravity, and viscosity of the liquids are relevant variables in the problem. The viscosity of both liquids were included although one of them, the viscosity of the core fluid, was replaced by the viscosity ratio to obtain a dimensionless number directly. Also, the radius of the pipe is chosen as the characteristic length that gives information on the geometry of the system. The radius of the core–flow is not included at this point. Although the position of the interface (α) constitutes a new dimensionless number that plays a role in the magnitude of the flow rate (Equations 5.10-5.19), this value cannot be controlled or established in the problem, and measurements of it are scarce. Further, owing to the characteristics of a self-ordered system in which intrinsic variables that control the fluid flow, such as pressure drop and arrangement of the liquids in the pipe, are not specified, the position of the interface might depend directly on the characteristics of the flow and properties of the liquids. Moreover, different arrangements of the liquids in the pipe are also relevant to this investigation, in which case the incorporation of this parameter is meaningless and it should be replaced by the volume fraction of the phases.

Initially, the interfacial tension is not considered so that the analysis is reduced to six variables and four dimensions (Table 5.1). As a result, two dimensionless groups are obtained:

$$\Pi_1 = \eta \tag{5.20}$$

$$\Pi_2 = \frac{Q\mu_a}{g\Delta\rho R^4} \tag{5.21}$$

The second group Π_2, herein called flux coefficient (C_Q), represents the ratio of viscous to buoyancy forces, and is related to the solution of the perfect core–annular flow expressed in

Table 5.1: Organization of the analysis of laminar flow of two immiscible liquids in conduits with the variables relevant to the problem and their primary dimensions: force (F), mass (M), length (L) and time (T).

		Dimensions			
Quantity	Symbol	F	M	L	T
Volumetric flux	Q	0	0	3	-1
Density difference	$\Delta\rho$	0	1	-3	0
Gravity	g	1	-1	0	0
Viscosity	μ_a	1	0	-2	1
Viscosity ratio	η	0	0	0	0
Characteristic length	R	0	0	1	0
Interfacial tension	γ	1	0	-1	0

Equations 5.17-5.19. In fact, the volumetric flux can be expressed as a relation between the two groups:

$$Q = C\,\frac{g\Delta\rho R^4}{\mu_a}\Phi(\eta) \tag{5.22}$$

where C is a constant and $\Phi(\eta)$ a function that takes into account the dependence of the volumetric flux on the viscosity ratio. In this case, and as it will be shown later, the flux coefficient is better defined as in Equation 5.22 but having the viscosity of the more dense fluid in the denominator of the equation, regardless of whether it goes in the core or annular region. This relationship was used by Stevenson and Blake (1998) and Huppert and Hallworth (2007) to describe their experiments of counter-current core–annular flow (see Section 5.3.2).

In order to incorporate the effects of inertial forces in the system, the organization of the dimensional analysis (Table 5.1) is modified so that only the three basic dimensions are used (mass, length and time). This yields a third dimensionless group, which has the form of a Reynolds number,

$$\Pi_3 = \frac{Q\Delta\rho}{\mu_a R} \tag{5.23}$$

or, alternatively,

$$\Pi_3 = \frac{Q\rho_c}{\mu_c R} \tag{5.24}$$

where the density of the core liquid has been introduced into the analysis. The choice of the density of the core liquid over the density of the annular liquid was arbitrary. The incorporation of either density yields another dimensionless group, $\Delta\rho/\rho$, which will be only relevant to this problem when combined with other groups.

Finally, the understanding and description of a liquid-liquid flow need the inclusion of the interfacial tension in the group of variables (Table 5.1). Indeed, it is well known that

a perfect core–annular flow is rarely stable (Joseph and Renardy, 1993a), and that several instabilities can arise from the unbalance between interfacial tension and shear stresses at the fluids interface (Joseph and Renardy, 1993b). The interfacial tension can also influence the characteristics of the curvature and position of the interface. Adding this new variable a fourth relevant dimensionless group is obtained, although in this case there are more options to consider. For instance, the Eötvös number

$$\Pi_4 = \frac{R^2 g \Delta\rho}{\gamma} \tag{5.25}$$

describes the balance between buoyancy forces and interfacial tension. Alternatively, dimensionless groups with the form of a Capillary number (viscous forces over surface tension) or Weber number (inertial forces over surface tension) can be formed. The selection of either of these groups must be studied with experiments.

Actually, the results of this analysis can be applied to problems of convective flow of immiscible fluids that are more general than the one that this chapter sets out to consider. Regarding the selection of a characteristic length, no restrictions have been imposed on the geometry of the conduit nor on the inclination of it. Moreover, the case of convective flow of miscible liquids could be analysed if mass diffusion and mixing is incorporated.

5.3.2 Poiseuille number and Flux coefficient

The axial-concentric intrusion of one fluid into another fluid with different densities and viscosities has been investigated by Koyaguchi and Blake (1989) and Stevenson and Blake (1998). They used a dimensionless Poiseuille number defined as the ratio between viscous and buoyancy forces. This number has been extensively used in the design of micro-devices to study the fluid flow in micro-channels (eg. Silber-Li *et al.* (2005); Croce and DíAgaro (2005)). The Poiseuille number can be obtained by direct dimensional analysis or by combination of the Reynolds number with either a Fanning friction factor or Froude number, and it is given by:

$$Po = \frac{\langle v \rangle \, \mu}{g \Delta\rho R^2} \tag{5.26}$$

where $\langle v \rangle$ is the average velocity of the intruding fluid, μ the dynamic viscosity of the surrounding fluid, $\Delta\rho$ the difference in density, and R the radius of the cylinder.

Koyaguchi and Blake (1989) used the Poiseuille number to classify the behavior of a relatively denser fluid intruding, with a given upwards velocity, a light fluid with different

viscosity. Later on, Stevenson and Blake (1998) used the Poiseuille number to relate the viscosity ratio with the overturn style (normal buoyant convection) and ratio of the radius of both fluids (position of the interface). However, we have seen that the buoyancy term in the Poiseuille number is not sufficient to describe the convective flow because it depends on the area occupied by the inner fluid (thus α). It is worth mentioning that Koyaguchi and Blake (1989) as well as Stevenson and Blake (1998) used, in the definition of the Poiseuille number, the velocity of the ascending fluid and the viscosity of the surrounding fluid instead of the velocity and viscosity of only one fluid (Equation 5.26).

Huppert and Hallworth (2007) defined a transport number (Te), which is analogous to the Poiseuille number, that uses the volumetric fluid flux instead of the velocity. I recall that Q can be expressed by the product of the area occupied by the flow, which is kept constant, and the averaged velocity of the fluid. Equations 5.17-5.19 show that the transport number, herein called flux coefficient (C_Q, Equation 5.21), specifies the relationship (and solution) between the pressure drop and position of the interface, for a given viscosity ratio (Figure 5.3). Inspection of Equation 5.17 provides an idea of the definition of the flux coefficient in the case of core-annular flow in cylindrical conduits:

$$C_Q = \frac{|Q|\ \mu_a}{g\Delta\rho R^4} = \pi\alpha^2 Po \tag{5.27}$$

where $|Q|$ is the absolute value of either Q_c or Q_a. The constant parameter $\frac{8}{\pi}$ that appeared in Equation 5.17 was dropped as it shall change with different geometries or when using the diameter instead of the radius of the conduit. Note that, for now, the viscosity used in this equation corresponds to the viscosity of the annular liquid. From the condition of conservation of volume (Equation 5.10):

$$C_Q = \widehat{Q}_c = -\widehat{Q}_a \tag{5.28}$$

Therefore, the volumetric flux of the uprising fluid is given by:

$$Q = C_Q \frac{\pi R^4 \Delta\rho g}{8\mu_a} \tag{5.29}$$

5.3.3 Interfacial and wall friction factors

The fully developed laminar flow investigated in this analysis is governed by buoyancy and viscous friction. As seen in Figure 5.2, in a perfect laminar core-annular flow the core

fluid experiences high shear stresses at the interface with the annular liquid, which induces momentum loss and reduces the volumetric flow rate. A common and practical approach to assess this momentum loss in mono-phase flows in pipes is the calculation of the *Fanning friction factor* f (Bird *et al.*, 1960; Massey, 2006). If the flow is laminar this friction factor can be derived from the Hagen-Poiseuille flow equation, but when the flow is turbulent it must be determined empirically. A general definition of the Fanning friction factor is (Bird *et al.*, 1960)

$$F_k = A \cdot K \cdot f \tag{5.30}$$

where F_k the force exerted by the fluid associated with the motion of the fluid on the surface that limits the flow, A is a characteristic area, and K a characteristic kinetic energy per unit volume. In the case of counter–current core–annular flow, and only for the core flow, A is the interfacial area $2\pi\tilde{R}L$ with $\tilde{R} = \alpha R$, $K = \frac{1}{2}\rho_c\langle v_c\rangle^2$ and

$$F_k = F_z|_{\tilde{R}} = \int_0^L \int_0^{2\pi} \tau_{rz}|_{\tilde{R}}\tilde{R}\, d\theta\, dz = P_c\pi\tilde{R}L \tag{5.31}$$

where $\tau_{rz}|_{\tilde{R}}$ is the flux of z-momentum in the positive r-direction evaluated at $\tilde{R}$ (Figure 5.2). Thus, Equation 5.30 becomes

$$\tau_i = \frac{1}{2}\rho_c\langle v_c\rangle^2 f_i \tag{5.32}$$

with $\tau_i = \frac{1}{2}P_c\tilde{R}$ the shear stress at the interface and f_i the interfacial friction factor. Thereby, when the friction factor f_i is known, it can be used to obtain the pressure gradient in the conduit. For the fully developed flow of one Newtonian fluid in a tube, the friction factor depends on the Reynolds number only, $f = f(Re)$. In the case considered here, and after manipulation of Equation 5.32 using the average velocities (Equations 5.6-5.7), the friction factor can be expressed as

$$f_i = \frac{16}{Re_c}\left(1 - \frac{v_c(\tilde{R})}{\langle v_c\rangle}\right) \tag{5.33}$$

where $Re_c = 2\tilde{R}\langle v_c\rangle\rho_c/\mu_c$ is the Reynolds number of the core flow, and $v_c(\tilde{R})$ the velocity at the interface. The term between brackets on the right–hand side of Equation 5.33 can be greater or lower than unity depending on the sign (lower or greater than zero) of $v_c(\tilde{R})$ (Equation 5.6), which itself depends on the viscosity ratio η (Figure 5.2). Thus, the magnitude of the friction factor f_i depends on the position of the interface, viscosity ratio and densities

of the liquids:

$$f_i = \frac{16}{Re_c}\Phi(\Delta p, \alpha, \eta, \Delta\rho) \tag{5.34}$$

where $\Phi(\cdot)$ refers to a function that requires the parameters between brackets. Therefore, in counter–current core–annular flow the friction factor associated to the core fluid flow can be greater or lower than the corresponding friction factor of the same fluid flowing alone in a pipe of radius $\tilde{R}$ (when $v_c(\tilde{R}) = 0$). Using Equation 5.6, Equation 5.8 and Equation 5.15, the relation that defines the interfacial friction factor in core-annular flows (Equation 5.33) becomes

$$f_i = \frac{(\rho_a - \rho_c)g}{\rho_c}\frac{\alpha R}{\langle v_c\rangle^2}\frac{(1-\alpha^2)^2}{1-(1-\eta^{-1})\alpha^4} \tag{5.35}$$

Similarly, the wall shear stress can be expressed following Equations 5.30-5.32:

$$\tau_w = \frac{1}{2}\rho_a\langle v_a\rangle^2 f_w = \frac{1}{2}(P_a R + \Delta\rho g\alpha^2 R) \tag{5.36}$$

with f_w the friction factor that constrains the effect of the wall to resist the flow (no–slip condition). Manipulation of the last equation yield the following expression for the wall friction factor:

$$f_w = -\frac{(\rho_a - \rho_c)g}{\rho_a}\frac{(1-\alpha^2)R}{\langle v_a\rangle^2}\left(1 - \frac{(1-\alpha^2)}{1-(1-\eta^{-1})\alpha^4}\right) \tag{5.37}$$

in which the term between brackets on the right is positive, and so f_w is negative as long as the density difference $(\rho_a - \rho_c)$ is positive.

5.4 Experimental studies

The following experiments were aimed to study convection of two liquids that occurs owing to their density difference, and whose flow rates are constrained by the conservation of volume in the system. The latter condition means that the volumetric flow rate of both fluids must be equal within the pipe, as assumed in a closed magmatic system where the degassed and more dense magma sinks and is replaced by the same volumetric amount of fresh melt that rises from deeper levels in the system.

Liquid-liquid flow behaviour in pipes is the focus of many investigations as it is a problem encountered in many industrial applications, particularly in the oil industry in order to assess the characteristics and efficiency of the extraction of oil (Joseph and Renardy, 1993b; Arney *et al.*, 1993; Joseph *et al.*, 1997; Bannwart, 2001; Prada and Bannwart, 2001). The analysis of liquid-liquid flows is a difficult problem in which several parameters come into play: flow regime, holdup (fraction of the pipe occupied by one of the fluids), flow rate, instabilities at the interface, arrangement of the liquids in the pipe, and the properties of the experiments such as the viscosity and density of the liquids, interfacial tension, and radius of the pipe. Most of the attention, however, has been on concurrent flows in which both liquids flow in the same direction under a commonly specified pressure drop. Although there is a considerable amount of literature that investigates the counter-current flow of liquid-gas systems (e.g. Shibata and Kaminaga, 2001; Oliemans and Pots, 2006), which to some extent could be considered as an extreme case of liquid-liquid systems (Brauner *et al.*, 1998), the results cannot be directly applied in the latter case.

Most of the experiments in this study involved immiscible fluids in order to study the variations of the flow rate obtained with different liquids, in vertical and inclined pipes. In addition, the characteristics of the liquid-liquid flow were analysed in terms of their configuration within the pipe. A few experiments with miscible fluids were conducted with the aim of constraining ideas about the flow characteristics, and to compare them with those observed with immiscible fluids. The liquids chosen for the experiments were different types of organic (cooking) oils, and variable mixtures of glycerol or golden syrup with water.

5.4.1 Density and viscosity of the liquids

All the measurements were performed at room temperature, which commonly was 18-19 Celsius degrees, although in a daily basis it fluctuated between 17 and 21 °C. It is

noteworthy that the viscosity of all the liquids is Newtonian, and that when glycerol or golden syrup are mixed with water, the viscosity of the resulting mixture lies between these two. The relation between dilution and viscosity is not necessarily linear, but it is monotonic (Figure 5.5). The same relation is valid with the density of the mixture. Two to four measurements of density and viscosity were carried out for each liquid. Consecutive measurements yielded essentially the same results and they were averaged.

Two methods were used to measure the density of the fluids: with hydrometers and with a set of digital scales. Five hydrometers were available to measure the density of the liquids. The hydrometer was gently placed inside a tall jar with the liquid of interest and, when the hydrometer stopped sinking, the density was measured directly from it. The weighing method was used to measure densities lower than 1000 kg m^{-3} and, to some extent, to corroborate some of the densities measured with the hydrometers. By pouring the liquid into a graduated cylinder lying on the digital scales, the variations in weight and volume of the liquid could be read and used to calculate the density by means of a linear fit of the data (inset in Figure 5.5). In general, measurements performed with the set of digital scales give values 5-10 kg m^{-3} lower ($\sim$1% of total density and $\sim$1-3% of density difference), perhaps due to the small bubbles created during the pouring of the liquid into the cylinder. These results are summarised in Table 5.2 and plotted in Figure 5.5.

The kinematic viscosity was measured with a set of glass capillary viscometers (U-tube type). Only two capillary tubes were required to measure the range of viscosities of the oil, glycerol and golden syrup: viscometers CF300 and #53509. Minimum kinematic viscosities that can be measured by these capillary viscometers are $9.56 \cdot 10^{-5}$ and $2.08 \cdot 10^{-4}$ $m^2 s^{-1}$, respectively. (It therefore follows that the viscosity measurement of the mixture golden syrup with water with the lowest viscosity in Figure 5.5 must be overestimated as its kinematic viscosity is lower than the minimum established for the viscometer.) An alternative methodology, the falling sphere method (Massey, 2006), was used with some liquids that had lower kinematic viscosity, or very high viscosity (e.g. pure golden syrup). To measure the settling velocity of the spheres, stainless steel ball bearings of 1 and 3.17 mm diameter were dropped in cylinders of 20 or 35 mm diameter. The wall correction factor of Haberman and Sayre (Clift *et al.* (1978), Table 9.2, page 225) was applied to these measurements. Comparison of some viscosities obtained using capillary viscometers with those obtained with the falling sphere method yielded differences between 20 and over 100%. This error is large because of the relatively high Reynolds number of the particle in some of these

Table 5.2: Density and viscosity measurements of the liquids used in the experiments[a].

Fluid	Density [kg m^{-3}]	Method	Viscosity[b] kinematic [m^2 s^{-1}]	dynamic [Pa s]	Method
Corn oil	900.78	Digital scales	2.252 10^{-4}	*2.029 10^{-1}*	visc. CF300
	911.75	Digital scales	2.252 10^{-4}	*2.054 10^{-1}*	visc. CF300
Sunflower oil	915.6	Digital scales	*7.480 10^{-5}*	6.849 10^{-2}	fall-sph. 1mm
	915.6	Digital scales	1.928 10^{-4}	*1.766 10^{-1}*	visc. CF300
Vegetable oil	917.27	Digital scales	1.983 10^{-4}	*1.819 10^{-1}*	visc. CF300
	920.96	Digital scales	1.924 10^{-4}	*1.772 10^{-1}*	visc. CF300
Water	1000	Hydrometer	1.085 10^{-6}	1.085 10^{-3}	literature[c]
Glycerol	1178.5	Hydrometer	*2.485 10^{-5}*	2.929 10^{-2}	fall-sph 1mm
	1145.0	Hydrometer	*1.234 10^{-5}*	1.363 10^{-2}	fall-sph 1mm
	1225.0	Hydrometer	*1.022 10^{-4}*	1.251 10^{-1}	fall-sph 1mm
	1225.0	Hydrometer	2.844 10^{-4}	*3.484 10^{-1}*	visc. CF300
	1236.5	Hydrometer	4.846 10^{-4}	*5.922 10^{-1}*	visc. CF300
	1253.8	Digital scales	1.584 10^{-3}	*1.986 10^{0}*	visc. #53509
	1251.5	Digital scales	1.313 10^{-3}	*1.643 10^{0}*	visc. #53509
	1256.9	Hydrometer	1.313 10^{-3}	*1.650 10^{0}*	visc. #53509
	1258.8	Hydrometer	1.313 10^{-3}	*1.653 10^{0}*	visc. #53509
	1260.5	Hydrometer	1.313 10^{-3}	*1.655 10^{0}*	visc. #53509
	1255.3	Digital scales	1.501 10^{-3}	*1.884 10^{0}*	visc. #53509
	1261.5	Hydrometer	1.501 10^{-3}	*1.894 10^{0}*	visc. #53509
Golden Syrup	1156.8	Hydrometer	1.072 10^{-5}	*1.240 10^{-2}*	visc. CF300
	1216.0	Hydrometer	*2.151 10^{-5}*	2.615 10^{-2}	fall-sph. 1mm
	1283.1	Hydrometer	1.035 10^{-4}	*1.328 10^{-1}*	visc. CF300
	1418.8	Digital scales	*3.746 10^{-2}*	5.315 10^{1}	fall-sph. 3.17mm

[a] Measurements with identical density or viscosity correspond to new measurements of viscosity or density only, respectively, before or after the experiments, in which case the other properties were taken from previous measurements.

[b] In roman font the values obtained by the method (measured) and in italics the values calculated using the density of the liquid.

[c] Lienhard-IV and Lienhard-V (2006)

calculations. Hence, viscosities obtained with capillary viscometers were preferred when they were available. A list of the kinematic and dynamic viscosities are given in Table 5.2.

5.4.2 Experimental apparatus

The experimental apparatus consisted of two square tanks, $3.375{\cdot}10^{-3}$ m^3 each, connected by a 30 cm long circular pipe (Figure 5.6). Attached to a metallic frame, the apparatus (made out of perspex) was able to rotate freely (360°) about a pivot located at the middle between the tanks, so the axis of rotation is perpendicular to the pipe. Thus, experiments with vertical and inclined pipes, at any angle, could be performed.

Three pipes with radii 2.5, 10 and 25 mm were available for the experiments, yielding aspect ratios (length/radius) of 120, 30 and 12, respectively. However, with the smallest radius pipe the convective flow through the pipe was impeded by the high surface tension

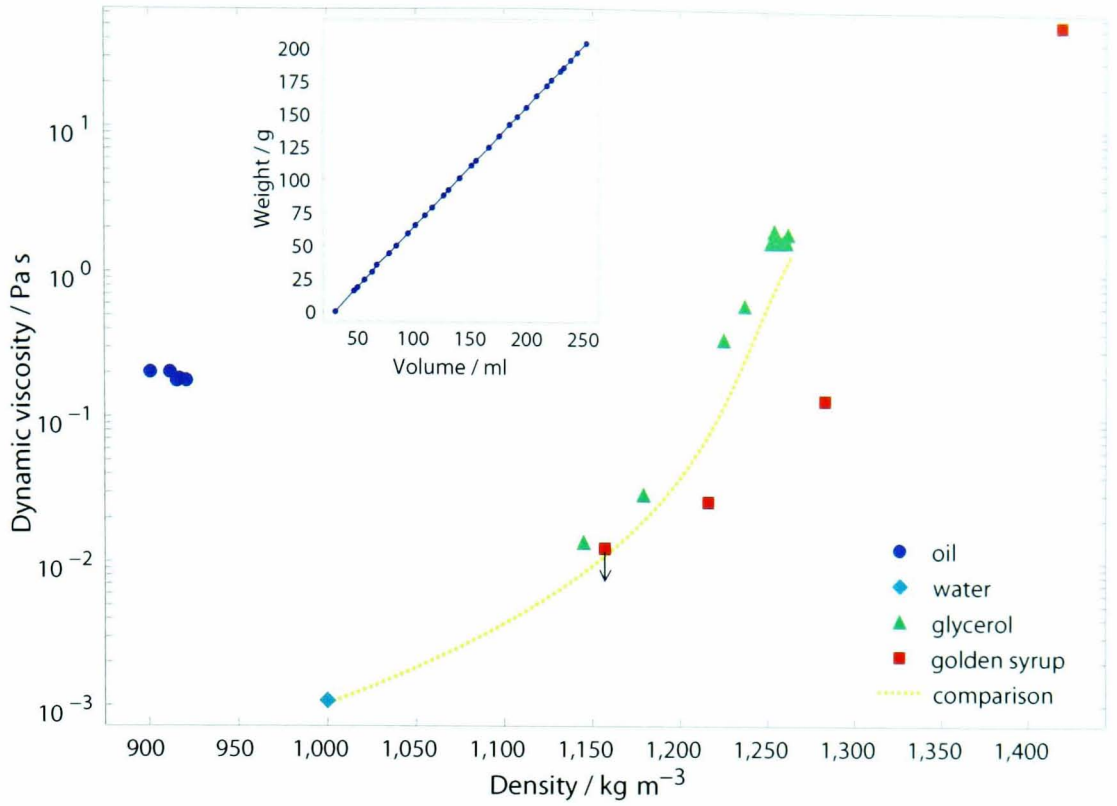

Figure 5.5: Density – viscosity plot of the liquids used in the experiments. Glycerol and golden syrup show a broad range of densities because of the different levels of dilution with water. For comparison, a third order polynomial best fit (R^2=.9994) of the data from Huppert and Hallworth (2007) for the mixture water-glycerol (dashed line) is included. The inset on top left of this plot shows an example of the linear fit applied to the data collected by the digital balance technique, using vegetable oil and obtaining a correlation coefficient R^2=0.99997.

of the liquids[7]. With the 25 mm radius pipe the flow was mostly turbulent due to the high Reynolds numbers reached by the relatively low viscosity liquids. The 10 mm radius pipe was the compromise between the other two, and it was used in most of the experiments conducted with this apparatus.

The flow was photographed and video recorded to facilitate a later inspection of the flow characteristics. On some occasions, blue, red or green dye was added to one of the fluids to provide a better visualization of the flow (differentiate between fluids) and qualitative mixing levels in the case of using miscible fluids. Once the system tank-pipe-tank had been filled up with two chosen liquids, the experiments were started by creating an unstable fluid stratification by simply flipping the apparatus up–side down.

[7]This problem arises when the surface tension exceeds the hydrostatic force. A critical parameter that measures the relative effect of buoyancy ($g\Delta\rho$), diameter of the pipe (d) and surface tension (σ) is the Bond (Eötvös) number (Massey, 2006): ($d^2 g\Delta\rho/\sigma$), where $\Delta\rho$ is the density difference between the fluids. Thus, relevant surface tension effects arise on a length scale corresponding to the capillary length (Bo=1)

$$l_c = \left(\frac{\sigma}{g\Delta\rho}\right)^{1/2}$$

For instance, l_c of water (in air, $\sigma \sim 0.072$ N m^{-1}) is approx. 2.7 mm. The interfacial tension between water and oil is less than a half of that of water-air (about 0.02 N m^{-1}, Batchelor, 1967), thereby the capillary length l_c is lower (about 1.4 mm).

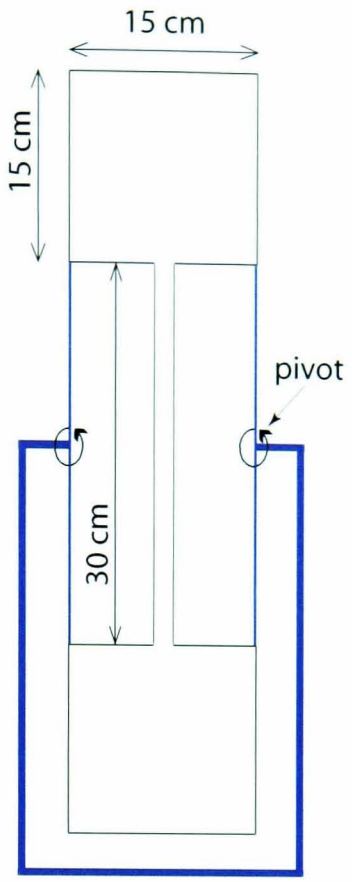

Figure 5.6: Sketch of the apparatus used in the two-tanks experiments. Two 3.375 litres tanks are connected by a cylindrical pipe and attached to a metal structure that allows the inclination the apparatus.

5.4.3 Characteristics of the flow

Several arrangements of the liquids were observed in these experiments, particularly with the pipe in a vertical or near–vertical position. Variations in the arrangement of the fluids in the pipe are typical of immiscible liquid-liquid flows (Joseph and Renardy, 1993a). Among the most common arrangements, my experiments of counter–current flow showed:

1. wavy core–annular flow,
2. medium to large-sized bubbles (relative to the radius of the pipe) of the lighter liquid rising uniformly within the pipe,
3. small to medium-size bubbles (or drops) of the heavier fluid immersed in a continuous lighter liquid,
4. non–uniform and thin threads of the heavier fluid, and
5. stratified flow with the lighter fluid on top of the heavier fluid

Some descriptions of individual experiments can be found in Appendix C. Detailed investigation of each of one of these flow patterns is beyond the scope of this chapter. Nevertheless, it is of interest to realise that the 'perfect' core–annular flow configuration might

be found only under specific circumstances. The conditions for counter–current core–annular flow and the consequences of the development of different flow patterns will be discussed later in this chapter.

Initial position of the interface

Before starting the experiments, by flipping the apparatus up-side down, the interface that separated the heavy liquid at the bottom from the light liquid above could be located either near the middle of the pipe, or in one of the tanks near the junction with the pipe. The initial position of the interface in every experiment is included in Tables 5.3 and 5.4. When this position was in the top tank, right after flipping the apparatus the light liquid, that then was in the bottom tank, started intruding the heavier liquid that occupied the whole pipe. This initial configuration is similar to that used by Huppert and Hallworth (2007) in their experiments. With the interface in the middle of the pipe the experiments are perhaps similar to, at least in the initial stage, those performed by Stevenson and Blake (1998).

Although the influence of the position of the interface could not systematically be analysed, due to the unchanged configuration used in experiments with a specific pair of liquids, most of the experiments showed no sign of experiencing a particular flow pattern related to a particular initial condition. Only one experiment exhibited clearly such influence: starting with the interface near the middle of the pipe in an experiment with corn oil and water (exp. 426a, vertical pipe), the position of the interface defined a level of asymmetry in which the flow below that position was characterised by medium to long-size bubbles of water descending in the middle of the pipe, while above this level both the water and oil were flowing next to the wall of the pipe. The flow pattern observed in the lower half of the pipe resembled the description of Stevenson and Blake (1998) for experiments with viscosity ratio higher than 0.1, in which the heavy fluid detached from the wall and descended through the core. A second experiment, performed soon after the previous one, with the same configuration and same pair of liquids did not show any spatial discontinuity in the flow pattern. A third experiment with vegetable oil and water but with the interface initially in the top tank, showed very long bubbles of oil rising in the middle of the pipe until the flow stopped, only after a few tens of seconds, leaving the pipe full of oil and both tanks with different amounts of water and oil.

One aspect of the initial configuration of the experiments that might influence the developed flow pattern is the wettability of the liquids. The degree of wetting determines the feasibility of the liquid to spread on or to 'stick' to the pipe wall. It depends on the

surface tension of the liquid–pipe wall interface[8]. A consequence of this property is that for a liquid located in the middle of the pipe it is difficult to replace a second liquid with a relatively high wettability that is in contact with the pipe wall. Thus, when the interface between the liquids is initially located in one of the tanks, the wetting of the liquid in the pipe will favour the intrusion and initial flow of the second liquid through the middle of the pipe. This characteristic is likely to have contributed to the development of the core–annular flow observed in the experiments of Huppert and Hallworth (2007), with the less dense liquid flowing in the core and the more dense liquid, which initially occupied the whole pipe, flowing in the annulus. In addition to the viscosity ratio, the wettability of the liquids might have also influenced the different flow patterns observed above and below the initial position of the interface in the experiments performed by Stevenson and Blake (1998).

Vertical pipe

The experiments performed with the apparatus in a vertical position were characterised by a variety of different fluid arrangements and flow patterns. These characteristics have been grouped in three main categories (Figure 5.7):

1. Unsteady core-annular flow (UCA),
2. Pseudo–stratified flow (PS), and
3. Bubbly or turbulent flow (BT).

A single experiment could show more than one flow pattern. It was common to observe that the beginning of an experiment started with a medium to large-sized bubble (relative to the radius of the pipe) of the lighter liquid rising through the pipe. Sometimes this bubble was as long as 2/3 the length of the pipe. Behind this bubble, another bubble or a thread of liquid flowing next to the wall followed until a particular flow pattern developed.

In the first category (UCA), the core–annular flow generally experienced wavy interfaces. These waves commonly propagated along the pipe and, after a few seconds, modified the arrangement of the liquids. Long bubbles, which are also considered here as part of UCA flow, also experienced waves at the interface (Figure 5.7a). Only one experiment (524a in Table 5.3) exhibited a core–annular configuration from the beginning until the end. In this case, with vegetable oil and pure glycerol, the experiment started with a train of very long

[8]The degree of wetting of a liquid on a surface can also be expressed by the 'contact angle' between them. This property is part of the characteristics of individual liquids, which may not be possible to generalise based on the viscosity ratio only.

Table 5.3: Summary of the experimental data and results for experiments in vertical pipes.

Exp.	Fluid light	Fluid heavy	Density ρ_l	Density ρ_h	Kin. viscosity ν_l	Kin. viscosity ν_h	Pipe R	Volume Flux	Pattern[a] Pipe	Pattern[a] Tanks top	Pattern[a] Tanks bottom	IPI[b]	η	Cq
			$[kg/m^3]$		$[m^2/s]$		$[mm]$	$[m^3/s]$						
816a	water	gly-p	1000.0	1253.8	1.085E-06	1.584E-03	10	1.289E-06	UCA,BT	LSN	TP	T	5.46E-04	1.03E-01
824a	oil-s	syr-p	915.6	1418.8	1.928E-04	3.746E-02	10	1.187E-07	PS	B	LS	B	3.32E-03	1.28E-01
524a	oil-v	gly-p	917.3	1253.8	1.983E-04	1.584E-03	10	1.528E-06	UCA	B,LSN	LS	P	9.16E-02	9.20E-02
524b	oil-v	gly-p	917.3	1253.8	1.983E-04	1.584E-03	10	2.983E-06	PS	LSN	LS	P	9.16E-02	1.80E-01
525a	oil-v	gly-p	917.3	1253.8	1.983E-04	1.584E-03	10	2.690E-06	UCA,PS	LSN	LS	P	9.16E-02	1.62E-01
525b	oil-v	gly-p	917.3	1253.8	1.983E-04	1.584E-03	10	2.740E-06	UCA,PS	LSN	LS	P	9.16E-02	1.65E-01
521a	oil-c	gly-p	900.8	1260.5	2.252E-04	1.313E-03	25	6.176E-05	BT	LS		T	1.23E-01	7.42E-02
522a	oil-c	gly-p	911.8	1256.9	2.252E-04	1.313E-03	25	6.559E-05	BT	LS		T	1.24E-01	8.19E-02
801a	oil-v	gly-d	921.0	1236.5	1.924E-04	4.846E-04	10	5.929E-06	PS	LSN	LS	B	2.96E-01	1.15E-01
801c	oil-v	gly-d	921.0	1236.5	1.924E-04	4.846E-04	10	4.377E-06	PS	LSN	LS	B	2.96E-01	8.48E-02
807a	oil-v	syr-d	921.0	1216.0	1.924E-04	2.151E-05	10	7.694E-06	BT,PS		LSB,LS	P	6.77E+00	6.96E-03
808a	oil-v	syr-d	921.0	1216.0	1.924E-04	2.151E-05	10	6.595E-06	BT,PS		LS	P	6.77E+00	5.97E-03
808b	oil-v	syr-d	921.0	1216.0	1.924E-04	2.151E-05	10	7.899E-06	BT,PS		LS	P	6.77E+00	7.14E-03
808c	oil-v	syr-d	921.0	1216.0	1.924E-04	2.151E-05	10	7.988E-06	BT,PS		LS	P	6.77E+00	7.23E-03
809a	oil-v	gly-d	917.3	1104.5	1.983E-04	1.234E-05	10	6.573E-06	BT,PS	LSB	LSB,LS	T	1.33E+01	4.88E-03
809b	oil-v	gly-d	917.3	1104.5	1.983E-04	1.234E-05	10	4.988E-06	BT,PS	LSB,LS	LSB,LS	T	1.33E+01	3.71E-03
809c	oil-v	gly-d	917.3	1104.5	1.983E-04	1.234E-05	10	3.533E-06	BT,PS	LSB,LS	LSB,LS	T	1.33E+01	2.63E-03
814a	oil-v	gly-d	917.3	1104.5	1.983E-04	1.234E-05	10	5.619E-06	BT	LSN	LS	T	1.33E+01	4.18E-03
426a	oil-c	water	897.1	1000.0	2.252E-04	1.085E-06	10	2.061E-06	UCA,PS	LSB	LSB	P	1.86E+02	2.22E-04
426b	oil-c	water	897.1	1000.0	2.252E-04	1.085E-06	10	1.774E-06	UCA	LSB	LSB	P	1.86E+02	1.91E-04

[a]Fluid abbreviations: oil-s, oil-v and oil-c correspond to sunflower, vegetable and corn oil, respectively; gly-p and gly-d correspond to glycerol pure and diluted, respectively; syr-d is diluted golden syrup. Pattern abbreviation: in the pipe UCA=unsteady core annular flow, BT=bubbly or turbulent flow, PS=pseudo-stratified flow; in the tanks B=bubbles, LSB=laminaar stream and bubbles, LSN=laminar stream with non-uniform thickness, LS=laminar stream, TP=turbulent plume.

[b]Initial position of the interface before flipping the apparatus up-side down: P=near the middle of the pipe, T=in the top tank, B=in the bottom tank.

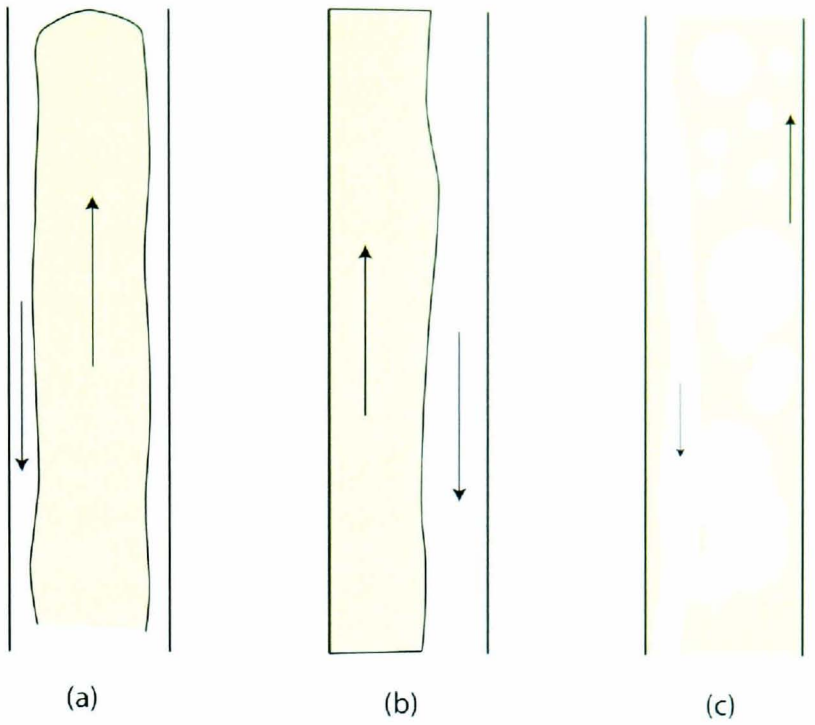

Figure 5.7: Cartoons of the flow patterns observed in vertical pipes. a) Very long bubble with wavy interface as unsteady core–annular flow, b) liquids flowing on opposite sides of the pipe as pseudo–stratified flow, and c) bubbles in a slightly turbulent flow. The dark region corresponds to the lighter fluid.

bubbles separated only one or two millimeters apart, with the wavy interface observed at the start of the experiment disappearing soon after the bubbles reached the top tank. A couple of experiments with oil and water (426a, 426b in Table 5.3), which are also identified as UCA flow, exhibited a cycle in which long water bubbles sunk through the middle of the pipe (with the oil next to the walls) that after reaching the bottom tank were followed by a rapid (and turbulent) rise of oil that, after reaching the top tank, started the new cycle (see Appendix B). This was the only experiment that showed long bubbles of the heavier liquid flowing downwards in the middle of the pipe.

Two similar flow patterns were identified as pseudo–stratified (PS) flow: liquids flowing on opposite sides of the pipe, and a thin thread of the heavier fluid descending next to the wall (Figure 5.7b). The first arrangement was common in experiments with oil and glycerol (pure and diluted; experiments 524b, 801a, 801b in Table 5.3). In this pseudo-stratification the position of the interface as well as the thickness of the streams changed with time (and with the position along the pipe). The development of a thin thread descending on one side of the pipe was characteristic of golden syrup in oil. In this case the thickness of the stream and its position also changed with time, but not as much as in the previous case. The best example occurred in an experiment with pure golden syrup in sunflower oil (824a in Table 5.3 and Appendix B), in which owing to the curvature of the stream, the syrup had the appearance

of developing eccentric flow, although it was touching the wall of the pipe.

A couple of experiments with diluted golden syrup and oil showed big blobs (size comparable to the diameter of the pipe; exp. 807a, 808b in Table 5.3) and small-sized bubbles of syrup dispersed in the continuous oil (Figure 5.7c). The blobs of syrup descended through the middle of the pipe and oscillated from one side of the pipe to the other. On some occasions, these blobs could agglomerate and form a more continuous but irregular stream of syrup. The small bubbles could either descend on one side of the pipe or some of them rose, being pulled up by the flow of oil. A similar pattern occurred with another experiment that involved oil and glycerol (exp. 809c). Apart from these examples of dispersed flow, a couple of experiments performed with the wider pipe of 25 mm radius exhibited turbulent flow (exp. 521a, 522a in Table 5.3 and Appendix B), as seen in mono–phase (only one liquid) flows at high Reynolds numbers.

Inclined pipe

With inclined pipes the flow was observed to be more stable than the flow in vertical pipes. Stratified flow (ST), with the lighter liquid flowing on top of the heavier one, was the flow pattern that dominated the counter–current flow at inclinations higher than 15 degrees (angle with respect to the vertical) (Figure 5.8a, Table 5.4). At lower inclinations, however, instabilities similar to those seen in vertical pipes were also observed, particularly at angles lower than 10 degrees (Figure 5.8b). For instance, with the pipe inclined at 6 degrees, the flow of oil and water exhibited water bubbles or wavy fluid interfaces (exp. 427c2 in Table 5.4), and in experiments with golden syrup and oil the stream of syrup was not uniform in thickness along the pipe (Table 5.4).

Despite the difficulty of observing the flow through the cylindrical pipe, some interesting observations of the interface between the liquids could be made. The shape of the interface in stratified flow was found to be planar in most of the experiments, but curved in experiments that involved pure golden syrup. In some experiments with golden syrup and oil (824a in Table 5.3 and 911a2 in Table 5.4), the interface showed long wavelengths in the direction of the flow. Apparently, these waves originated at the upper pipe–tank junction and were related to the entrance of blobs of oil into the tank, which created oscillations in the cross-sectional area of both liquids. These oscillations would then propagate downstream without growing into severe instabilities.

A few measurements of the position of the interface in stratified flow (with a planar

Table 5.4: Summary of the experimental data and results for experiments with inclined pipes.

Exp.	Fluid light	Fluid heavy	ρ_l $[kg/m^3]$	ρ_h $[kg/m^3]$	ν_l $[m^2/s]$	ν_h $[m^2/s]$	Pipe R $[mm]$	Pipe ang $[deg]$	Volume Flux $[m^3/s]$	Pattern[a] Pipe	Pattern[a] Tanks top	Pattern[a] Tanks bottom	IPI[b]	η	Cq
731c	air	gly-d	1.22	1236.5	1.475E-05	4.846E-04	10	6	3.630E-05	ST			B	3.00E-05	1.81E-01
731a	air	gly-d	1.22	1236.5	1.475E-05	4.846E-04	10	11	3.768E-05	ST			B	3.00E-05	1.90E-01
731b	air	gly-d	1.22	1236.5	1.475E-05	4.846E-04	10	23	4.162E-05	ST			B	3.00E-05	2.24E-01
727a	water	gly-p	1000.0	1261.5	1.085E-06	1.501E-03	10	16	3.962E-06	ST	LSN	LS	B	5.73E-04	3.05E-01
911a	oil-s	syr-p	915.6	1418.8	1.928E-04	3.746E-02	10	7	2.450E-07	ST	B	LS	B	3.32E-03	2.66E-01
911a2	oil-s	syr-p	915.6	1418.8	1.928E-04	3.746E-02	10	7	1.989E-07	STI	B	LS	B	3.32E-03	2.16E-01
823a	oil-s	syr-p	915.6	1418.8	1.928E-04	3.746E-02	10	15	1.798E-07	ST	LS	LS	B	3.32E-03	2.01E-01
1203a	oil-s	syr-p	915.6	1418.8	1.928E-04	3.746E-02	10	31	2.280E-07	ST		LS	B	3.32E-03	2.87E-01
524c	oil-v	gly-p	917.3	1261.5	1.983E-04	1.584E-03	10	6	2.906E-06	ST	LS	LS	P	9.10E-02	1.73E-01
622c	oil-v	gly-p	917.3	1261.5	1.983E-04	1.584E-03	10	12	2.524E-06	ST	LSN	LS	P	9.10E-02	1.53E-01
524d	oil-v	gly-p	917.3	1261.5	1.983E-04	1.584E-03	10	23	3.130E-06	ST	LS	LS	P	9.10E-02	2.01E-01
622a	oil-v	gly-p	917.3	1261.5	1.983E-04	1.584E-03	10	24	2.269E-06	ST	LSN	LS	P	9.10E-02	1.47E-01
622b	oil-v	gly-p	917.3	1261.5	1.983E-04	1.584E-03	10	36	2.230E-06	ST	LSN	LS	P	9.10E-02	1.63E-01
524e	oil-v	gly-p	917.3	1261.5	1.983E-04	1.584E-03	10	40	2.709E-06	ST	LS	LS	P	9.10E-02	2.09E-01
801d	oil-v	gly-d	921.0	1236.5	1.924E-04	4.846E-04	10	9	6.487E-06	ST	LS	LS	B	2.96E-01	1.27E-01
801b	oil-v	gly-d	921.0	1236.5	1.924E-04	4.846E-04	10	18	7.054E-06	ST	LS	LS	B	2.96E-01	1.44E-01
808g	oil-v	syr-d	921.0	1216.0	1.924E-04	2.151E-05	10	4	6.459E-06	STI		LS	P	6.77E+00	5.86E-03
808h	oil-v	syr-d	921.0	1216.0	1.924E-04	2.151E-05	10	9	7.342E-06	STI		LS	P	6.77E+00	6.72E-03
808d	oil-v	syr-d	921.0	1216.0	1.924E-04	2.151E-05	10	12	9.625E-06	ST		LS	P	6.77E+00	8.90E-03
807b	oil-v	syr-d	921.0	1216.0	1.924E-04	2.151E-05	10	20	1.146E-05	ST	LS	LS	P	6.77E+00	1.10E-02
808f	oil-v	syr-d	921.0	1216.0	1.924E-04	2.151E-05	10	24	1.058E-05	ST		LS	P	6.77E+00	1.05E-02
808e	oil-v	syr-d	921.0	1216.0	1.924E-04	2.151E-05	10	28	1.160E-05	ST		LS	P	6.77E+00	1.19E-02
814c	oil-v	gly-d	917.3	1104.5	1.983E-04	1.234E-05	10	6	5.032E-06	STI			T	1.33E+01	3.76E-03
814b	oil-v	gly-d	917.3	1104.5	1.983E-04	1.234E-05	10	16	6.841E-06	ST			T	1.33E+01	5.29E-03
814d	oil-v	gly-d	917.3	1104.5	1.983E-04	1.234E-05	10	31	7.707E-06	ST			T	1.33E+01	6.68E-03
427c	oil-c	water	897.1	1000.0	2.252E-04	1.085E-06	10	6	6.106E-06	ST	LS	LS	P	1.86E+02	6.60E-04
427c2	oil-c	water	897.1	1000.0	2.252E-04	1.085E-06	10	6	2.572E-06	STI	LS	LS	P	1.86E+02	2.78E-04
428a	oil-c	water	897.1	1000.0	2.252E-04	1.085E-06	10	15	6.645E-06	ST,STI	B	LS	P	1.86E+02	7.40E-04
427a	oil-c	water	897.1	1000.0	2.252E-04	1.085E-06	10	21	6.514E-06	ST		LS	P	1.86E+02	7.50E-04
428b	oil-c	water	897.1	1000.0	2.252E-04	1.085E-06	10	35	6.474E-06	ST		LS	P	1.86E+02	8.50E-04
427b	oil-c	water	897.1	1000.0	2.252E-04	1.085E-06	10	50	6.035E-06	ST		LS	P	1.86E+02	1.01E-03

[a]Fluid abbreviations: oil-s, oil-v and oil-c correspond to sunflower, vegetable and corn oil, respectively; gly-p and gly-d correspond to glycerol pure and diluted, respectively; syr-d is diluted golden syrup. Pattern abbreviation: in the pipe ST=stratified flow, STI=stratified flow with instabilities; in the tanks B=bubbles, LSB=laminar stream and bubbles, LSN=laminar stream with non-uniform thickness, LS=laminar stream.

[b]Initial position of the interface before flipping the apparatus up-side down: P=near the middle of the pipe, T=in the top tank, B=in the bottom tank.

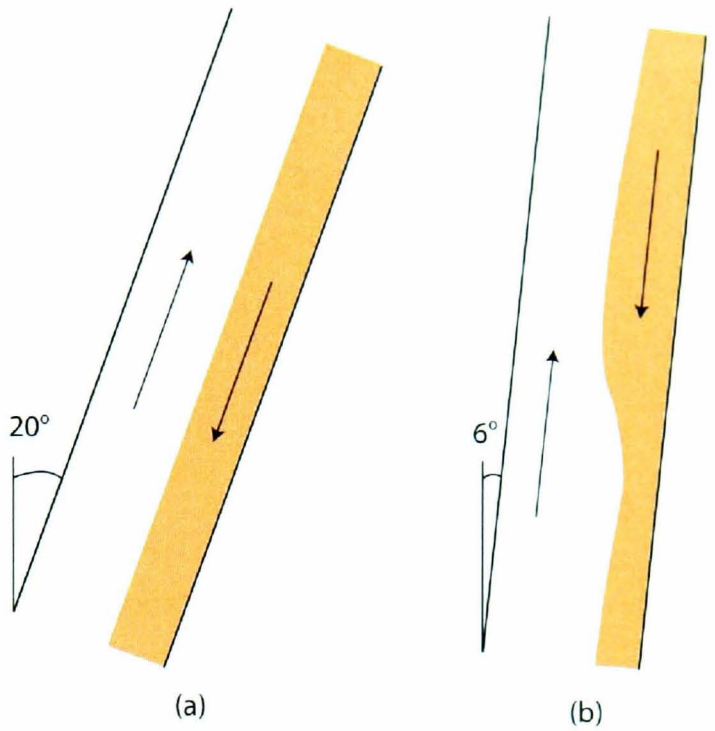

Figure 5.8: Cartoons of flow patterns observed in inclined pipes. a) Well defined and steady stratified flow in a pipe inclined 20 degrees; b) stratified flow with undulating interface in a pipe inclined 6 degrees. The darker region corresponds to the heavier fluid.

interface) reveal variations in the cross-sectional area occupied by the heavier and lighter liquids, and thus the relative average velocity of the fluids. Expressed in terms of the ratio between the pipe diameter and the 'height' of the heavier fluid ($\tilde{H}$, in cross-section of the pipe, see Figure 5.19 to see the configuration), the position of the interface varied between about $\tilde{H} = 0.25$ and $\tilde{H} = 0.7$ (see footnote[9]). A summary of the observations and measurements is in Table 5.5. For instance, in flows of diluted golden syrup and vegetable oil, in which the angle of inclination of the apparatus was greater than 10 degrees (exp. 807b, 808d, 808f, 808e; $\kappa = 6.8$), the syrup clearly occupied a smaller area than the oil ($\tilde{H} \sim 0.3$ or lower). With an inclination of 9 degrees (exp. 808h), the same liquids exhibited unstable flow in which the cross-sectional area of the syrup was not uniform along the pipe, being bigger than that of the oil at the upper end but much smaller at the lower end of the pipe; in the middle-upper part of the pipe the interface was located at $\tilde{H} \sim 0.65$. Although not measured, observations of the convective flow of corn oil and water suggest that the oil occupied a smaller area than the water ($\tilde{H} > 0.5, \kappa = 186$). Conversely, the flow of vegetable oil and diluted glycerol (exp. 814b,d) showed a thin and undulating thread of glycerol that descended next to the wall ($\tilde{H} < 0.5, \kappa = 13$). In experiments with water and pure glycerol the interface was observed to be located near the middle of the pipe (but perhaps with

[9]Care must be taken to relate these values directly to the area occupied by the liquid, as the size of the cross–sectional area also depends on the curvature of the fluid interface.

Table 5.5: Observations of the position of the interface in stratified flow.

Fluid[a] light	Fluid[a] heavy	Experiments[b]	Visc. ratio $\kappa = \mu_l/\mu_h$	Side[c] $\tilde{H}$	Measurement $\tilde{H}$
oil-v	syr-d	807b, 808d,f,e	6.77	< 0.5	$\leqslant 0.3$
oil-v	gly-d	814b,d	13.3	< 0.5	< 0.3
oil-v	gly-d	801b,d	0.3	< 0.5	
oil-s	syr-p	823a, 1203a	$3.3 \cdot 10^{-3}$	< 0.5	$\leqslant 0.45$
air	gly-d	731,a,b	$3 \cdot 10^{-5}$	< 0.5	
oil-c	water	427a,b, 428a,b	186	> 0.5	
water	gly-p	727a	$5.7 \cdot 10^{-4}$	> 0.5	$\geqslant 0.5$

[a] Nomenclature: oil-v, oil-s and oil-c correspond to vegetable, sunflower and corn oil, respectively; syr-d and syr-p are diluted and pure syrup, respectively; gly-d and gly-p are diluted and pure glycerol, respectively.

[b] See Table 5.4.

[c] $\tilde{H} > 0.5$ means that the cross-sectional area of the heavier fluid (at the bottom), assuming a planar interface, is bigger than that of the lighter fluid on top. When $\tilde{H} < 0.5$ the opposite is true.

glycerol occupying a slightly bigger area; $\tilde{H} \geqslant 0.5, \kappa = 6 \cdot 10^{-4}$). Experiments with pure golden syrup and oil exhibited a curved interface that, if it was planar, would be located at $\tilde{H} \sim 0.45$ (the corresponding cross-sectional area of the syrup is actually smaller). These observations, although not quantitatively accurate, indicate that the position of the interface does not depend on the viscosity ratio only, but on other variables too.

Miscible liquids

The flow of liquids with high viscosity contrast, using water and pure glycerol, exhibited slow mixing rates, evidenced by laminar flow of constant flow rate in stratified flow (16 degrees), and by the clear identification of blobs and streams of glycerol in vertical pipes, despite the turbulent flow. In the case of the vertical pipe, most of the mixing occurred in the bottom tank, where the glycerol descended as a turbulent plume. With the pipe inclined, however, the glycerol sank in the bottom tank in a laminar manner (see Appendix C). With a pair of liquids having a low viscosity ratio (e.g. water with dilute glycerol or water with dilute golden syrup), mixing in the pipe was observed to be more strong than in the previous case. Mixing in the tanks was so efficient that it was not possible to track the position of the interface, and so the volume flux could not be measured. These experiments were not included in the results presented in this chapter.

Similar observations were reported by Huppert and Hallworth (2007) from their experiments with miscible fluids in vertical pipes. They distinguished two flow patterns: vigorous turbulent mixing when both liquids had low viscosity, and core annular flow with varicose

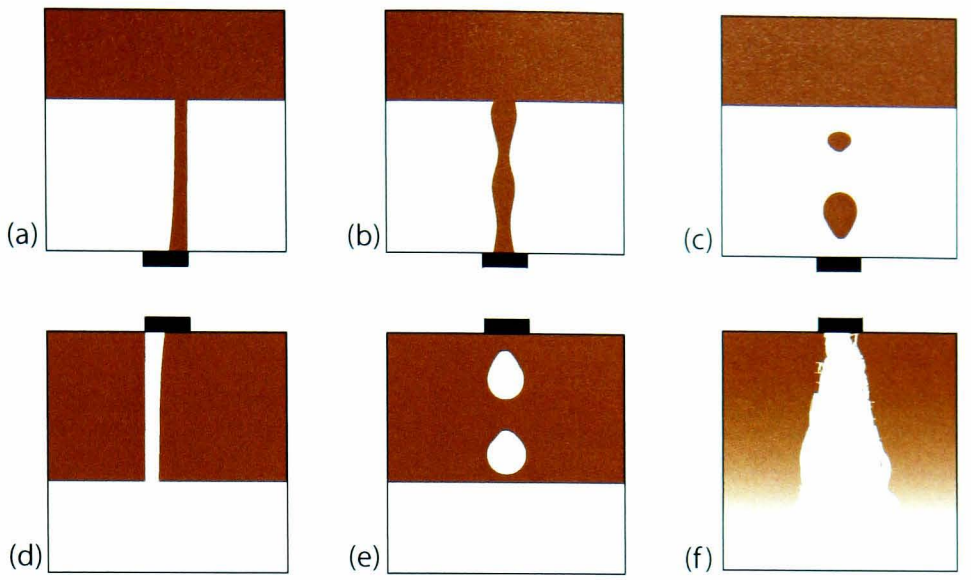

Figure 5.9: Cartoons illustrating the flow patterns observed in the top tank (a, b and c) and bottom tank (d, e, and f). a) Laminar stream of the lighter fluid rising through the more dense liquid, b) non-uniform stream of the less dense liquid, c) bubbles of the lighter liquid, d) laminar stream of the heavier fluid, e) bubble of the heavier liquid, f) turbulent plume of the more dense fluid mixing with the lighter liquid. Dark regions correspond to the less dense liquid.

instabilities with little or no mixing when one of the liquids had high viscosity (and so high viscosity ratio).

Flow in the bottom and top tanks

The following are the flow patterns observed in the top tank (Figure 5.9a-c):

1. laminar stream (rising vertically or next to the bottom wall of the tank),
2. laminar with non-uniform thickness or undulations,
3. fluctuation between a laminar stream and bubbles, and
4. only bubbles.

The buoyant intrusion of the light fluid into the top tank occurred mainly as a laminar stream rising either vertically through the heavier liquid or next to the bottom of the tank (Figure 5.9a). The latter occurred only in experiments with corn oil and water and the pipe inclined more than 20 degrees from vertical, presumably related to the wetting of the oil. All experiments with miscible liquids, and some others with immiscible liquids, exhibited a stream with non–uniform thickness when the pipe was vertical, or with undulations when the pipe was inclined (Figure 5.9b). The stream could also break up into bubbles and create fluctuations between a laminar stream and bubbles of the lighter liquid (Figure 5.9c).

In the bottom tank the descent of the heavier liquid created the following flow patterns (Figure 5.9d-f):

1. laminar stream,
2. fluctuation of a laminar stream with a train of bubbles,
3. bubbles of the heavier fluid, and
4. a turbulent plume.

Among these patterns the laminar stream was the most common (Figure 5.9d). The train of bubbles was related to the formation of bubbles or irregular blobs of the heavier liquid in the pipe (Figure 5.9e). The turbulent plume was observed only with miscible fluids and with the pipe in the vertical position (Figure 5.9f). When the pipe was inclined the stability of the stratified flow caused miscible fluid to sink in laminar form.

5.4.4 Force balance and volumetric flux

The volume flux of the convecting fluids was calculated by timing the position of the horizontal interface in the tanks and calculating the volumetric change of the liquids in one or both tanks (Figure 5.10). The volume flux of the liquids moving from one tank to the other throughout the pipe was found to be constant, with the readings showing a very high precision as evidenced by a high correlation factor (Figure 5.10). Thus, most of the error in the calculation of the flux coefficient or other dimensionless number is contributed by the error in the measurements of the properties of the liquids, rather than the measurements of the flow rates during the experiments. A summary of the experiments that include the properties of the liquids and volumetric fluxes is presented in Tables 5.3 and 5.4. These results will be contrasted to those of Stevenson and Blake (1998) and Huppert and Hallworth (2007), as they have presented results from similar experiments in vertical pipes[10].

Inertial, viscous and interfacial tension forces

The dimensionless groups used herein to analyse the results of the experiments in vertical and inclined pipes, which were derived from dimensional analysis (Section 5.3.1), are presented in Table 5.6. The selected dimensionless groups represent the relative magnitudes of buoyancy, viscous, inertial and interfacial forces. Some of them can be obtained from a

[10] I have not been able to find more data on counter-current flow of immiscible liquids.

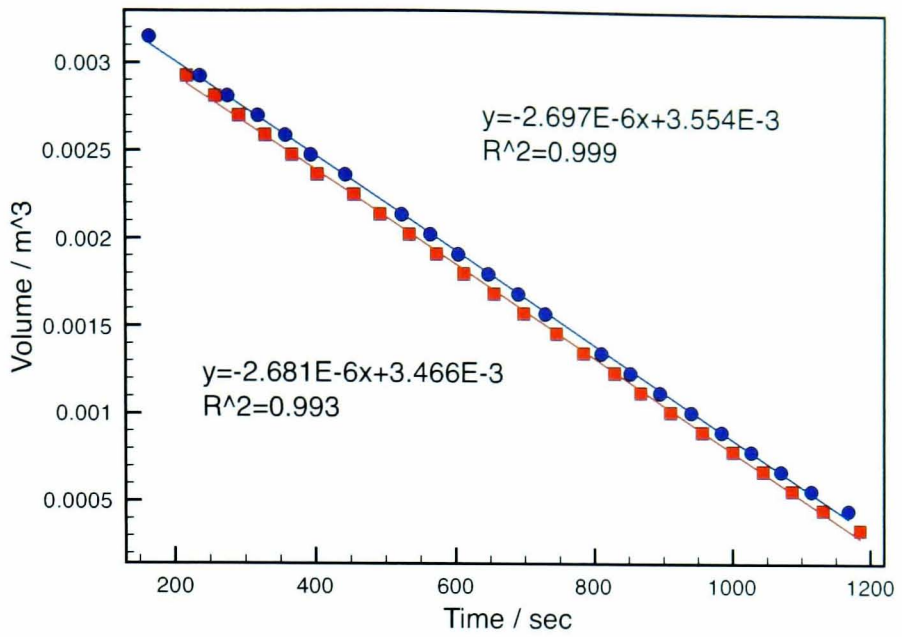

Figure 5.10: Example of the calculation of the flow rate based on the measurements of change in volume of the heavier liquid in the top tank (circles) and of the lighter liquid in the bottom tank (squares) (exp. 525a). The slope of the linear regression line represents the volumetric flux in each case.

combination of the others, but they have been included as they can give extra information about the force balance in the system. I was unable to find, however, values for the interfacial tension between the liquids used in the experiments, and so a constant value of 20 mN m^{-1}, which corresponds to the interfacial tension of olive oil–water (Batchelor, 1967), was used in the formulation of the Eo, Ca and We numbers and, therefore, the analysis using Eo, Ca and We is rather qualitative. Nevertheless, variations of the interfacial tension for different pairs of liquids less than three-fold is expected, which is low compared to the orders of magnitude variations observed for Ca and We. Note that the properties of the less dense (lighter) and more dense (heavier) liquids have been used, regardless of their arrangement in the pipe (instead of core or annular)[11]. Thus, a different viscosity ratio is introduced in this section, $\kappa = \mu_l/\mu_h$, which is identical to $\eta = \mu_c/\mu_a$ in the case of core–annular flow when the core liquid is lighter than the annular liquid. This liquid-liquid arrangement has been observed by Huppert and Hallworth (2007) for all the viscosity ratios considered in their experiments. From a practical point of view, this change is more convenient as it allows the analysis of flow patterns other than only core–annular flow.

The predominance of buoyancy forces in the developed counter–current flow is shown in Figure 5.11, with three regions in which inertial forces ($J > 0.004$, $C_Q < 0.02$), viscous forces ($C_Q > 0.02$, $J < 0.004$), or both inertial and viscous forces ($J > 0.004$, $C_Q > 0.02$)

[11] From the dimensional analysis, the value of the viscosities can be swapped by combining the dimensionless viscosity ratio (in the form of μ_c/μ_a).

Table 5.6: Dimensionless numbers used in the experimental analysis of convective flow.

Name	Symbol	Definition[a]	Forces
Viscosity ratio	κ	$\frac{\mu_l}{\mu_h}$	
Flux coefficient	C_Q	$\frac{Q\mu_h}{g'\Delta\rho R^4}$	viscous/buoyancy
Reynolds number	$Re(Q_l)$	$\frac{Q\rho_l}{\mu_l R}$	inertia/viscous
Reynolds number	$Re(Q_h)$	$\frac{Q\rho_h}{\mu_h R}$	inertia/viscous
$Re(Q_h)\cdot Cq$	J	$\frac{Q^2}{g'R^5}\frac{\rho_h}{\Delta\rho}$	inertia/buoyancy
Eötvös number	Eo	$\frac{g'\Delta\rho R^2}{2\gamma}$	buoyancy/interfacial tension
Capillary number	Ca	$\frac{\mu_h Q}{\gamma R^2}$	viscous/interfacial tension
Weber number	We	$\frac{\rho_l Q^2}{\gamma R^3}$	inertia/interfacial tension

[a] The subscripts l and h stand for the lighter (less dense) and heavier (more dense) liquids; $g' = g\cos\theta$, with θ the angle of inclination of the pipe.

contrast the buoyancy-driven force of the flow. Note the oblique trend of some groups of data from experiments with vertical and inclined pipes; they are the result of different flow rates obtained for the same pair of liquids. Flows with well developed stratification (by density segregation of the liquids) show greater inertial and viscous effects. It is noteworthy that most of the experiments exhibited only one flow rate and that it was constant along the experiment, despite the instabilities and changes in flow patterns observed in vertical pipes. Some differences in the distribution of the data associated with particular flow patterns observed with vertical pipes can be seen in this diagram (Figure 5.11), although the cluster of flow patterns could be related to the grouping of experiments with the same pair of liquids (same properties). For example, experiments that exhibited bubbly or turbulent flow pattern (BT and BT,PS) are grouped in the area where inertial forces are relatively more important. Also, experiments that showed a pseudo-stratified flow pattern only (PS) plot where viscous forces are relatively important. In addition, in the experiments of Stevenson and Blake (1998) inertial forces were not as important as they were in most of the experiments presented in this work. Data from Stevenson and Blake (1998) show lower values of $Re(Q_h)$ compared with the data from Huppert and Hallworth (2007) and this work, which show high values of both $Re(Q_h)$ and $Re(Q_l)$ numbers (Figure 5.12). In terms of Reynolds numbers, however, the different flow patterns observed in vertical pipes cannot be explained. In general, experiments with miscible liquids (and little mixing) show similar relations between viscous, inertial and

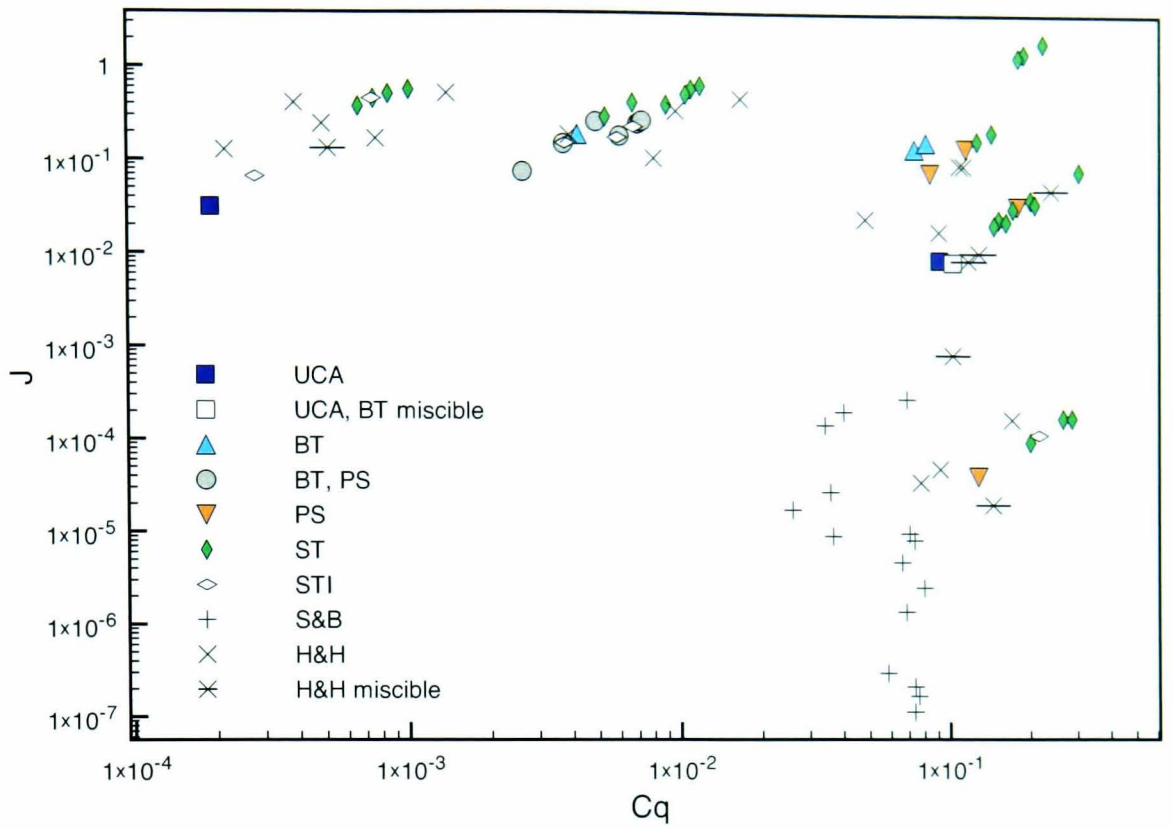

Figure 5.11: Relation between buoyancy, viscous and inertial forces: J vs Cq dimensionless numbers (see Table 5.6). Nomenclature: UCA= unsteady core–annular, BT= bubbly and/or turbulent, PS= pseudo–stratified, ST= stratified, STI= stratified with instabilities, S&B= Stevenson and Blake (1998), H&H= Huppert and Hallworth (2007).

buoyancy forces to those with immiscible fluids.

The variable influence of the interfacial tension in experiments carried out with the pipe in vertical position are shown in Figure 5.13. Whilst the experiments of Stevenson and Blake (1998) are characterised by lower Eo and We numbers, those presented in this work show the highest values of Ca. Considering that the interfacial tension contributes to stabilise the core–annular flow, this characteristic can, perhaps, explain in part the instabilities and flow patterns observed. However, the similitude in values of these three dimensionless numbers between the experiments of Huppert and Hallworth (2007) and some experiments presented in this work, prevent the use of the role of the interfacial tension as an explanation for the different flow patterns observed. As discussed above, it is possible that the initial configuration of the experiments (position of the interface) could have played a major role in the development of different flow patterns.

Volume flux coefficient

Obtaining the volumetric flow rate of the convection of known liquids is one of the end goals of this analysis. To this end, a general expression of the flux coefficient is used,

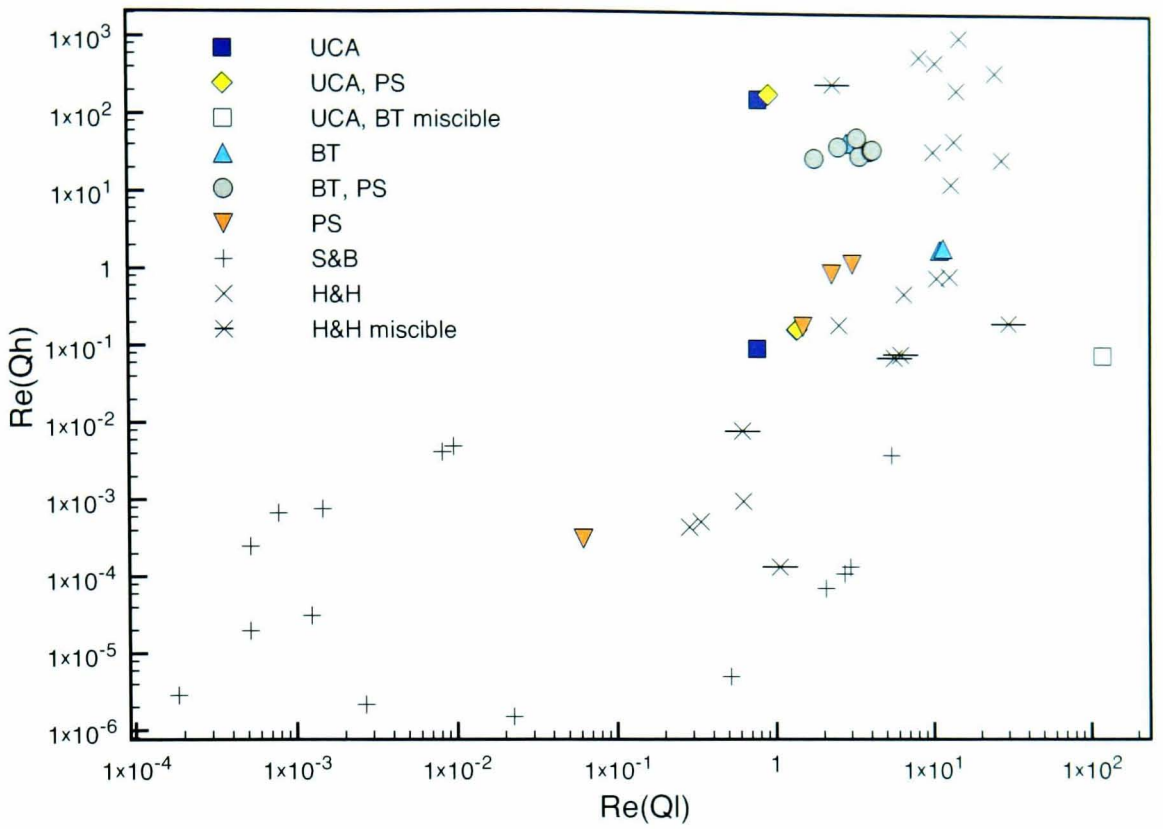

Figure 5.12: Reynolds numbers of the light and heavy liquids, Re(Ql) and Re(Qh), respectively. Nomenclature: UCA= unsteady core–annular, BT= bubbly and/or turbulent, PS= pseudo–stratified, S&B= Stevenson and Blake (1998), H&H= Huppert and Hallworth (2007).

that is valid for both vertical and inclined pipes (Table 5.6). It is worth mentioning again that, although the numerical analysis of core–annular flow was carried out considering the viscosity ratio of the core and annular fluids η, the viscosity ratio has been re-defined as the ratio between the lighter and heavier fluids κ, irrespective of their arrangement in the pipe. Also, the expression for the flux coefficient C_Q (Equation 5.27) was re-defined using the viscosity of the heavier liquid instead of the viscosity of the liquid that flows in the annulus.

As mentioned above, Stevenson and Blake (1998) and Huppert and Hallworth (2007) have used the flux coefficient (or Poiseuille number, see Section 5.3.2) to show their experimental results on counter–current core-annular flows in vertical pipes. The results of the experiments carried out in this work are in agreement with the values of the flux coefficient C_Q obtained by the previous authors (Figure 5.14a). Nevertheless, it is noticeable that the values of C_Q obtained herein are slightly higher. The reason for that difference is the development of instabilities and flow patterns other than perfect core–annular. In effect, the experimental results presented here, with vertical and inclined pipes, evidence a relation between the flow pattern and the steady volume flux (and C_Q). Examples of the variation of the flux coefficient with varying angle of inclination of the pipe and flow pattern, for a given viscosity ratio, are shown in Figures 5.15-5.16; experimental results with similar liquids taken

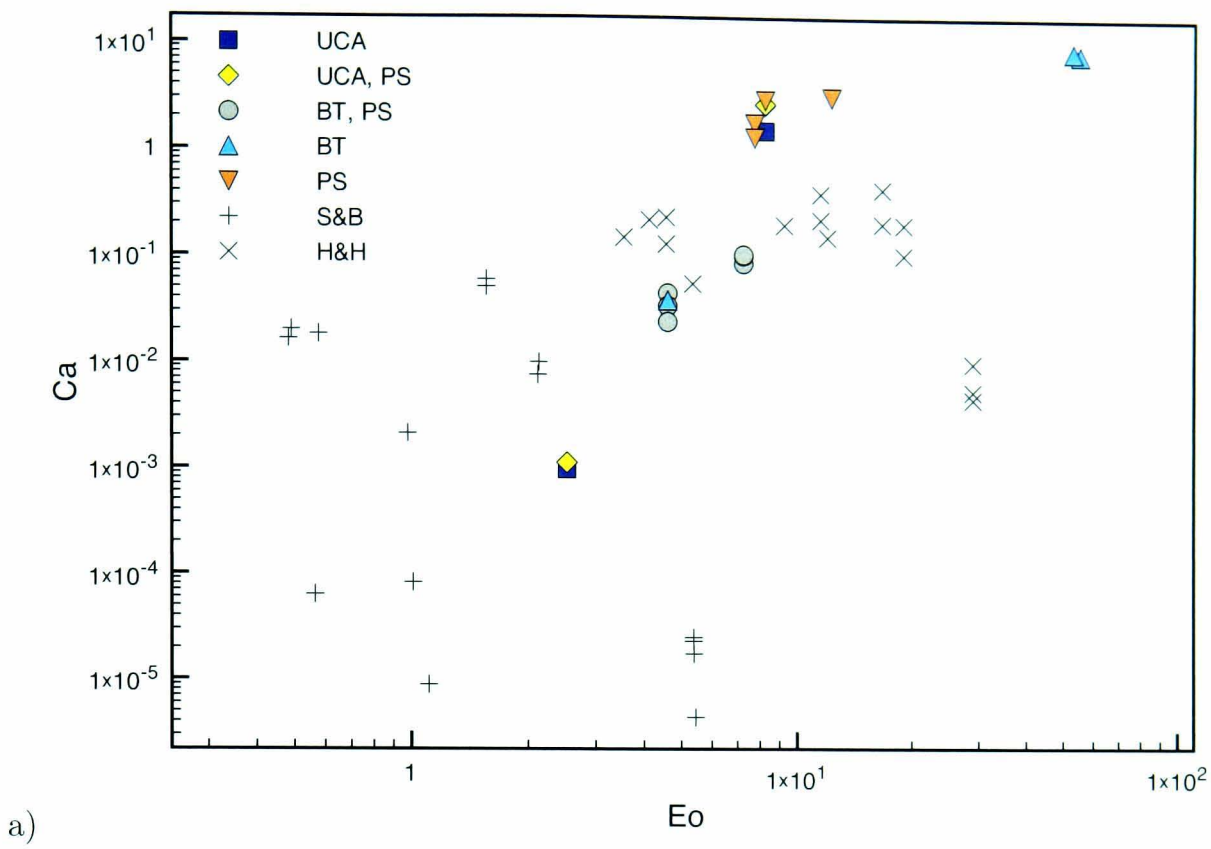

a)

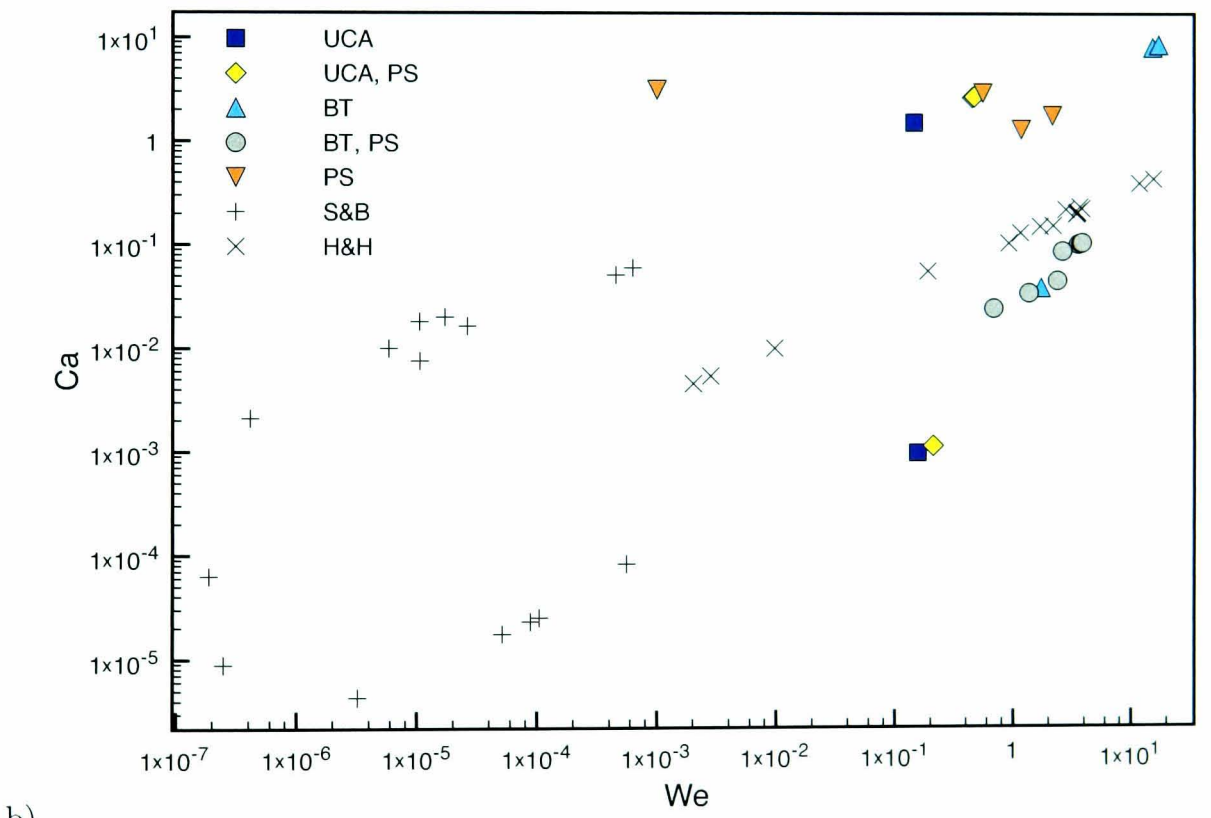

b)

Figure 5.13: Relative influence of the interfacial tension in experiments with vertical pipes, shown with Ca, Eo and We numbers (see Table 5.6). Nomenclature: UCA= unsteady core–annular, BT= bubbly and/or turbulent, PS= pseudo–stratified, S&B= Stevenson and Blake (1998), H&H= Huppert and Hallworth (2007). Note that the values of these three dimensionless numbers are not accurate since the same value of interfacial tension has been used in all experiments; nevertheless, the interfacial tension for different pair of liquids is expected to vary less than one order of magnitude and, therefore, they allow the comparison between experiments.

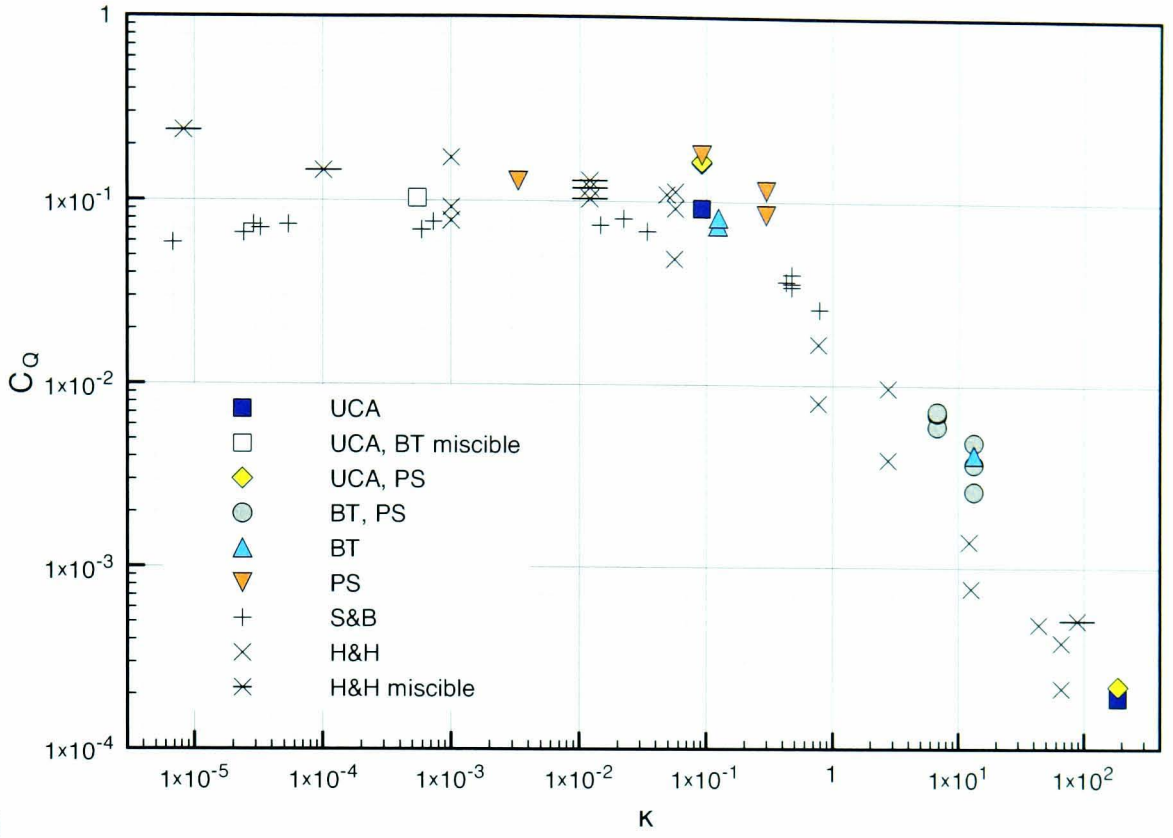

a)

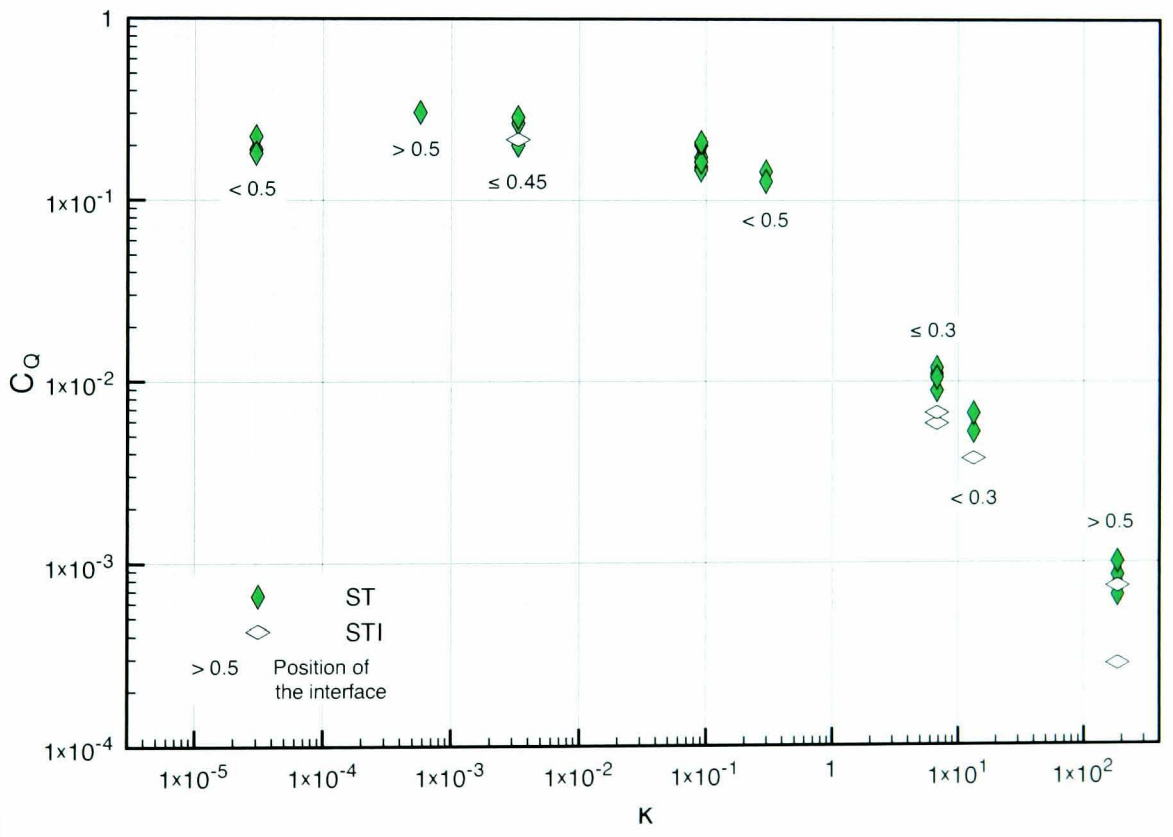

b)

Figure 5.14: Flux coefficient calculated from experiments with a) vertical and b) inclined pipes. Observations of the position of the interface in stratified flow are also shown (see Table 5.5). Nomenclature: UCA= unsteady core–annular, BT= bubbly and/or turbulent, PS= pseudo–stratified, ST= stratified, STI= stratified with instabilities, S&B= Stevenson and Blake (1998), H&H= Huppert and Hallworth (2007).

from Huppert and Hallworth (2007) were also included. In general, for a given pair of liquids those experiments that exhibited core–annular flow show lower flow rates than those that exhibited bubbly or turbulent flow, and experiments that exhibited pseudo–stratified flow can show even higher flow rates. Similarly, experiments with inclined pipes that exhibited well developed stratified flow yielded the highest values of C_Q, and those experiments that showed instabilities yielded some of the lower values (Figures 5.14-5.16). Thus, for a given viscosity ratio (or pair of liquids), these new results suggest that for any flow pattern developed within the pipe, the flux coefficient lies in the range of values defined by the perfect core–annular flow (lower limit) and stratified flow (upper limit).

Apart from the flow pattern, the values of C_Q in vertical pipes strongly depend on the viscosity ratio κ of the liquids, in the case of κ greater than about 0.1 (Figure 5.14a). Below this value, C_Q appears to lie in a constant range between about 0.05 and 0.2. A similar scatter of the data is observed in experiments with $\kappa > 0.1$. Variations of C_Q within the range of variation for a particular viscosity ratio are likely to be related to inaccuracies of the measurements, unknown position of the interface in the case of some data from Stevenson and Blake (1998) (see Section 5.3.2), different flow patterns (see Figures 5.15-5.16 for examples), and miscibility of the liquids. The values of C_Q obtained with inclined pipes are generally greater than those obtained with vertical pipes, and they slightly increase at higher inclination angles. (This increase of C_Q with the angle of inclination does not necessarily mean an increase in flow rate, since the inclination angle is also considered in the expression of C_Q.) Values of C_Q are also higher when the cross-sectional area of the heavier fluid is bigger (higher position of the interface) in the case of $\kappa < 1$ (Figure 5.14b). This particular observation seems reasonable since the heavier liquid is also more viscous and, therefore, experiences a higher viscous dissipation that reduces its velocity further than that of the lighter and less viscous fluid. The opposite effect is expected when the position of the interface is higher in experiments with $\kappa > 1$. These observations suggest a similar influence of the position of the interface in core–annular flows, that is, the bigger the cross-sectional area of the more viscous liquid (but only to a certain unknown value), the higher flow rate.

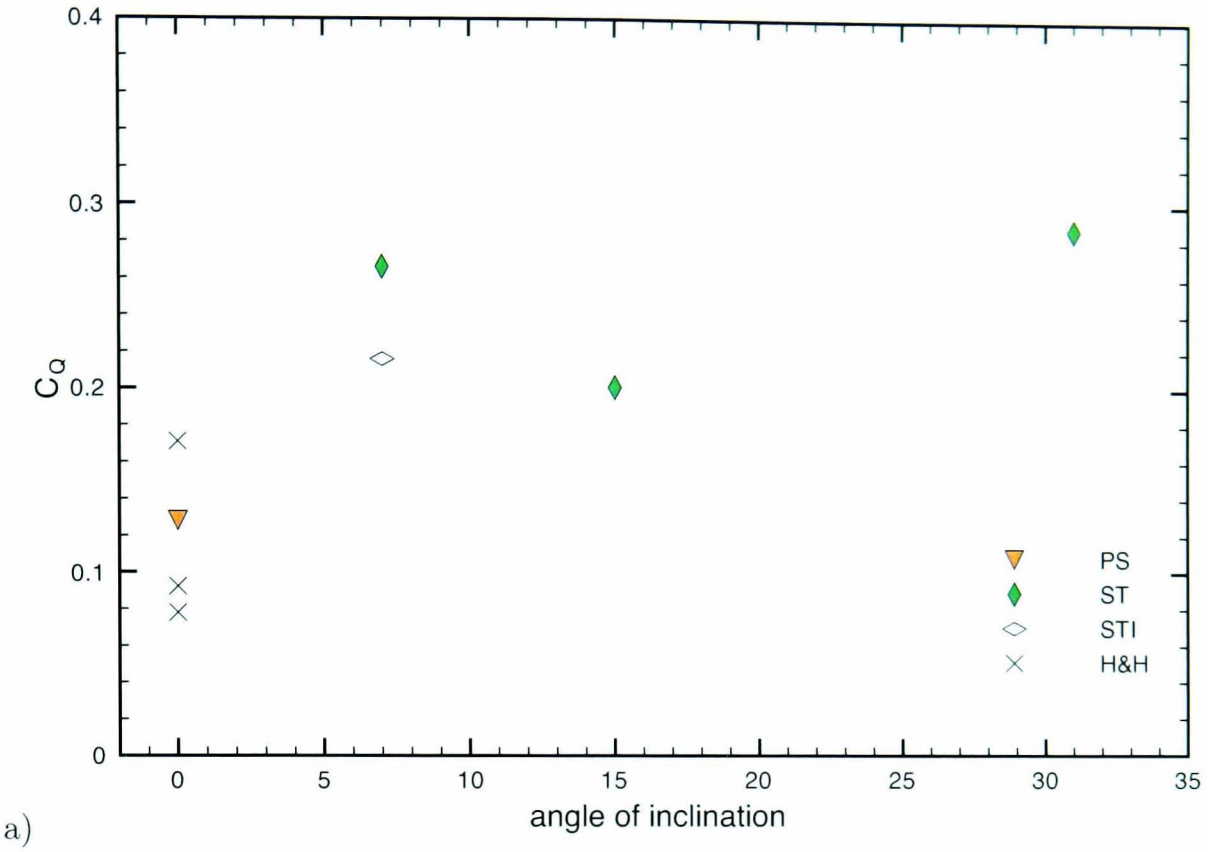

a)

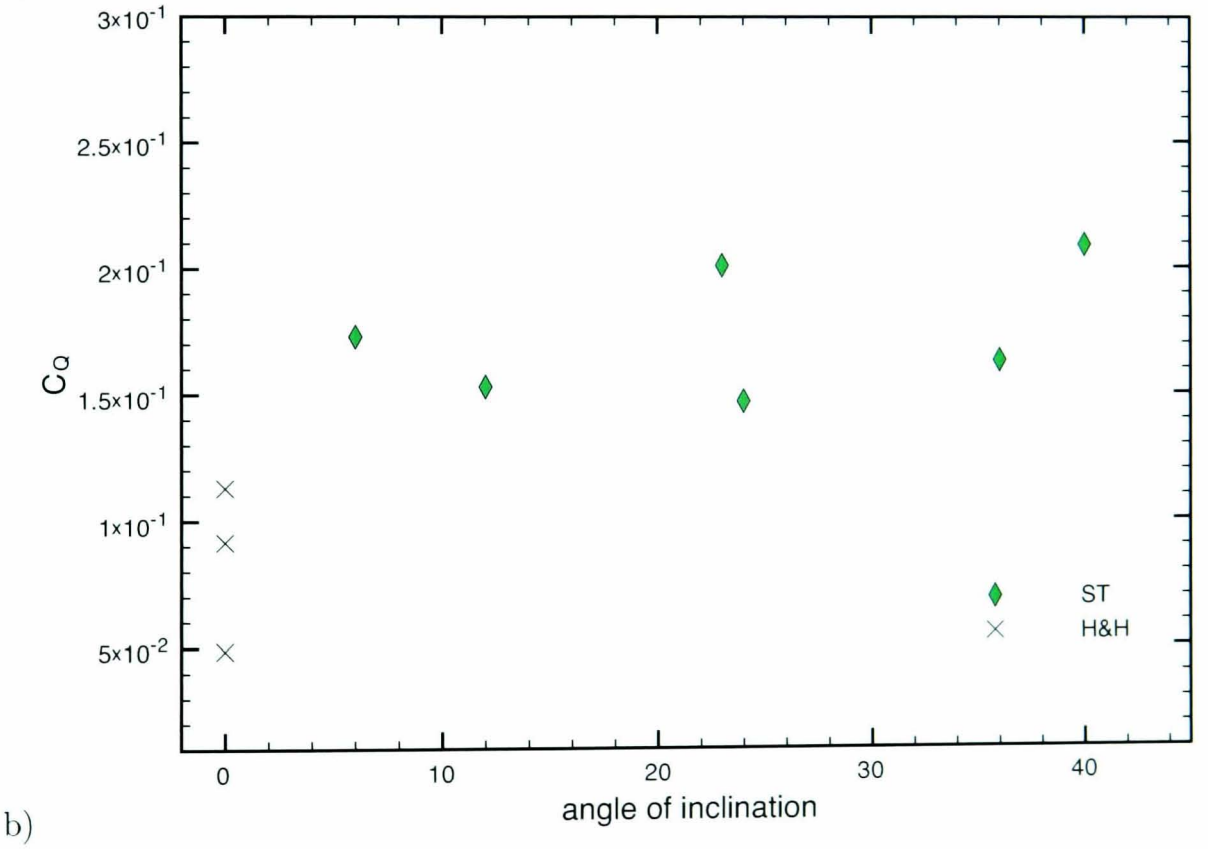

b)

Figure 5.15: Variation of C_Q with the angle of inclination of the pipe and flow pattern for viscosity ratios lower than 1. a) Experiments with sunflower oil and pure golden syrup, $\kappa = 3,32{\cdot}10^{-3}$; b) Experiments with vegetable oil and pure glycerol, $\kappa = 9,1{\cdot}10^{-2}$. Nomenclature: PS= pseudo–stratified, ST= stratified, STI= stratified with instabilities, H&H= Huppert and Hallworth (2007) (in a) exp. with rapeseed oil and pure syrup, $\kappa = 1,002 \cdot 10^{-3}$; in b) exp. with corn and rapeseed oil and pure glycerol, $\kappa \sim 5,6 \cdot 10^{-2}$).

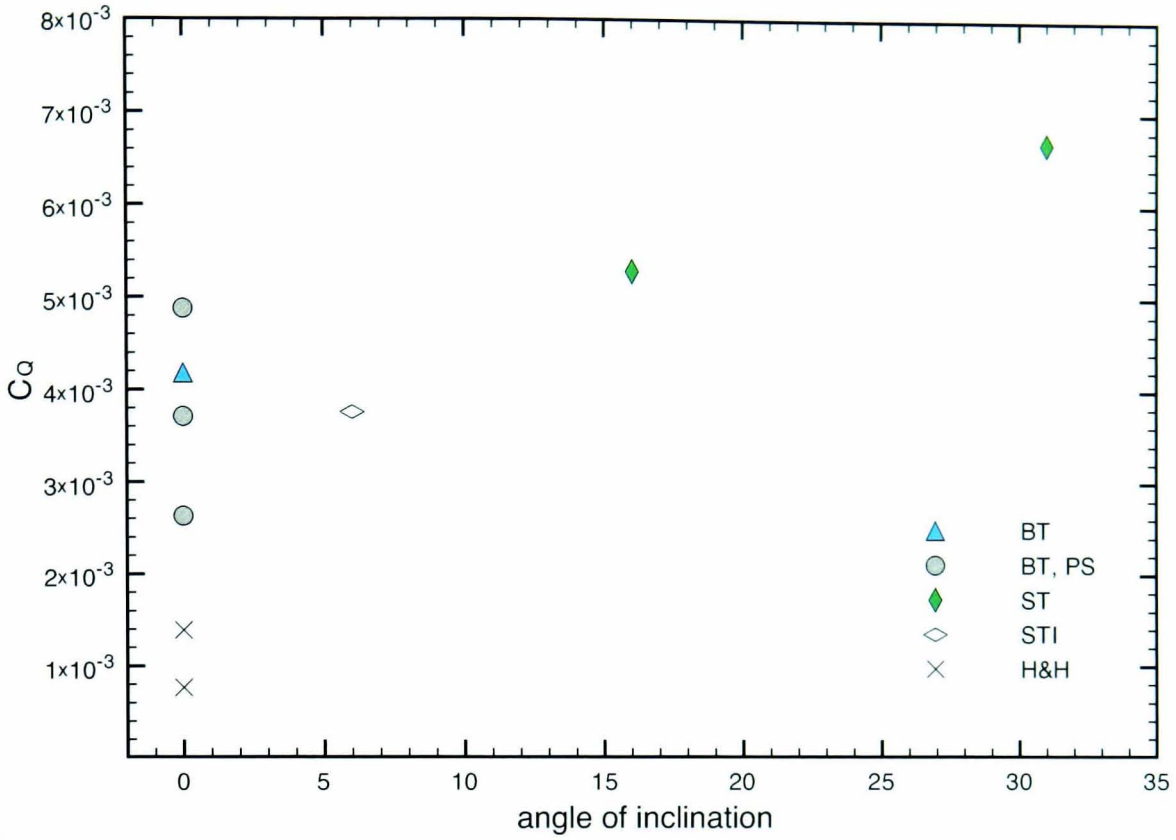

a)

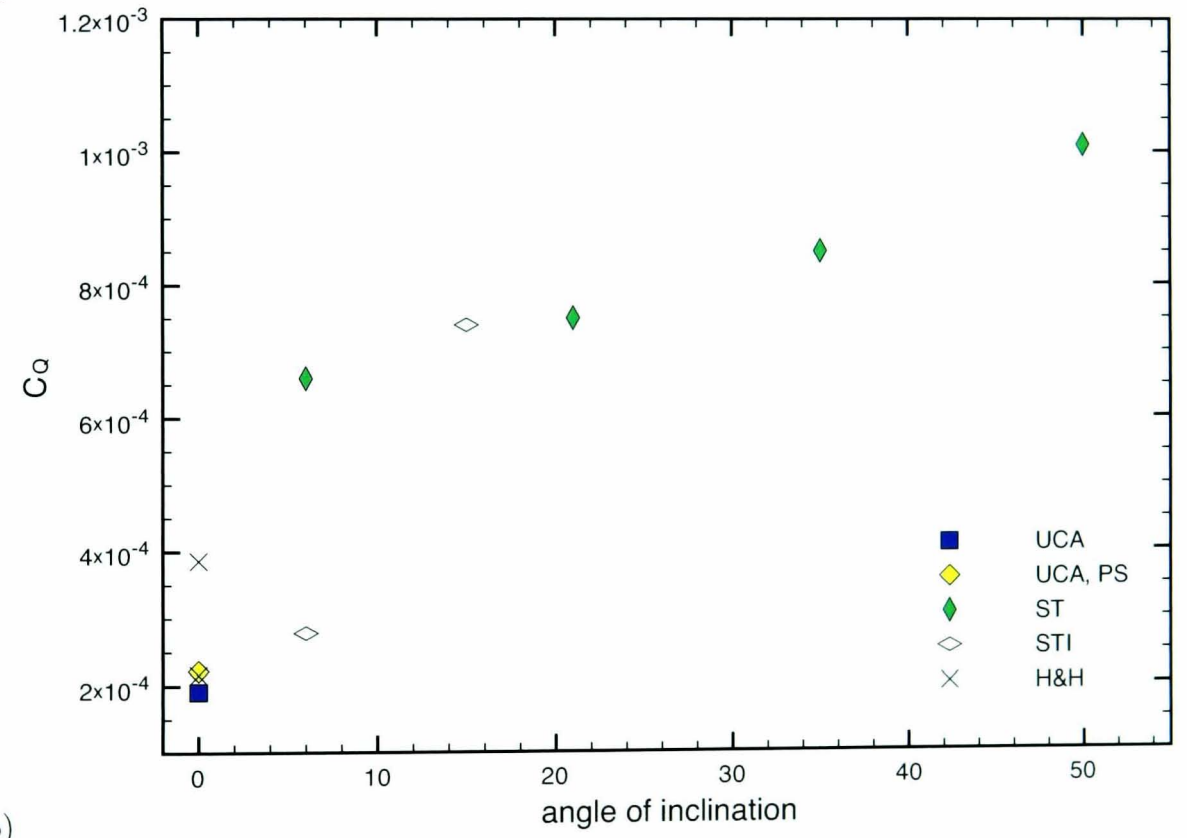

b)

Figure 5.16: Variation of C_Q with the angle of inclination of the pipe and flow pattern for viscosity ratios higher than 1. a) Experiments with vegetable oil and dilute glycerol, $\kappa = 1,33 \cdot 10^1$; b) Experiments with corn oil and water, $\kappa = 1,86 \cdot 10^2$. Nomenclature: UCA= unsteady core–annular, BT= bubbly and/or turbulent, PS= pseudo–stratified, ST= stratified, STI= stratified with instabilities, H&H= Huppert and Hallworth (2007) (in a) exp. with rapeseed oil and dilute glycerol, $\kappa \sim 1,25 \cdot 10^1$; in b) exp. with rapeseed oil and water, $\kappa = 6,6 \cdot 10^1$).

5.5 Two-fluid model of convection in tubes

One option to model multiphase flows in constrained systems is the modeling of each phase (or fluid) with their own set of conservation equations, plus constitutive relations for the interfacial transfer (e.g. Park *et al.*, 1998). For isothermal steady-state flows the continuity equations reduce to Equation 5.10 in the case of convective flow:

$$\begin{aligned} \tfrac{\partial}{\partial x}(\alpha_a U_a) + \tfrac{\partial}{\partial x}(\alpha_b U_b) &= 0 \\ \alpha_a U_a + \alpha_b U_b &= U_m \\ Q_a + Q_b &= Q_m \end{aligned} \tag{5.38}$$

where these three equations are analogous, and the last two equations are the integral form of the first one; α_j is the volume fraction of a phase j ($\sum_j \alpha_j = 1$), U is the average velocity, the x co-ordinate is parallel to the axis of the pipe, and Q the volumetric flux; the subscripts a and b denote two different phases, and m the mixture.

By assuming the same pressure in both fluids, which means neglecting pressure differences due to curved interfaces as well as mass transfer and dynamic effects, the momentum equations of both liquids can be combined to eliminate the pressure term and to yield an expression for the averaged balance of stresses in the tube. Thus, the general equation that describes the combined momentum of the mixture with two phases a and b is (Johnston, 1984; Ullmann *et al.*, 2003)

$$\begin{aligned} &\rho_b \tfrac{\partial U_b}{\partial t} - \rho_a \tfrac{\partial U_a}{\partial t} + \rho_b U_b \tfrac{\partial U_b}{U_x} - \rho_a U_a \tfrac{\partial U_a}{\partial x} + (\rho_b - \rho_a) g \cos\beta \tfrac{\partial h_b}{\partial x} + \tfrac{\partial}{\partial x}(P_{ib} - P_{ia}) \\ &\quad = -\tau_b \tfrac{S_b}{\alpha_b A} \pm \tau_i S_i \left(\tfrac{1}{\alpha_a A} + \tfrac{1}{\alpha_b A} \right) + \tau_a \tfrac{S_a}{\alpha_a A} + (\rho_b - \rho_a) g \sin\beta \end{aligned} \tag{5.39}$$

where h is the position of the interface, P the pressure, ρ the density, β the angle with the horizontal line, $\tau_{a,b}$ the wall shear stress, τ_i the interfacial shear stress, S the wetted perimeter of the liquid, A the cross-sectional area of the tube, and g the acceleration of gravity. The left-hand side of Equation 5.39 models the unsteadiness of the flow as well as the non-uniform velocity and pressure gradients at the interface, whereas the right-hand side models the stresses and buoyancy of the flow. For the cases of perfect core–annular flow and perfect (steady and uniform) stratified flow, all the terms on the left hand side of Equation 5.39 can be neglected.

Thus, this model uses the one–dimensional momentum equation to model the flow of a two-phase or liquid–liquid flow under certain assumptions and simplifications. The most

common assumptions in the modeling of two immiscible liquids is that the flow is laminar, thus neglecting inertial terms, and that the shear stresses can be modeled using the Blasius equations, which establish a relation between the magnitude of the friction at the walls or liquid interface and the Reynolds number of the fluids. The closure of the model can involve the arrangement of some equations that describe the relation between the shear stress and the velocity of the fluid, as well as some empirical parameters that are necessary to fit the laboratory data with the results. It is noteworthy that the one-dimensional two-fluid model is semi-empirical, and many slightly different approaches can be incorporated into the model. In this section, the best results obtained using the approaches that use the minimum amount of empirical parameters, and that are able to represent the laboratory data, are presented.

5.5.1 Vertical core–annular flow

The integral form of the momentum equations for each fluid in a core-annular arrangement depicted in Figure 5.17 can be expressed as follow:

$$-A_a \frac{dp}{dz} + \tau_a S_a + \tau_i S_i - A_a \rho_a g = 0 \tag{5.40}$$

$$-A_c \frac{dp}{dz} - \tau_i S_i - A_c \rho_c g = 0 \tag{5.41}$$

where the superscripts a, c and i refer to the annular and core fluids, and to the interface between them, respectively; also $A_a = \alpha_a A$ and $A_c = \alpha_c A$. Substraction of the two equations yield:

$$\tau_a \frac{S_a}{A_a} + \tau_i S_i \left(\frac{1}{A_a} + \frac{1}{A_c} \right) - (\rho_a - \rho_c) g = 0 \tag{5.42}$$

which corresponds to Equation 5.39 for the case of perfect core–annular flow.

The average shear stress acting on the wall and at the fluid interface are expressed in terms of the average velocities of the fluids (Ullmann *et al.*, 2003; Wongwises *et al.*, 1998; Johnston, 1984; Fairuzov, 2003):

$$\tau_a = -\frac{1}{2} f_w \rho_a U_a |U_a| \tag{5.43}$$

$$\tau_i = \frac{1}{2} f_i \rho_c (U_c - U_a) |U_c - U_a| \tag{5.44}$$

where f_w and f_i are appropriate friction factors that depend on the fluid properties, configuration of the flow in the tube, and constants associated with the type of flow. The friction

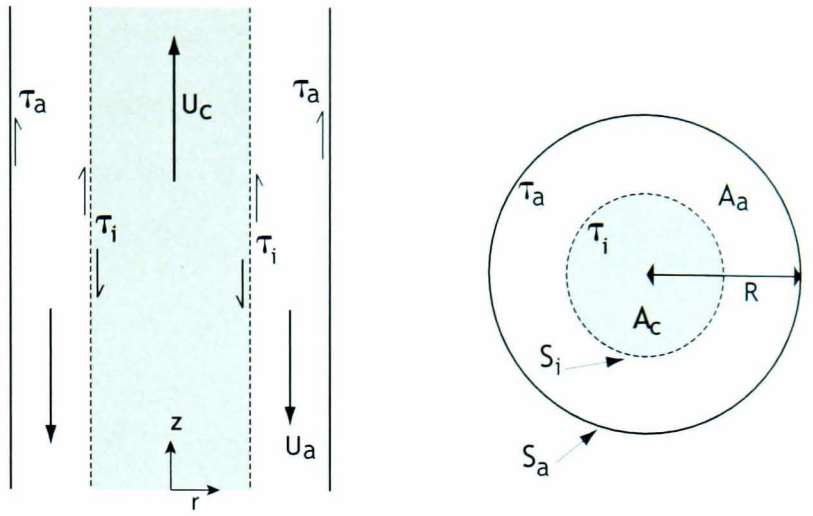

Figure 5.17: Profile and cross–section of the core-annular counter-current flow for the solution of the two-fluid model.

factor for the interfacial and fluid-wall stresses are given, in general form, by (e.g. Johnston, 1984; Fairuzov, 2003):

$$f_w = \frac{C_w}{(Re_a)^n} = C_w \left(\frac{\rho_a D_a |U_a|}{\mu_a} \right)^{-n} \tag{5.45}$$

$$f_i = \frac{C_i}{(Re_c)^m} = C_i \left(\frac{\rho_c D_c |U_c|}{\mu_c} \right)^{-m} \tag{5.46}$$

where $D_{a,c}$ is the equivalent hydraulic diameter of the annular or core liquids, $Re_{a,c}$ the Reynolds number of the fluid and $\mu_{a,c}$ its viscosity. The equivalent hydraulic diameter for both the annular and core liquids is defined as

$$D_{a,c} = 4\frac{A_{a,c}}{S_{a,c}} \tag{5.47}$$

For laminar flows $C_{w,i} = 16$ and $n = m = 1$ (Brauner, 1998; Ullmann *et al.*, 2003). Thus, following Equations 5.43-5.44 the shear stresses can be expressed as follow:

$$\tau_a = -8\mu_a \frac{U_a}{D_a} \tag{5.48}$$

$$\tau_i = 8\frac{\mu_c}{D_c} \frac{(U_c - U_a)^2}{|U_c|} \tag{5.49}$$

It is common to find that in studies of co–current flow of oil and water, the interfacial stress is defined similar to that of the wall shear stress but using the density of the fastest fluid and the velocity difference between the fluids (e.g. Brauner, 1998; Ullmann *et al.*, 2003). Likewise, the interfacial friction factor is defined equivalently to the liquid-wall friction factor (Equation 5.45), with the density, viscosity, hydraulic diameter and velocity of one of the

fluids, which is normally chosen to be the fastest. In this work, however, the constitutive relation of the interfacial shear stress and the corresponding friction factor are based on a slightly different formulation that yielded a better fit to the experimental data. This formulation has also been used in models of stratified flows (Brauner *et al.*, 1998).

Combination of the above definitions with the general momentum equation (Equation 5.42) yield

$$-Q_a \mu_a K_a + Q_c \mu_c K_c = \Delta \rho g \tag{5.50}$$

where the two factors

$$K_a = 8 \frac{S_a}{D_a A_a^2} \tag{5.51}$$

$$K_c = 8 \frac{S_i A_c}{D_c} \left(\frac{1}{A_a} + \frac{1}{A_c} \right)^3 \tag{5.52}$$

depend on the geometry of the system (conduit radius and position of the interface). Using the continuity equation to replace the volume flow rate of the annular liquid in Equation 5.50, and replacing the equivalent hydraulic diameter, wetted and interfacial perimeters, and cross–sectional areas in the last two equations, an expression for the volumetric flux of the core fluid is obtained:

$$Q_c = \frac{\Delta \rho g R^4}{\mu_a} \chi \tag{5.53}$$

where

$$\chi = (\tilde{K}_a + \eta \tilde{K}_c)^{-1} \tag{5.54}$$

is a function that depends on the position of the interface α and viscosity ratio η, where

$$\tilde{K}_a = \frac{8}{\pi} (1 - \alpha^2)^{-3} \tag{5.55}$$

$$\tilde{K}_c = \frac{8}{\pi} (1 - \alpha^2)^{-3} \alpha^{-4} \tag{5.56}$$

Note that in order to obtain the relationship between the volumetric flux Q and the flux coefficient C_Q in Equation 5.53, the dynamic viscosity in such equation must correspond to that of the more dense (or heavier) fluid, and the viscosity ratio between the core and annular liquids, $\eta = \mu_c / \mu_a$, must be replaced by the viscosity ratio between the lighter and heavier liquids, $\kappa = \mu_l / \mu_h$, and thus $C_Q = \chi$. In effect, results from the laboratory experiments carried out by Stevenson and Blake (1998) and Huppert and Hallworth (2007) are in agreement with this idea. That is, in core–annular flows the heavier liquid goes in the

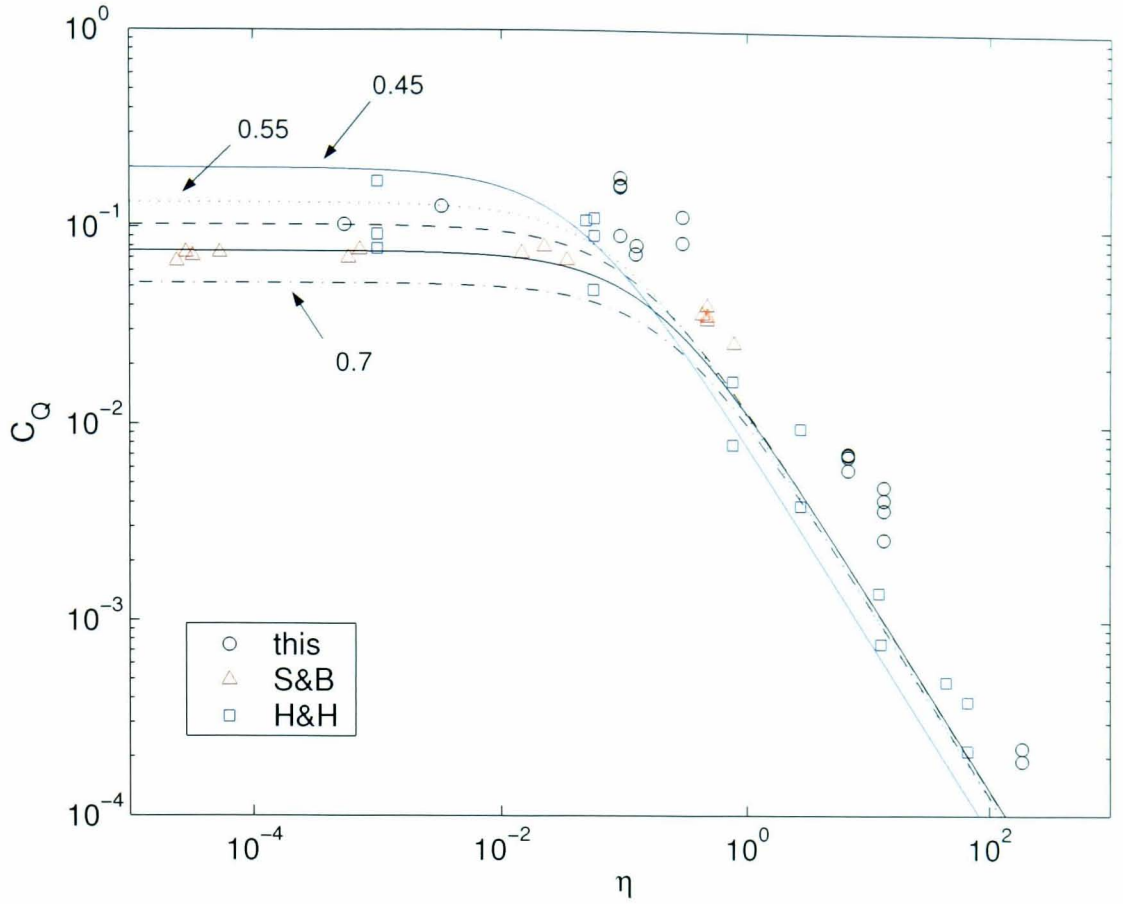

Figure 5.18: Flux coefficient obtained from Equations 5.53-5.54 considering five values for the position of the interface: 0.45 (solid line), 0.5 (dotted line), 0.6 (dashed line), 0.65 (solid dark line) and 0.7 (dash-dot line). Laboratory data from Stevenson and Blake (1998) ('S&B'), Huppert and Hallworth (2007) ('H&H') and this work ('this'). This solution assumes that the core and annular fluids correspond to the lighter and heavier liquids, respectively, and $C_Q = \chi$.

annulus of the tube.

The relation between the flux coefficient ($C_Q = \chi$) and viscosity ratio, based on Equation 5.54, is shown in Figure 5.18. Note that this model correctly predicts that C_Q increases as the cross-sectional area of the heavy fluid increases (α decreases) when its viscosity is greater than that of the less dense fluid, at least for η less than about 0.1. When the viscosity of the light fluid (flowing in the core) is greater, C_Q increases when its cross-sectional area (α) increases. It is clear that, in order to determine the flow rate of the convection, information about the position of the interface is required (Equations 5.53-5.54). Unfortunately, only a few measurements of this value were performed by Stevenson and Blake (1998). Nevertheless, and as discussed in Section 5.4.4, for a given viscosity ratio the core–annular flow is better represented by the minimum experimental value of C_Q. Inspection of Figure 5.18 indicates that a good approximation to the data available, for viscosity ratios lower than about 0.2, is obtained with a value of $\alpha = 0.65$. Replacing this value in the equations above

(Equations 5.54-5.56), the following expression of the 'minimum' C_Q is obtained:

$$C_Q = (13.22 + \kappa\ 2.36)^{-1} \tag{5.57}$$

in which the viscosity ratio based on the core and annular liquids η has been changed by the viscosity ratio of the light and heavy fluids κ. With this relationship, the value of the flux coefficient within the range where it is nearly constant ($\kappa < 0.01$) is $C_Q = 0.075$. For $\kappa > 0.2$ the solution obtained by setting $\alpha = 0.65$ seems to overestimate the experimental data, and lower values between $\alpha = 0.45$ and $\alpha = 0.65$ are required to fit the solution with the data at different viscosity ratios. This variation might be the result of different configurations of the fluids (positions of the interface) in experiments that involved different pair of liquids.

5.5.2 Stratified laminar flow

The procedure to obtain a model for the steady-state stratified flow in inclined tubes is similar to that of core–annular flows. It follows from the fluid arrangement depicted in Figure 5.19 that the momentum equations for each fluid are

$$-A_h \frac{dp}{dz} + \tau_h S_h + \tau_i S_i - A_h \rho_h g \cos\theta = 0 \tag{5.58}$$

$$-A_l \frac{dp}{dz} - \tau_l S_l - \tau_i S_i - A_l \rho_l g \cos\theta = 0 \tag{5.59}$$

were the subscripts h and l refer to the heavier (more dense) and lighter (less dense) fluids. Note that a planar fluid interface is considered in this case, with no consideration of curvature. Combination of both equations yield

$$\tau_h \frac{S_h}{A_h} + \tau_l \frac{S_l}{A_l} + \tau_i S_i \left(\frac{1}{A_h} + \frac{1}{A_l} \right) - (\rho_h - \rho_l) g \cos\theta = 0 \tag{5.60}$$

Like in the case of core–annular flow (Equations 5.43-5.44), closure relationships are needed for the shear stresses. A first approximation considers the typical relation for the shear stresses at the wall (Brauner and Maron, 1992; Brauner, 1998; Wongwises *et al.*, 1998), like in the model for core-annular flow, but a different relation for the interfacial shear stress (Ullmann *et al.*, 2003):

$$\tau_h = -\frac{1}{2} \rho_h f_h U_h |U_h| \tag{5.61}$$

$$\tau_l = \frac{1}{2} \rho_l f_l U_l |U_l| \tag{5.62}$$

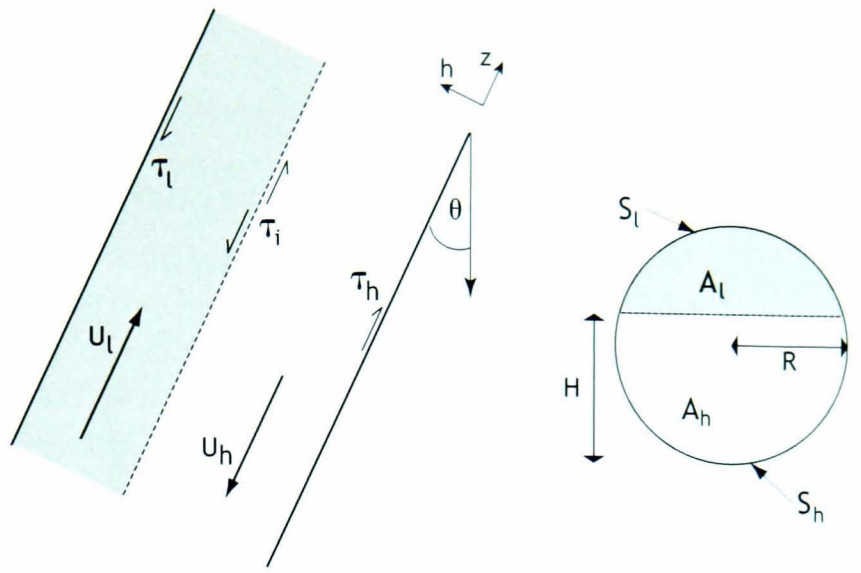

Figure 5.19: Profile and cross–section of the stratified laminar counter-current flow for the solution of the two-fluid model. The heavier liquid goes at the bottom of the pipe and the lighter liquid on top, and the interface is planar. The position of the interface is represented by the parameter H.

$$\tau_i = \frac{1}{2}\rho_i f_i |U_i|(U_l - U_h) \tag{5.63}$$

where the density ρ_i, velocity U_i and friction factor f_i correspond to those of the faster liquid; by conservation of volume, the faster fluid is associated to a smaller cross-sectional area. Then,

$$\begin{aligned} \rho_i = \rho_h, \quad U_i = U_h, \quad f_i = f_h \qquad H < 0.5 \\ \rho_i = \rho_l, \quad U_i = U_l, \quad f_i = f_l \qquad H \geqslant 0.5 \end{aligned} \tag{5.64}$$

The hydraulic radius of both fluids is defined as in Equation 5.47. Combining these equations into Equation 5.60, the following relation is obtained:

$$Q_l = \frac{\Delta\rho g \cos\theta R^4}{\mu_h} C_Q \tag{5.65}$$

with

$$C_Q = (\tilde{K}_h + \kappa\tilde{K}_l + \kappa\tilde{K}_i)^{-1} \tag{5.66}$$

where $\kappa = \mu_l/\mu_h$, and

$$\tilde{K}_h = \frac{\tilde{S}_h^2}{\tilde{A}_h^3}, \qquad \tilde{K}_l = \frac{\tilde{S}_l^2}{\tilde{A}_l^3} \tag{5.67}$$

$$\begin{aligned} \tilde{K}_i &= \frac{\tilde{S}_i\tilde{S}_h}{\tilde{A}_h}\left(\frac{1}{\tilde{A}_l} + \frac{1}{\tilde{A}_h}\right)^2 \qquad H < 0.5 \\ \tilde{K}_i &= \frac{\tilde{S}_i\tilde{S}_l}{\tilde{A}_l}\left(\frac{1}{\tilde{A}_l} + \frac{1}{\tilde{A}_h}\right)^2 \qquad H \geqslant 0.5 \end{aligned} \tag{5.68}$$

Here, $\tilde{K}_{h,l,i}$ are coefficients that describe the geometry of the system, which strongly depend on the position of the interface. The expressions for the non-dimensional cross-sectional

Table 5.7: Expressions for the areas and perimeters considered in a stratified flow developed in a pipe, as shown in Figure 5.19. $\xi = 2\tilde{H} - 1$ with $\tilde{H} = H/D$ where D is the diameter of the pipe. After Brauner and Maron (1992).

Parameter	Expression
$\tilde{A} = A/D^2$	$\pi/4$
$\tilde{A}_l = A_l/D^2$	$\frac{1}{4}\left[\cos^{-1}(\xi) - \xi(1-\xi^2)^{1/2}\right]$
$\tilde{A}_h = A_h/D^2$	$\frac{1}{4}\left[\pi - \cos^{-1}(\xi) + \xi(1-\xi^2)^{1/2}\right]$
$\tilde{S}_l = S_l/D$	$\cos^{-1}(\xi)$
$\tilde{S}_h = S_h/D$	$\pi - \cos^{-1}(\xi)$
$\tilde{S}_i = S_i/D$	$(1-\xi^2)^{1/2}$

areas $\tilde{A}_{h,l}$ and perimeters $\tilde{S}_{h,l,i}$ are given in Table 5.7 (after Brauner and Maron (1992)). The relationship between C_Q and the viscosity ratio $\kappa = \mu_l/\mu_h$ that arise from Equation 5.66 is shown in Figure 5.20. Clearly, for values of the viscosity ratio lower than unity (lighter liquid less viscous than heavier liquid) the solution is better represented by the case in which $\tilde{H} \geqslant 0.5$, that is, when the average velocity of the lighter fluid (on top) is higher. When $\kappa > 1$ the solution for the case $\tilde{H} < 0.5$ shows a better fit of the experimental data, as the curve should pass over the data with highest C_Q (for a given viscosity ratio). These results, however, are in disagreement with observations of the position of the interface obtained from experiments (Section 5.4.3, Table 5.5), in which the heavier fluid occupied a bigger cross-sectional area at viscosity ratios below and above one (and the same is true for the lighter fluid).

On the basis of the exact solution of fully developed laminar flow between two parallel plates, Ullmann *et al.* (2004) proposed some modifications to the shear stresses that made the two-fluid model compare well with the exact solution of concurrent and counter-current flow in pipes. These modifications are based on the formulation of the interfacial shear stress, similar to the expression in Equation 5.68, and the introduction of correction factors in the wall and interfacial stresses. Hence, for the case of buoyancy-driven counter-current flow investigated herein, and following Ullmann *et al.* (2004), the stresses τ_h, τ_l, and τ_i were multiplied by the correction factors F_h, F_l and F_i, respectively (Equations 5.61-5.63):

$$F_h = \frac{1 + \frac{g_{h1}}{\tilde{a}\kappa} + g_{h2}\tilde{a}}{1 + \frac{1}{\tilde{a}\kappa}} \tag{5.69}$$

$$F_l = \frac{1 + g_{l1}\tilde{a}\kappa + \frac{g_{l2}}{\tilde{a}}}{1 + \tilde{a}\kappa} \tag{5.70}$$

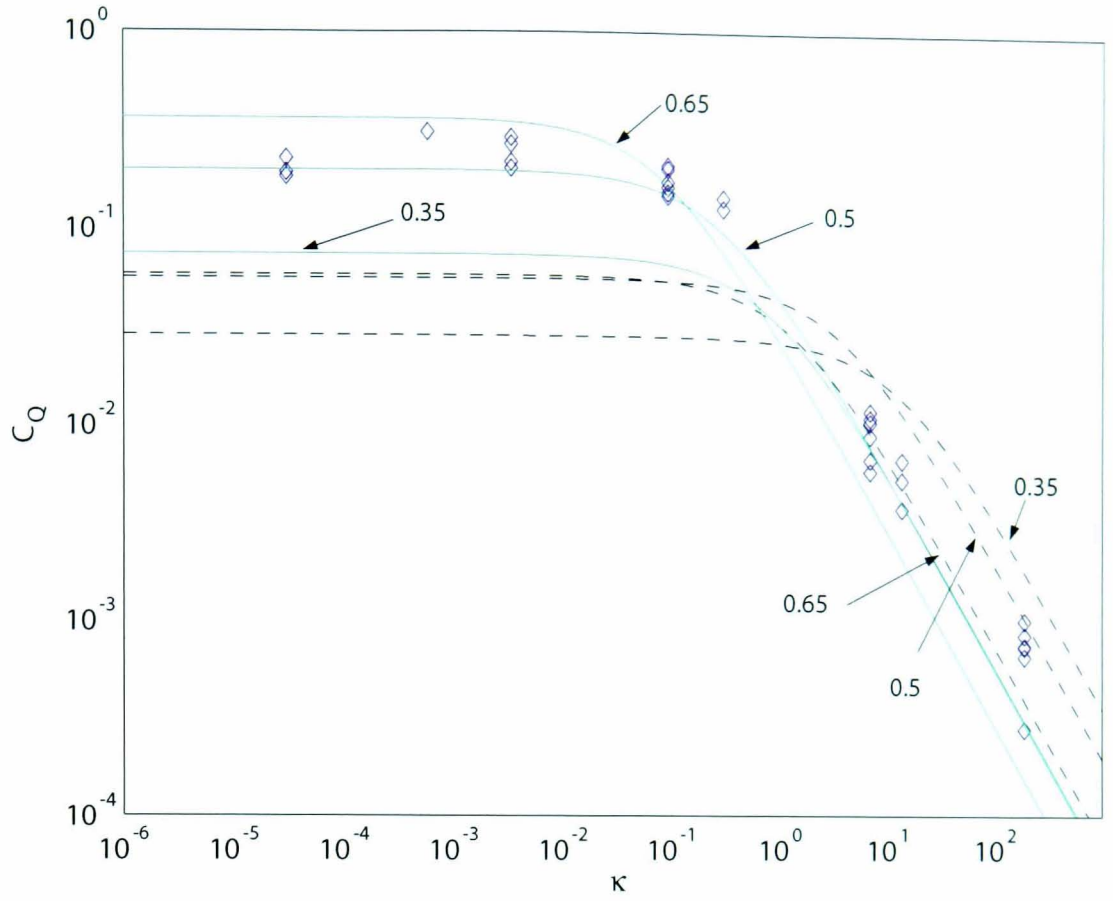

Figure 5.20: Relationship between the flux coefficient and viscosity ratio calculated in Equation 5.66. Results for three positions of the interface are shown: $\tilde{H} = 0.35, 0.5$ and 0.65. The continuous lines correspond to the solution when $H \geqslant 0.5$ (velocity of lighter fluid is greater), and the dashed lines correspond to the case $H < 0.5$. The curves $\tilde{H} = 0.35$ with continuous line, and $\tilde{H} = 0.65$ with dashed line, are not part of the solution obtained in Equations 5.66-5.68, but were included here to show the values that C_Q adopts in these cases. Results from the laboratory experiments of counter–current flow in inclined pipes are also shown (diamonds).

$$\begin{aligned} F_i &= \frac{1}{1+\frac{1}{\tilde{a}\kappa}} \qquad \tilde{H} < 0.5 \\ F_i &= \frac{1}{1+\tilde{a}\kappa} \qquad \tilde{H} \geqslant 0.5 \end{aligned} \tag{5.71}$$

where

$$\begin{aligned} g_{h1} &= \frac{\tilde{S}_h}{(\tilde{S}_h+\tilde{S}_i)} \\ g_{l1} &= \frac{\tilde{S}_l}{(\tilde{S}_l+\tilde{S}_i)} \\ g_{h2} &= \frac{4}{\pi+2} g_{l1} \\ g_{l2} &= \frac{4}{\pi+2} g_{h1} \end{aligned} \tag{5.72}$$

and $\tilde{a} = \tilde{A}_h/\tilde{A}_l$. The equivalent hydraulic radius of the bottom and top fluids ($D_{h,l}$) in the model of Ullmann *et al.* (2004) includes the perimeter of the interface. In the model presented here, however, the hydraulic radius considers the wall–liquid perimeter only, as in the previous model (Equation 5.47), because it yielded a better fit to the experimental data.

The final model equation that relates the volume flux to the properties of the liquids

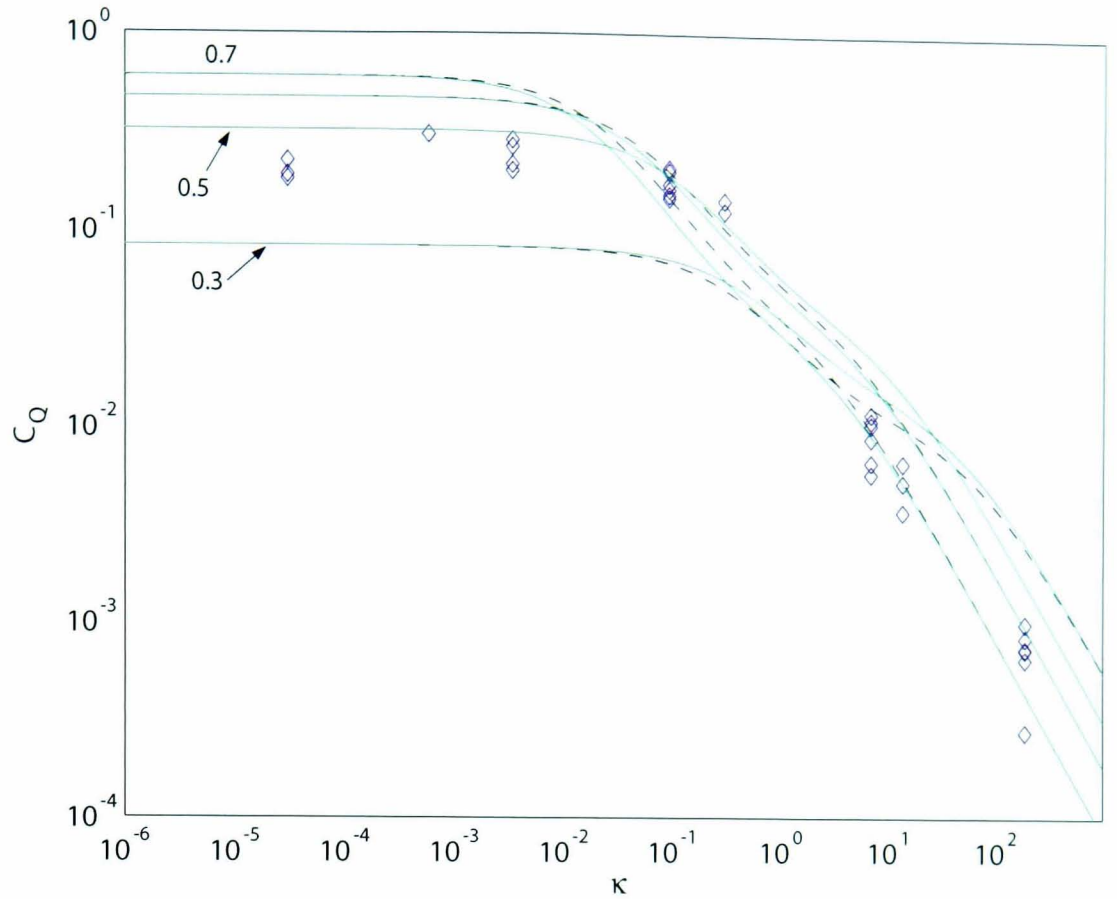

Figure 5.21: Results of the modified model of counter–current stratified laminar flow in inclined pipes. The continuous lines are the solution for the case $\tilde{H} < 0.5$ (heavier liquid flows faster) and the dashed lines for the case $\tilde{H} \geqslant 0.5$. Values of the position of the interface illustrated here are $\tilde{H} = 0.3, 0.5, 0.6$ and 0.7.

and geometry of the system has the same form of Equation 5.66. The results of this modified model are presented in Figure 5.21. It is clear that these new results exhibit a much better agreement between calculated values and experimental observations of the position of the interface (see Table 5.5 for a summary of these observations). For instance, the convective flow of dilute syrup with oil (exp. 808d, 807b, 808f, 808e; $\kappa = 6.8$) and the flow of dilute glycerol with oil (exp. 814b, 814d; $\kappa = 13.3$) can be modeled with $\tilde{H} \leqslant 0.3$, whereas the flow of water with oil (exp. 428a, 427a, 428b, 427b; $\kappa = 186$) can be modeled with $\tilde{H} \sim 0.6$. In the case of viscosity ratios lower than one, the flow of water with pure glycerol (exp. 727a; $\kappa = 5.710^{-4}$) and the flow of pure golden syrup with oil (exp. 823a, 1203a; $\kappa = 3.310^{-3}$) can be modeled with a position of the interface near the middle (or slightly lower) of the pipe.

The variations in C_Q related to the different positions of the interface adopted in experiments with separate pair of liquids do not allow the statement of a solution independent of this parameter ($\tilde{H}$). For viscosity ratios κ lower than 0.1, the experimental data show C_Q maxima between 0.22 and 0.32. Within this range of κ and using $\tilde{H} = 0.5$, the model approximates the highest values of C_Q measured in the laboratory experiments. For $\kappa > 0.1$, however, the choice of a single $\tilde{H}$ to fit the model results with the data is difficult because

of the higher variations of C_Q and the lack of data within the range $0.3 < \kappa < 6.5$. Thus, this new modified two-fluid model is in agreement with the experimental data available but its implementation requires the position of the interface to yield a more accurate solution.

5.6 Discussion and conclusions

5.6.1 Convective flow in vertical and inclined pipes

In this chapter, the equations of counter–current core–annular flow in a vertical pipe have been presented as a basic model of convection in conduits. In this model the liquids are immiscible and the flow is steady and uniform. In spite of these simplifications, the analytical analysis of this model yielded important insights into the relationship between the variables that influence or determine the resulting velocity profile and volume flow rate. Building upon the theoretical and experimental work of convection in vertical conduits carried out by Kazahaya *et al.* (1994); Stevenson and Blake (1998) and Huppert and Hallworth (2007), new data on the flow rate and characteristics (flow patterns) of the convection in vertical pipes were presented, which complement those obtained by the previous authors. It was found that the development of core–annular flow requires the predominance of viscous forces and interfacial tension to contrast the buoyancy-driven flow, and that it can be very unstable when buoyancy and inertial forces become relatively higher. Bubbles, turbulent flow and pseudo-stratification of the liquids were other types of flow patterns observed in the experiments with vertical pipes. In these experiments, it is possible that some of the differences in the flow pattern were influenced by the initial position of the interface. For a given pair of liquids, with specified viscosity ratio and density difference, flow patterns other than core–annular flow yielded higher flow rates and flux coefficient values (C_Q). The general form of the flux coefficient is

$$C_Q = \frac{Q\mu_h}{g\Delta\rho\cos\theta R^4} \tag{5.73}$$

where Q is the flow rate of the ascending (less dense) fluid, μ_h the viscosity of the descending (heavier) fluid, $\Delta\rho$ the density difference between the heavier and lighter liquids, θ the angle of inclination with respect to the vertical, R the radius of the pipe, and g the magnitude of gravity.

In order to further extend the investigation of convection in narrow conduits, laboratory experiments with tilted pipes were carried out within the same range of viscosity ratios that was considered in the experiments with vertical pipes (same pair of liquids). In this case, the inclination of the pipe and oblique direction (relative to the axis of the pipe) of buoyancy (gravity) forces gave rise to the segregation of the fluids, with the lighter liquid moving on top of the heavier liquid. At low angles from the vertical, commonly lower than 10 degrees, the flow exhibited instabilities and in some occasions similar flow patterns to those

observed in vertical pipes. At angles above 10 degrees, the stratification was generally well developed. For a given pair of liquids, stratified counter–current flows yielded higher values of the flux coefficient than core–annular, bubbly and turbulent flows, reaching the highest values with the pipe tilted at the highest angle considered in the experiments. Another variable that determined the value of the flux coefficient in stratified flow is the position of the interface. Value of C_Q were higher when the cross-sectional area of the more viscous liquid was bigger. Although not investigated in this work, it is likely that the same relation applies to core–annular flows.

5.6.2 Comparison with concurrent flow of oil and water

The characteristics of the flow of immiscible fluids in a core–annular arrangement are different depending on whether the flow is concurrent or counter–current. In lubricated pipeling, which correspond to concurrent flows of two immiscible liquids, there is a strong tendency for the liquids to be arranged so that the lower viscosity liquid flows in the annular region and the liquid with greater viscosity is placed in the core of the flow (Joseph and Renardy, 1993a,b). Conversely, in the case of counter–current flow, data from laboratory experiments and the solution of the two-fluid model suggest that in core–annular flow the tendency is for the lighter liquid to flow in the core and the heavier liquid in the annulus, regardless of the viscosity of the liquids. This means that for viscosity ratios $\kappa = \mu_l/\mu_h$ lower than one, the more viscous fluid goes in the annulus, but for κ higher than 1 the more viscous fluid goes in the core of the flow. When the flow is not perfect core–annular, however, some experiments have shown that with $\kappa > 1$ the more viscous liquid can also flow next to the wall. Variations in the flow pattern and configuration of the liquids within the pipe might also depend on the initial conditions of the experiments, wettability of the liquids and interfacial tension. The particular effect of these variables was not investigated in this work but some observations regarding their influence on the characteristics of the flow were described.

In the case of lubricated pipeling with oil flowing in the core and water in the annulus, the shear at the interface is lower than in the case of counter-current flow, and the region with the highest shear is located at the wall of the pipe. Thus, due to the lower viscosity of the water, the oil (lighter liquid) is lubricated by the water decreasing substantially the work required to transport the oil (Joseph and Renardy, 1993a). Joseph and Renardy (1993a) found that, although the liquids could adopt different arrangements (similar to the ones described herein), the core–annular flow had the greatest volume flux for a given pressure

drop. Therefore, the core–annular arrangement is a desirable characteristic. Conversely, in counter–current flow the core–annular pattern yielded the lowest volumetric flux. This flow rate increased with the development of instabilities and turbulence in the pipe. When the two–fluid flow became perfectly stratified, the volume flow rate seemed to reach a maximum value, given the same fluid properties and geometry of the conduit. Thus, for any given viscosity ratio, the experimental data show that the value of C_Q lies in between that of perfect core–annular flow (minimum C_Q) and that of stratified flow (maximum C_Q).

5.6.3 Results and further insights gained from the two-fluid model

Two analytical models were developed in order to find adequate solutions for the problems of core–annular flows in vertical pipes, and stratified flows in inclined pipes (Section 5.5). These 'two-fluid' models were based on the assumptions that the flow is steady, laminar, with equal pressure drop for both fluids, and that the fluid interface is smooth, so the inertial terms in the momentum equation can be neglected. Another assumption that was taken into consideration in the development of these models, which is based on the experimental results discussed above, is that the perfect core–annular flow and perfect stratified flow yield the lower and upper limits, respectively, of the flux coefficient for any inclination of the pipe (within the range analysed) and flow pattern developed in the pipe. Thus, these models constrain the flow rate in buoyancy-driven convection of any pair of liquids and conduit geometry.

The results obtained from the two-fluid model yielded expressions for the total volume flux and flux coefficient that are in agreement with the experimental data, in both vertical and inclined pipes. These expressions can be generalised with the following equation:

$$C_Q = (K_h + \kappa K_l + \kappa K_i)^{-1} \tag{5.74}$$

where κ is the viscosity ratio between the less and more dense fluids, and K_h, K_l and K_i are dimensionless parameters that depend on the configuration of the flow only. K_h and K_l are derived from the definition of shear stresses (and friction factors) at the wall, for the heavy and light liquids, respectively, whereas K_i is related to the shear stress at the fluids interface. In the case of core–annular flow K_l is zero, and K_h and K_i depend on the position of the interface only (Section 5.5.1). In order to represent the lowest values of C_Q, values of $K_h = 13.22$ and $K_i = 2.36$ were found to yield a good approximation for $\kappa < 0.2$. For

viscosity ratios higher than 0.2, the solution was found to depend on the pair of liquids as well as the viscosity ratio. Although the same values of K_h and K_i can be used, the results are less accurate (Figure 5.18).

The two-fluid model of stratified flows required the introduction of correction factors in the formulation of the shear stresses, which were originally derived by Ullmann *et al.* (2004) from the exact solution of stratified flows between parallel plates (Section 5.5.2). The results, in agreement with the available experimental data, exhibit a strong dependence on the position of the interface (and pair of liquids). For $\kappa < 0.1$ the maximum values of C_Q plot in the range 0.22-0.32. For $\kappa > 0.1$ the value of C_Q depends strongly on the viscosity ratio and position of the interface; the dependence with the viscosity ratio is resolved by the model, but the accuracy depends on the knowledge of the position of the interface (Section 5.5.2, Figure 5.21).

In these models the non–uniqueness of the solution is evident and critical variables, such as the position of the interface, are needed in order to obtain accurate results. Nevertheless, it has been shown that with calibrated friction factors for the liquid–wall and liquid-liquid interfaces, a one-dimensional two-fluid model is a good approach to obtain a continuous solution for the problems of core-annular and stratified flows, that constrain the flow rate of the convection.

5.6.4 On the application of the results to model convection in volcanic systems

Convection of magma within the plumbing system of open-vent volcanoes consists of the buoyant rise of relatively gas-rich, lighter and less dense magma, along with the descent of degassed, more dense and more viscous magma. In order to calculate the magma flux of the convection, it is necessary to know some properties of the magma, the radius of the conduit, and an estimation of the flux coefficient C_Q. Thus, from Equation 5.73 the magma flow rate is

$$Q = C_Q \frac{g\Delta\rho\cos\theta}{\mu_{deg}} R^4 \tag{5.75}$$

where μ_{deg} is the viscosity of the degassed magma; the other variables as in Equation 5.73. The viscosity of the ascending magma is not part of this equation, but it is needed for the estimation of the flux coefficient. C_Q can be obtained graphically from Figure 5.14, or numerically using Equation 5.74 (Section 4.5).

Chapter 6

Discussion: magma degassing in open–vent low–silica volcanoes

6.1 Introduction

Degassing of magma at open-vent volcanoes involves the transport of gas-bearing magma to shallow depths where volatiles can exsolve, segregate from the melt, and escape from the system. In order to understand and gain insights about the characteristics of magma degassing, it is necessary to analyse the conditions under which this fresh magma ascends within the plumbing system of the volcano, its interaction with more evolved and perhaps degassed magma, and the flow regime of the two-phase flow at the upper part of the conduit.

As discussed in Chapter 5, convection of magma is a suitable mechanism for the transport of gas-rich magma towards shallow levels. Measurements of gas emissions yield valuable information about the characteristics of the magma and changes in the stability of the system (e.g. Gerlach, 1986; Allard *et al.*, 1994; Shinohara and Witter, 2005; Allard *et al.*, 2005; Burton *et al.*, 2007a). Modelling magma degassing sustained by convection in conduits requires petrological information regarding the gas burden of the fresh magma, gas solubilities, composition of the melt and phenocryst content for the calculation of the physical properties of the magma (e.g. Stevenson and Blake, 1998; Burton *et al.*, 2007b). For instance, the solubility of gases, specially of the major components H_2O and CO_2, plays a major role changing the density and viscosity of the magma and in the transformation from a laminar single-phase flow to a two-phase flow. The geometry or shape of the plumbing system are also important variables that constrain the ascent of magma and bubbles (e.g. Vergniolle and Jaupart, 1986; Jaupart and Vergniolle, 1989; James *et al.*, 2004; Parfitt, 2004).

In this chapter, I investigate the characteristics of magma degassing at Villarrica and Stromboli volcanoes. Similar studies have been carried out at Stromboli by Stevenson and Blake (1998) and Burton *et al.* (2007b), and at Villarrica by Witter *et al.* (2004). The analysis presented herein, however, uses a slightly different approach and the new results obtained in Chapters 3, 4 and 5.

6.2 Magma transport in open magmatic systems

6.2.1 Conceptual model

Degassing of magma in open volcanic systems relies on 1) the transport of volatile-bearing magmas from deep levels in the crust towards relatively shallow levels where the gas can reach supersaturation, 2) diffusion and exsolution of gas, and 3) outgassing through hydrothermal systems, conduit walls, open vents, etc. A schematic of the degassing in an open-vent volcanic system is depicted in Figure 6.1a. In this model it is assumed that most of the gas escapes at the vent. The transport of volatile-bearing magma towards the surface, alongside with the sinking of degassed magma occurs at relatively deep levels in the crust, where most of the gas is still dissolved in the melt (Figure 6.1, letter A). It is in this part of the system where the convection of two different magmas, as described in Chapter 4, takes place. One of these magmas ascends from deeper levels and is more 'primitive', less dense, and probably less viscous than the degassed and relatively dense magma that descends from shallow levels in the plumbing system. I recall that volcanic systems with less differentiated magmas (e.g. basalts, hawaiite) can extend connected conduits and chambers for several kilometers below the surface. For instance, in subduction zones the roots of magma storage and supply are located at depths of several tens of kilometers (Rutherford and Gardner, 2000). Thus, this convective magma transport is also likely to occur below shallow magma chambers.

At shallow levels in the plumbing system (within several hundreds of meters below the surface, see Section 6.3) the ascent of gas is achieved mainly in the form of bubbles, configuring a two-phase flow (Figure 6.1, letter B). Big bubbles are able to detach from the motion of the melt, reaching higher velocities and enhancing turbulent flow. On reaching the uppermost section of the plumbing system, the originally gas-rich magma becomes more dense, owing to the exsolution and detachment of the gas phase, crystalisation, and overall cooling. The changes in properties of this magma, particularly its density and viscosity, constrain the rate of convection (Chapter 4).

The transitional zone in Figure 6.1 corresponds to the level at which the vesicularity and bubble size increase to the point where the relative velocity of individual bubbles to that of the melt is no longer negligible. In this zone, the original magma starts changing its properties considerably owing to the saturation and exsolution of gas. At this level it is likely that most of the gas phase is CO_2. The quantification of these changes and their influence in

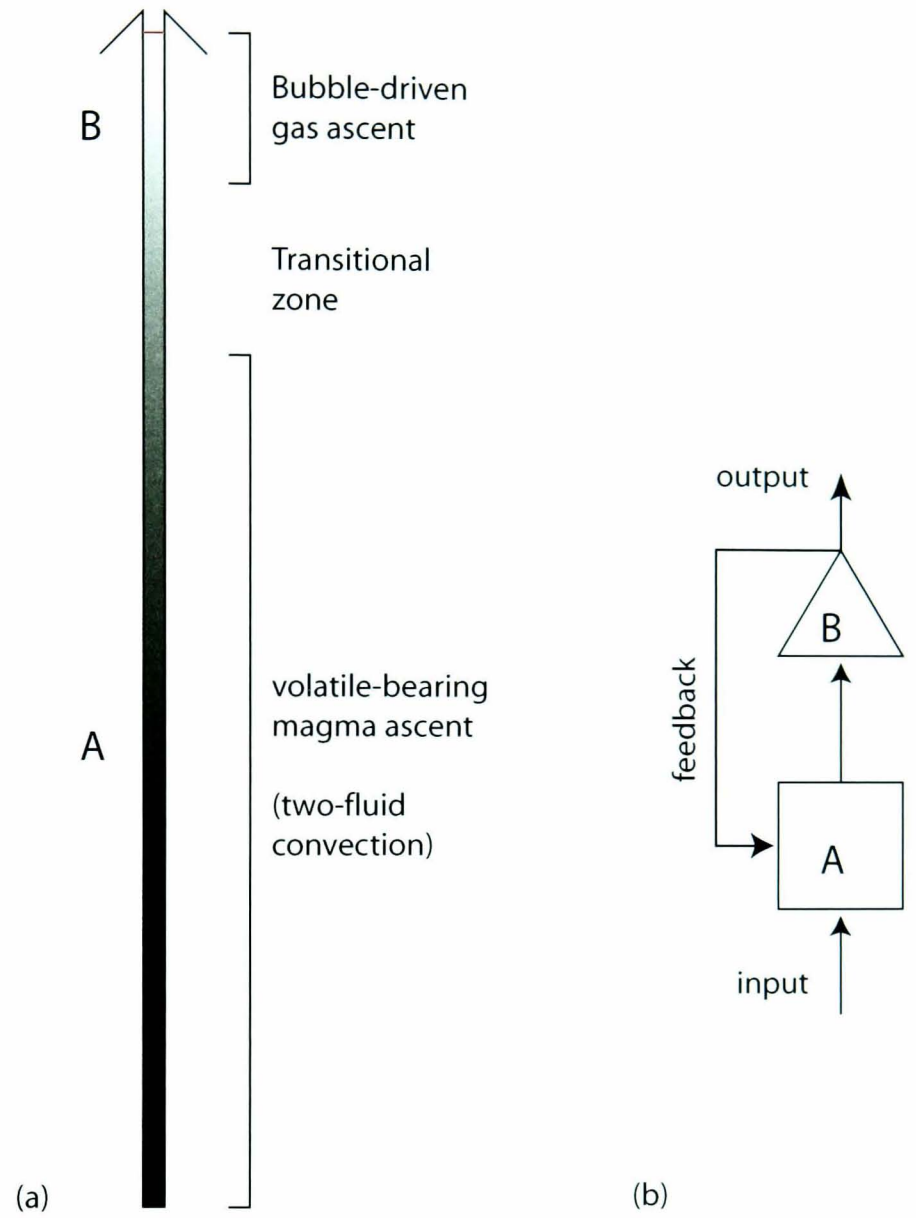

Figure 6.1: Conceptual model of magma transport and degassing in open-vent volcanoes. In (a) the plumbing system, a few kilometers depth, shows magma transport to the surface (A), gas exsolution and ascent to the top of the magma column (B). The scale of grey indicates an approximation of the vesicularity of the magma: the lighter the colour, the more vesicular. In the transitional zone the relatively high amount and size of bubbles generates a two-phase flow. In (b) the volcanic system is represented with a conceptual model of two processes with feedback, that include: the input of magma and gas, convective transport of gas-rich magma to shallower levels (A), bubble ascent (B) and outgassing (output). The properties of the degassed melt at the end of (B) influence the magma transport in (A).

the magma flow taking place at both deeper (A) and shallower (B) levels, requires a thorough analysis of the evolution of the properties of the magma as it ascends, which has not been developed in this thesis. In the rather simplified model presented here, the transitional zone is considered less important in the development and characteristics of convection and outgassing.

Focused on the above processes that occur during degassing, and the interaction between them, a schematic of an open-vent system is presented in Figure 6.1b. As in Figure 6.1a, the two-fluid type magma convection and bubble-driven gas ascent are represented with the letters A and B, respectively. The input of the system corresponds to the injection (ascent) of 'new' magma into the system. The ascent flow rate of this magma in (A) is determined essentially by its density and the radius of the conduit. The flow rate and gas content of the 'new' magma then constrain the gas flow rate coming into the upper plumbing system (B). Within this stage, the characteristics of the two-phase flow and outgassing vary depending on the geometry of the upper plumbing system. The magma continues exsolving gases, crystallizing and outgassing (output). The final properties of the degassed magma are the feedback of the system that partly constrain the two-magma convection in (A). Therefore, if the radius of the conduit, gas content, and fluid properties of both the input and output magmas are known, the total magma and gas transport in the system can be calculated (Chapter 4).

6.2.2 Constraints on the geometry of the system

Equivalent radius

The flow rate of the two-fluid convection determined in Chapter 4 is strongly dependent on the radius of the pipe. Previous investigations on the degassing rate at open vent volcanoes have used this relation to estimate the radius of the conduit (Witter *et al.*, 2004; Stix, 2007). However, the geometry of the plumbing system can be much more complex than a cylindrical pipe. Indeed, the conduits might consist of more than one pipe or a dyke (e.g. Stromboli volcano, see next section). Regarding the volume flux of magma, the relation between a cylindrical pipe and a dyke or a branch of pipes is linear. For example, if a flow rate Q is obtained with a pipe of radius R, doubling that flow rate can be achieved increasing the radius of the pipe 1.19 times, or with two pipes of radius R; likewise, the same flow rate Q can be obtained in a dyke with specific width and length related linearly to the radius R (Appendix B).

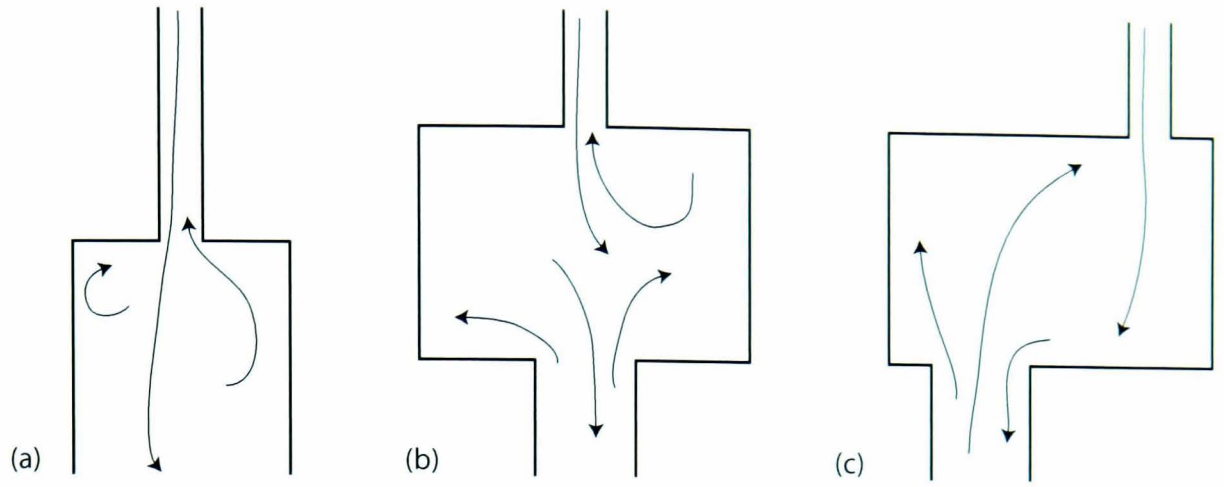

Figure 6.2: Cartoons of three possible changes in the geometry (size) of the plumbing system. a) A narrow pipe connected to a wider conduit or reservoir, b) a reservoir connected to a narrow conduit at the top, and to a wider conduit at the bottom, and c) a reservoir connected to two conduits of different size (diameter) which are located away from each other. Assuming exchange flow between the conduits and the reservoir, which resemble the configuration of the laboratory experiments presented in Section 5.4, the maximum flow rate is constrained by the conduit with the smallest radius.

Therefore, it is suggested here that the size (radius) of the conduit[1] calculated with the model of convection must be considered as an "equivalent" radius. The equivalent radius is the radius of a cylindrical pipe in which buoyancy-driven convection reaches the same flow rate calculated in the real system of unknown geometry. Thus, the equivalent radius does not necessarily represent the actual size of the conduit, but it yields an idea of its dimensions, and can be used in any system regardless of the geometry of the conduits.

The control of the smallest pipe

In sections of the plumbing system where the radius of the conduits change, or a major reservoir of magma is connected to it, the maximum flow rate reached in the system as a whole is expected to be determined by the conduit with the smallest equivalent radius. Three schematic examples of a narrow pipe connected to a reservoir are shown in Figure 6.2. This reservoir represents a small magma chamber. The configuration of the reservoir and conduit in Figure 6.2a is similar to the bottom tank–pipe part of the experimental apparatus where the experiments of convection were carried out (Section 5.4). As seen in the laboratory experiments, the volume of the liquids in the reservoirs does not influence the volumetric flux of the convective flow developed within the pipe (e.g. see Figure 5.10); thereby, the size of the reservoir is not relevant to the characteristics of the flow. (For instance, Huppert

[1]With conduit I now refer to cylindrical pipes, dykes or any other geometry that serve as a pathway for the magma to go through.

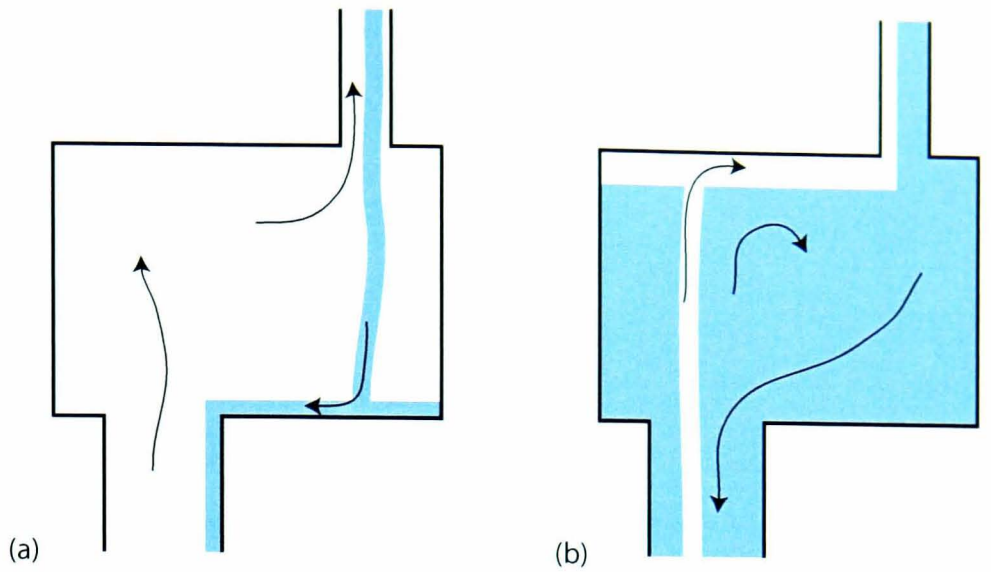

Figure 6.3: Two extreme examples of the flow configuration within a system that consists of a relatively wide conduit at the bottom, a reservoir, and a relatively narrow conduit at the top, all connected. The less dense magma is white and the more dense magma is grey. They show a reservoir almost completely filled with a) the less dense magma ascending from below, and b) the more dense magma descending through the narrow conduit.

and Hallworth (2007) set up two experiments with upper reservoirs of different sizes and they obtained consistent results). Figure 6.2b-c depict a similar arrangement in which the reservoir is connected to a second wider conduit at the bottom. Similarly, the characteristics of the countercurrent flow developed within the pipe at the top of the reservoir, depend on the properties of the magma coming from above and the magma in the reservoir that ascends into the pipe. The flow rate in this conduit is also determined by the radius of the pipe, which by being the smallest in this configuration, dictates the maximum flow rate reached by the two magmas in the system. It is noteworthy that the same principle applies when the narrowest conduit is at the bottom of the reservoir. Moreover, the bottom (wider) conduit could represent a dyke, pipe or group of pipes whose equivalent radius is higher than that of the conduit at the top.

The distribution of the two magmas in the reservoir can affect the fluid flow of gas-rich magma towards the surface. In Figure 6.3, two examples of a magma reservoir with the configuration of Figure 6.2c are shown. They resemble the conditions of the laboratory experiments at the start (a), when most of the light liquid is in the bottom tank, and at the end (b), when the bottom tank has been almost filled up with more dense liquid. In the first case (Figure 6.3a), the flow rate of the gas-rich (or new) magma entering into the reservoir is initially greater than that of the degassed (more dense) magma. This ensures availability of the gas-rich magma to ascend through the narrow pipe, and reduces the mixing of the new magma with the degassed melt. Mixing of these two magmas depends on the residence time

of the degassed magma (also related to its flow rate), viscosity contrast, and the strength of the convection generated within the reservoir, among other causes. If enough degassed and dense magma is produced at the top end of the narrow conduit, the supply of this melt into the reservoir will be steady.

In the case of Figure 6.3b, the injection of the gas-rich magma into the reservoir is initially lower than that of the degassed magma. It could also be caused by a low recharge of the chamber with new magma. Although the flow rate of the convection can equate with that of (a), the eventual shortage of supply of gas-rich magma into the narrow conduit would cause instabilities in the flow and unsteady outgassing at the top end of the conduit. If bubbles are present in the magma, the roof of the reservoir becomes a geometrical trap that favours the coalescence of bubbles and its subsequent ascent as big slugs.

6.2.3 Buoyancy-driven countercurrent flow with mixing

As shown by Huppert and Hallworth (2007), the effect of mixing on the countercurrent flow is to reduce the flow rate. This reduction is a direct consequence of the decrease in density difference and buoyancy forces. Mixing is particularly strong when both fluids have low viscosities, but a high viscosity contrast can prevent (decrease the efficiency) mixing to the point where the convection can exhibit flow rates comparable to those obtained with immiscible fluids (Section 5.4). In a vertical pipe, the total volume flow of miscible liquids that undergo mixing decreases with the length of the pipe, but this effect is lower with pipes of larger radius (Huppert and Hallworth, 2007).

In a series of related papers, Debacq *et al.* (2001, 2003) and Séon *et al.* (2004, 2005, 2006) investigated the buoyancy-driven mixing of two fluids in long cylindrical pipes. In vertical tubes, Debacq *et al.* (2003) observed three flow regimes: turbulent-diffusive, convective-diffusive and stable counterflow. These flow patterns depend on the density contrast, determined with the Atwood number (At=$(\rho_2-\rho_1)/(\rho_2+\rho_1)$ with $\rho_2 > \rho_1$), viscosity of the liquids, and diameter of the pipe. The turbulent and convective-diffusive flows exhibited a relatively effective mixing induced by turbulence or wavy motions, whereas the stable counterflow exhibited none or low transversal mixing. In the first two cases, the mean concentration profile $\bar{C}(x,t)$ (where x is the coordinate parallel to the axis of the cylinder and t is the time) followed a diffusive spreading law

$$\frac{\partial \bar{C}}{\partial t} = D\frac{\partial^2 \bar{C}}{\partial x^2} \tag{6.1}$$

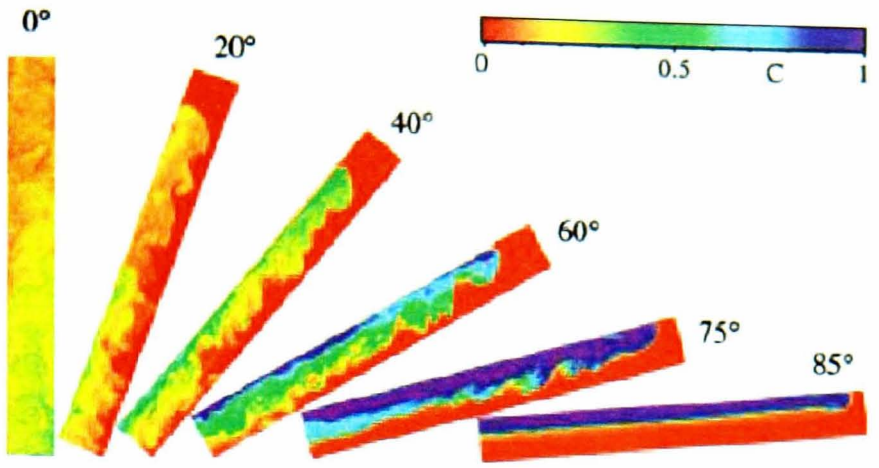

Figure 6.4: "Images of the normalized relative fraction of light fluid obtained at different tilt angles θ=0, 20°, 40°, 60°, 75° and 85° (field of view 20x3000 mm). The colour code for the normalized fraction is shown at the top right of the figure." Images captured with laser-induced fluorescence technique. Figure taken from Séon *et al.* (2006).

with D a diffusivity coefficient which is several orders of magnitude larger than the molecular diffusion coefficient (Debacq *et al.*, 2001, 2003). The stable counterflow was modelled by Debacq *et al.* (2003) as a Poiseuille-type flow, obtaining the following expression for the Reynolds number:

$$Re_c = \frac{gd^3At}{48\nu^2} \tag{6.2}$$

where d is the diameter of the pipe, and ν the kinematic viscosity of the liquid (both liquids have similar viscosity). A critical Reynolds number Re_c for this flow was found of the order of 130 (Debacq *et al.*, 2003). Analysis of the flow patterns obtained with different parameters of At, d and ν, showed that increasing the viscosity can shift the type of flow from turbulent-diffusive to convective-diffusive, and then to stable counterflow. The same occurred reducing the value of At or reducing d (Debacq *et al.*, 2003). Further analysis on the variation of the velocity of the flow and changes in the diffusivity coefficient with variations in At, d and ν, indicated that the extent of the buoyancy forces driven the flow are determined by the local density contrast (between the intruding and surrounding fluids) rather than the global density difference (between unmixed fluids) (Debacq *et al.*, 2003).

In tilted tubes, fluids of different density segregate by virtue of their oblique buoyancy, creating a stable stratification (Section 5.4) (Figure 6.4). Séon *et al.* (2004, 2005) investigated the degree of mixing in relation to the density contrast, angle of inclination (from vertical), and viscosity of the fluids. They found that the transverse mixing was reduced by increasing the angle of inclination and decreasing the dynamic viscosity. Also, the diffusivity coefficient increased rapidly at higher angles of inclination (Séon *et al.*, 2004, 2005). The velocity of the

front exhibited a strong increase from 0 to about 40-60° (depending on the density contrast and viscosity), at which angle the velocity reached the maximum value. Again, the velocity of the front depends on the local density contrast, which is lower than the overall density difference owing to the mixing of the advancing lighter fluid. The efficiency of the mixing at the front of the flow is favoured by lower viscosity and higher density contrasts (Séon *et al.*, 2005).

In summary, these results point out the reduced mixing in countercurrent flow caused by high viscosity and high viscosity contrast (or ratio) between the liquids, small cross-sectional area and higher inclination of the conduit. In particular, the pronounced increase in viscosity (2-5 orders of magnitude) during degassing and crystallisation of the melt suggests that mixing is not a significant process during magma convection in narrow conduits. For instance, laboratory experiments have shown that mixing does not take place even in the case of a turbulent plume injected into a reservoir containing a higher viscosity liquid, if the viscosity ratio is higher than 400 (Campbell and Turner, 1986). Nevertheless, since the results of Chapter 4 were obtained on the basis of flow of immiscible liquids, the flux coefficient C_Q must be regarded as maximum value, and so the volume flux Q.

6.3 Quantifying magma degassing at open–vent volcanoes

6.3.1 Constraints on the amount of degassing

Emission rates of magmatic gases at open vent volcanoes depend on the availability of volatiles at depth and the conditions of their transport to the surface (Section 6.2.1). While the flux of outgassed SO_2, H_2O, CO_2 and other species can be measured with remote sensing (spectroscopic) and direct (in-situ) sampling techniques (Symonds *et al.*, 1994), the composition and concentration of volatiles in the melt can be measured in melt inclusions trapped in phenocrysts. Thus, the degassing rate can be quantified, for instance, based on measurements of sulphur (petrologic method) (Kazahaya *et al.*, 1994; Gerlach *et al.*, 1996; Witter *et al.*, 2004):

$$Q_m = 10^6 \frac{M_{(S)}}{M_{(SO_2)}} \frac{Q_{SO_2}}{\Delta S} \tag{6.3}$$

where Q_m $[kg/s]$ is the magma degassing rate, ΔS $[ppm]$ is the sulfur lost from the melt, $M_{(S)} = 32.066$ $[g/mol]$ and $M_{(SO_2)} = 64.065$ $[g/mol]$ are the molecular mass of sulphur and sulphur dioxide, respectively, and Q_{SO_2} $[kg/s]$ is the SO_2 flux measured at the surface. The outgassed sulphur ΔS is obtained from measurements of the gas in melt inclusions and in matrix glass of lava (or scoria) samples, that represent the volatile content of the relatively gas-rich and degassed magmas, respectively:

$$\Delta S = S_{(mi)}(1 - C_m) - S_{(mg)}(1 - C_g) \tag{6.4}$$

with $S_{(mi)}$ $[ppm]$ the concentration of sulphur measured in the melt inclusion and $S_{(mg)}$ $[ppm]$ the concentration of sulphur in the matrix glass of the sample. C_m and C_g correspond to the mass fraction of crystals at the time of the melt entrapment and in the matrix of the sample (pyroclast or lava); the two terms in brackets $(1 - C_{m,g})$ represent the mass fraction of the silicate melt, and both should be used in order to obtain the sulphur exsolved from the melt (S. Blake, personal communication). Thus, providing that the melt inclusion is trapped before supersaturation of sulphur, Equation 6.3 yields an estimation of the amount of magma being degassed during open–vent activity (as explain in Section 6.2.1).

The volume flow rate Q_v $[m^3/s]$ of the gas-rich magma that ascends within the plumbing system can be calculated as follows:

$$Q_v = \frac{Q_m}{\rho_m} \tag{6.5}$$

where Q_m $[kg/s]$ is the degassing rate (or mass flow rate) obtained from Equation 6.3. and ρ_m $[kg/m^3]$ is the density of the ascending magma. Q_v (Equation 6.5) can be introduced in the volume flux of the convective flow investigated in Chapter 5,

$$Q_v = C_Q R^4 g \cos\theta \frac{\Delta\rho}{\mu_d} \tag{6.6}$$

where C_Q is a parameter that depends on the flow regime, R is the equivalent radius of the conduit (Section 6.2.2), θ the angle of inclination of the conduit, $\Delta\rho$ the density difference between the convecting magmas, and μ_d the viscosity of the descending (degassed) magma. Then, combining Equation 6.6 with Equation 6.3, the following expression is obtained:

$$Q_{SO_2} = \Gamma \frac{C_Q}{\mu_d} \rho_m \Delta\rho \Delta S \tag{6.7}$$

with

$$\Gamma = 2 \cdot 10^{-6} R^4 g \cos\theta \tag{6.8}$$

a factor with units $[m^5/s^2]$ that depends on the geometry of the system only; the number 2 results from the ratio $M_{(SO_2)}/M_{(S)} \simeq 2$. Thus, from the measurements of SO_2 fluxes and sulphur loss (ΔS), along with the properties of the magma, the value of Γ can be calculated. Then, using Equation 6.8 and for a given value of θ, the equivalent radius R is obtained.

Once the magma degassing rate (Q_m) and Γ are calculated for a combination of gas flux (Q_{SO_2}), sulfur loss (ΔS), flow regime (C_Q), and properties of the magma (ρ_m, ρ_d, μ_d), small variations in the degassing rate can be investigated. With the assumption that the geometry of the plumbing system, and thus Γ, does not change during the period of interest, variations in gas emissions measured at the surface (volcanic plume) can be directly related to variations in the gas content and density of the magma (Equation 6.7). Moreover, it is expected that, at least with small variations in the gas content of the magma, the ratio C_Q/μ_d in Equation 6.7 will not change either. Thus, the proportionality of Q_{SO_2} and ΔS is mainly determined by changes in density of the magma ($\rho_m \Delta\rho$). This relationship is, however, difficult to constrain since the density of a magma is a function of several variables: composition (major oxides), gas dissolved in the melt, degree of crystallisation, vesicularity, pressure and temperature. The investigation on the applicability of models available in the literature to calculate magma properties is beyond the scope of this thesis. Nevertheless, the quantification of magma degassing through Equations 6.3-6.7 require the use of such models

(and equations of state), which will be briefly discussed in the following section.

6.3.2 Density, viscosity and gas solubilities

Most low–silica magmas are composed of a multiphase mixture of silicate or carbonatitic melt, crystals and gas (mainly H_2O and CO_2). Since the mass and volume fraction of each component vary considerably depending on the composition, source, temperature, pressure, evolution, and other parametres, it is common to find great variations on the properties of the magma as it flows, within a magma reservoir and plumbing system, and erupts. The determination of the properties of the mixture is generally carried out first on the silicate melt, and then corrected for the presence of crystals and gas bubbles.

Density

The density of the melt is calculated with the model of Spera (2000), which was modified after Lange and Carmichael (1990), Lange (1997) and Ochs III and Lange (1997):

$$\rho_l(T, P, X) = \frac{\sum_i X_i M_i}{\sum_i X_i \overline{V}_i(T, P)} \tag{6.9}$$

where ρ_l is the density of the melt and the letters in brackets T, P and X refer to temperature, pressure and composition; X_i is the mole fraction, M_i is the molar mass, and $\overline{V}_i$ is the partial molar volume of the ith oxide component in the melt. $\overline{V}_i$ is assumed to be a function of temperature and pressure only, and is calculated using isothermal-partial-molar compressibility and isobaric expansivity coefficients (see Table II in Spera, 2000). This model also takes into account the burden of dissolved water and carbon dioxide. Spera (2000) reports uncertainties of 1σ. An alternative method to incorporate the effect of volatiles dissolved in the melt is (Lange and Carmichael, 1990):

$$\rho_l = \rho_{l0}(1 - \beta w_{gd}) \tag{6.10}$$

where ρ_l and ρ_{l0} are the densities of the 'wet' and anhydrous melt, respectively, w_{gd} is the mass fraction of the dissolved volatile, and β is the coefficient of compositional expansion (Stevenson and Blake, 1998) ($\beta \sim 1.55$ for water and ~ 0.8 for carbon in basalts, Lange and Carmichael, 1990).

The density increase owing to crystallisation of the melt is calculated with the formula

$$\frac{1}{\rho_m} = \frac{w_{cx}}{\rho_{cx}} + \frac{(1 - w_{cx})}{\rho_l} \tag{6.11}$$

where ρ_m is the density of the mixture crystals–melt, ρ_{cx} and ρ_l are the densities of the mineral phase and melt, respectively, and w_{cx} is the mass fraction of crystals. Estimation of the average density of olivine and plagioclase are 3500 and 2700 kg/m^3, respectively. Note that the vesicularity of the magma is not considered in the calculation of the mass fraction of crystals w_{cx}.

In order to incorporate the variation in density from the exsolution of volatiles, the solubility of the predominant gas species is required to calculate the mass fraction of the vapor phase at a specified pressure. The mass fraction (in the mixture melt-crystals-bubbles) of exsolved volatiles w_b is calculated as follows (Mastin and Ghiorso, 2000):

$$w_b = \frac{w_{g0} - w_g(1 - w_{cx})}{1 - w_g(1 - w_{cx})} \tag{6.12}$$

where w_{g0} is the mass fraction of the total amount of volatiles, that initially might have all been dissolved in the melt, and w_g is the mass fraction of the dissolved gas obtained from the solubility model. If the presence of crystals was not considered in the calculation of density of the magma, the above equation would be reduced to

$$w_b = \frac{w_{g0} - w_g}{1 - w_g} \tag{6.13}$$

This could be the case if the density of the mixture melt–crystals was calculated using the whole-rock composition. From the ideal gas law, the density of a gas species at certain pressure and temperature can be calculated using the formula

$$P = \rho_i \frac{R}{M_i} T \tag{6.14}$$

with P the pressure in Pascals, ρ_i the density of a specified vapor component i of the magma, R the gas constant (8.315 m^3 Pa mol^{-1} K^{-1}), M_i the molecular mass of the gas i (g/mol), and T the temperature in Kelvin. Thus, the density of the mixture can be calculated as follows:

$$\frac{1}{\rho_m} = w_b \frac{RT}{M_i P} 1000 + \frac{1 - w_b}{\rho_{l+cxx}} \tag{6.15}$$

where ρ_{l+cxx} is the density of the mixture melt-crystals; the factor 1000 is to obtain the density in units of kg/m^3. Note that, for the sake of simplicity in the description of the method, only one gas species was considered in these equations. Adding more volatile components is straightforward.

Viscosity

Melt viscosities are estimated here with the empirical model of Hui and Zhang (2007). With only one equation, this model attempts to estimate the viscosity of a wide range of melt compositions, from basalts to rhyolites, as well as its variations at different temperature and water content:

$$\log\ \mu_l = A + \frac{B}{T} + \exp\left(C + \frac{D}{T}\right) \tag{6.16}$$

where μ_l is the viscosity of the melt in Pa s, T is the temperature in Kelvin, and A, B, C, and D are linear functions of mole fractions of oxide components except for H_2O (see coefficients in Hui and Zhang, 2007). Fitting measurements of 1451 samples of natural silicate melts, Hui and Zhang (2007) obtained a 2σ deviation of 0.61 log μ_l units.

Previous studies on Villarrica (Witter *et al.*, 2004) and Stromboli (Burton *et al.*, 2007b) applied an empirical non–Arrhenian model derived for Etna's magmas (Giordano and Dingwell, 2003):

$$\log\ \mu_l = -4.643 + \frac{5812.44 - 427.04H_2O}{T - 499.31 + 28.74\ln(H_2O)} \tag{6.17}$$

where μ_l is the viscosity in Pa s, T is the temperature in Kelvin, and H_2O is the water content in wt%. The use of this model to calculate the viscosity of low-silica melts is tempting, particularly because of its simplicity. However, although the viscosity model of Giordano and Dingwell (2003) exhibits a good fit on the basaltic melt of Etna volcano, it does not take into account compositional variations. Therefore, the accuracy of the model of Giordano and Dingwell (2003) in modelling other melts of basaltic or basaltic andesite composition is arguable. A comparison of this two models[2] is presented in Figure 6.5, where it is clear that the model of Hui and Zhang (2007)[3] fits the data better than the model of Giordano and Dingwell (2003).

The presence of crystals within the magma can increase its viscosity more than 2-5 times (Spera, 2000). Several empirical relationships are available in the literature to estimate the increase in viscosity of a Newtonian liquid bearing variable concentration of solids (e.g. Jaupart and Tait, 1990; Lejeune and Richet, 1995). The viscosity of the mixture silicate melt–crystals also depends on the shape and size distribution of the crystals (Spera, 2000).

[2]Whilst the data set of Giordano and Dingwell (2003) comprise samples with H_2O wt% of 0.02–2.29 and temperatures 525–1545 C (SiO_2=47%), the data shown in Figure 6.5, which is a subgroup of the whole data set compiled by Hui and Zhang (2007), comprise water contents of 0–6.36 wt%, temperatures of 500–1600 C, and SiO_2 between 47 and 53.5 wt%.

[3]By reducing the range in composition of the data set, it may be possible to improve the original equation of Hui and Zhang (2007) with a new regression of the subgroup SiO_2=47-54 wt%.

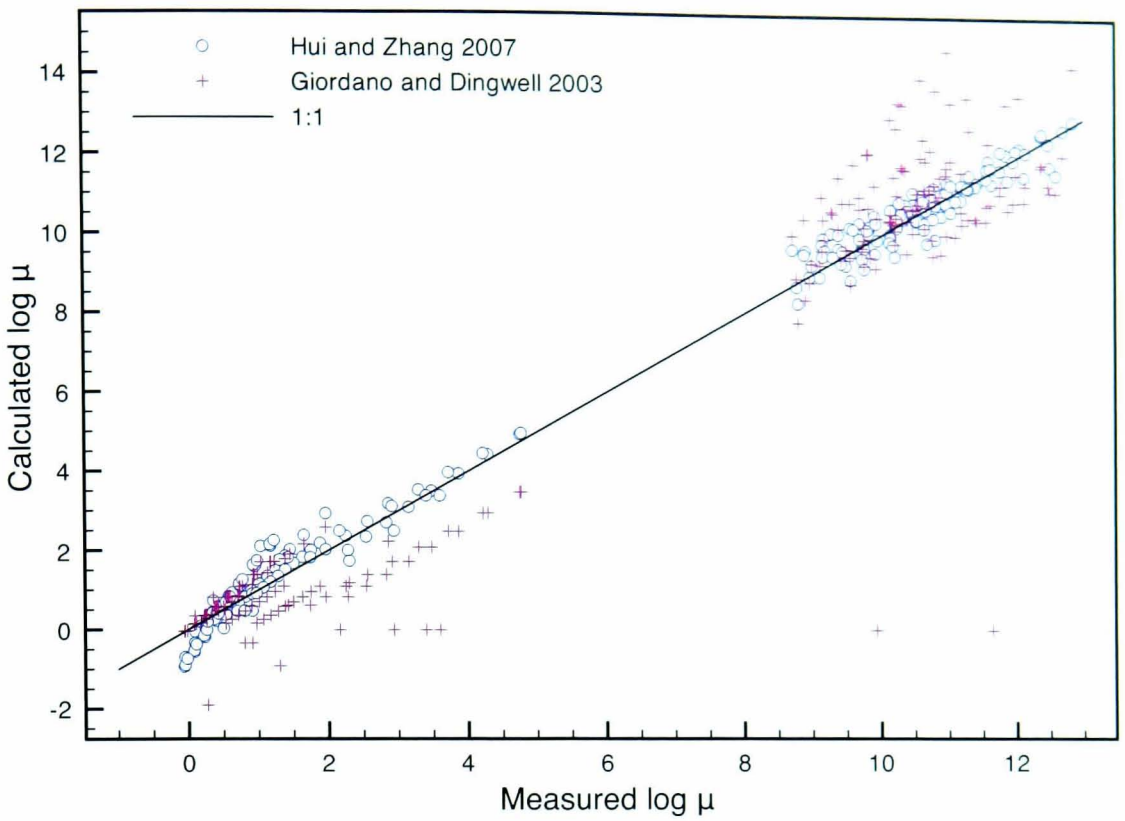

Figure 6.5: Comparison of the empirical models of Hui and Zhang (2007) and Giordano and Dingwell (2003). The viscosity data comprise 211 samples of natural silicate melts between 47 and 53.5 wt% of SiO_2, which is a subset of the data compiled by Hui and Zhang (2007). Dry samples (with no water) cannot be entered in the model of Giordano and Dingwell (2003), and in this figure plot at 0 calculated logμ.

Moreover, at high concentration of solid particles the viscosity might be strain-rate dependent (non-Newtonian) (e.g. Lavallée *et al.*, 2007). Here, the relatively simple relation of Spera (2000) is used, which is a modification of the well known Einstein–Roscoe formula (Marsh, 1981; Lejeune and Richet, 1995):

$$\mu_m = \mu_l \left(1 - \phi_c/\Psi\right)^{-n} \tag{6.18}$$

with μ_m and μ_l the viscosities of the magma (mixture melt plus crystals) and melt, respectively, ϕ_c the volume fraction of crystals, n a parameter in the range 2-3, and

$$\Psi = 1 - \phi_c \frac{1 - \phi_0}{\phi_0} \tag{6.19}$$

in which ϕ_0 is a third parameter in the range 0.5–0.75. This model takes into account melt entrapped between solid particles that are not available for shear (Spera, 2000). If Ψ was replaced by the maximum packing parameter and n=2.5, Equation 6.18 would adopt the same form of the Einstein-Roscoe formula. In Equations 6.18-6.19 the values chosen for the

calculations performed in this section are $n = 2.5$ and $\phi_0 = 0.6$, yielding viscosities in between the values obtained with the Einstein-Roscoe equation and the formula provided by Jaupart and Tait (1990).

For lower volume fraction of bubbles within the magma, their effect on the viscosity of the mixture (at low Reynolds numbers) is expected to change by a factor of less than 3 (Manga and Loewenberg, 2001; Rust and Manga, 2002), although Llewellin *et al.* (2002) found variations of up to one order of magnitude.

Gas solubilities

The solubility of water in silicate melts is strongly dependent on pressure, but also on temperature and composition of the melt (Wallace and Anderson, 2000). At low concentrations, solubility of H_2O and CO_2 follow Henry's law (Jaupart and Tait, 1990), and can be modelled with an equation of the form:

$$X_i(P) = aP^b \tag{6.20}$$

where X_i is the concentration of the gas species, P is the pressure, and a, b are coefficients of the model that depend on the composition of the melt, pressure and temperature. Equation 6.20 can be used as an empirical model to calculate gas dissolved in magmas, providing that the coefficients of the equation are obtained from measurements on real samples of similar chemical composition, and under similar conditions of pressure and temperature. A set of measurements and calculations of water solubility in mafic melt compositions is shown in Figure 6.6 (references and characteristics of the measurements are in Table 6.1). The data from Dixon *et al.* (1995) are actually calculations of the solubility of water, based on measurements at 1200 C and pressures between 200 and 980 bars, and using a regular solution model for albitic glass with the activity of water in the melt given by Henry's law for molecular water (Dixon *et al.*, 1995). The rest of the data in Figure 6.6 are measurements performed on natural silicate melts (see Table 6.1). For instance, if Equation 6.20 was used to model the solubility of water in a melt of basaltic andesite composition similar to that of Pineau *et al.* (1998) (at least in major oxides SiO_2, Al_2O_3, FeO_t and Na_2O (Dixon, 1997; Moore *et al.*, 1998)), the results would be in agreement with the data only at pressures greater than 1 kbar and temperatures of 1200-1250 C. The coefficients a and b calculated for this set of data exhibit a broad variation (Table 6.1), and extrapolation to lower pressures could yield

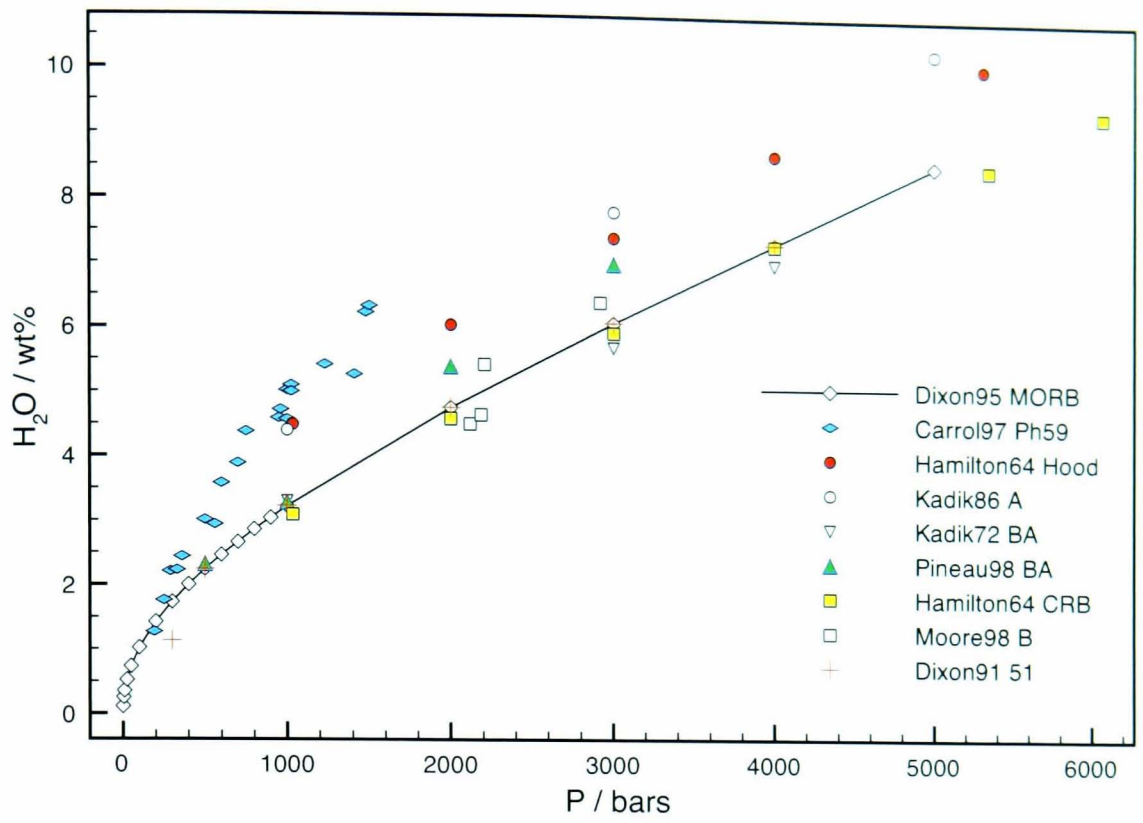

Figure 6.6: Measurements of water solubility collated from the literature. Solubility of water is expressed as a relation between dissolved water (wt%) and pressure (bars). References and conditions of these measurements in Table 6.1.

Table 6.1: Characteristics of the measurements of water solubility presented in Figure 6.6.

Label	Rock	SiO_2 [wt%]	T [C]	a	b	Reference
Dixon95	MORB	~50	1200	1.05e-1	0.5	Dixon (1997)
Moore98	Basalt	50.6	1050-1100	-	-	Moore *et al.* (1998)
Hamilton64	CRB	50.71	1100	3.93e-2	0.628	Hamilton *et al.* (1964)
Dixon91	Basalt	50.8	1200	2.94e-2	0.67	Dixon *et al.* (1991)
Kadik72	B. andesite	52.5	1200	8.20e-2	0.533	in Pineau *et al.* (1998)
Pineau98	B. andesite	53.8	1200-1250	4.59e-2	0.626	Pineau *et al.* (1998)
Hamilton64	Mt Hood	58.41	1100	1.42e-1	0.496	Hamilton *et al.* (1964)
Kadik86	Andesite	59.5	1150-1200	1.15e-1	0.527	in Pineau *et al.* (1998)
Carrol97	Phonolite	59.4	850-970	3.66e-2	0.706	Carroll and Blank (1997)

inaccurate results. Unfortunately, the data available regarding water solubilities at pressures lower than 1 kbar are scarce.

More sophisticated models based on thermodynamic relations between pressure, temperature, fugacity of the water, melt composition, etc., are also available (e.g. Dixon and Stolper, 1995; Dixon, 1997; Papale, 1999; Newman and Lowenstern, 2002). However, these models are either restricted to a certain melt composition (and range of pressures), or they are difficult to implement. For instance, some of the magmas erupted at Stromboli can be modeled with the software VolatileCalc of Newman and Lowenstern (2002) (Burton *et al.*, 2007a,b), but in the case of the basaltic andesite of Villarrica volcano, its composition is out

of the compositional range accepted by the software (49 wt% SiO_2 maximum for calculations of solubility). Other models available in the literature utilize experimental data to create empirical models, which rely on a fixed amount of coefficients determined by regression of the data (e.g. Moore *et al.*, 1998; Liu *et al.*, 2004). In this chapter, the solubility of water is modelled based on the calculated values given by Dixon *et al.* (1995), for a basaltic liquid at 1200 C and pressures in the range 1–5000 bars (Figure 6.6). These values were fitted with the following relation:

$$X_i = aP^b + cP^d \tag{6.21}$$

with X_i the fraction of the volatile (in this case water) in wt%, $a = 1.842 \cdot 10^{-5}, b = 1.372, c = 0.115$ and $d = 0.4711$, and P the pressure in bars. Note that this model is also in agreement with the measured water solubilities in basalts and basaltic andesites of Dixon *et al.* (1991), Hamilton *et al.* (1964), Kadik *et al.* (1972), and Moore *et al.* (1998) (Figure 6.6).

The solubility of carbon dioxide in basaltic melts is less constrained than that of water. As with water, an empirical formula was derived based on the values of solubility given by Dixon *et al.* (1995), which were calculated for a basalt at 1200 C. Using Equation 6.21, a simple regression of the data yielded the following coefficients: $a = 0.004971, b = 1.345, c = 0.3686, d = 1.025$. Again, the advantage of working with these data is the broad pressure range. Also, the calculations by Dixon *et al.* (1995) are close to the measurements reported by Stolper and Holloway (1988) for a basalt from the Juan de Fuca ridge.

Thus, the following formulas were obtained to estimate the solubility of water and carbon dioxide in melts of basaltic to low-silica basaltic andesite composition:

$$X_{H_2O}[wt\%] = 1.842 \cdot 10^{-5} P^{1.372} + 0.115 P^{0.4711} \tag{6.22}$$

$$X_{CO_2}[ppm] = 4.971 \cdot 10^{-3} P^{1.345} + 0.3686 P^{1.025} \tag{6.23}$$

where the pressure P is in bars. These equations are plotted in Figure 6.7 along with the model of Newman and Lowenstern (2002).

6.3.3 Magma degassing at Villarrica volcano

At Villarrica, only Witter *et al.* (2004) have analysed melt inclusions and measured the volatile content of the magma. They analysed the chemistry of melt inclusions, phenocryst and matrix glass of reticulite collected in February 29 and March 1, 2000. They also made

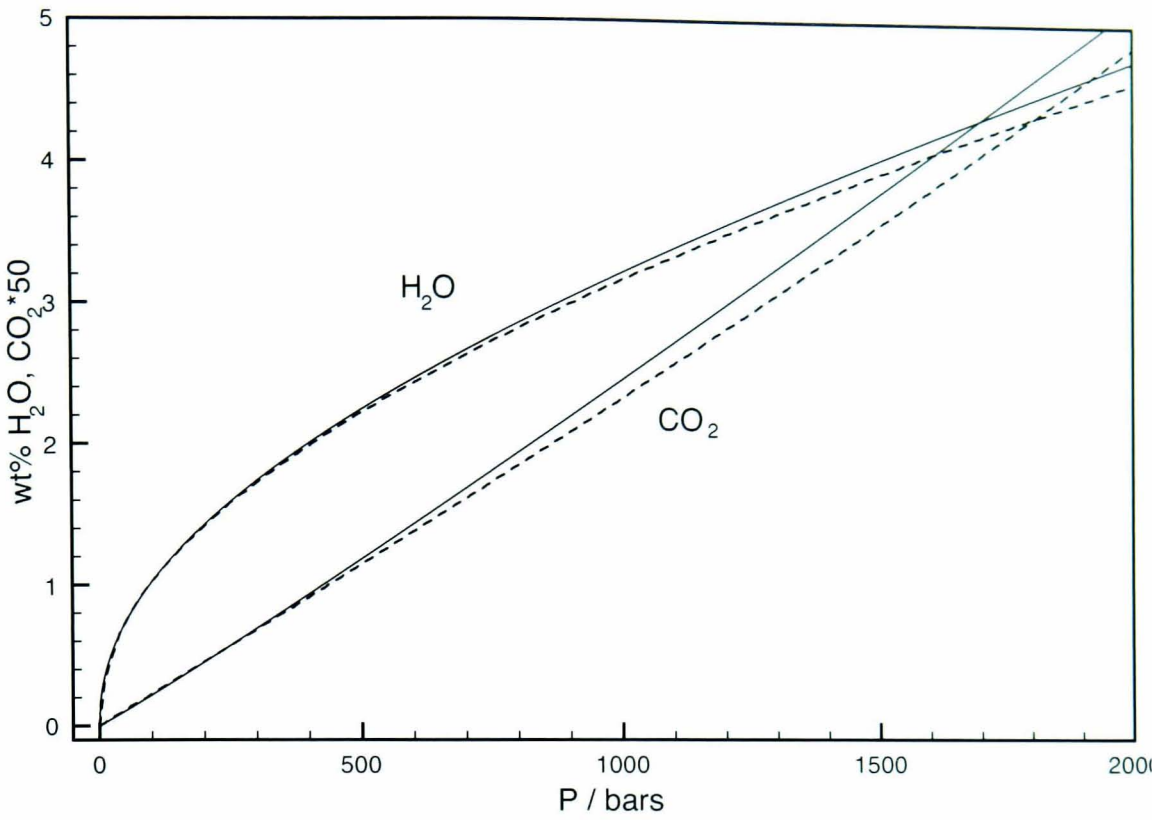

Figure 6.7: Solubility of water (wt%) and carbon dioxide (x50 wt%) modelled with Equations 6.22-6.23 (solid lines). Also shown are the solubility models given by VolatileCalc (Newman and Lowenstern, 2002) for a rock wt% 49 SiO_2, at 1100 C (dashed lines).

some analysis on scoria samples from October–November 1999, and on samples of a lava flow extruded in the eruption of 1984. All these examples exhibited similar whole rock composition as well as phenocryst content.

In this section, I use the rock composition and melt inclusions data of the reticulite samples published by Witter *et al.* (2004).

Degassing rate

The magma degassing rate can be obtained from Equation 6.3, with the calculation of sulphur loss using Equation 6.4. It is clear in the relation of Equation 6.3 that the higher the sulphur loss, the smaller the magma degassing rate. Thus, the lower limit could be obtained assuming a gas-rich source magma, as measured by Witter *et al.* (2004) in one melt inclusion trapped in olivine. An alternative to estimate the original amount of sulphur is through the comparison with other incompatible elements of the melt (S. Blake, personal communication). The relation between S and TiO_2 is shown in Figure 6.8. Since both S and TiO_2 are incompatible elements, fractionation of the melt during temporary storage and ascent to the surface should lead to a positive correlation between them, providing that only a small amount of TiO_2 is taken from the melt, for example by spinel, and negligible

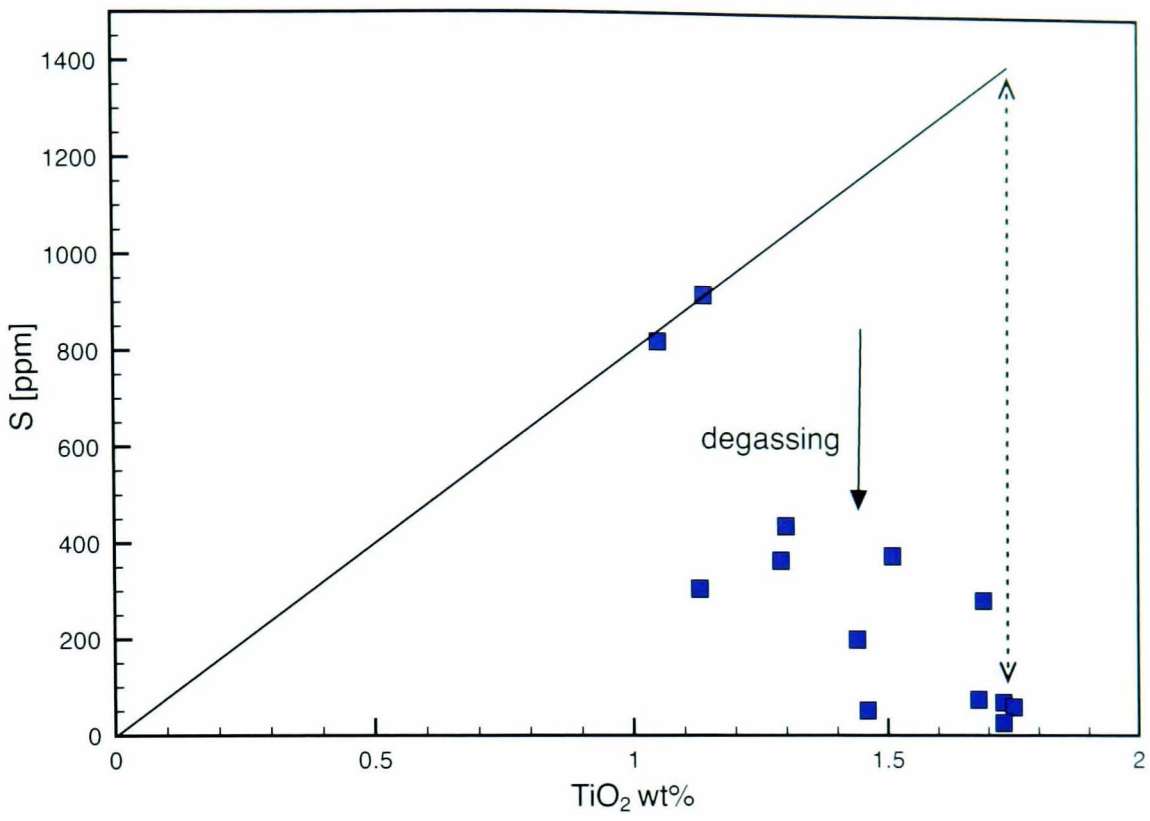

Figure 6.8: Concentration of sulphur and TiO_2 of the gas-rich and some gas-poor melt inclusions measured by Witter *et al.* (2004) in phenocrystals of olivine and plagioclase.

exsolution of sulphur. This correlation is constrained by the depth of entrapment of the melt. If crystallisation occurs mainly at shallow levels (low pressure), the melt could undergo degassing before it gets trapped within a crystal, and the inclusion will not preserve the same amount (nor the relative abundance) of volatiles. Thereby, in this case the relation between S and TiO_2 becomes inverse. This effect of melt inclusion entrapment concurrent with degassing of the melt can be observed in Figure 6.8. Although gas-rich samples are scarce, an estimation of the original content of sulphur can be obtained by extrapolating the positive correlation expected between S and TiO_2. Thus, a greater value of 1400 ppm of initial sulphur is obtained, which is likely to be closer to the original composition of the melt at depth where most of the sulphur is dissolved.

A summary of the values considered for the calculation of the magma degassing rate is presented in Table 6.2. Three possible scenarios are considered: one with the estimated concentration, the second one with the gas-rich sample measured by Witter *et al.* (2004), and the third one with a relatively degassed sample measured by the same authors. The SO_2 flux considered here corresponds to the average gas emission measured by Witter *et al.* (2004) in 2000 (Chapter 3), during which the samples with melt inclusions were collected. After calculation of the magma degassing rate using Equation 6.3, the results show a variation between 1119 and 5000 kg/s. Assuming a moderate volatile composition of the magma at

Table 6.2: Summary of the variables and measurements used to estimate the degassing rate the magma at Villarrica volcano (Equations 6.3-6.4).

$S_{(mi)}$ $[ppm]$	$S_{(mg)}$ $[ppm]$	C_m (wt frac.)	C_g (wt frac.)	ΔS $[ppm]$	Q_{SO_2} $[kg\ s^{-1}]$	Q_m $[kg\ s^{-1}]$	Q_v $[m^3\ s^{-1}]$
1400	100	0	0.4	1340	3	1119	0.43
1000	100	0	0.4	940	3	1596	0.61
400	100	0.1	0.4	300	3	5000	1.92

depth, with 1 wt% H_2O, the calculated density is ~2600 kg/m^3 (with 2 wt% H_2O $\rho_m \sim 2535 kg/m^3$). With this value, the calculated volume degassing rates yielded values in the range 0.43-1.92 m^3/s (Table 6.2). For comparison, Witter *et al.* (2004) calculated a degassing rate of 2.2 m^3/s.

Equivalent radius

The viscosity of the degassed melt was calculated based on the average composition of the matrix glass of the 2000 reticulite, at T=1100°C (Witter *et al.*, 2004). Using the formula of Hui and Zhang (2007), the calculations of viscosity of the melt with 0 and 0.1 wt% H_2O yielded $1.78 \cdot 10^4$ and $7.91 \cdot 10^3$ Pa s, respectively. Reducing the temperature of the melt by 100°C increases the viscosity, with variations of up to an order of magnitude in the case of the dry melt. Considering the final crystal content of 37 vol% measured in pyroclasts, and using Equations 6.18-6.19, the viscosity of the mixture melt+crystals is $9.64 \cdot 10^4$ and $4.28 \cdot 10^4$ Pa·s, for melts with 0 and 0.1 wt% H_2O, respectively. These results are more than an order of magnitude higher than those calculated by Witter *et al.* (2004).

To calculate the viscosity of the ascending magma, a whole-rock composition of reticulite and scoria is taken from Witter *et al.* (2004), considering a temperature of 1200°C, no phenocryst, and water contents of 0.5, 1 and 2 wt%; the results are $1.88 \cdot 10^2$, $5.86 \cdot 10^1$ and $1.44 \cdot 10^1$ Pa s, respectively. Again, these results are an order of magnitude different from those of Witter *et al.* (2004). The viscosity ratio between the ascending (lighter) and descending (heavier) magmas ranges between $1.5 \cdot 10^{-4}$ and $4.4 \cdot 10^{-3}$. Although the exact values of the viscosity of the ascending magma is not relevant to quantify degassing rates (Section 6.3.1), the estimation of C_Q in Equation 6.7 requires to know whether the viscosity ratio is lower or greater than 0.2 (Chapter 5). Thus, for the convection of magmas in a vertical conduit with viscosity ratio much lower than 0.2, the flux coefficient C_Q is estimated as 0.1.

The density difference between the relatively gas-rich magma and degassed magma is an important variable in the calculation of the dynamics of the convection (Equations 6.5-

Table 6.3: Variables used in the calculation of the equivalent radius R. Other values used are: $\rho_d = 2650$ kg m^{-3}, $\mu_d = 1.78 \cdot 10^4$ Pa s, $C_Q = 0.1$ ($C_Q/\mu_d = 5.6 \cdot 10^{-6}$), θ=0, $Q_{SO_2} = 3$ kg s^{-1}.

ΔS [ppm]	ρ_m [$kg\ m^{-3}$]	$\Delta\rho$ [$kg\ m^{-3}$]	Γ [$m^5\ s^{-2}$]	R [m]
1340	2519	131	$1.2 \cdot 10^{-3}$	2.8
940	2548	102	$2.2 \cdot 10^{-3}$	3.3
300	2614	36	$1.9 \cdot 10^{-2}$	5.6

6.8). The density of the fresh magma was calculated with the formula of Spera (2000), at 1200°C and with water contents of 0.5, 1.5 and 2 wt%, yielding densities of 2614, 2548 and 2519 kg m^{-3}, respectively. These concentrations of water were chosen so they could roughly agree with the content of sulphur used for the calculation of sulphur loss (S=400, 1000 and 1400 ppm). Because of the large uncertainty in the estimation of water content (Witter *et al.*, 2004; Shinohara and Witter, 2005), the proportion between these two species is not well constrained. Nevertheless, based on the composition of the melt inclusions (Witter *et al.*, 2004) and the ratio measured in the volcanic plume (Shinohara and Witter, 2005), these values are considered reasonable. A density of 2650 kg m^{-3} was calculated for the degassed melt at 1100°C, based on the composition of the matrix glass of reticulite (Witter *et al.*, 2004). The values used in the calculation of the equivalent radius (Equations 6.7-6.8) are presented in Table 6.3. The equivalent radius obtained ranges between 2.8 and 5.6 m.

Interpretation and discussion of the results

An estimation of the density profile was calculated for Villarrica magma for three initial volatile contents (Figure 6.9). In the calculations of density, and to simplify the calculations, crystallisation was not included and changes in density owing to variable water contents were calculated with Equation 6.10. In this model, the melt density increases only as a consequence of gas loss. It is expected that crystallisation and eventually cooling of the magma will increase the density of the degassing melt, increasing the density difference between ascending and descending magma. The sudden decrease in density is caused by exsolution of water at pressures where the solubility of water drops rapidly (Figure 6.9). Because water is the most abundant volatile in low-silica magmas, and owing to the lower solubility of CO_2 (Figure 6.7), the variations in vesicularity of the magma at shallow levels (<100 MPa for H_2O wt% <3) are dominated by exsolution of water. This is also a consequence of low volatile contents and high solubility of water (Figure 6.9). Moreover, note that the effect of exsolution of CO_2 on the density of the magma is small compared with that of H_2O, and the strong effect

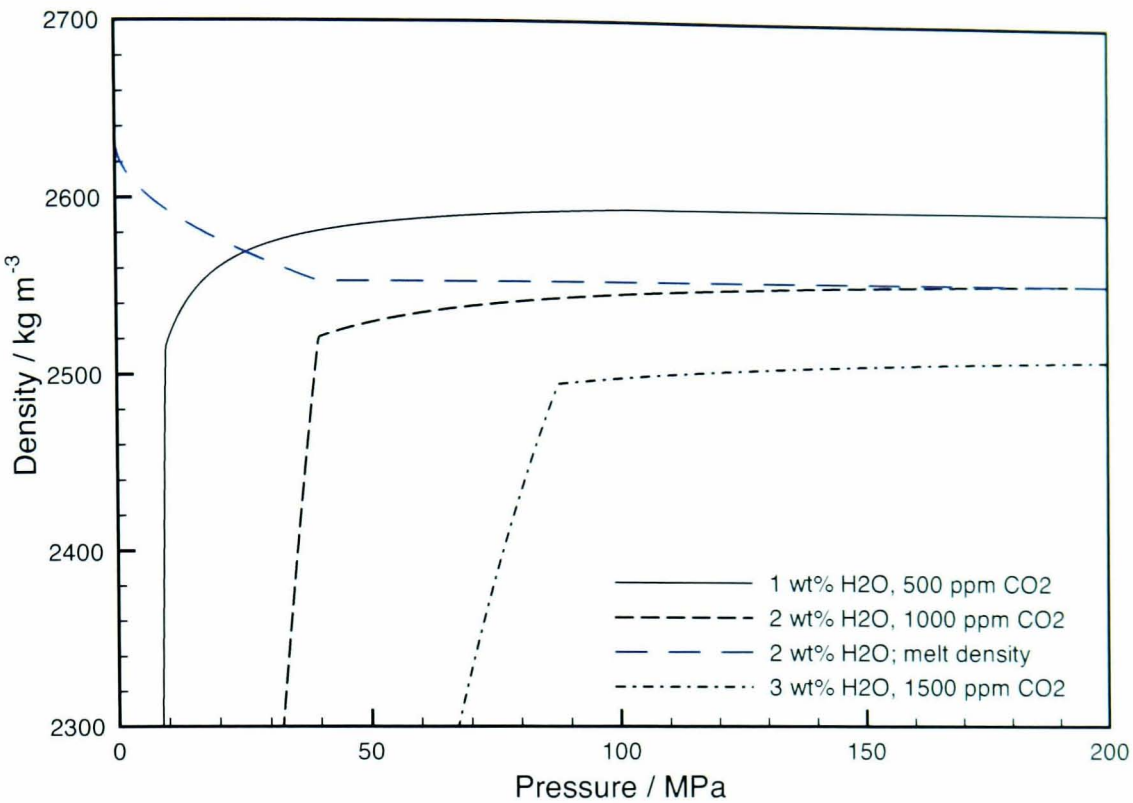

Figure 6.9: Density profile along the conduit of Villarrica volcano. Three examples of magmas with different initial volatile content are shown: a) 1 wt% H_2O, 500 ppm CO_2, b) 2 wt% H_2O, 1000 ppm CO_2, and c) 3 wt% H_2O, 1500 ppm CO_2. For the calculations, the density of anhydrous magma was set to 2635 kg m^{-3}. The abrupt change in density is due to the rapid exsolution of water.

of increasing volatile content on shifting the supersaturation level towards higher confining pressures. Thus, increasing the volatile content implies that a separate gas phase forms at deeper levels, the density of the ascending magma decreases, coalescence of bubbles is enhanced, and the convective flow rate increases. Observations of the continual bursting of bubbles of different sizes, during seething magma and strombolian explosions, and the arrival of large gas pockets, as represented by small lava fountaining, constitute strong evidence of separation of the gas phase in the upper conduit, and absence of a geometrical trap in which bubbles could accumulate.

Three scenarios of volatile loss have been considered in the calculation of magma degassing rate (Table 6.2) and equivalent radius (Table 6.3). With the lowest value of initial sulphur (400 ppm S, 0.5 wt% H_2O) the magma degassing rate and equivalent radius obtained were the highest. It also yielded the most realistic relation between SO_2 emission rate and sulphur loss (Figure 6.10), in which small increases of initial sulphur content (<0.5 wt% H_2O) can explain an increase of SO_2 flux from 3 to 15 kg/s, as measured during the elevated activity in 2005 (Chapter 3). Since a sulphur concentration of 400 ppm in melt inclusions is one of the highest measured by Witter *et al.* (2004), this concentration may well represent the

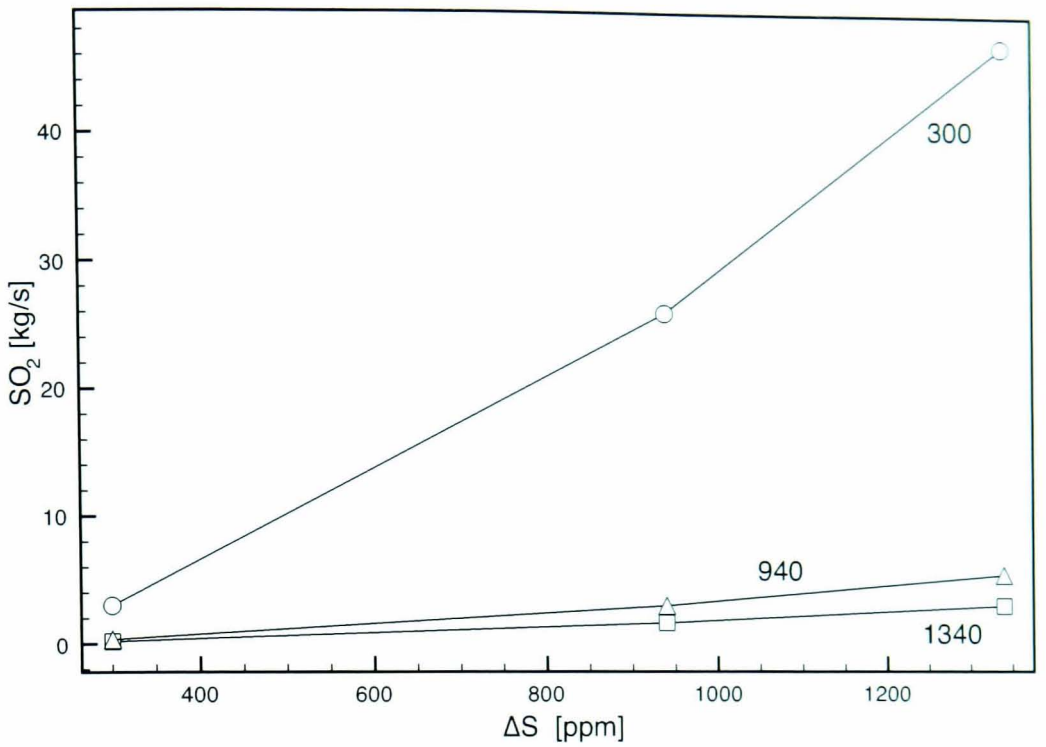

Figure 6.10: Relation between SO_2 flux and sulphur degassed for the cases considered in Table 6.3. Each line represents a relation based on a calculated SO_2 flux of 3 kg s^{-1} associated with a sulphur loss of 300, 940 or 1340 ppm.

volatile content of the ascending magma, and the inverse correlation observed between S and TiO_2 (Figure 6.8) may be caused by crystallisation at shallow levels. Therefore, degassing of magma in the upper part of the plumbing system (less than a few kilometers in depth) can be explained by convection of relatively degassed magma, with initial volatile contents of about 400 ppm S and 0.5 wt% H_2O. Modelling the crystallisation of magma with MELTS (Ghiorso and Sack, 1995) under isothermal decompression and using bulk rock composition of Villarrica samples (T=1130-1140 C, H_2O=2wt%), Witter *et al.* (2004) predicted crystallisation at P<17 MPa. This low pressure of crystallisation would explain the degassed melt inclusions found in phenocryst (Figure 6.8).

6.3.4 Magma degassing at Stromboli volcano

Recent studies of the petrology of scoria produced during normal strombolian activity, and 'pumice' produced during more vigorous explosions, revealed a rather complex magma system consisting of multiple reservoirs in which magma undergoes multi-stage degassing (Métrich *et al.*, 2001; Bertagnini *et al.*, 2003; Vaggelli *et al.*, 2003; Francalanci *et al.*, 2004, 2005). The following is a list of relevant conclusions obtained from those studies:

1. most of the volcanic products, produced during normal strombolian activity, are derived from a degassed and highly porphyritic magma (HP-magma).

2. more energetic (vigorous) explosive eruptions also produce 'pumices' derived from a volatile-rich magma with low phenocryst content and more mafic composition (LP-magma).

3. the volatile-rich (crystal-poor) magma contains 1.8-3.4 wt% H_2O, 707-1887 ppm CO_2. 1420-2400 ppm S.

4. crystal fractionation is a suitable mechanism to account for the erupted high-K basaltic magmas, and also induces significant degassing of sulphur (may be at least 15%).

5. sulphur partitioning in to the gas phase could begin at high pressures (as high as 3-3.5 kbar), during early stages of crystallisation.

6. crystallisation of the gas oversaturated magma during decompression occurs rapidly (between 4 and 46 hours, or less).

7. rise of volatile-rich magma is rapid, inhibiting crystal nucleation induced by volatile loss as well as decoupling of the gas phase from the melt; it occurs as a buoyant, and probably turbulent, ascent of relatively light blobs of magma.

8. two magma reservoirs, at ca. 11 and 3 km depth contain the LP- and HP-magma respectively; a cumulus crystal mush reservoir might be situated just below the shallow magma chamber (>3 km depth).

9. mixing of the HP-magma with the LP-magma occurs in the shallow magma reservoir, where the HP-magma is not fully degassed, producing a homogeneous and well overturned magma that feeds the activity observed at the surface; further degassing and crystallisation occurs as the HP-magma ascends to the surface.

The geometry of the plumbing system is another important characteristic of Stromboli volcano. Several studies show that the plumbing system of Stromboli is a dyke, or crack, with strike NE-SW and dip to the northwest. Tibaldi (2003) and Tibaldi *et al.* (2003) showed that since 100 ka BP, the edifice has faulted along a NE-SW weakness zone, which coincides with the current lineament of craters at the summit, and with the lineament defined by the summit terrace and the vent from where lava extruded during the eruptions of 2003 and 2007 (e.g. Calvari *et al.*, 2006). Dykes intruding the edifice dip to the northwest, with dykes younger than 13 ka BP dipping in the range 20-80 degrees (Tibaldi, 2003). Chouet *et al.* (2003) imaged

the source of very-long-period seismic transients, characteristic of the seismicity associated with the current explosive activity, as a NE-SW crack that dips $\sim 60°$ to the northwest.

Degassing rate and equivalent radius

The calculation of the magma degassing rate and equivalent radius follows the same procedure used in the case of Villarrica volcano. In the case of Stromboli, the flux coefficient is corresponds to that of an inclined conduit with very low viscosity ratio, which is estimated as 0.25 (Chapter 4).

Following the model of Francalanci *et al.* (2005) (see Figure 10 in that paper), two magma flow rates could be obtained from the convection between 1) a shallow magma reservoir situated at a depth of ~3 km that contains partly degassed HP-magma, and a deeper magma reservoir (depth ~11 km) containing LP-magma, and between 2) the shallow magma chamber with mixed LP- and HP-magma and the uppermost part of the system where gas escapes. The properties of the volatile-rich LP-magma and degassed HP-magma are taken from Métrich *et al.* (2001). An intermediate volatile composition of the partly degassed HP-magma is obtained from melt inclusions in scoria samples (Métrich *et al.*, 2001; Bertagnini *et al.*, 2003). The calculated magma degassing rates are 1013 and 2332 kg/s for the convection between the reservoirs and convection in the upper part of the conduit, respectively. The associated volume flow rates are 0.4 and 0.9 m^3/s, and the equivalent radii are 1.3 and 3.2 m, respectively.

Interpretation and discussion of the results

Magma degassing at Stromboli is controlled by the circulation of magma through at least 3 reservoirs (Francalanci *et al.*, 2005). For instance, LP-magma ascends and interacts with degassed HP-magma, but it rarely erupts (only one to three events per year Francalanci *et al.* (2005)). Thus, the main role of the LP-magma during normal explosive activity at Stromboli is the supply of a hot, poorly crystallised and gas-rich melt to the HP-magma reservoir. Calculations made by Burton *et al.* (2007b) suggest that in this shallow reservoir the melt can exhibit a high vesicularity (up to ~0.5). Mixing of magma and gas segregation in this reservoir will determine the ascent of wet magma and bubbles to the surface. Calculated degassing rates of the mixed HP-magma are twice as much of that of the LP-magma, which could be explained by a lower magma flux caused by a smaller equivalent radius of the conduit. Thus, the transport of gas from deep levels to the surface, dissolved in the melt and

as a separate phase, cannot be modelled assuming a single-conduit plumbing system.

The geometry of the plumbing system has important implications to the outgassing activity observed at Stromboli volcano. First of all, the upper part of the plumbing system is likely to comprise narrow conduits accommodated in a planar structure, delimited by the NE-SW weakness zone. Secondly, the inclination of the conduits favours the stratification of the convective melts, and the segregation and coalescence of bubbles towards the upper side of the conduits. Thus, the accumulation and coalescence of bubbles within inclined conduits with irregular geometry (and shape) explain the source of the intermittent ascent of large gas slugs that generate the characteristics strombolian activity at Stromboli.

6.4 Outgassing at open-vent low-silica volcanoes

6.4.1 Relationship between bubble bursting styles

At the uppermost section of the plumbing system, the explosive outgassing activity at open volcanoes is the result of gas pockets rising through the melt and bursting at the magma free–surface. The amount of gas that reaches the surface in the form of bubbles, the size distribution of these bubbles, and the properties of the melts, are some of the most relevant variables that define the style of activity. Regardless of the position of this surface within the system (i.e. lava lake near the top end of the vent or deeper in the conduit), the style of the activity ranges in a continuum from a single mild burst (involving only one bubble) to a continual and high frequency bursting sequence.

A schematic diagram of the relationship between different explosive outgassing events is proposed on the basis of their duration and strength (Figure 6.11). Here, the strength of the bubble bursting activity is estimated as the height above the surface of the lava lake that pyroclastic material can reach, which is related to the mass fraction of volatiles, overpressure and magma rise velocity (Wilson, 1980). Thus, the different outgassing styles observed at Villarrica and Stromboli volcanoes can be listed in order based on their strength: gas-puffing, seething magma, small lava fountain, strombolian explosions, and lava fountains. And in terms of the duration (and persistency) of the event: single bubble burst, strombolian explosion, small lava fountain, hawaiian lava fountain, seething magma, and gas puffing. This arrangement is qualitative and is intended to clarify the identification of new styles of bubble burst events described herein that, in a general sense, have been described in previous work as 'Strombolian activity' (e.g. Ortiz *et al.*, 2003; Witter *et al.*, 2004).

At one end, gas puffing is considered the activity with the longest duration and lowest strength. Seething magma is also considered as showing low strength. Although its duration has not been constrained, on the basis of direct visual observations of the lava lake it is believed that this activity is continuous in time but with fluctuations in strength: from mild seething magma, whose lower end corresponds to gentle roll-over of the lava surface, to vigorous seething magma, whose upper end is lava fountaining. Seething magma has been observed to evolve into a small lava fountain in a time span of a few seconds. Occasionally, the activity falls in between the two extremes, appearing as a vigorous seething magma or as a very small lava fountain (Figure 6.11).

At the other extreme, strombolian explosions are relatively short and display a broad

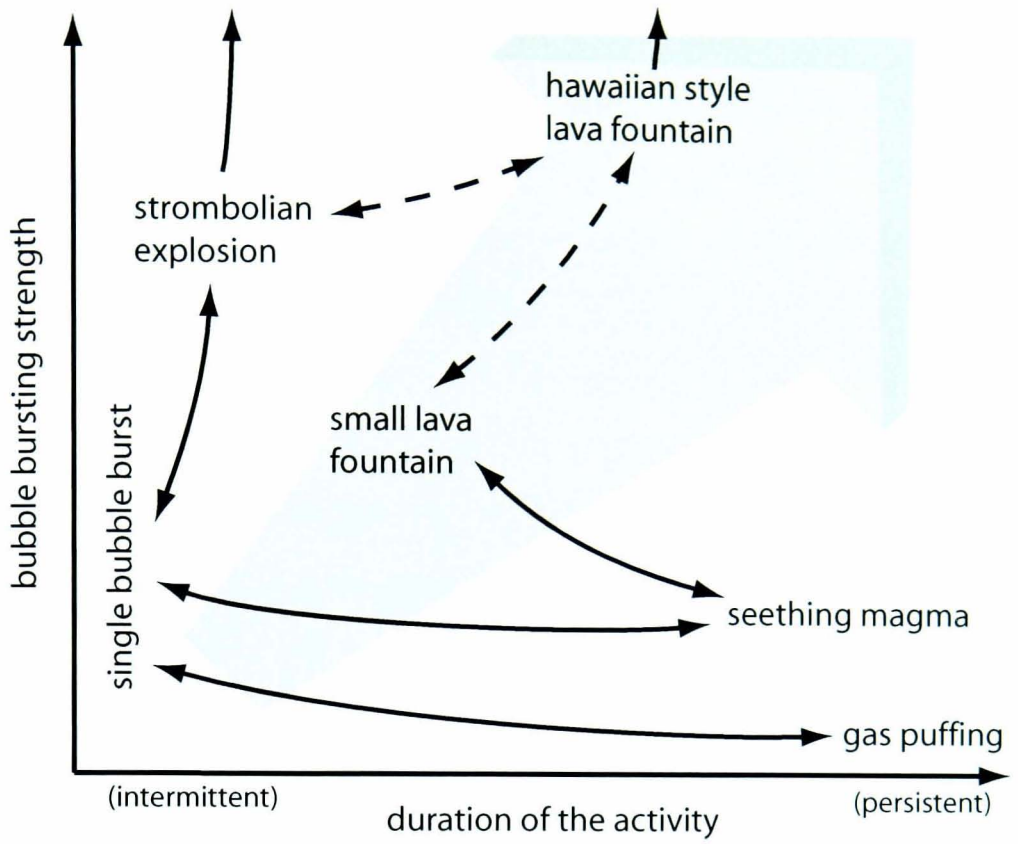

Figure 6.11: Schematic diagram of bubble burst styles that shows the relationship between the duration and strength of the events. Continuous line connections denote the continuum between events, whereas dashed line connections denote the feasible occurrence, although not observed directly at Villarrica or Stromboli, of a continuum between strombolian explosions or small lava fountains, and the Hawaiian-style fountaining. The grey arrow denotes the increase in total gas emission as the duration and strength of the events increases.

range of behavior, from relatively mild single bubble bursts to major explosions that can send pyroclastic material hundreds of meters above the lava lake. The link between strombolian explosions and seething magma is not a continuum. Strombolian explosions are considered isolated events that interrupt the seething magma activity.

Although Hawaiian style lava fountaining is not part of the common activity seen at Villarrica during periods of volcanic quiescence, in which the lava is confined inside the crater, it is included in Figure 6.11 to map the relation with respect to the other types of primary bubble burst. For instance, at Mount Etna strombolian explosions have been observed having a very high bursting frequency, which made them look similar to a Hawaiian-style lava fountain (e.g. Chester *et al.*, 1985, p. 126–130). And at Stromboli, Type 1 explosions sometimes resemble a short lava fountain (Chapter 3 in this thesis; Patrick *et al.*, 2007).

6.4.2 Interpreting the dynamics of volcanic outgassing

At Villarrica, the continuous bubble bursting activity observed at the surface of the lava lake reflects the highly dynamic convection of magma developed at shallow depths in the conduit. This convection is caused by the density difference between the hot and relatively gas-rich magma rising from deep levels in the magma column (or magma chamber), and the degassed and cooler magma that has reached the uppermost part of the system, which must sink back owing to its higher density (Chapter 5, this thesis; Kazahaya *et al.*, 1994; Stevenson and Blake, 1998). In addition, the intensity of the convection is enhanced by the growing bubbles that form above gas supersaturation levels, by displacing the melt sideways and downward as they pass upwards. Hence, near the surface the convection is governed by a bubbly to churn-type flow regime whose strength is dependent on the ascending gas flux (Mudde, 2005; Xu *et al.*, 1999). I am not aware of this very dynamic flow regime, as represented by seething magma and small lava fountains, having been observed elsewhere. Convection of magma at the lava lake, as observed during the persistent seething magma activity, inhibits the development of a continuous crust over the lake surface.

Infrasonic records offer a good opportunity to investigate different styles of activity at open-vent volcanoes (Johnson *et al.*, 1998; Ripepe and Marchetti, 2002; Johnson *et al.*, 2004). Johnson *et al.* (2004) showed that there exists a comparable amplitude in the infrasonic signal for bubble bursting events at Stromboli, Erebus and Villarrica volcanoes. For instance, infrequent (<1 per day) explosions at Mount Erebus, from single bubbles of radii ca. 5 m bursting at the surface of the lava lake, exhibited infrasonic N-wave amplitudes ranging from 2 to 100 Pa at 1 km from source (Johnson *et al.*, 2004). Analysis of very-long-period seismic oscillations at Mount Erebus, led Aster *et al.* (2003) to interpret the presence of a near-summit magma reservoir in which bubbles coalescence supports the ascent of large gas slugs that generate the observed strombolian explosions. This behaviour is in agreement with the model of strombolian activity originated with the accumulation and coalescence of gas bubbles at the roof of a reservoir (or big cavity) (Jaupart and Vergniolle, 1988, 1989). At Villarrica, however, the infrasound trace shows continuous pressure oscillations, including impulsive transients and small amplitude waveforms that repeat along the whole time series (see Figure 3 in Johnson *et al.*, 2004). This type of data reflect very well the remarkable continuous bubble bursting activity developed at Villarrica volcano. In this case, the outgassing activity might rather be determined by the 'free' (with no constrictions or obstacles) ascent of bubbles in the vertical conduit.

At Villarrica, the occurrence of the small lava fountain activity at or near the surface of the lava lake, involving a higher amount of bubbles bursts than seething magma, indicates higher gas contents rising in packets at slightly higher velocities determined by the density of the melt-bubble mixture. A possible interpretation for these fluctuations in gas (bubble) content in the vertical column of magma arise on the basis of waves of bubbles (Manga, 1996), in which bubbles ascending within the conduit tend to concentrate into layers (or clusters) owing to the decreasing rise speed of the bubbles as their concentration increases. Consequently, gas bubbles reach the surface in packets rather than with an uniform vertical distribution. A similar mechanism has been invoked to explain gas puffing activity at Stromboli volcano (Ripepe *et al.*, 2002). Nevertheless, not only rapid fluctuations in the style of outgassing activity are seen at Villarrica, but also progression to strong strombolian explosions or high (few hundred metres) lava fountains during episodes of elevated and/or eruptive activity (Chapter 4). Parfitt and Wilson (1995) stated that it is the combination of the rise speed of the magma and the degree of bubble coalescence that defines the respective style of activity, where the magma gas content and viscosity influence only the conditions in which the transition between these two styles occurs. Hawaiian-style lava fountaining requires a relatively high magma rise speed and little coalescence of bubbles, which cause a highly vesicular melt that disrupts at deep levels (high pressure), whereas strombolian explosions are caused by a slow rise of the magma in which coalescence plays a fundamental role in the generation of large bubbles that disrupt the magma at the magma-atmosphere surface. A two-fold change in magma rise speed might be sufficient for the transition between one style of activity to the other (Parfitt and Wilson, 1995). Both changes, increase in magma gas content and decrease in viscosity of the melt, are plausible within the open system of Villarrica volcano. They can be a consequence of either heterogeneous magma distribution and convection in a magma chamber, that could eventually vary the properties of the magma rising into the upper plumbing system, or entry of new gas-rich batches of magma into the system.

Chapter 7

Conclusions

Throughout this thesis I investigated the dynamics of degassing in open volcanic systems with magmas of low viscosity, using a multidisciplinary approach that involved (i) measurements of passive, explosive and total SO_2 emissions, (ii) visual and video-recorded observations of outgassing activity, (iii) analysis of seismic data, (iv) analogue modelling of convective flow in narrow pipes, (v) analytical modelling of countercurrent flow using a one-dimensional two-fluid model, and (vi) investigation of magma properties and conceptual modelling of magma flow in plumbing systems with narrow conduits.

In this last chapter I present a summary of the main achievements and conclusions made in this thesis, and future research directions that would complement the work developed herein and contribute to a better understanding of magma degassing at open-vent volcanoes.

7.1 Understanding degassing of open-vent low-silica volcanoes

7.1.1 Outgassing activity: geophysical measurements

Measurements of SO_2 fluxes and column path-length concentrations were performed with a portable UV spectrometer called FLYSPEC. In order to correct for problems with the calibration of the instrument, and for post-processing analysis of the results, a new algorithm for spectra processing was developed. This new algorithm shows very good results when compared with those obtained with other instruments (Chapter 2).

Measurements of SO_2 path-length concentration of the volcanic plume at the summit of Stromboli and Villarrica volcanoes exhibited variations of more than 50% in the gas emissions from the craters. This variation contributes to the heterogeneous gas concentrations within the plume, which must be taken into account when measuring gas fluxes. Direct

measurements of SO_2 emissions during explosive outgassing have been made at Villarrica and Stromboli volcanoes (Chapter 3). However, an accurate quantification of gas emitted during strombolian explosions (at Stromboli volcano) could not be obtained owing to instrumental and technical limitations. Measurements of SO_2 concentrations in ash-rich plumes require new research on the relationship between optical depth, mass of pyroclasts and SO_2 concentration in the plume (Chapter 3).

At Villarrica, variations of the seismic amplitude, evaluated as RSAM, and changes in the relative amplitude of the dominant peaks in the frequency of the tremor were correlated with morphological changes in the crater floor and elevated levels of activity observed during November 2004–April 2005. Most of the seismic tremor is likely caused by the explosive outgassing activity taking place at the upper part of the conduit and lava lake. SO_2 flux measurements made at different periods between 2000-2006 correlate linearly with seismic energy (expressed as RSAM values). This correlation emphasizes the strong link between degassing magnitude and outgassing, as measured by seismometers (Chapter 4). Potentially, this correlation offers the possibility to estimate gas fluxes from seismic measurements.

At Villarrica, background (low) levels of activity correspond to a lava lake located >80 m below the crater rim, small and/or blocky morphology of the roof, seismic amplitude (RSAM) lower than 25 units, few volcano-tectonic earthquakes, and daily averages of SO_2 emissions lower than 600 Mg/day. Higher SO_2 emissions appeared to be related to higher levels of the lava lake, stronger bubble bursting activity and changes in the morphology and texture of the crater floor. SO_2 flux as high as 1500 Mg/day has been measured during periods of elevated activity (Chapter 4).

7.1.2 Outgassing activity: bubble bursting styles

Different styles of bubble bursting activity can be recognised at these volcanoes: seething magma, small lava fountains, strombolian explosions and gas puffing. The first two have been observed only at the lava lake of Villarrica volcano. Seething magma consists of continual burst of bubbles a few metres in diameter, and with varying strength, over the entire surface of the lava lake. Small short-lived lava fountains, seen as a vigorous extension of seething magma, commonly have durations of 20-120 s and reach 10-40 m high above the lava free-surface. Gas puffing consists of small and repetitive bubble bursts with a generally stable eruption frequency in the range 0.1-1.2 s^{-1}. This style of activity has been described at Stromboli volcano only, and it has not been observed at Villarrica (Chapter 3).

At Stromboli, temperature time series of explosion plumes (of gas and pyroclastic material) measured with the FLIR, yield valuable insights into the variability of bubble-burst sequences during strombolian explosions (Chapter 3). Distinct bubble-burst sequences were identified for Type-1 and Type-2 explosions (as defined by Patrick *et al.*, 2007). Unlike the particular style of strombolian explosions originated by single-bubble bursts observed at Mount Erebus (Aster *et al.*, 2003), at Stromboli the wide range of bursting styles is product of large gas packets reaching the surface. Strombolian explosions may exhibit a wide spectrum of duration and particle size distribution of the material ejected. At Villarrica, strombolian explosions commonly eject spatter-rich (ash-poor) pyroclastic material from ten to hundreds of metres above the lava lake. These explosions exhibit variable durations from less than 1 s in a single bubble burst to more than 15 s in a bursting sequence. At Stromboli, explosions taking place at the northeast and southeast craters can have durations of between 5 and more than 40 seconds, and can be ash-rich or ash-poor (spatter-rich). In this bursting sequence, commonly the intensity of the bursts is highest within the first stages of the explosion.

Other types of activity have been observed at Villarrica volcano, that originate from the interaction between bubble bursting activity and the spatter roof: gas jetting and splashing magma. Gas jetting consists of a strong exhalation of gas and generally fine (ash-lapilli in size) material. Splashing magma consists of coarse (poorly fragmented) spatter expelled out of the vent which fragments on exit and accumulates around the vent.

7.1.3 Fluid mechanical modelling of magma convection in narrow conduits

Magma convection in narrow conduits was investigated through analysis of the steady-state axisymmetric flow of immiscible liquids in a vertical cylinder, with laboratory experiments of convection of immiscible fluids in vertical and tilted pipes, and modelled with a two-fluid model of axisymetric and stratified flow in vertical and tilted pipes, respectively (Chapter 5).

The volume flux of the convection was constrained in terms of 'flux coefficient', which depends on the viscosity ratio between the liquids, flow regime, angle of inclination of the pipe, and position of the interface between the fluids. Overall, the viscosity ratio can control most of the variation in the flux coefficient. However, at viscosity ratios (light liquid over the dense liquid) lower than $\sim$0.1, the influence of variable viscosity ratios apparently disappear.

In tilted pipes the liquids tend to segregate and stratify, increasing the flow rate of the convection. The flux coefficient in tilted pipes showing stratified flow can be up to 5 times

higher than the flux coefficient in vertical core-annular flows.

Flow regimes other than laminar core-annular flow and laminar stratified flow exhibit values of the flux coefficient in between those obtained in these two main flow regimes.

7.1.4 Dynamics of magma degassing at Villarrica and Stromboli volcanoes

Convection of magma in the plumbing system is proposed as the driving mechanism of persistent outgassing. A simple model of magma degassing has been devised in which gas-rich magma ascends from a reservoir to the surface within dikes or cylindrical conduits. The model is implemented through the calculation of the properties of the melt and gas solubilities, and by using a determined flux coefficient value to calculate the 'equivalent radius' of the system (Chapters 5 and 6). Constraints on the variations of gas emission rates and in the style (or strength) of the activity can be obtained using the equivalent radius and changes in the properties of the magma with varying initial volatiles content.

Magma degassing at Villarrica is characterised by the ascent of a relatively gas-rich magma through, perhaps, a shallow reservoir (2-5 km deep). Most of the gas exsolves at shallow levels in the upper part of a vertical conduit, leading to continuous bubble bursting activity and changes in position of the lava lake that correlate with the gas emission rates (Chapters 3, 4 and 6).

At Stromboli, magma degassing takes place in an inclined dyke (or dykes). Within this geometry, magma convection adopts a stratified regime of the gas-rich and lighter magma overlying the degassed and denser melt. Gas segregation towards the upper wall favours coalescence of bubbles and efficient convection. Interconnected conduits at the uppermost part of the system constrain the release of the large gas slugs observed during strombolian explosions (Chapter 6).

7.2 Further work

7.2.1 Volcanic activity

In this thesis only the activity of Villarrica and Stromboli volcanoes has been investigated. In general, the persistent outgassing activity observed at other open-vent volcanoes, such as Mount Erebus, Ambrym, Yasur, Fuego, Pacaya and Masaya, share similar characteristics to those observed at Villarrica and Stromboli volcanoes. For instance, they all exhibit a gas plume emitted from their summit crater, occasionally interrupted by the explosive emis-

sion of pyroclastic material (explosive outgassing). At volcanoes with a visible lava lake, such as Villarrica and Mount Erebus, the characteristics of bubble bursting styles are better constrained. From single bubble-burst to seething magma, or ash-poor strombolian explosions, these styles can be investigated in detail through video recordings, thermal measurements, seismicity, infrasound and high-time resolution measurements of gas emissions. To date, such multidisciplinary investigation has not been carried out (or published). These data would allow the quantification and correlation of variables such as gas emission during explosive outgassing, bubble size, bubble overpressure, seismic-acoustic energy partitioning, and a better understanding of the magma dynamics within the uppermost part of the plumbing system as well as changes in magma properties related to magma degassing.

Correlations between seismicity, level and type of volcanic activity, and gas emissions, as found for Villarrica volcano (Chapter 4), can be very important for volcano monitoring and yield insights into the dynamics of magma degassing (Chapters 4 and 6). Correlations like these, however, have not been investigated extensively in open-vent volcanoes. To this end, it is necessary to identify and isolate the seismic signal associated with the outgassing activity. Further investigation quantifying passive and explosive outgassing can contribute to establish and interpret this link. In order to carry out direct measurements of gas emissions during ash-rich explosions, it is necessary to develop new techniques to measure ash content and total pyroclastic mass in volcanic plumes. It is also compulsory to find a relationship between the concentration of pyroclasts and the concentration of gas in the plume.

7.2.2 Magma convection controlled by magma degassing

The model of magma convection developed in this thesis allows the calculation of a new parameter that constrains the dimensions of the plumbing system, the equivalent radius. In theory, the equivalent radius is unique for each volcano and determines the relationship between gas concentration in the source magma (at depth) and gas emission rates measured at the surface. This model endorses possibilities for studying the causes and consequences, in terms of varying magma composition, of changes in the outgassing activity. This model has been applied to Villarrica and Stromboli volcanoes, but it can be used to study magma degassing at other open-vent systems.

The results obtained from the laboratory experiments show that the volumetric flux change when the flow regime is core-annular, turbulent or stratified (Chapter 5). However, the limits for the development of each of these flow regimes (in terms of a specific dimen-

sionless number, for instance) could not be identified. Further analysis of the variables that control the type of flow and position of the interface could improve the determination of the flux coefficient for different pairs of liquids. Moreover, new investigations should address the problem of buoyancy-driven convection of miscible fluids, developing both laminar and turbulent flow regimes.

Appendix A

Steady state laminar flow in a slot

In this section we shall study the problem analysed in Section 5.2 with a different geometry: a narrow slit separated a distance W by two parallel walls. Let first consider the case of a vertical slot with co-axial and symmetric flow on a center plane parallel to the walls. This configuration is similar to the axisymmetric fluid flow in a cylinder (Figure 5.1), thereby a similar solution is expected. The details of the geometry and the parameters involved in the following calculations are shown in Figure A.1.

The Hagen-Poiseuille solution for a vertical slot with only one fluid is:

$$v^{HP}(x) = -\left(\frac{dp^*}{dz}\right)\frac{A^2 - x^2}{2\mu} \tag{A.1}$$

where $p^* = p + \rho g z$ is the piezometric pressure, $A = W/2$ half width of the slot, and μ the viscosity of the fluid.

With two fluids flowing with the configuration depicted in Figure A.1, the velocity profile is given by:

$$v^i(x) = \frac{P^i}{2\mu^i}((\alpha A)^2 - x^2) + v^o(\alpha A) \qquad 0 \le x \le \alpha A \tag{A.2}$$

$$v^o(x) = \frac{P^o}{2\mu^o}(A^2 - x^2) + (\alpha A)\frac{(P^i - P^o)}{\mu^o}(A - x) \qquad \alpha A \le x \le A \tag{A.3}$$

The volumetric flux is given by:

$$Q^i = \frac{2}{3}L\frac{P^i}{\mu^i}(\alpha A)^3 + L\frac{A^3\alpha}{\mu^o}\left(P^o(1-\alpha)^2 + 2\alpha P^i(1-\alpha)\right) \tag{A.4}$$

$$Q^o = \frac{2}{3}L\frac{P^o}{\mu^o}A^3 - L\frac{\alpha A^3}{\mu^o}\left[\frac{2}{3}P^o(1+\alpha^2) - P^i(1+\alpha^2) + 2(P^i - P^o)\alpha\right] \tag{A.5}$$

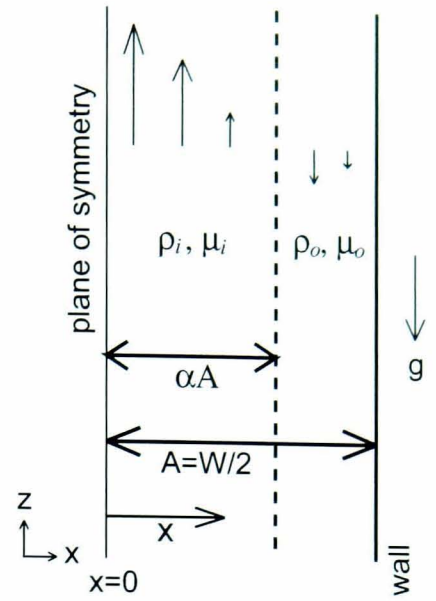

Figure A.1: Definition of the geometry and parameters for the problem of laminar convection in a vertical slot.

Using the definition of the pressure drop as a given weight of fluid (Equation 5.8), the volumetric flux becomes:

$$Q^i = \widehat{Q}^i \; Q^s, \qquad Q^o = \widehat{Q}^o \; Q^s \tag{A.6}$$

with

$$Q^s = \frac{2L}{3A} \frac{A^4 g \Delta\rho}{\mu^o} \tag{A.7}$$

$$\widehat{Q}^i(\phi, \alpha, \eta) = \frac{3}{2}\alpha \left[\frac{2}{3}\phi\alpha^2\eta^{-1} + \phi(1-\alpha^2) - (1-\alpha)^2 \right] \tag{A.8}$$

$$\widehat{Q}^o(\phi, \alpha) = \phi - 1 + \frac{\phi}{2}\alpha(1+\alpha^2) + \alpha(1 - 3\alpha^+\alpha^2) \tag{A.9}$$

With the condition of conservation of volume ($Q^i + Q^o = 0$) the equation for the position of the interface is given by:

$$\alpha^3(2\phi\eta^{-1} - 2\phi - 7) + 6\alpha^2 + \alpha(4\phi - 1) + 2\phi - 2 = 0 \tag{A.10}$$

And finally, from the last equation we obtain an expression for the pressure drop:

$$\phi = \frac{7\alpha^3 - 6\alpha^2 + \alpha + 2}{2\alpha^3(\eta^{-1} - 1) + 4\alpha + 2} \tag{A.11}$$

Appendix B

Convective fluid flow in pipes: Notes from the laboratory experiments

The following are descriptions of selected experiments carried out in the laboratory. These experiments consisted of counter–current (convective) flow of two liquids with different densities and viscosities. Unless specified, all the experiments were performed with a pipe of 20 mm in diameter. The results are presented in Chapter 5 and the fluid properties are listed in Tables 5.3 and 5.4.

B.1 Vertical pipe

0426b. Corn oil and water.

- The experiment started with the interface in the middle of the pipe, and disappeared as soon as the experiment started.
- In the pipe, the water was flowing in the middle and the oil next to the wall.
- The flow showed a cycle of instabilities that started at the upper end of the pipe, creating a long water bubble that moved slowly downwards behind a front of one to three medium–sized bubbles (bubble length similar to pipe radius).
- As soon as the long bubble reached the bottom tank (after 38-50 sec), a wavy and turbulent arrangement of water-oil moved upwards and, after flowing into the top tank, the cycle started again. The whole sequence took 55-70 sec.

Figure B.1: 0426b. Sequence of the instability that evolved from an irregular configuration (left) to the creation of a few uniform-sized bubbles and a long bubble of water. Video stills at 0, 7, 12, 15, 25, 28 and 31 seconds.

- After 50 min the flow stopped. Domes (bulges) of oil were created at the upper tube–tank joint.

0521a Corn oil and glycerol. Vertical 50 mm diameter pipe.

- With the wide pipe the convection within the pipe turned up to be turbulent with an occasional pulsating character.
- The flow experienced the encounter of the fluid fronts accompanied by transversal flow and swirls.
- Oil flowing through the glycerol in the upper tank showed a fairly uniform but oscillating laminar stream, in the limit of turbulence. The pulsating behaviour was cause, at least in part, of the irregular influx from the pipe-tank joint.

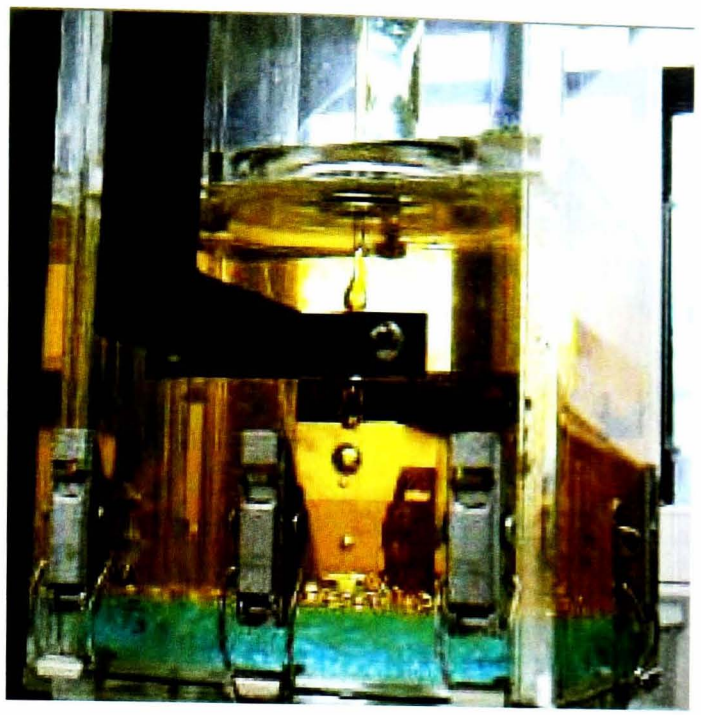

Figure B.2: 0426b. Bubbles of water in the bottom tank.

- The duration of the experiments was less than 1min.

809a. Vegetable oil and glycerol (diluted). 3 experiments.

- Three experiments were carried out with the same liquids in a vertical pipe, and three different flow arrangements were observed.

- The first experiment showed the two liquids flowing on different sides of the pipe with the oil occupying a smaller cross-section area than the glycerol (position of the interface at 0.72). The interface was irregular.

- In the second experiment the liquids were flowing on opposite sides of the pipe, but apparently with a concentric configuration, such that there were vertical eddies in the middle of the pipe. This was evidenced by the continual up and down movement of two small bubbles located in the middle of pipe.

- The third experiment started with a few bubbles of glycerol formed just before the start of the experiment by the shaking of the instrument. The amount of bubbles increased by the sudden initial convective flow that made the oil rise in big slugs. Throughout the experiment the glycerol flowed only as a disperse phase, although at the top of the pipe the influx of glycerol to the pipe was through a continuous stream. However, this stream rapidly broke up into bubbles owing to the bubbly /slug flow that governed in the middle of the pipe. Next to the walls small bubbles of glycerol could rise pulled up by the flow of oil.

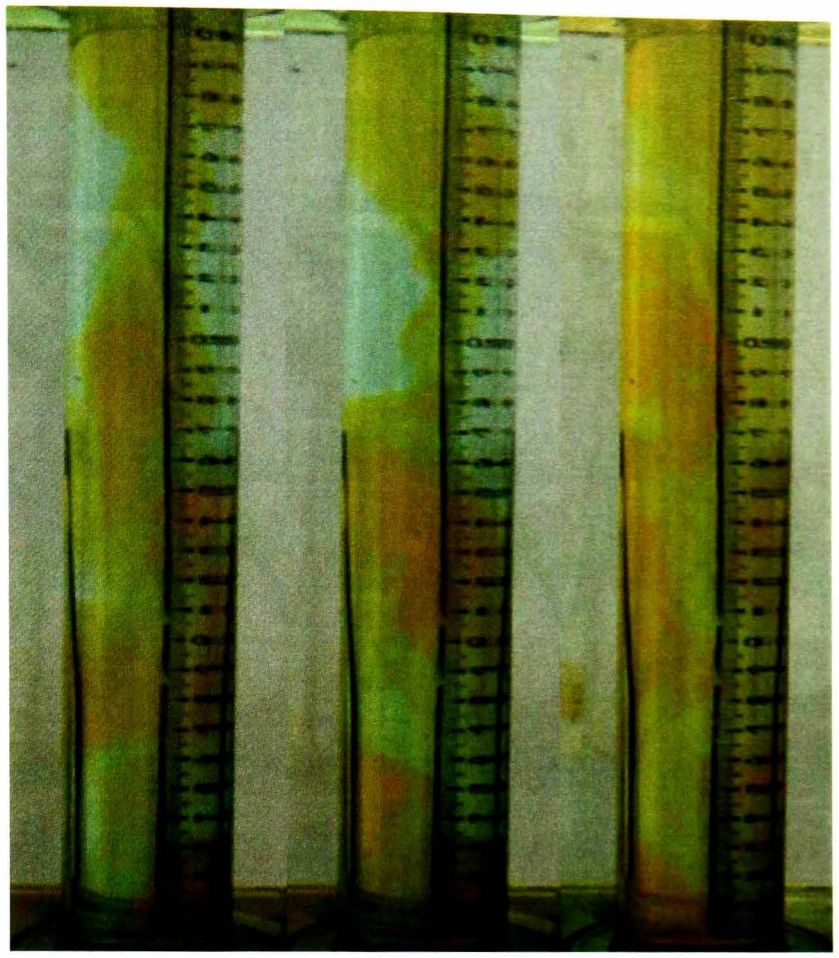

Figure B.3: 0521a. Three examples of the turbulent flow (corn oil and glycerol) through the 50mm wide pipe.

- The volumetric flux decreased from the first to the third experiment.

824a. Sunflower oil and golden syrup (pure).

- The flow showed a stream of golden syrup with a curved (convex) interface. The thickness of the stream was not uniform and its position changed along the pipe.
- In the bottom tank the syrup sunk as a thin laminar thread.
- In the top tank the oil rose as medium-sized blobs; it fluctuated between a single bubble and a bubble with tail.
- The flux of oil to the tank was unsteady owing to the changing cross–sectional area of the stream of syrup at the pipe–tank junction. This oscillation propagated downwards and it was the cause of non-uniform thickness (or cross-section area) of syrup.
- This experiment took more than 5 hours to complete.

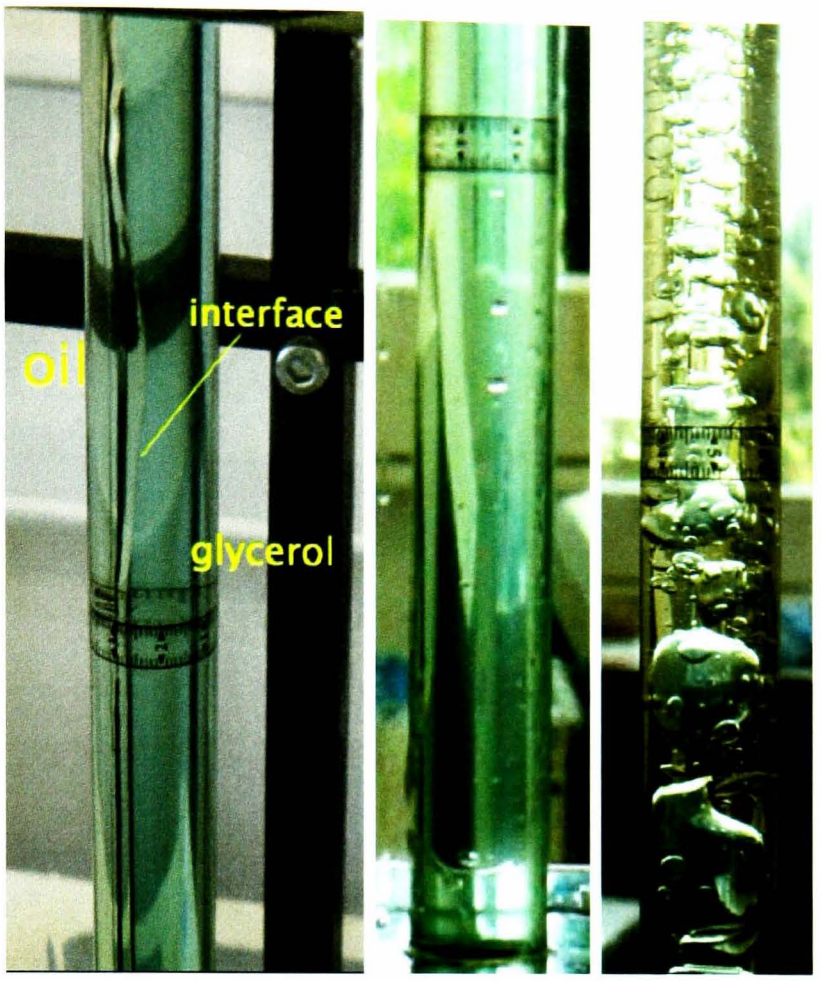

Figure B.4: 809a. Examples of the flow pattern developed in the three experiments (first on the left and the last on the right).

B.2 Inclined pipe

0427a. Corn oil and water (dyed blue). Pipe inclined 21 degrees.

- The first 30 sec of the experiment showed an asymmetry in the pipe at the position of the fluid interface set at the start. It soon disappeared and the oil occupied most of the upper part of the pipe although still showing a wavy interface, perhaps originated at the lower junction pipe-tank.

- Only after ~60 sec the two fluid flow exhibited a stratified flow in a fairly steady state, and with both liquids flowing uniformly in the pipe.

- Within the pipe, the cross-sectional area occupied by the oil (on top) is smaller than the that of the water stream.

- In the top tank, the oil flows suck to the bottom and flowed almost to the wall of the tank before it detached to and flowed up trough the water. From the bottom of the pipe, the water sunk directly to the bottom of the oil portion in the tank.

Figure B.5: 824a. Left: stream of pure golden syrup flowing down next to the wall. Right: blobs of oil rising through the syrup in the top tank.

- This experiment took only 9 min to complete. For comparison, the last one (with vertical pipe) took more than 20 min.

823a. Sunflower oil and golden syrup (pure). Pipe inclined 15 degrees.

- In this experiment the flow rate was very slow, taking more than 3 hours to complete.
- The flow of golden syrup in the pipe was characterised by a stable and uniform stream located next to the wall. However, instead of the classical stratification with plane interface, the syrup showed a curved (convex) interface.
- Right at the beginning the thickness of the syrup was no uniform but gradually changed to the final configuration. At 2 min the thickness was about 13 mm (in the middle of the pipe) and after 4.5min it was about 15 mm.
- The flow of syrup in the bottom tank was laminar, with a thread much thinner than the one in the pipe. In the top tank the oil also flowed in a laminar manner.

727a. Glycerol (pure) and water (dyed red). Pipe inclined 16 degrees.

- The flow was stratified and laminar, with the water flowing on top of the glycerol. Although the liquids were miscible there was very little mixing in the pipe.

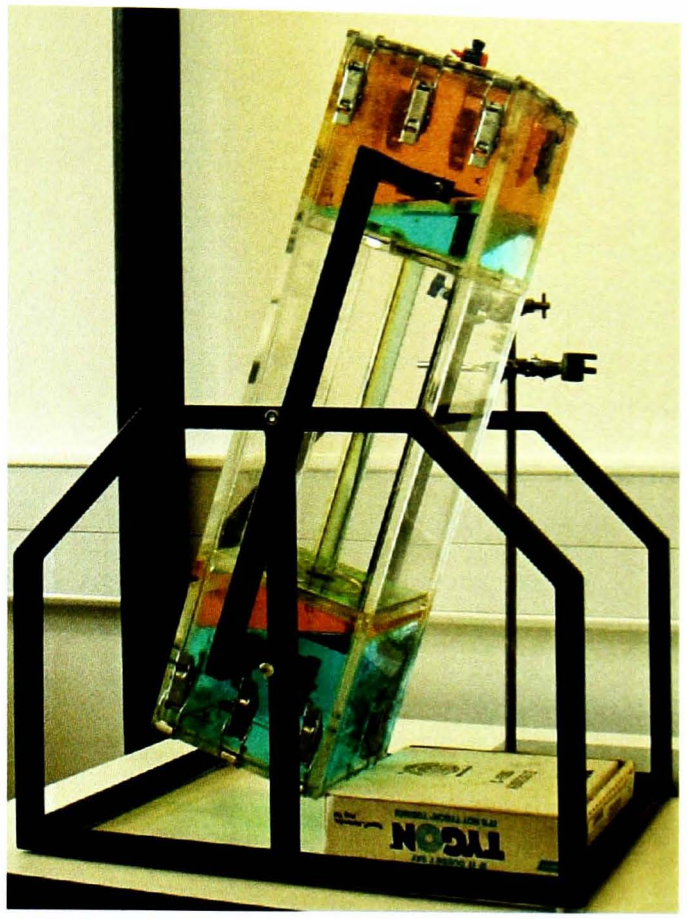

Figure B.6: 0427a. Stratified flow of oil and water.

- The uniform and sharp interface was located near the middle of the pipe, but perhaps with the water occupying a slightly smaller cross-sectional area than the glycerol.
- Most of the mixing occurred around the interface water-glycerol within the tanks.
- In the bottom tank the glycerol sank with a laminar and vertical stream. In the top tank the flow of water showed an irregular and undulating pattern.
- It was difficult to read the changes in volume in both upper and lower tank due to the thick interface water-glycerol. After 4min, it was about 0.5 cm thick.

B.3 More examples

The following are other examples of flow patterns observed in vertical pipes (Figure B.9), inclined pipes (Figure B.10), and flow in the bottom and top tanks(Figure B.11).

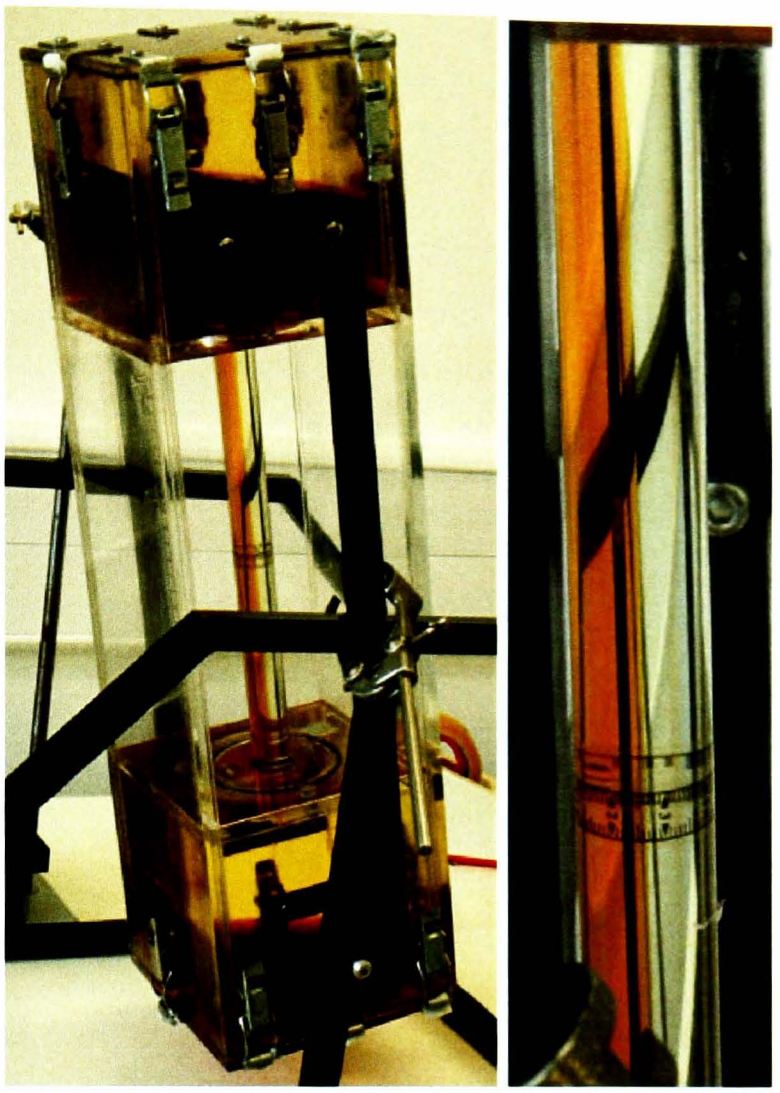

Figure B.7: 823a. Stratified flow of golden syrup in oil.

Figure B.8: 0727a. Stratified flow of glycerol pure (red) and water. The left photo shows the pipe and bottom tank and the photo on the right the pipe and the top tank.

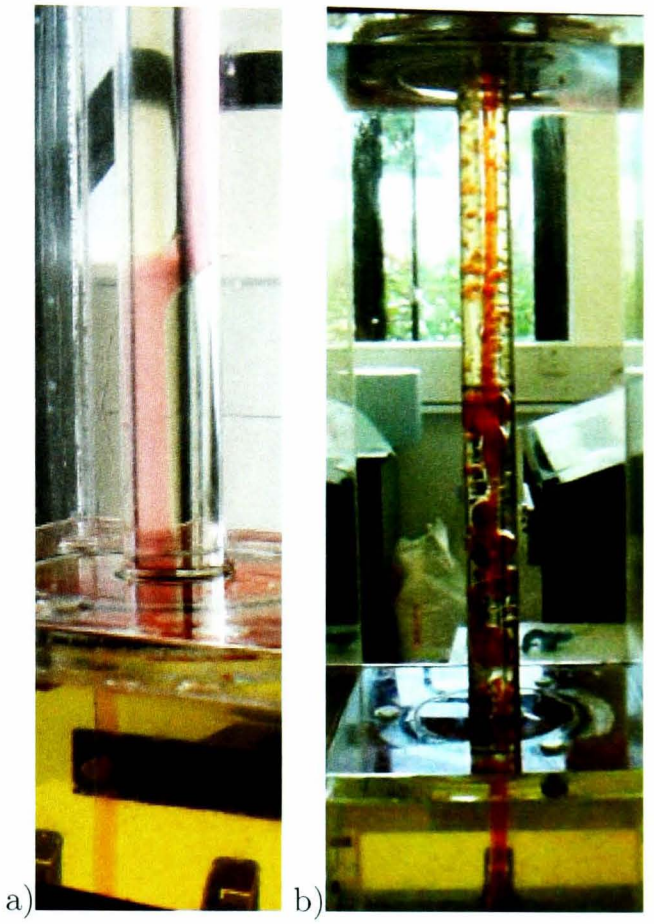

Figure B.9: Examples of the flow pattern developed in vertical pipes. a) Stream of glycerol flowing next to the wall and swapping the sides (801a). b) Thread of golden syrup (diluted) in the upper part of the pipe and blobs in the lower part descending through oil (807a).

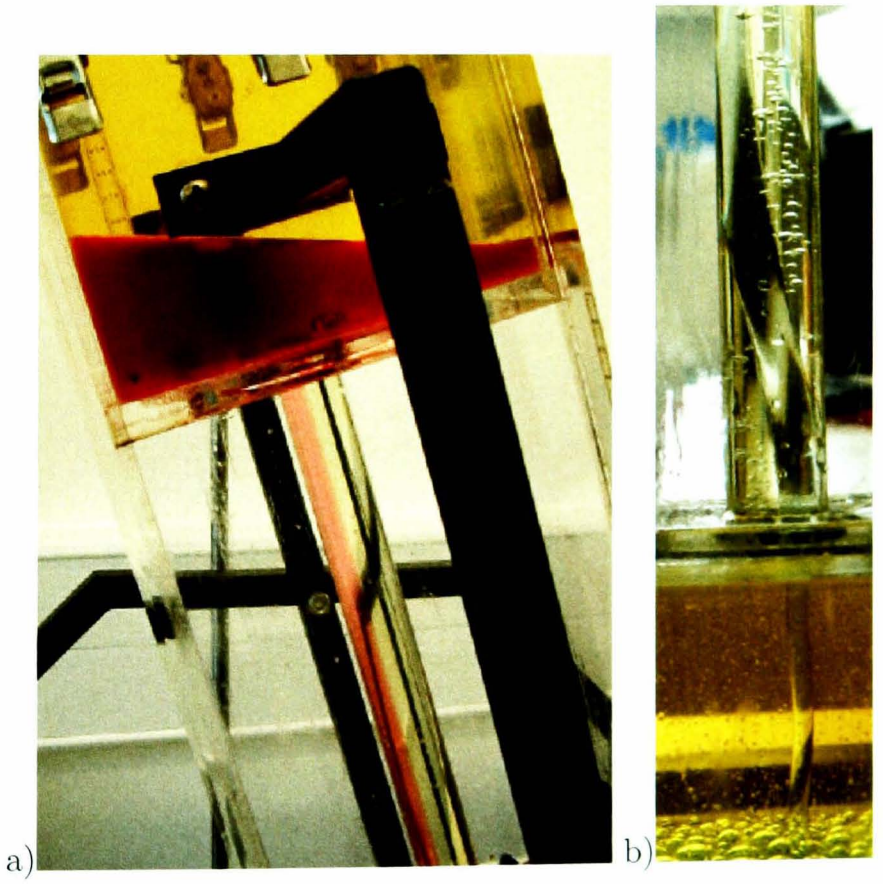

Figure B.10: Examples of the flow pattern developed in inclined pipes. a) stratified flow of oil on top of diluted golden syrup (801b). b) undulating stream of glycerol descending next to the wall (814b).

a)

b)

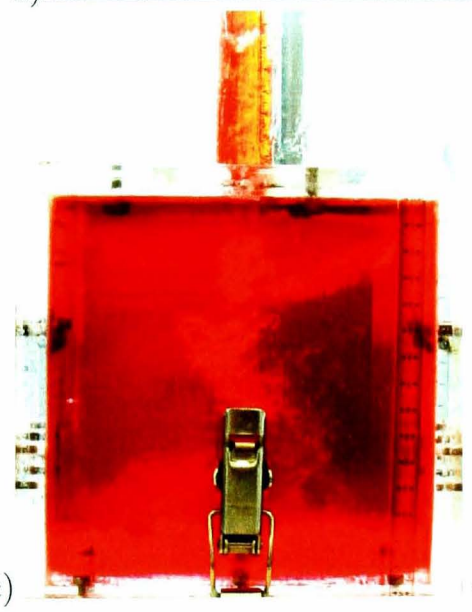

c)

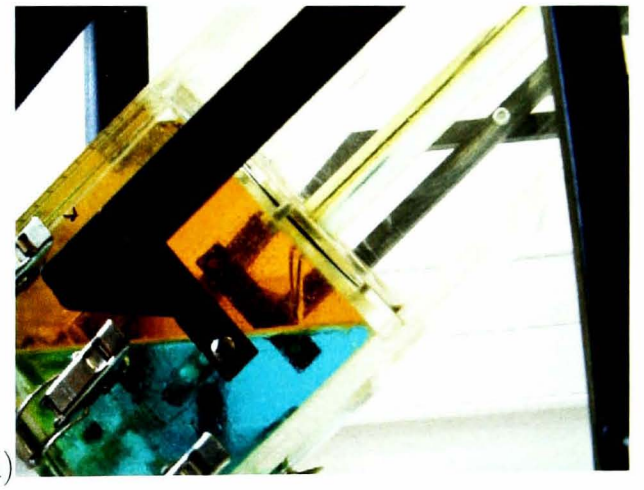

d)

Figure B.11: Examples of flow patterns developed in the top and bottom tanks: a) laminar stream of oil flowing through water in the top tank (exp. 427c), b) bubbles of water connected by a tiny thread rising through pure glycerol (exp. 816a), c) turbulent plume of glycerol mixing with water in the bottom tank, and d) laminar stream of water sinking through corn oil (exp. 427b).

References

Adams, N. K., Houghton, B. F., and Hildreth, W. (2006). Abrupt transitions during sustained explosive eruptions: examples from the 1912 eruption of Novarupta, Alaska. *Bulletin of Volcanology*, **69**, 189–206.

Allard, P., Carbonnelle, J., Mètrich, N., Loyer, H., and Zettwoog, P. (1994). Sulphur output and magma degassing budget of Stromboli volcano. *Nature*, **368**, 326-329.

Allard, P., Burton, M., and Mure, F. (2005). Spectroscopic evidence for a lava fountain driven by previously accumulated magmatic gas. *Nature*, **433**, 407–410.

Andres, R. and Kasgnoc, A. (1998). A time-averaged inventory of subaerial volcanic sulfur emissions. *Journal of Geophysical Research*, **103**(D19), 22,251–25,261.

Andres, R. and Schmid, J. (2001). The effects of volcanic ash on COSPEC measurements. *Journal of Volcanology and Geothermal Research*, **108**, 237–244.

Andronico, D., Branca, S., Calvari, S., Burton, M., Caltabiano, T., Corsaro, R. A., Carlo, P. D., Garfi, G., Lodato, L., Miraglia, L., Murè, F., Neri, M., Pecora, E., Pompilio, M., Salerno, G., and Spampinato, L. (2005). A multi-disciplinary study of the 2002-03 Etna eruption: insights into a complex plumbing system. *Bulletin of Volcanology*, **67**, 314-330.

Arakeri, J. H., Avila, F. E., Dada, J. M., and Tovar, R. O. (2000). Convection in a long vertical tube due to unstable stratification- a new type of turbulent flow *Current Science*, **79**(6), 859–866.

Arney, M., Bai, R., Guevara, E., Joseph, D., and Liu, K. (1993). Friction factor and holdup studies for lubricated pipelining-I. *International Journal of Multiphase Flow*, **19**(6), 1061-1076.

Aster, R., Mah, S., Kyle, P., McIntosh, W., Dunbar, N., Johnson, J., Ruiz, M., and Mc-

Namara, S. (2003). Very long period oscillations of Mount Erebus volcano. *Journal of Geophysical Research*, **108**(B11), 2522–2544.

Bani, P. and Lardi, M. (2007). Sulphur dioxide emission rates from Yasur volcano, Vanuatu archipielago. *Geophysical Research Letters*, **34**(L20309).

Bannwart, A. C. (2001). Modeling aspects of oil–water core–annular flows. *Journal of Petroleum Science and Engineering*, **32**(2-4), 127–143.

Barker, S. R., Sherrod, D. R., Lisowski, M., Heliker, C., and Nakata, J. S. (2003). Correlation between lava-pond drainback, seismicity, and ground deformation at Pu'u Ö'ö. In C. Heliker, D. A. Swanson, and T. J. Takahashi, editors, *The Pu'u Ö'ö-Küpaianaha Eruption of Kilauea Volcano, Hawai'i: The First 20 Years*, U.S. Geological Survey Professional Paper 1676, pages 53–62.

Batchelor, G. (1967). *An Introduction to Fluid Dynamics*. Cambridge University Press, 2nd edition. 615p.

Bertagnini, A., Métrich, N., Landi, P., and Rosi, M. (2003). Stromboli volcano (Aeolian Archipelago, Italy): An open window on the deep-feeding system of a steady state basaltic volcano. *Journal of Geophysical Research*, **108**(B7), 2336–2350.

Bird, R. B., Stewart, W. E., and Lightfoot, E. N. (1960). *Transport Phenomena*. John Wiley and Sons, Inc., 1st edition. 780p.

Blackburn, E., Wilson, L., and Sparks, R. (1976). Mechanisms and dynamics of strombolian activity. *Journal of the Geological Society of London*, **132**, 429–440.

Blake, S. and Campbell, I. (1986). The dynamics of magma–mixing during flow in volcanic conduits. *Contributions to Mineralogy and Petrology*, **94**, 72–81.

Bluth, G., Shannon, J. M., Watson, I., Prata, A., and Realmuto, V. (2007). Development of an ultra-violet digital camera for volcanic SO_2 imaging. *Journal of Volcanology and Geothermal Research*, **161**, 47–56.

Bohm, M., Luth, S., Echtler, H., Asch, G., Bataille, K., Bruhn, C., Rietbrock, A., and Wigger, P. (2002). The Southern Andes between 36 and 40 S latitude: seismicity and average seismic velocities. *Tectonophysics*, **356**, 275–289.

Booth, B. and Walker, G. (1973). Ash deposits from the new explosion crater, Etna 1971. *Philosophical Transactions of the Royal Society of London A*, **274**, 147–161.

Brandeis, G. and Jaupart, C. (1986). On the interaction between convection and crystallization in cooling magma chambers. *Earth and Planetary Science Letters*, **77**, 145–161.

Brauner, N. (1998). Liquid-liquid two-phase flow. *Heat Exchanger Design Update*, **5**(1), 1–40.

Brauner, N. and Maron, D. M. (1992). Stability analysis of stratified liquid-liquid flow. *International Journal of Multiphase Flow*, **18**(1), 103–121.

Brauner, N., Maron, D. M., and Rovinsky, J. (1998). A two-fluid model for stratified flows with curved interfaces. *International Journal of Multiphase Flow*, **24**, 975–1004.

Brown, C. (2000). Ultraviolet, visible, and near-infrared spectrophotometers. *Applied Spectroscopy Reviews*, **35**(3), 151–173.

Burgi, P.-Y., Caillet, M., and Haefeli, S. (2002). Field temperature measurements at Erta 'Ale Lava Lake, Ethiopia. *Bulletin of Volcanology*, **64**, 472–485.

Burrows, J. P., Richter, A., Dehn, A., Deters, B., Himmelmann, S., Voigt, S., and Orphal, J. (1999). Atmospheric remote-sensing reference data from GOME —2. temperature-dependent absorption cross sections of O_3 in the 231—794 nm range. *Journal of Quanitative Spectroscopy and Radiative Transfer*, **61**(4), 509–517.

Burton, M. R., Allard, P., Murè, F., and La Spina, A. (2007a). Magmatic gas composition reveals the source of Strombolian explosive activity. *Science*, **317**, 227–230.

Burton, M. R., Mader, H., and Polacci, M. (2007b). The role of gas percolation in quiescent degassing of persistently active basaltic volcanoes. *Earth and Planetary Science Letters*, **264**, 46–60.

Calder, E. S., Harris, A. J. L., Peña, P., Pilger, E., Flynn, L. P., Fuentealba, G., and Moreno, H. (2004). Combined thermal and seismic analysis of the Villarrica volcano lava lake, Chile. *Revista Geológica de Chile*, **31**(2), 259–272.

Calvari, S., Spampinato, L., and Lodato, L. (2006). The 5 April 2003 vulcanian paroxysmal explosion at Stromboli volcano (Italy) from field observations and thermal data. *Journal of Volcanology and Geothermal Research*, **149**(1-2), 160–175.

Campbell, I. H. and Turner, J. S. (1986). The influence of viscosity on fountains in magma chambers. *Journal of Petrology*, **27**(1), 1–30.

Carbone, D., G., B., and Grecco, F. (2003). Bulk processes prior to the 2001 Mount Etna eruption, highlighted through microgravity studies. *Journal of Geophysical Research*, **108**(B12, 2556).

Cardoso, S. S. and Woods, A. W. (1999). On convection in a volatile-saturated magma. *Earth and Planetary Science Letters*, **168**, 301–310.

Carniel, R., Di Cecca, M., and Rouland, D. (2003). Ambrym, Vanuatu (July-August 2000): spectral and dynamical transitions on the hours-to-days timescale. *Journal of Volcanology and Geothermal Research*, **128**, 1–13.

Carroll, M. R. and Blank, J. G. (1997). The solubility of H_2O in phonolitic melts. *American Mineralogist*, **82**, 549–556.

Casertano, L. (1963). Activity of Villarrica volcano in the current century. *Boletín Universidad de Chile*, **40**, 22–28, 48–54. (in Spanish).

Chester, D., Duncan, A., Guest, J., and Kilburn, C. (1985). *Mount Etna: the anatomy of a volcano*. Chapman and Hall Ltd.

Chouet, B., Hamisevicz, N., and McGetchin, T. R. (1974). Photoballistics of volcanic jet activity at Stromboli, Italy. *Journal of Geophysical Research*, **79**(32), 4961–4976.

Chouet, B., Saccorotti, G., Dawson, P., Martini, M., Scarpa, R., Luca, G. D., Milana, G., and Cattaneo, M. (1999). Broadband measurements of the source of explosions at Stromboli volcano, Italy. *Geophysical Research Letters*, **26**(13), 1937–1940.

Chouet, B., Dawson, P., Ohminato, T., Martini, M., Saccorotti, G., Giudicepietro, F., De Luca, G., Milana, G., and Scarpa, R. (2003). Source mechanisms of explosions at Stromboli volcano, Italy, determined from moment-tensor inversions of very-long-period data. *Journal of Geophysical Research*, **108**(B1), 2019.

Clavero, J. and Moreno, H. (2004). Evolution of Villarrica volcano. In L. E. Lara and J. Clavero, editors, *Villarrica volcano (39.5° S), Southern Andes, Chile*. Servicio Nacional de Geología y Minería, Boletín No. 61, pages 17–27.

Clift, R., Grace, J., and Weber, M. (1978). *Bubbles, drops, and particles*. Academic Press, Inc.

Croce, G. and DíAgaro, P. (2005). Numerical simulation of roughness effect on microchannel heat transfer and pressure drop in laminar flow. *Journal of Physics D: Applied Physics*, **38**, 1518ñ1530.

Debacq, M., Fanguet, V., Hulin, J., Salin, D., and Perrin, B. (2001). Self-similar concentration profiles in buoyant mixing of miscible fluids in a vertical tube. *Physics of Fluids*, **13**(11), 3097–3100.

Debacq, M., Hulin, J., Salin, D., Perrin, B., and Hinch, E. (2003). Buoyant mixing of miscible fluids of varying viscosities in vertical tubes. *Physics of Fluids*, **15**(12), 3846–3855.

Dixon, E., Clague, D., and Stolper, E. (1991). Degassing history of water, sulphur and carbon in submarine lavas from Kilauea volcano, Hawaii. *Journal of Geology*, **99**, 371–394.

Dixon, J. E. (1997). Degassing of alkalic basalts. *American Mineralogist*, **82**, 368–378.

Dixon, J. E. and Stolper, E. M. (1995). An experimental study of water and carbon dioxide solubilities in Mid-Ocean Ridge Basaltic liquids. part II: applications to degassing. *Journal of Petrology*, **36**(6), 1633–1646.

Dixon, J. E., Stolper, E. M., and Holloway, J. (1995). An experimental study of water and carbon dioxide solubilities in Mid-Ocean Ridge Basaltic liquids. part I: calibration and solubility models. *Journal of Petrology*, **36**(6), 1607–1631.

Duffell, H. J., Oppenheimer, C., Pyle, D. M., Galle, B., McGonigle, A. J., and Burton, M. R. (2003). Changes in gas composition prior to a minor explosive eruption at Masaya volcano, Nicaragua. *Journal of Volcanology and Geothermal Research*, **126**, 327–229.

Edmonds, M., Herd, R., Galle, B., and Oppenheimer, C. (2003). Automatic, high time-resolution measurements of SO_2 flux at Soufrière Hills volcano, Montserrat. *Bulletin of Volcanology*, **65**, 578–586.

Elias, T. and Sutton, A. J. (2007). Sulfur dioxide emission rates from Kilauea volcano, Hawaii, an update: 2002-2006. U.S. Geological Survey: Open-file Report 2007-1114, 37 p.

Elias, T., Sutton, A. J., Oppenheimer, C., Horton, K. A., Garbeil, H., Tsanev, V., McGonigle, A. J. S., and Williams-Jones, G. (2006). Comparison of COSPEC and two miniature

ultraviolet spectrometer systems for SO_2 measurements using scattered sunlight. *Bulletin of Volcanology*, **68**, 313–322.

Endo, T. and Murray, T. (1991). Real-time seismic amplitude measurement (RSAM): A volcano monitoring and prediction tool. *Bulletin of Volcanology*, **53**, 533–545.

Fairuzov, Y. (2003). Transient gravity-driven countercurrent two-phase liquid-liquid flow in horizontal and inclined pipes. *International Journal of Multiphase flow*, **29**, 1759–1769.

Falsaperla, S., Alparone, S., D'Amico, S., Granzia, G., Ferrari, F., Langer, H., Sgroi, T., and Spampinato, S. (2005). Volcanic tremor at Mt. Etna, Italy, preceding and accompanying the eruption of July-August, 2001. *Pure and Applied Geophysics*, **162**, 2111–2132.

Fischer, T. P., Roggensack, K., and Kyle, P. R. (2002). Open and almost shut case for explosive eruptions: vent processes determined by SO_2 emission rates at Karymsky Volcano, Kamchatka. *Geology*, **30**(12), 1059–1062.

Francalanci, L., Tommasini, S., and Conticelli, S. (2004). The volcanic activity of Stromboli in the 1906-1998 AD period: mineralogical, geochemical and isotope data relevant to the understanding of the plumbing system. *Journal of Volcanology and Geothermal Research*, **131**, 179–211.

Francalanci, L., Davies, G., Lustenhouwer, W., Tommasini, S., Mason, P., and Conticelli, S. (2005). Intra-gran Sr isotope evidence for crystal recycling and multiple magma reservoirs in the recent activity of Stromboli volcano, southern Italy. *Journal of Petrology*, **46**(10), 1997–2021.

Fuentealba, G. and Peña, P. (1998). Instalación y puesta en funcionamiento del sistema de monitoreo sismológico del volcán Villarrica, durante el primer semestre de 1998. Unpublished, Servicio Nacional de Geología y Minería. 13p.

Fuentealba, G., Peña, P., and Calder, E. (2000). Sustained tremor, open system degassing and annual perturbations at the Villarrica volcano lava lake, Chile. In *Congreso Geológico Chileno, No. 9, Actas*, volume 2, pages 26–29, Puerto Varas, Chile.

Fujita, E. (2008). Banded tremor at Miyakejima volcano, Japan: Implications for two-phase flow instability. *Journal of Geophysical Research*, **113**(B04207).

Galle, B., Oppenheimer, C., Geyer, A., McGonigle, A., Edmonds, M., and Horrocks, L. (2002). A miniaturised ultraviolet spectrometer for remote sensing of SO_2 fluxes: a new tool for volcano surveillance. *Journal of Volcanology and Geothermal Research*, **119**(1), 241–254.

Gerlach, T. (2003). Elevation effects in volcano applications of the COSPEC. In C. Oppenheimer, D. Pyle, and J. Barclay, editors, *Volcanic Degassing*, pages 169–175. Geological Society, London, Special Publication, 213.

Gerlach, T., Westrich, H., and Symonds, R. (1996). Preeruption vapor in magma of the climactic Mount Pinatubo eruption: source of the giant stratospheric sulfur dioxide cloud. In C. Newhall and R. Punongbayan, editors, *Fire and Mud: Eruptions and Lahars of Mount Pinatubo, Philippines*, pages 415–433. PHIVOLCS, Quezon City and University of Washington Press, Seattle.

Gerlach, T. M. (1986). Exsolution of H_2O, CO_2, and S during eruptive episodes at Kilauea volcano, Hawaii. *Journal of Geophysical Research*, **91**, 12177–12185.

Ghiorso, M. S. and Sack, R. O. (1995). Chemical mass transfer in magmatic processes: IV. a revised and internally consistent thermodynamic model for the interpolation and extrapolation of liquid-solid equilibria in magmatic systems at elevated temperatures and pressures. *Contributions to Mineralogy and Petrology*, **119**, 197–212.

Giberti, G., Jaupart, C., and Sartoris, G. (1992). Steady-state operation of Stromboli volcano, Italy: constraints on the feeding system. *Bulletin of Volcanology*, **54**, 535–541.

Giordano, D. and Dingwell, D. B. (2003). Viscosity of hydrous Etna basalt: implications for Plinian-style basaltic eruptions. *Bulletin of Volcanology*, **65**, 8–14.

Gurenko, A., Belousov, A., Trumbull, R., and Sobolev, A. (2005). Explosive basaltic volcanism of the Chikurachki volcano (Kurile arc, Russia): insights on pre-eruptive magmatic conditions and volatile budget revealed from phenocryst-hosted melt inclusions and groundmass glasses. *Journal of Volcanology and Geothermal Research*, **147**, 203–232.

Hamilton, D., Burnham, C., and Osborn, E. (1964). The solubility of water and effects of oxygen fugacity and water content on crystallisation in mafic magmas. *Journal of Petrology*, **5**, 21–39.

Harris, A. J. L. and Ripepe, M. (2007a). Synergy of multiple geophysical approaches to unravel explosive eruption conduit and source dynamics: A case study from Stromboli. *Chemie der Erde Geochemistry*, **67**, 1–35.

Harris, A. J. L. and Ripepe, M. (2007b). Temperature and dynamics of degassing at Stromboli. *Journal of Geophysical Research*, **112**(B03205).

Harris, A. J. L., Carniel, R., and Jones, J. (2005). Identification of variable convective regimes at Erta Ale lava lake. *Journal of Volcanology and Geothermal Research*, **142**, 207–223.

Head, J. and Wilson, L. (1987). Lava fountain heights at Pu'u'O'o, Kilauea, Hawaii: indicators of amount and variations of exsolved magma volatiles. *Journal of Geophysical Research*, **92**, 13715–13719.

Hearn, C. H. and Joens, J. A. (1991). The near U.V. absorption spectrum of CS_2 and SO_2 at 300 K. *Journal of Quanitative Spectroscopy and Radiative Transfer*, **45**(2), 69–75.

Hickey-Vargas, R., López-Escobar, L., Moreno, H., Clavero, J., Lara, L., and Sun, M. (2004). Magmatic evolution of the villarrica volcano. In L. E. Lara and J. Clavero, editors, *Villarrica volcano (39.5° S), Southern Andes, Chile*, Servicio Nacional de Geología y Minería, Boletín No. 61, pages 39–45.

Hickox, C. E. (1971). Instability due to viscosity and density stratification in axisymmetric pipe flow. *Physics of Fluids*, **14**(2), 251–262.

Horton, K., Williams-Jones, G., Garbeil, H., Elias, T., Sutton, A., Mouginis-Mark, P., Porter, J., and Clegg, S. (2006). Real-time measurement of volcanic SO_2 emissions: Validation of a new UV correlation spectrometer (FLYSPEC). *Bulletin of Volcanology*, **68**, 323–327.

Hui, H. and Zhang, Y. (2007). Toward a general viscosity equation for natural anhyrdrous and hydrous silicate melts. *Geochimica et Cosmochimica Acta*, **71**, 403–416.

Huppert, H. E. and Hallworth, M. A. (2007). Bi-directional flows in constrained systems. *Journal of Fluid Mechanics*, **578**, 95–112.

Ida, Y. (1995). Magma chamber and eruptive processes at Izu-Oshima volcano, Japan:buoyancy control of magma migration. *Journal of Volcanology and Geothermal Research*, **66**, 53–67.

Ingle, V. and Proakis, J. (2000). *Digital Signal Procesing using MATLAB*. BookWare Companion Series. Brooks/Cole.

James, M., Lane, S., Chouet, B., and Gilbert, J. (2004). Pressure changes associated with the ascent and bursting of gas slugs in liquid-filled vertical and inclined conduits. *Journal of Volcanology and Geothermal Research*, **129**, 61–82.

Jaupart, C. and Tait, S. (1990). Dynamics of eruptive phenomena. In J. Nicholls and J. Russell, editors, *Modern Methods of Igneous Petrology: Understanding Magmatic Processes*, volume 24 of *Reviews in Mineralogy*, chapter 8, pages 213–238. Mineralogical Society of America.

Jaupart, C. and Vergniolle, S. (1988). Laboratory models of Hawaiian and Strombolian eruptions. *Nature*, **331**, 58–60.

Jaupart, C. and Vergniolle, S. (1989). The generation and collapse of foam layer at the roof of a basaltic magma chamber. *Journal of Fluid Mechanics*, **203**, 347–380.

Johnson, J. B., Lees, J. M., and Gordeev, E. I. (1998). Degassing explosions at Karymsky volcano, Kamchatka. *Geophysical Research Letters*, **25**(21), 3999–4002.

Johnson, J. B., Aster, R. C., and Kyle, P. R. (2004). Volcanic eruptions observed with infrasound. *Geophysical Research Letters*, **31**, L14604.

Johnston, A. (1984). An investigation into the interfacial shear stress contribution in two-phase stratified flow. *International Journal of Multiphase Flow*, **10**(3), 371–383.

Joseph, D., Bai, R., Chen, K., and Y.Y., R. (1997). Core-annular flows. *Annual Review of Fluid Mechanics*, **29**, 65–90.

Joseph, D. D. and Renardy, Y. Y. (1993a). *Fundamentals of Two-Fluid Dynamics. Part I: Mathematical theory and applications*, volume 3 of *Interdisciplinary Applied Mathematics*. Springer-Verlag.

Joseph, D. D. and Renardy, Y. Y. (1993b). *Fundamentals of Two-Fluid Dynamics. Part II: Lubricated transport, drops and miscible liquids*, volume 4 of *Interdisciplinary Applied Mathematics*. Springer-Verlag.

Kadik, A., Lukanin, O., Lebedev, Y., and Korovughkina. E. (1972). Solubility of H_2O and CO_2 in granie and basalt melts at high pressures. *Geochemistry International*. **9**. 1041–1051.

Kalnay, E., M. Kanamitsu, R. K., Collins, W., Deaven, D., Gandin, L., Iredell, M., Saha. S., White, G., Woollen, J., Zhu, Y., A. Leetmaa and, B. R., Chelliah. M., Ebisuzaki. W., Higgins, W., Janowiak, J., Mo, K., Ropelewski, C., Wang, J., Jenne, R., and Joseph. D. (1996). The NCEP/NCAR 40-year reanalysis project. *Bulletin of the American Meteorological Society*, **77**(3), 437–471.

Kaminuma, K., Miura, S., and Dibble, R. R. (1988). A process of Mount Erebus eruption. *Proceedings of the NIPR symposium on Antarctic geosciences*, **2**(7-16).

Kazahaya, K., Shinohara, H., and Saito, G. (1994). Excessive degassing of Izu-Oshima volcano: magma convection in a conduit. *Bulletin of Volcanology*, **56**, 207–216.

Koyaguchi, T. and Blake, S. (1989). The dynamics of magma mixing in a rising magma batch. *Bulletin of Volcanology*, **52**, 127–137.

Koyaguchi, T., Hallworth, M. A., and Huppert, H. E. (1993). An experimental study on the effects of phenocrysts on convection in magmas. *Journal of Volcanology and Geothermal Research*, **55**, 15–32.

Koyanagi, R., Chouet, B., and Aki, K. (1987). Origin of volcanic tremor in Hawaii, Part I, Data from the Hawaiian Volcano Observatory 1969–1985. In R. W. Decker, T. L. Wright, and P. H. Stauffer, editors, *Volcanism in Hawaii*, U.S. Geological Survey Professional Paper 1350, chapter 45, pages 1221–1258.

Kyle, P., Sybeldon, L., McIntosh, W., Meeker, K., and Symonds, R. (1994). Sulfur dioxide emission rates from Mount Erebus, Antartica. In P. Kyle, editor, *Volcanological and Environmental Studies of Mount Erebus, Antartica.*, volume 66 of *Antartic Research Series*, pages 69–82.

Lange, R. A. (1997). A revised model for the density and thermal expansivity of K_2O-Na_2O-CaO-MgO-Al_2O_3-SiO_2 liquids from 700 to 1900 K: extension to crustal magmatic temperatures. *Contributions to Mineralogy and Petrology*, **130**, 1–11.

Lange, R. A. and Carmichael, I. S. E. (1990). Thermodynamic properties of silicate liquids

with emphasis on density, thermal expansion and compressibility. *Review of Mineralogy*, **24**, 25–59.

Lautze, N. C. and Houghton, B. F. (2007). Linking variable explosion style and magma textures during 2002 at Stromboli volcano, Italy. *Bulletin of Volcanology*, **69**, 445–460.

Lavallée, Y., Hess, K.-U., Cordonnier, B., and Dingwell, D. B. (2007). Non-newtonian rheological law for highle crystalline dome lavas. *Geology*, **35**(9), 843–846.

Lavenu, A. and Cembrano, J. (1999). Compressional and transpressional-stress pattern for Pliocene and Quaternary brittle deformation in fore arc and intra-arc zones (Andes of Central and Southern Chile). *Journal of Structural Geology*, **21**, 1669–1691.

Lejeune, A. M. and Richet, P. (1995). Rheology od crystal-bearing silicate melts: an experimental study at high viscosities. *Journal of Geophysical Research*, **100**, 4215–4229.

Leonardi, S., Gresta, S., and Mulargia, F. (2000). Cross-correlation between volcanic tremor and SO_2: Flux data from Mount Etna volcano, 1987-1992. *Physics and Chemistry of the Earth (A)*, **25**(9-11), 737–740.

Lienhard-IV, J. H. and Lienhard-V, J. H. (2006). *A heat transfer textbook*. Phlogiston Press, 3rd edition.

Liu, Y., Zhang, Y., and Behrens, H. (2004). Solubility of H_2O in rhyolitic melts at low pressures and a new empirical model to predict H_2O and CO_2 solubility in rhyolitic melts. *Journal of Volcanology and Geothermal Research*, **143**, 219–235.

Llewellin, E., Mader, H., and Wilson, S. (2002). The rheology of a bubble liquid. *Proccedings of the Royal Society of London A*, **458**, 987–1016.

Locke, C. A., Rymer, H., and Cassidy, J. (2003). Magma transfer processes at persistently active volcanoes: insights from gravity observations. *Journal of Volcanology and Geothermal Research*, **127**, 73–86.

López-Escobar, L., Cembrano, J., and Moreno, H. (1995). Geochemistry and tectonics of the Chilean Southern Andes basaltic Quaternary volcanism (37°-46° S). *Revista Geológica de Chile*, **22**(2), 219–234.

Mandal, T. K., Chakrabarti, D. P., and Das, G. (2007). Oil water flow through different diameter pipes: Similarities and differences. *Chemical Engineering Research and Design*, **85**(A8), 1123–1128.

Manga, M. (1996). Waves of bubbles in basaltic magmas and lavas. *Journal of Geophysical Research*, **101**(B8), 17,457–17,465.

Manga, M. and Loewenberg, M. (2001). Viscosity of magmas containing highly deformable bubbles. *Journal of Volcanology and Geothermal Research*, **105**, 19–24.

Marsh, B. (1981). On the crystallinity, probability of occurrence and rheology of lava and magma. *Contributions to Mineralogy and Petrology*, **78**, 85–98.

Massart, D., Vandeginste, B., Deming, S., Michotte, Y., and Kaufman, L. (1988). *Chemometrics: a textbook*. Elsevier. Data Handling in Science and Technology, Volume 2.

Massey, B. S. (2006). *Mechanics of Fluids*. Taylor and Francis, 8th edition. 696p.

Mastin, L. and Ghiorso, M. (2000). A numerical program for steady-state flow of magma-gas mixtures through vertical eruptive conduits. Open-File Report 00-209, U.S. Geological Survey.

Mather, T. A., Tsanev, V. I., Pyle, D. M., McGonigle, A. J. S., Oppenheimer, C., and Allen, A. G. (2004). Characterization and evolution of tropospheric plumes from Láscar and Villarrica volcanoes, Chile. *Journal of Geophysical Research (Atmospheres)*, **109**(D18), D21303.

McGonigle, A. and Oppenheimer, C. (2003). Optical sensing of volcanic gas and aerosol emissions. In C. Oppenheimer, D. Pyle, and J. Barclay, editors, *Volcanic Degassing*, pages 149–168. Geological Society, London, Special Publication, 213.

McGonigle, A. J. S., Oppenheimer, C., Hayes, A. R., Galle, B., Edmonds, M., , Caltabiano, T., Salerno, G., Burton, M., and Mather, T. A. (2003). Sulphur dioxide fluxes from Mount Etna, Vulcano, and Stromboli measured with an automated scanning ultraviolet spectrometer. *Journal of Geophysical Research*, **108**(B9), 2455.

McGreger, A. D. and Lees, J. M. (2004). Vent discrimination at Stromboli volcano, Italy. *Journal of Volcanology and Geothermal Research*, **137**, 169–185.

McNutt, S. (2000). Seismic Monitoring. In H. Sigurdsson, J. Stix, B. Houghton, S. R. McNutt, and H. Rymer, editors, *Encyclopedia of Volcanoes*, pages 1095–1119. Academic Press.

McNutt, S. R. (2005). Volcanic seismology. *Annual Review of Earth and Planetary Sciences*, **32**, 461–491.

McGonigle, A., Thomson, C., Tsanev, V., and Oppenheimer, C. (2004). A simple technique for measuring power station SO_2 and NO_2 emissions. *Atmospheric Environment*, **38**, 21–25.

Métaxian, J., Lesage, P., and Dorel, J. (1997). Permanent tremor of Masaya volcano, Nicaragua: wave field analysis and source location. *Journal of Geophysical Research*, **102**(B10), 22529–22545.

Métrich, N., Bertagnini, A., Landi, P., and Rosi, M. (2001). Crystallization driven by decompression and water loss at Stromboli volcano (Aeolian islands, Italy). *Journal of Petrology*, **42**(8), 1471–1490.

Millán, M. (2007). Absorption correlation spectroscopy. In G. Williams-Jones, J. Stix, and C. Hickson, editors, *The COSPEC cookbook. Making SO_2 gas measurements at active volcanoes*, IAVCEI Methods in Volcanology.

Moore, G., Vennemann, T., and Carmichael, I. (1998). An empirical model for the solubility of H_2O in magmas to 3 kilobars. *American Mineralogist*, **83**, 36–42.

Moreno, H., Clavero, J., and Lara, L. (1994). Explosive post-glacial activity of Villarrica volcano, southern Andes (39°25' S). In *Congreso Geológico Chileno, No. 7, Actas*, volume 1, pages 329–333, University of Concepción, Chile. (in Spanish).

Mudde, R. F. (2005). Gravity-driven bubbly flows. *Annual Review of Fluid Mechanics*, **37**, 393–423.

Newman, S. and Lowenstern, J. B. (2002). VolatileCalc: a silicate melt-H_2O-CO_2 solution model written in Visual Basic for Excel. *Computers & Geosciences*, **28**, 597-604.

Ochs III, F. A. and Lange, R. A. (1997). The partial molar volume, thermal expansivity, and compressibility of H_2O in $AnAlSi_3O_8$ liquid: new measurements and an internally consistent model. *Contributions to Mineralogy and Petrology*, **129**, 155-165.

Oliemans, R. and Pots, B. (2006). Gas–liquid transport in ducts. In C. T. Crowe, editor, *Multiphase Flow Handbook*, Mechanical Engineering Series, chapter 2. Taylor & Francis.

Oppenheimer, C. and Yirgu, G. (2002). Thermal imaging of an active lava lake: Erta Ale volcano, Ethiopia. *International Journal of Remote Sensing*, **23**(22), 4777–4782.

Ortiz, R., Moreno, H., García, A., Fuentealba, G., Astiz, M., Peña, P., Sánchez, N., and Tárraga, M. (2003). Villarrica volcano (Chile): characteristics of the volcanic tremor and forecasting of small explosions by means of a material failure method. *Journal of Volcanology and Geothermal Research*, **128**, 247–259.

Papale, P. (1999). Modeling of the solubility of a two-component $H_2O + CO_2$ fluid in silicate liquids. *American Mineralogist*, **84**, 477–492.

Parfitt, E. and Wilson, L. (1995). Explosive volcanism IX. the transition between Hawaiian-style lava fountaining and strombolian explosive activity. *Geophysical Journal International*, **121**, 226–232.

Parfitt, E. A. (2004). A discussion of the mechanisms of explosive basaltic eruptions. *Journal of Volcanology and Geothermal Research*, **134**(1-2), 77–107.

Park, J.-W., Drew, D., and R.T. Lahey, J. (1998). The analysis of void wave propagation in adiabatic monodispersed bubbly two-phase flows using an ensemble-averaged two-fluid model. *International Journal of Multiphase Flow*, **24**, 1205–1244.

Patrick, M. R., Harris, A. J. L., Ripepe, M., Dehn, J., Rothery, D. A., and Calvari, S. (2007). Strombolian explosive styles and source conditions: insights from thermal (FLIR) video. *Bulletin of Volcanology*, **69**(7), 769–784.

Petit-Breuilh, M. (1994). Contribución al conocimiento de la cronologia eruptiva del volcán Villarrica (39-25's) 1558-1985. *Revista de la Frontera*, **13**, 71–99.

Pineau, F., Shilobreeva, S., Kadik, A., and Javoy, M. (1998). Water solubility and D/H fractionation in the system basaltic andesite- H_2O at 1250°C and between 0.5 and 3 kbars. *Chemical Geology*, **147**, 173–184.

Platt, U. (1994). Differential optical absorption spectroscopy (DOAS). In M. Sigrist, editor, *Air monitoring by spectroscopic techniques. Chemical Analysis Series, vol. 127*, pages 27–84. Wiley, NewYork.

Prada, J. W. V. and Bannwart, A. C. (2001). Modeling of vertical core-annular flows and application to heavy oil production. *Journal of Energy Resources Technology*, **123** 3), 194–199.

Ripepe, M. (1996). Evidence for gas influence on volcanic seismic signal recorded at Stromboli. *Journal of Volcanology and Geothermal Research*, **70**, 221–233.

Ripepe, M. and Gordeev, E. (1999). Gas bubble dynamics model for shallow volcanic tremor at Stromboli. *Journal of Geophysical Research*, **104**, 10639–10654.

Ripepe, M. and Marchetti, E. (2002). Array tracking of infrasonic sources at Stromboli volcano. *Geophysical Research Letters*, **29**(22), 2076.

Ripepe, M., Poggi, P., Braun, T., and Gordeev, E. (1996). Infrasonic waves and volcanic tremor at Stromboli. *Geophysical Research Letters*, **23**(2), 181–184.

Ripepe, M., Coltelli, M., Provitera, E., Gresta, S., Moretti, M., and Piccinini, D. (2001a). Seismic and infrasonic evidences for an impulsive source of the shallow volcanic tremor at Mt. Etna, Italy. *Geophysical Research Letters*, **28**(6), 1071–1074.

Ripepe, M., Ciliberto, S., and Della-Schiava, M. (2001b). Time constraints for modeling source dynamics of volcanic explosions at Stromboli. *Journal of Geophysical Research*, **106**(B5), 8713–8727.

Ripepe, M., Harris, A. J. L., and Carniel, R. (2002). Thermal, seismic and infrasonic evidences of variable degassing rates at Stromboli volcano. *Journal of Volcanology and Geothermal Research*, **118**, 285–297.

Ripepe, M., Marchetti, E., Poggi, P., Harris, A. J. L., Fiaschi, A., and Ulivieri, G. (2004). Seismic, acoustic, and thermal network monitors the 2003 eruption of Stromboli volcano. *EOS Transactions, American Geophysical Union*, **85**(35).

Ripepe, M., Harris, A. J. L., and Marchetti, E. (2005). Coupled thermal oscillations in explosive activity at different craters of Stromboli volcano. *Geophysical Research Letters*, **32**, L17302. doi:10.1029/2005GL022711.

Rodríguez, L. A., Watson, I. M., Rose, W. I., Branan, Y. K., Bluth, G. J., Chigna, G., Matías, O., Escobar, D., Carn, S. A., and Fischer, T. P. (2004). SO_2 emissions to the atmosphere from active volcanoes in Guatemala and El Salvador, 1999–2002. *Journal of Volcanology and Geothermal Research*, **138**, 325–344.

Rosi, M. Bertagnini, A. and Landi, P. (2000). Onset of the persistent activity at Stromboli volcano (italy). *Bulletin of Volcanology*, **62**, 294–300.

Rowe, C., Aster, R., Kyle, P., Schlue, J., and Dibble, R. (1998). Broadband recording of strombolian explosions and associated very long period seismic signals on Mount Erebus volcano, Ross Island, Antarctica. *Geophysical Research Letters*, **25**, 2297–2300.

Rowe, C., Aster, R., Kyle, P., Dibble, R., and Schlue, J. (2000). Seismic and acoustic observations at Mount Erebus Volcano,Ross Island, Antarctica, 1994 ñ 1998. *Journal of Volcanology and Geothermal Research*, **101**, 105 ñ 128.

Rudman, M. (1992). Two-phase natural convection: implications for crystal settling in magma chambers. *Physics of the Earth and Planetary Interiors*, **72**, 153–172.

Rust, A. and Manga, M. (2002). Effects of bubble deformation on the viscosity of dilute suspensions. *Journal of Non-Newtonian Fluid Mechanics*, **104**, 53–63.

Rutherford, M. J. and Gardner, J. E. (2000). Rates of magma ascent. In H. Sigurdsson, B. Houghton, H. Rymer, J. Stix, and S. R. McNutt, editors, *Encyclopedia of Volcanoes*, pages 207–217. Academic Press.

Ryan, S. (1995). Quiescent outgassing of Mauna Loa volcano 1958-1994. In J. Rhodes and J. P. Lockwood, editors, *Mauna Loa Revealed: Structure, Composition, History, and Hazards*, number 92 in Geophysical Monograph, pages 95–115. American Geophysical Union.

Rymer, H., van Wyk de Vries, B., Stix, J., and Williams-Jones, G. (1998). Pit crater structure and processes governing persistent activity at Masaya volcano, Nicaragua. *Bulletin of Volcanology*, **59**, 345–355.

Salisbury, J. and D'Aria, D. (1992). Emissivity of terrestial materials in the 8-14 μm atmospheric window. *Remote Sensing of Environment*, **42**, 83–106.

Séon, T., Hulin, J., Salin, D., Perrin, B., and Hinch, E. (2004). Buoyant mixing of miscible fluids in tilted tubes. *Physics of Fluids*, **16**(12), L103–L106.

Séon, T., Hulin, J., Salin, D., Perrin, B., and Hinch, E. (2005). Buoyancy driven miscible front dynamics in tilted tubes. *Physics of Fluids*, **17**(031702).

Séon, T., Hulin, J., Salin, D., Perrin, B., and Hinch, E. (2006). Laser-induced fluorescence measurements of buoyancy driven mixing in tilted tubes. *Physics of Fluids*, 18(041701).

Settle, M. and McGetchin, T. (1980). Statistical analysis of persistent explosive activity at stromboli, 1971: implications for eruption prediction. *Journal of Volcanology and Geothermal Research*, **8**, 45–58.

Shibata, Y. and Kaminaga, F. (2001). Instability of interfacial waves on countercurrent two-phase flow in a vertical tube. *JSME International Journal Series B*, **44**(3), 352–360.

Shinohara, H. and Witter, J. (2005). Volcanic gases emitted during mild strombolian activity of Villarrica volcano, Chile. *Geophysical Research Letters*, **32**(20), L20308.1–L20308.5.

Silber-Li, Z., Cui, H., Tan, Y., and Tabeling, P. (2005). Flow characteristics of liquid with pressure-dependent viscosities in microtubes. *Acta Mechanica Sinica*, **12**, 1–5.

Simakin, A. and Botcharnikov, R. (2001). Degassing of stratified magma by compositional convection. *Journal of Volcanology and Geothermal Research*, **105**, 207–224.

Smith, B. C. (2002). *Quantitative Spectroscopy: Theory and Practice*. Academic Press.

Snyder, D. (2000). Thermal effects of the intrusion of basaltic magma into a more silicic magma chamber and implications for eruption triggering. *Earth and Planetary Science Letters*, **175**, 257–273.

Sparks, R. S. J. (2003). Dynamics of magma degassing. In C. Oppenheimer, D. Pyle, and J. Barclay, editors, *Volcanic Degassing*, volume 213, pages 5–22. Geological Society, London.

Sparks, R. S. J., Huppert, H. E., and Turner, J. S. (1984). The fluid dynamics of evolving magma chambers. *Philosophical Transactions of the Royal Society of London A*, **310**, 511–534.

Spera, F. J. (2000). Physical properties of magma. In H. Sigurdsson, B. Houghton, H. Rymer, J. Stix, and S. R. McNutt, editors, *Encyclopedia of Volcanoes*, pages 171–190. Academic Press.

Stevenson, D. and Blake, S. (1998). Modelling the dynamics and thermodynamics of volcanic degassing. *Bulletin of Volcanology*, **60**, 307–317.

Stix, J. (2007). Stability and instability of quiescently active volcanoes: the case of Masaya, Nicaragua. *Geology*, **35**(6), 535–538.

Stoiber, R. E., Malinconico, L. L., and Williams, S. N. (1983). Use of the correlation spectrometer at volcanoes. In H. Tazieff and J. C. Sabroux, editors, *Forecasting Volcanic Events*, pages 425–444. Amsterdam-New York.

Stolper, E. M. and Holloway, J. R. (1988). Experimental determinaion of the solubility of carbon dioxide in molten basalt at low pressure. *Earth and Planetary Science Letters*, **87**, 397–408.

Sutton, A. J., Elias, T., Gerlach, T. M., and Stokes, J. B. (2001). Implications for eruptive processes as indicated by sulfur dioxide emissions from Kilauea volcano, Hawai'i, 1979-1997. *Journal of Volcanology and Geothermal Research*, **108**, 283–302.

Symonds, R. B., Rose, W. I., Bluth, G. J., and Gerlach, T. (1994). Volcanic-gas studies: methods, results, and applications. In M. R. Carrol and J. Holloway, editors, *Volatiles in Magmas*, volume 30 of *Reviews in Mineralogy*, chapter 1, pages 1–66. Mineralogical Society of America.

Taddeucci, J., Pompilio, M., and Scarlato, P. (2004). Conduit processes during the July-August 2001 explosive activity of Mt. Etna (Italy): inferences from glass chemistry and crystal size distribution of ash particles. *Journal of Volcanology and Geothermal Research*, **137**, 33–54.

Tait, S. and Jaupart, C. (1989). Compositional convection in viscous melts. *Nature*, **338**, 571–574.

Taylor, E. S. (1974). *Dimensional analysis for engineers*. Oxford University Press.

Tazieff, H. (1994). Permanent lava lakes: observed facts and induced mechanisms. *Journal of Volcanology and Geothermal Research*, **63**, 3–11.

Thorburn, D. (1993). Principles of spectrophotometric measurements with particular reference to the UV-visible region. In B. Clark, T. Frost, and M. Russell, editors, *UV Spectroscopy. Techniques, instrumentation, data handling*, Techniques in Visible and Ultraviolet Spectrometry, Volume 4. Cahpman & Hall.

Tibaldi, A. (2003). Influence of cone morphology on dykes, Stromboli, Italy. *Journal of Volcanology and Geothermal Research*, **126**, 79–95.

Tibaldi, A., Corazzato, C., Apuani, T., and Cancelli, A. (2003). Deformation at Stromboli volcano (Italy) revealed by rock mechanics and structural geology. *Tectonophysics*, **361**, 187–204.

Ullmann, A., Zamir, M., Ludmer, Z., and Brauner, N. (2003). Stratified laminar countercurrent flow of two liquid phases in inclined tubes. *International Journal of Multiphase Flow*, **29**, 1583–1604.

Ullmann, A., Goldstein, A., Zamir, M., and Brauner, N. (2004). Closure relations for the shear stresses in two-fluid models for laminar stratified flow. *International Journal of Multiphase Flow*, **30**, 877–900.

Vaggelli, G., Francalanci, L., Ruggieri, G., and Testi, S. (2003). Persisten polybaric rests of calc-alkaline magmas at stromboli volcano, Italy: pressure data from fluid inclusions in restitic quartzite nodules. *Bulletin of Volcanology*, **65**, 385–404.

Vergniolle, S. (1996). Bubble size distribution in magma chambers and dynamics of basaltic eruptions. *Earth and Planetary Science Letters*, **140**, 269–279.

Vergniolle, S. and Jaupart, C. (1986). Separated two-phase flow and basaltic eruptions. *Journal of Geophysical Research*, **91**, 12842–12860.

Vergniolle, S. and Mangan, M. (2000). Hawaiian and Strombolian eruptions. In H. Sigurdsson, J. Stix, B. Houghton, S. R. McNutt, and H. Rymer, editors, *Encyclopedia of Volcanoes*, pages 447–461. Academic Press.

Wallace, P. and Anderson, A. (1998). Effect of eruption and lava drainback on the h2o contents of basaltic magmas at Kilauea volcano. *Bulletin of Volcanology*, **59**, 327–344.

Wallace, P. and Anderson, A. (2000). Volatiles in magmas. In H. Sigurdsson, B. Houghton, H. Rymer, J. Stix, and S. R. McNutt, editors, *Encyclopedia of Volcanoes*, pages 149–170. Academic Press.

Weinstein, S. A., Yuen, D. A., and Olson, P. L. (1988). Evolution of crystal-settling in magma-chamber convection. *Earth and Planetary Science Letters*, **87**, 237–248.

Williams-Jones, G., Stix, J., Heiligmann, M., Barquero, J., Fernandez, E., and Gonzalez, E. (2001). A model of degassing and seismicity at Arenal Volcano, Costa Rica. *Journal of Volcanology and Geothermal Research*, **108**, 121–139.

Williams-Jones, G., Rymer, H., and Rothery, D. A. (2003). Gravity changes and passive SO_2 degassing at the Masaya caldera complex, Nicaragua. *Journal of Volcanology and Geothermal Research*, **123**, 137–160.

Williams-Jones, G., Horton, K. A., Elias, T., Garbeil, H., Mouginis, P. J., Sutton, M. A. J., and Harris, A. J. L. (2006). Accurately measuring volcanic plume velocity with multiple UV spectrometers. *Bulletin of Volcanology*, **68**, 328–332.

Williams-Jones, G., Stix, J., and Nadeau, P. (2007). Using the COSPEC in the field. In G. Williams-Jones, J. Stix, and C. Hickson, editors, *The COSPEC cookbook. Making SO_2 gas measurements at active volcanoes*, IAVCEI Methods in Volcanology, pages 64–124.

Wilson, L. (1980). Relationships between pressure, volatile content and ejecta velocity in three types of volcanic explosion. *Journal of Volcanology and Geothermal Research*, **8**, 297–313.

Witter, J. B. and Calder, E. S. (2004). Magma degassing at Villarrica volcano. In L. E. Lara and J. Clavero, editors, *Villarrica volcano (39.5° S), Southern Andes, Chile*, Servicio Nacional de Geología y Minería, Boletín No. 61, pages 46–52.

Witter, J. B., Kress, V. C., Delmelle, P., and Stix, J. (2004). Volatile degassing, petrology, and magma dynamics of the Villarrica Lava Lake, Southern Chile. *Journal of Volcanology and Geothermal Research*, **134**, 303–337.

Wongwises, S., Khankaew, W., and Vetchsupakhun, W. (1998). Prediction of liquid holdup in horizontal stratified two-phase flow. *Thammasat International Journal of Science and Technology*, **3**(2), 48–59.

Worster, M. G., Huppert, H. E., and Sparks, S. J. (1990). Convection and crystallization in magma cooled from above. *Earth and Planetary Science Letters*, **101**, 78–89.

Xu, J., Cheng, P., and Zhao, T. (1999). Gas-liquid two-phase flow regimes in rectangular channels with mini/micro gaps. *International Journal of Multiphase Flow*, **25**, 411–432.

Young, S. R., Voight, B., and Duffell, H. J. (2003). Magma extrusion dynamics revealed by high-frequency gas monitoring at Soufriére Hills volcano, Montserrat. In C. Oppenheimer, D. Pyle, and J. Barclay, editors, *Volcanic Degassing*. Geological Society, London, Special Publication, 213. 219-230.

Zobin, V. (2003). *Introduction to Volcanic Seismology*. Elsevier Science B.V., first edition. 290p.